Dissertation

submitted to the

Combined Faculty of Mathematics, Engineering and Natural Sciences

of the Ruperto-Carola-University of Heidelberg,

Germany

for the degree of

Doctor of Natural Sciences
(Dr. rer. nat.)

submitted by

Tanja Schmitt

born in Schweinfurt (Germany)

Oral examination: March 3rd, 2023

Laser spectroscopy of functional materials

Referees: Prof. Dr. Petra Tegeder
Prof. Dr. Eva Blasco

Contents

Abstract . . . . . **VII**

Kurzfassung . . . . . **VIII**

Abbreviations . . . . . **X**

List of Figures . . . . . **XIV**

List of Tables . . . . . **XXII**

1. Introduction **1**

2. Theoretical Background **5**
2.1. Materials 5
2.1.1. Bulk and surface electronic states of metals 5
2.1.2. Organic semiconductors 7
2.1.3. Photochromism 8
2.2. Spectroscopic methods 9
2.2.1. One-photon photoemission 10
2.2.2. Two-photon photoemission 11
2.2.3. Temperature-programmed desorption 16
2.2.4. Kinetic linear spectroscopy 19
2.2.5. Transient absorption 20
2.2.6. Scanning near-field optical microscopy 24

3. Experimental Details **31**
3.1. Two-photon photoemission setup 31
3.1.1. UHV chamber and sample preparation 31
3.1.2. Laser system 35
3.1.3. Time of flight spectrometer 38
3.1.4. Data acquisition 40
3.2. Transient absorption setup 44
3.3. Linear optical spectroscopes 46
3.4. Scanning near-field optical microscope 47

4. 6,13-Diazapentacene on Au(111) **49**
4.1. Characterisation of the Au(111) metal substrate 50
4.2. Adsorption and desorption properties of DAP/Au(111) 52
4.3. Electronic structure of DAP on Au(111) 54

5. Orthogonal photoswitches **59**
5.1. Sample preparation 63
5.2. Steady state absorption 65
5.3. Transient absorption measurements 68
5.3.1. Non-polar solutions using toluene 68
5.3.2. Polar solutions using acetonitrile 86
5.3.3. Thin films using PMMA blends 102
5.3.4. Comparison of the TA results 121
5.4. UV/VIS kinetic measurements 128
5.4.1. Switching processes of Azo 129
5.4.2. Switching processes of DASA 139
5.5. IR kinetic studies of the switching processes of DASA 152
5.6. Summary of the results of the orthogonal photoswitches 163

6. Block copolymer **168**
6.1. IR characterisation of the blocks and the block copolymer 170
6.2. Microscopic structure of the block copolymer 172
6.3. 3D printed block copolymer 175

7. Conclusion **178**

References **183**

List of Publications, Conference contributions and supervised Theses . . . **207**

Acknowledgements **210**

Appendix **A1**
A. Data evaluation of 2PPE data A1
B. Photoswitches A4

Abstract

In a world of increasing energy consumption and man-made global warming, the knowledge of electronic and structural properties of organic materials is crucial for their implementation and use in innovative (smart) devices since those determine device performance. Herein, the electronic and structural properties of new promising materials are studied in detail utilising advanced laser spectroscopic techniques.
Considering optoelectronic devices such as organic field effect transistors and solar cells, the metal/organic interface plays an important role for device performance. Therefore, the electronic properties of an n-type semiconducting N-substituted pentacene derivative and its change at higher layer thicknesses in contact with a metal electrode is studied via two-photon photoemission spectroscopy as well as the adsorption and desorption properties via temperature-programmed desorption. Several molecular electronic states such as the highest occupied and the lowest unoccupied molecular orbital as well as the optical gap are thereby determined quantitatively.
Developing optoelectronic devices further, smart devices covering more complex needs can be achieved by implementing multiresponsive mixtures reacting in differentiated ways to light, which acts as sustainable external stimulus with high spatio-temporal resolution. Hence, the switching behaviour of a mixture of two individually as well as simultaneously addressable photoswitches is researched in detail. Furthermore, the investigated mixture is 3D printable allowing fast and easy implementation in 3D structures. The photoswitches are a push-pull azobenzene derivative and a first generation donor-acceptor Stenhouse adduct absorbing longer wavelengths in the visible region of the spectrum compared to the azobenzene derivative. All steps of the trans-to-cis isomerisation of the former and the linear-to-closed isomerisation of the latter photoresponsive molecule are studied as well as the respective back reactions with special emphasis on the environmental influence and the impact of the photoswitches on each other. Therefore, several techniques, such as femtosecond transient absorption, temperature dependent kinetic visible absorption and kinetic infrared absorption spectroscopy, are used to gain a full picture. Dynamic effects of the environment and the photoswitches on each other are thereby found such that individual switching of both molecules takes place with minor impacts on each other in the mixture.
Other 3D printable materials are diblock copolymers exhibiting microphase separation such as a derivative of a standard diblock copolymer for high-resolution nanolithography with additional functional groups allowing 3D printing. The lamellar structure and its regularity is studied by means of a scattering-scanning near-field optical microscope before and after 3D printing upon which a polymeric network is formed. Before printing, lamellae are thereby found whereas the printing process needs to be optimised to maintain this structure after 3D printing.

Kurzfassung

In einer Welt des zunehmenden Energieverbrauchs und der menschengemachten Erderwärmung ist die Kenntnis der elektronischen und strukturellen Eigenschaften von organischen Materialien entscheidend für deren Implementierung und Anwendung in innovativen (intelligenten) Geräten, da diese die Leistungsfähigkeit der Geräte bestimmt. Entsprechend werden die elektronischen und strukturellen Eigenschaften neuer vielversprechender Materialien unter Verwendung fortgeschrittener Laserspektroskopie im Detail untersucht.
Die Grenzfläche Metall/Organik spielt eine wichtige Rolle bei optoelektronischen Geräten wie organische Feldeffekttransistoren und Solarzellen. Daher werden die elektronischen Eigenschaften eines n-halbleitenden N-substituierten Pentacenderivats im Kontakt mit einer Metallelektrode bei unterschiedlichen Schichtdicken mittels zwei-Photonen Photoemissionsspektroskopie untersucht sowie die Adsorptions- und Desorptionseigenschaften mittels temperaturprogrammierter Desorption. Dabei werden mehrere molekulare elektronische Zustände wie das höchste besetzte und das niedrigste unbesetzte Molekülorbital sowie die optische Lücke quantitativ bestimmt.
Durch die Weiterentwicklung optoelektronischer Geräte können intelligente Geräte zur Erfüllung komplizierterer Bedürfnisse durch die Implementierung von Mischungen mit mehreren Reaktionsmöglichkeiten nach Lichteinwirkung erziehlt werden, wobei Licht als nachhaltige externe Anregung mit hoher räumlicher und zeitlicher Auflösung dient. Daher wird das Schaltverhalten einer Mischung zweier sowohl individuell als auch gleichzeitig ansprechbarer Photoschalter im Detail erforscht. Zudem ist die untersuchte Mischung 3D druckbar, was einen schnellen und einfachen Einbau in 3D Strukturen erlaubt. Die Photoschalter sind ein Azobenzolderivat mit elektronenspendender und -ziehender Gruppe sowie ein Donor-Akzeptor Stenhouse Addukt der ersten Generation, welches im sichtbaren Spektralbereich längere Wellenlängen als das Azobenzolderivat absorbiert. Alle Schritte der trans-zu-cis Isomerisierung des erstgenannten und der linear-zu-geschlossen Isomerisierung des zweitgenannten Photoschalters, genauso wie die entsprechenden Rückreaktionen, werden mit besonderem Augenmerk auf den Einfluss der Umgebung und den gegenseitigen Einfluss der Photoschalter aufeinander untersucht. Dafür werden verschiedene Methoden verwendet, wie beispielsweise transiente Absorption im Femtosekundenbereich, temperaturabhängige kinetische Absorption im sichtbaren und kinetische Absorption im infraroten Bereich, um ein vollständiges Bild zu erhalten. Dabei werden dynamische Effekte der Umgebung und der Photoschalter aufeinander offenbar, wobei die Schaltermoleküle individuell schalten mit nur geringen gegenseiten Einflüssen in der Mischung.
Andere 3D druckbare Materialien sind Zwei-Block-Copolymere, die Mikrophasentrennung zeigen, wie beispielsweise ein Derivat eines Standard-Zwei-Block-Copolymers

für hochauflösende Nanolithographie mit zusätzlichen funktionellen Gruppen, die den 3D Druck ermöglichen. Die lamellare Struktur und ihre Regelmäßigkeit wird mit einem streuend abrasternden optischen Nahfeldmikroskop vor und nach dem 3D Druck erforscht, wobei durch den 3D Druck ein Polymernetzwerk erhalten wird. Vor dem Druck treten Lamellen auf, wohingegen der Druckprozess optimiert werden muss, um diese auch nach dem Druck beizubehalten.

Abbreviations

1C-2PPE	one-colour two-photon photoemission spectroscopy
2C-2PPE	two-colour two-photon photoemission spectroscopy
2PPE	two-photon photoemission spectroscopy
AFM	atomic force microscope
AFM-IR	atomic force microscope infrared
AR-2PPE	angle-resolved two-photon photoemission spectroscopy
Azo	nonyl-(*E*)-4-((4-(methyl(nonyl)amino)phenyl)diazenyl)-benzoate
B3LYP	Becke, 3-parameter, Lee-Yang-Parr
BBO	β-barium borate
BIS	bremsstrahlung isochromat spectroscopy
CCD	charge-coupled device
CPU	central processing unit
CW	continuous wave
DAP	6,13-diazapentacene
DASA	5-((2*Z*,4*E*)-5-(diethylamino)-2-hydroxypenta-2,4-dien-1-ylidene)-1,3-dimethylpyrimidine-2,4,6(1*H*,3*H*,5*H*)-trione
DAQ	data acquisition
DCM	dichloromethane
DFT	density functional theory
DOS	density of states
EADS	evolution associated difference spectrum/spectra
ESA	excited state absorption
ESCA	electron spectroscopy for chemical analysis
fcc	face-centered cubic
FTIR	Fourier transform infrared spectroscopy

FWHM	full width at half maximum
GA	global analysis
GPIB	general purpose interface bus
GSB	ground state bleach
GVD	group velocity dispersion
hcp	hexagonal-close packed
HEMA	hydroxyethylmethacrylate
HOMO	highest occupied molecular orbital
HREELS	high-resolution electron energy loss spectroscopy
IPES	inverse photoemission spectroscopy
IPS	image potential state
IR	infrared
IRF	instrument response function
LED	light emitting diode
LEED	low energy electron diffraction
LUMO	lowest unoccupied molecular orbital
MCP	microchannel plate
MCT	mercury cadmium telluride
MeCN	acetonitrile
ML	monolayer
MMA	methyl methacrylate
nano-FTIR	nanoscale Fourier transform infrared spectroscope
Nd:YAG	neodymium-doped yttrium-aluminium-garnet
NIR	near-infrared
OFET	organic field effect transistor

OLED	organic light-emitting diode
OPA	optical parametric amplifier
PCI	peripheral component interconnect
PES	photoemission spectroscopy
PID	proportional-integral-derivative
PMMA	polymethyl methacrylate
P(MMA-*co*-HEMA)	poly(methyl methacrylate-*co*-2-hydroxyethyl methacrylate)
PS	polystyrene
PsHet	pseudo-heterodyne
QCL	quantum cascade laser
QMS	quadrupole mass spectrometer
RAM	random-access memory
RegA	regenerative amplifier
RS	recommended standard
SE	stimulated emission
SS	surface state
SSD	solid state drive
SNOM	scanning near-field optical microscope
s-SNOM	scattering scanning near-field optical microscope
STM	scanning tunneling microscope
SVD	singular value decomposition
TA	transient absorption
Ti:Sa	titanium sapphire oscillator
TOF	time-of-flight
Tol	toluene

TPD	temperature-programmed desorption
TR-2PPE	time-resolved two-photon photoemission spectroscopy
UHV	ultra-high vacuum
UV	ultraviolet
UPS	ultraviolet photoelectron spectroscopy
VI	virtual instrument
VIS	visible
XPS	X-ray photoelectron spectroscopy
YAG	yttrium-aluminium-garnet
ZPD	zero path difference

List of Figures

2.1. Periodic parabolic dispersion of a free electron and an electron in an lattice with and without applying a periodic potential. 6

2.2. Scheme of photon energy dependent 2PPE measurements to assign peaks to occupied, unoccupied and final states. 12

2.3. Scheme of a typical 2PPE spectrum of an adsorbate on a conductive substrate. 15

2.4. Scheme of a TPD spectrum and the respective processes on a molecular scale. 17

2.5. Calculated desorption spectra according to the Polanyi-Wigner equation for the most common orders and for different initial coverages. . . 18

2.6. Processes contributing to TA experiments. 21

2.7. Energy level diagrams for the processes involved in a TA experiment and how those compose the total TA spectrum. 22

2.8. Asymmetric Michelson interferometer used in the s-SNOM setup. . . . 26

3.1. Scheme of the UHV Chamber used in 2PPE and TPD experiments. . . 32

3.2. Sample holder within the UHV Chamber of the 2PPE setup. 33

3.3. Temperature versus time profile for the substrate annealing prior to 2PPE experiments. 34

3.4. PES laser setup used for 2PPE measurements. 36

3.5. Beam characteristics of the 2PPE setup. 37

3.6. Scheme of the TOF spectrometer in the 2PPE setup. 38

3.7. Cut-off of the 2PPE spectrum due to the difference in work function of the sample and the analyser. 40

3.8. Connection diagram of the electronics within the 2PPE setup. 41

3.9. Scheme of the TA setup. 45

3.10. s-SNOM setup used in this thesis. 47

4.1. Structural formula of DAP. 50

4.2. Characterisation of the Au(111) substrate. 51

4.3. AR-2PPE of the Au(111) substrate. 51

4.4. Mass spectrum of DAP. 52

4.5. TPD spectra of DAP adsorbed on Au(111) for different initial coverages and distinct ionic fragments. 53

4.6. 1C-2PPE ($h\nu$ = 4.11 eV) spectra of DAP at different coverages. 54

4.7. 1C-2PPE spectra of DAP at different photon energies and slope analysis of the identified states. 56

4.8. Energy level diagram of 3 ML thick DAP on Au(111). 57

5.1. Photoswitching of Azo. 59

5.2. General excitation scheme of trans-to-cis isomerisation of azobenzene derivatives upon $S_0 \rightarrow S_2$ excitation. 60

5.3. General scaffold of donor-acceptor Stenhouse adducts. 61

5.4. Switching mechanism of DASA. 62

5.5. Absorption spectra of Azo in Tol, MeCN, as neat film and as PMMA blend before and during illumination to induce photoswitching. 65

5.6. Absorption spectra of DASA in Tol, MeCN, as neat film and as PMMA blend before and during illumination to induce switching. 66

5.7. Absorption spectra of DASA+Azo in Tol, MeCN and as PMMA blend film. 67

5.8. TA data and results of Azo in Tol excited with light of a wavelength of 431 nm. 69

5.9. TA data and results of Azo in Tol excited with light of a wavelength of 431 nm while DASA is present. 71

5.10. TA data and results of Azo in Tol excited with light of a wavelength of 431 nm while switched DASA is present. 72

5.11. TA data and results of Azo in Tol excited with light of a wavelength of 379 nm to induce backswitching. 74

5.12. TA data and results of Azo in Tol excited with light of a wavelength of 379 nm to induce backswitching while DASA is present. 75

5.13. TA data and results of Azo in Tol excited with light of a wavelength of 379 nm to induce backswitching while switched DASA is present. . . . 77

5.14. TA data and results of DASA in Tol excited with light of a wavelength of 582 nm. 78

5.15. TA data and results of DASA in Tol excited with light of a wavelength of 582 nm while Azo is present. 79

5.16. TA data and results of DASA in Tol excited with light of a wavelength of 582 nm while switched Azo is present. 81

5.17. TA data and results of Azo in Tol excited with light of a wavelength of 506 nm. 82

5.18. TA data and results of DASA in Tol excited with light of a wavelength of 506 nm. 83

5.19. TA data and results of Azo and DASA in Tol simultaneously excited with light of a wavelength of 506 nm. 85

5.20. TA data and results of Azo in MeCN excited with light of a wavelength of 415 nm. 87

5.21. TA data and results of Azo in MeCN excited with light of a wavelength of 415 nm while DASA is present. 89

5.22. TA data and results of Azo in MeCN excited with light of a wavelength of 415 nm while switched DASA is present. 90

5.23. TA data and results of Azo in MeCN excited with light of a wavelength of 379 nm to induce backswitching. 91

5.24. TA data and results of Azo in MeCN excited with light of a wavelength of 379 nm to induce backswitching while DASA is present. 93

5.25. TA data and results of DASA in MeCN excited with light of a wavelength of 582 nm. 94

5.26. TA data and results of DASA in MeCN excited with light of a wavelength of 582 nm while Azo is present. 96

5.27. TA data and results of DASA in MeCN excited with light of a wavelength of 582 nm while switched Azo is present. 97

5.28. TA data and results of Azo in MeCN excited with light of a wavelength of 510 nm. 98

5.29. TA data and results of DASA in MeCN excited with light of a wavelength of 510 nm. 100

5.30. TA data and results of Azo and DASA in MeCN simultaneously excited with light of a wavelength of 510 nm. 101

5.31. TA data and results of an Azo film as PMMA blend excited with light of a wavelength of 431 nm. 104

5.32. TA data and results of an Azo film as PMMA blend excited with light of a wavelength of 431 nm while DASA is present. 105

5.33. TA data and results of an Azo film as PMMA blend excited with light of a wavelength of 431 nm while switched DASA is present. 106

5.34. TA data and results of an Azo film as PMMA blend excited with light of a wavelength of 369 nm to induce backswitching. 108

5.35. TA data and results of an Azo film as PMMA blend excited with light of a wavelength of 369 nm to induce backswitching while DASA is present. 110

5.36. TA data and results of an Azo film as PMMA blend excited with light of a wavelength of 369 nm to induce backswitching while switched DASA is present. 111

5.37. TA data and results of a DASA film as PMMA blend excited with light of a wavelength of 585 nm. 113

5.38. TA data and results of a DASA film as PMMA blend excited with light of a wavelength of 585 nm while Azo is present. 114

5.39. TA data and results of a DASA film as PMMA blend excited with light of a wavelength of 585 nm while switched Azo is present. 116

5.40. TA data and results of an Azo film as PMMA blend excited with light of a wavelength of 515 nm. 117

5.41. TA data and results of a DASA film as PMMA blend excited with light of a wavelength of 515 nm. 118

5.42. TA data and results of an Azo and DASA film as PMMA blend simultaneously excited with 515 nm. 120

5.43. Absorption spectra of Azo in Tol upon photoswitching and thermal backswitching. 130

5.44. Absorption spectra of Azo in Tol at different temperatures. 130

5.45. Rise curves of the maximum absorption of Azo in Tol at different temperatures with their respective fits and corresponding Arrhenius plot upon thermal backswitching. 131

5.46. Absorption spectra of Azo in Tol while DASA is present upon switching and thermal backswitching. 132

5.47. Change of absorbance of the signals at 378, 448, 570 and 625 nm upon switching Azo in Tol while DASA is present. 133

5.48. Change of absorbance of the signals at 378, 448, 570 and 625 nm upon thermal backswitching Azo in Tol while DASA is present. 133

5.49. Rise curves of the maximum absorption of Azo in Tol at different temperatures with their respective fits and corresponding Arrhenius plot upon thermal backswitching while DASA is present. 134

5.50. Absorption spectra of Azo+DASA in Tol switched simultaneously. . . . 135

5.51. Rise curves of the maximum absorption of Azo in Tol at different temperatures with their respective fits and corresponding Arrhenius plot upon thermal backswitching while DASA is backswitched simultaneously. 136

5.52. Percentage of switched and backswitched Azo after switching and thermal backswitching. 137

5.53. Absorption spectra of DASA in Tol upon switching and backswitching. . 140

5.54. Change of absorbance of the DASA signals at 571 and 625 nm upon switching and backswitching. 140

5.55. Monoexponential fits of the DASA signals at 571 and 625 nm upon photoswitching. 141

5.56. Absorption spectra of DASA in Tol at different temperatures. 142

5.57. Decay curves of the maximum absorption of DASA in Tol at different temperatures with their respective fits and corresponding Arrhenius plot upon photoswitching. 142

5.58. Rise curves of the maximum absorption of DASA in Tol at different temperatures with their respective fits and corresponding Arrhenius plot upon thermal backswitching. 143

5.59. Absorption spectra of DASA in Tol upon switching and backswitching while Azo is present. 144

5.60. Change of absorbance of the signals at 441, 570 and 625 nm upon switching DASA in Tol while Azo is present. 145

5.61. Decay curves of the maximum absorption of DASA in Tol at different temperatures with their respective fits and corresponding Arrhenius plot upon photoswitching while Azo is present. 145

5.62. Rise curves of the maximum absorption of DASA in Tol at different temperatures with their respective fits and corresponding Arrhenius plot upon backswitching while Azo is present. 146

5.63. Decay curves of the maximum absorption of DASA in Tol at different temperatures with their respective fits and corresponding Arrhenius plot upon switching while Azo is switched simultaneously. 147

5.64. Rise curves of the maximum absorption of DASA in Tol at different temperatures while Azo is backswitched simultaneously. 148

5.65. Rise curves of the maximum absorption of DASA in Tol at different temperatures with their respective fits and corresponding Arrhenius plot upon backswitching while Azo is backswitched simultaneously. 148

5.66. Percentage of switched and backswitched DASA for pure Tol solution, with Azo being present and Azo being switched simultaneously. 149

5.67. Comparison of the calculated and experimental vibrational frequencies of the DASA isomer **A**. 153

5.68. Calculated IR spectra of the DASA isomers **A**, **C** and **C'**. 154

5.69. Comparison of the IR spectra of the DASA isomer **A** in Tol, in a KBr matrix and the DFT calculated spectrum. 155

5.70. Change of IR absorbance of DASA in Tol upon photoswitching. 155

5.71. Kinetic traces of the bands at 1487.0 cm^{-1} and 1575.6 cm^{-1} upon photoswitching DASA in Tol. 156

5.72. Change of absorbance of DASA in Tol upon thermal backswitching. . . 157

5.73. Comparison of the IR spectra of DASA in Tol at room temperature before photoswitching, after photoswitching and after thermal backswitching. 158

5.74. Comparison of the IR spectra of the DASA isomer **A** in MeCN, in a KBr matrix and DFT calculated spectrum. 159

5.75. Change of IR absorbance of DASA in MeCN upon photoswitching. . . 160

5.76. Kinetic traces of the bands at 1500.6 cm^{-1} and 1616.3 cm^{-1} upon switching DASA in MeCN. 160

5.77. Change of absorbance of DASA in MeCN upon thermal backswitching. 161

5.78. Kinetic traces of the bands at 1500.6 cm^{-1} and 1616.3 cm^{-1} upon thermal backswitching of DASA in MeCN. 162

5.79. Scheme of the excited state dynamics of Azo after $S_0 \rightarrow S_2$ excitation by light and the reverse reaction induced by light or thermal energy with all determined time constants and activation energies. 164

5.80. Scheme of the excited state dynamics of DASA after $S_0 \rightarrow S_1$ excitation by light and the reverse reaction induced by thermal energy with all determined time constants and activation energies. 166

6.1. Structure of the P(MMA-*co*-HEMA)-*b*-PS block copolymer. 169

6.2. Comparison of the far- and near-field IR spectra of P(MMA-*co*-HEMA). 170

6.3. Comparison of the far- and near-field IR spectra of PS. 171

6.4. Far-field spectrum of the P(MMA-*co*-HEMA)-*b*-PS block copolymer in comparison to the spectra of P(MMA-*co*-HEMA) and PS. 172

6.5. Near-field phase optical imaging of the signal obtained by irradiation of P(MMA-*co*-HEMA)-*b*-PS at 1152 cm^{-1}. 173

6.6. Near-field phase optical imaging using IR radiation at 1152 cm^{-1} of regular lamellae of the P(MMA-*co*-HEMA)-*b*-PS sample. 174

6.7. Structure of the P(MMA-*co*-HEMA)-*b*-PS block copolymer analysed by complementary images recorded by AFM-IR. 175

6.8. IR far-field spectra of printed crosslinked P(MMA-*co*-HEMA)-*b*-PS blocks and the P(MMA-*co*-HEMA)-*b*-PS starting material. 176

6.9. AFM-IR amplitude optical imaging with IR radiation at 1152 cm^{-1} absorbed by P(MMA-*co*-HEMA) and at 1602 cm^{-1} absorbed by PS, respectively, in the printed P(MMA-*co*-HEMA)-*b*-PS polymer. 177

A.1. 1C-2PPE spectrum of three ML of DAP on Au(111) with a photon energy of 4.50 eV. A2

A.2. 2C-2PPE spectra of DAP on Au(111) at different photon energies and coverages. A2

A.3. Dispersion and slope analysis of the signals found in 2C-2PPE spectra of DAP on Au(111). A3

B.1. Spectra of the LEDs used for switching DASA and Azo. A4

B.2. Spectra of Azo, DASA and their equimolar mixture Azo+DASA. A4

B.3. Spectra of DASA before and during illumination by an LED while mimicking the geometric conditions of the TA setup in different environments. A5

B.4. Spectra of Azo before and during illumination by an LED while mimicking the geometric conditions of the TA setup in different environments. A6

B.5. Decay of the maximum intensity of *trans*-Azo upon photoexcitation. . . A11

B.6. Kinetic traces of the bands at 1487.0 cm^{-1} and 1575.6 cm^{-1} upon thermal backswitching DASA in Tol. A14

B.7. Kinetic trace of the band at 1616.3 cm^{-1} upon thermal backswitching of DASA in MeCN with its fit converging as expected. A16

List of Tables

5.1. Comparison of the lifetimes upon switching Azo obtained by GA. 122

5.2. Comparison of the lifetimes upon photochemically backswitching Azo obtained by GA. 123

5.3. Comparison of the lifetimes upon switching DASA obtained by GA. . . 125

5.4. Comparison of the lifetimes upon simultaneous switching of Azo and DASA obtained by GA. 127

5.5. Determined effective cross sections of photoswitching Azo. 138

5.6. Comparison of the lifetimes upon thermal backswitching of Azo in Tol of pure Azo, DASA being present and DASA being backswitched simultaneously. 138

5.7. Comparison of the activation energies upon thermal backswitching of Azo in Tol for pure Azo, DASA being present and DASA being backswitched simultaneously. 139

5.8. Comparison of the effective cross sections of DASA in Tol upon photoswitching in different environments. 150

5.9. Comparison of the lifetimes of DASA in Tol upon switching of pure DASA, Azo being present and Azo being switched simultaneously. . . . 151

5.10. Comparison of the lifetimes of DASA in Tol upon backswitching of pure DASA, Azo being present and Azo being backswitched simultaneously. 151

5.11. Comparison of the activation energies upon switching and backswitching of DASA in Tol for pure DASA, Azo being present and Azo being (back-)switched simultaneously. 152

5.12. Comparison of the determined rate constants of DASA using IR spectroscopy in different solvents. 163

B.1. Optimised geometry and dipole moment of DASA isomer **A** by DFT using 6-31++G(d,p). A7

B.2. Optimised geometry of DASA isomer **A** by DFT using 6-31++G(d,p). . A8

B.3. Optimised geometry and dipole moment of Azo isomer **A** by DFT using 6-31++G(d,p). A9

B.4. Optimised geometry and dipole moment of Azo isomer **B** by DFT using 6-31++G(d,p). A10

B.5. Optimised geometry of DASA isomer **A** by DFT using 6-311G(d,p). . . A12

B.6. Optimised geometry of DASA isomer **A** by DFT using 6-311G(d,p). . . A13

B.7. Optimised geometry of DASA isomer **A** by DFT using 6-311G(d,p). . . A14

B.8. Assignment of the frequencies found in DASA in different environments to the vibrational modes based on DFT calculations. A15

1. Introduction

Electronic devices are omnipresent in everyday life. They help to organise daily routines and connect people around the world. Today, an increasing energy consumption[1] and man-made global warming[2][3] impact the everyday life and urge innovations.
At the beginning, electronic devices were composed solely of inorganic conducting materials. Since their discovery about 45 years ago, organic electronics revolutionised electronic devices and entered the market of mass production around 20 years ago.[4, pp. V f.][5] The companies Kodak and Philips played thereby pioneering roles with the demonstration of an efficient electroluminescent organic light-emitting diode (OLED) published in 1987 by Tang and van Slyke at Kodak[6][7] and the first commercial product featuring a display panel composed of OLEDs from Philips in 2002.[5][8] Nowadays, electronic devices using organic materials are ubiquitous in solar cells, organic field effect transistors (OFETs), OLEDs, displays, sensors and information storage for instance.[4, pp. V f.][5]
Compared to inorganic devices, with silicon and gallium arsenide as the most-important inorganic semiconductors,[9, p. 1] organic electronics exhibit several advantages. While there are only limited inorganic semiconductors, a wide variety of organic materials can be synthesised and customised to meet different functionalities. Furthermore, organic materials are more compossible with living organisms such that they can be implemented in biological systems and medicine.[4, pp. VI ff.] Important for mass production, organic compounds are inexpensive compared to inorganic materials and they can be used for light and thin devices at low costs by printing methods. Hence, foldable devices and smart materials are created which cover the nowadays more complex needs by differentiated functionalities.[4, pp. V ff.][10, pp. 1 ff.]
To date, several printing techniques are available for material creation with the 3D printing technologies offering the opportunity to fabricate 3D objects and devices.[11] Introduced in 1984 by Hull patenting a stereolithographic process, 3D printing made huge progress towards industrialisation. All 3D printing techniques, also termed additive manufacturing, have a sequential computer-controlled layer-by-layer formation in common providing high accuracy, high speed and low costs.[12] While entirely 3D printed goods like the car "Strati", which was released in 2014 by Local Motors,[13][14] are rare, many devices and products feature nowadays 3D printed components such as Airbus planes.[12] The application of 3D printed materials ranges from production of shaped parts to electronic devices, tissue engineering and high-performance metamaterials.[15]
In 2013, Tibbits first introduced 4D printing as further development at the TED conference (Technology, Entertainment, Design). 4D printing refers to the 3D printing of smart materials with the fourth dimension being the time. An external stimulus, such

as light or chemicals, thereby initialises a change in shape, property or functionality. Since its introduction, the research on 4D printing boosted dramatically.[15]-[19]
The research in this thesis concerns the in-depth investigation of new materials with promising properties for the above mentioned purposes. In fact, the electronic and structural properties of functional materials play a crucial role for device performance. Considering a simple device such as a solar cell composed of organic materials, the electronic and structural properties are most important. While e.g. the electronic structure defines the wavelength range which can be absorbed to form charges, the structure of the material defines the transport range for instance since e.g. grain boundaries lead to unintended charge recombination. This way, both properties are important for device performance and efficiency.[7][9] Hence, the investigated properties within this thesis cover the electronic and structural characteristics of functional materials. Those properties are investigated utilising several advanced laser spectroscopic techniques.
To begin with, a small organic semiconductor is studied with respect to its electronic properties since those are relevant for potential future applications in solar cells and OFETs. Because the electronic structure of a material is influenced by adjacent components, the device performance is often limited by the electronic structure at the interface.[4, pp. 50, 123 f.] Most organic electronics still feature inorganic electrodes such that the metal/organic interface is of great interest.[20][21] Hence, the electronic structure of a pentacene derivative on an Au(111) electrode is investigated. Pentacene and its derivatives are organic semiconductors with high charge carrier mobility and mechanical flexibility making them ideal for applications in OFETs.[22]-[25] However, most are p-type semiconductors providing good hole transport while n-type semiconductors offering good electron transport properties are rare.[24][26] Thus, pentacene as promising starting material is modified by nitrogen substitution as the use of electronegative elements stabilises the valence orbitals providing an n-type semiconductor while maintaining the planar molecular structure.[26] The N-substituted pentacene derivative is studied by temperature-programmed desorption (TPD) and two-photon photoemission spectroscopy (2PPE) techniques. TPD is used to gain information of the evaporation process of the organic compound, which is important for device fabrication, as well as the layer thickness. 2PPE in contrast is utilised to study the electronic structure of the pentacene derivative in contact with gold to determine quantitatively the energetic positions of occupied and unoccupied electronic states of both the organic compound as well as the metal substrate.
Next, small organic compounds are studied acting as smart materials allowing 4D printing. The mixture of two photoresponsive molecules serves as multiresponsive actuator offering differentiated reactions upon light exposure. Thus, light acts as the external stimulus inducing a photoswitching reaction. Light is the most beneficial stimulus since it is omnipresent, sustainable and offers high spatio-temporal resolution.[27] The mo-

lecule absorbing in the blue region of the visible spectrum is a push-pull azobenzene derivative performing trans-to-cis isomerisation upon irradiation with light. The reverse reaction can be initiated by light of shorter wavelength or heat. The second smart molecule absorbing in the red region of the visible spectrum is a first generation donor-acceptor Stenhouse adduct which undergoes linear-to-closed isomerisation upon light exposure with several steps involved. The reverse reaction is thermally activated. Using a mixture of both photoswitches, they can be addressed independently as well as simultaneously by adapting the used wavelength. Such mixtures composed of two smart materials are applied in the fields of robotic, actuation, lithography and information storage for instance.[28]-[30] In order to understand the switching behaviour and how the switching properties are influenced, a detailed study is carried out. Special emphasis is put on the environmental influences on the photoswitching behaviour as well as the impact of the photoswitches on each other. To account for effects of the surrounding such as polarity, two different solvents are used. Furthermore, thin film samples more close to thin film devices are investigated. All steps involved in the switching process are thereby analysed. The ultrafast steps are researched using transient absorption (TA) spectroscopy with femtosecond time resolution for all photoswitchings. Since the ring closure of the donor-acceptor Stenhouse adduct generating the closed structure happens on a longer time scale, this process is analysed using temperature-dependent kinetic ultraviolet (UV)/visible (VIS) spectroscopy in the millisecond to second range. Indeed, not only the photoinduced switchings but also the thermally activated backreactions are studied. The activation energies of the thermal steps are thereby determined. The ring closure and subsequent proton transfer is also researched by making use of kinetic infrared (IR) spectroscopy with second time resolution. The involved isomers are thereby identified with the help of quantum chemical density functional theory (DFT) calculations.

Beside small organic molecules, polymers are also of high interest for 3D printing since to date polymers are more widely used.[12][15] To control the material properties of the printed object, the structure, also on the micro- and nanometer scale, plays a crucial role. The polymer class of diblock copolymers afford the opportunity to form microstructures on the tens-of-nanometer scale due to microphase separation caused by the chemical incompatibility of the covalently connected blocks of different homopolymers. The structure can thereby be controlled by the chemical composition.[31]-[34] By post-treatment of 3D printed structures composed of block copolymers, only one block can be addressed offering versatile possibilities to create new materials.[34] Hence, the microstructure of a derivative of a standard diblock copolymer for high-resolution nanolithography patterns[34][35] is investigated using scattering scanning near-field optical microscope (s-SNOM) techniques. The parent diblock copolymer is modified by the introduction of additional functional groups. After further treatment, the derivative block

copolymer can be 3D printed with the formation of a polymeric network upon printing. Hence, the microphase segregation and structure of the derivative diblock copolymer as well as of the printed structure is researched. Due to the chemical composition, a lamellar structure is thereby expected. The study aims at the identification of the structure and how the structure is affected by the 3D printing process.
In the following, first a general theoretical background is presented in chapter 2 covering both the material properties and spectroscopic methods used in this thesis. Subsequently, the experimental details concerning the experimental setups are given in chapter 3. After those fundamentals are explained, the research results and interpretations are presented in the next three chapters. Thus, chapter 4 focuses on the electronic structure of Au(111) and of the N-substituted pentacene derivative 6,13-diazapentacene (DAP) on the Au(111) substrate as well as the adsorption and desorption properties of DAP on Au(111). The following chapter 5 unveils the detailed study of the switching properties of the azobenzene derivative nonyl-(*E*)-4-((4-(methyl(nonyl)-amino)phenyl)diazenyl)-benzoate (Azo), the donor-acceptor Stenhouse adduct 5-((2*Z*, 4*E*)-5-(diethylamino)-2-hydroxypenta-2,4-dien-1-ylidene)-1,3-dimethylpyrimidine-2,4,6 (1*H*,3*H*,5*H*)-trione (DASA) and their mixture in toluene, acetonitrile and as thin film using different techniques and time resolutions to analyse all involved steps of isomerisation. In chapter 6, the microstructure of a diblock copolymer composed of one block of poly(methyl methacrylate-*co*-2-hydroxyethyl methacrylate) (P(MMA-*co*-HEMA)) and one block of polystyrene (PS) is investigated before and after 3D printing. After that, the thesis is concluded with a summary and outlook in chapter 7.

2. Theoretical Background

To start with, an overview about the theoretical background is given for both the materials and the spectroscopic methods used in this study. First, important material properties of the investigated systems are discussed in section 2.1. Next, the spectroscopic techniques used in this thesis are explained in section 2.2.

2.1. Materials

The materials used in this thesis include inorganic metallic conductors utilised as substrates as well as organic materials. Hence, the electronic properties of metals are discussed at first in section 2.1.1. Next, the organic molecules investigated, which range from small semiconducting molecules to big insulating polymers, and their electronic properties are explained in section 2.1.2. Special emphasis is put on the phenomenon of photochromism in section 2.1.3 since part of the detailed studied molecules partake of this property.

2.1.1. Bulk and surface electronic states of metals

Metals and their metallic bonds can be described by the free electron gas model. While the atomic cores, each composed of the atomic nucleus and the core electrons, are strongly localised, their valence electrons behave approximately like free electrons and can mathematically be depicted as electron gas or Fermi gas. This model was introduced in 1933 by Sommerfeld and is therefore also named Sommerfeld-theory. Within this model, the valence electrons are described as particles in a box with a constant potential inside the box and an infinitely large potential at the walls. By this means, with redefining the potential at the bottom of the box as $\tilde{V}$, being about zero, only the kinetic energy has to be taken into account such that the Schrödinger equation for one electron can be simplified according to equation 2.1 where $\hbar$ corresponds to the reduced Planck's quantum of action, m_e to the mass of the electron, Δ to the Laplace operator, Ψ to the wave function depending on the position r and the energy E.

$$-\frac{\hbar^2}{2\,m_e}\,\Delta\,\Psi(r)\;=\;E\,\Psi(r) \tag{2.1}$$

Applying a plane wave containing the normalisation factor N_f and the wave vector k_w for the wave function as described in equation 2.2 yields the energy eigenvalues E_k of equation 2.3 which depend on the wave vector (blue curve figure 2.1**a**).

$$\Psi(r)\;=\;\frac{1}{\sqrt{N_f}}\,e^{i\;k_w\;r} \tag{2.2}$$

$$E_{k_w} = \frac{\hbar^2 \, k_w^2}{2 \, m_e} \tag{2.3}$$

However, in a real metal the potential is not constant but of periodic structure due to the periodic lattice structure. Assuming a periodic potential $\tilde{V}(r)$ repeating after an arbitrarily lattice vector R_l such that equation 2.4 is fulfilled, the solution of the Schrödinger equation yields the eigenvalues according to equation 2.5.

$$\tilde{V}(r) = \tilde{V}(r + R_l) \tag{2.4}$$

$$E_{k_w} = E_{k_w+G} = \frac{\hbar^2}{2 \, m_e} |k_w + G|^2 \tag{2.5}$$

Thus, for a periodic potential, the eigenvalues depend on the wave vector as well as the reciprocal lattice vector G. Assuming a potential $\tilde{V}$ being about zero, this ansatz provides the so-called empty lattice (figure 2.1**a**). However, as the periodic potential is not about zero, this induces a splitting resulting in band gaps and bands. Band gaps are thereby forbidden energy ranges and bands represent energy ranges possible to be occupied by electrons (figure 2.1**b**).[36, pp. 280 ff.] [37, pp. 136 ff.]

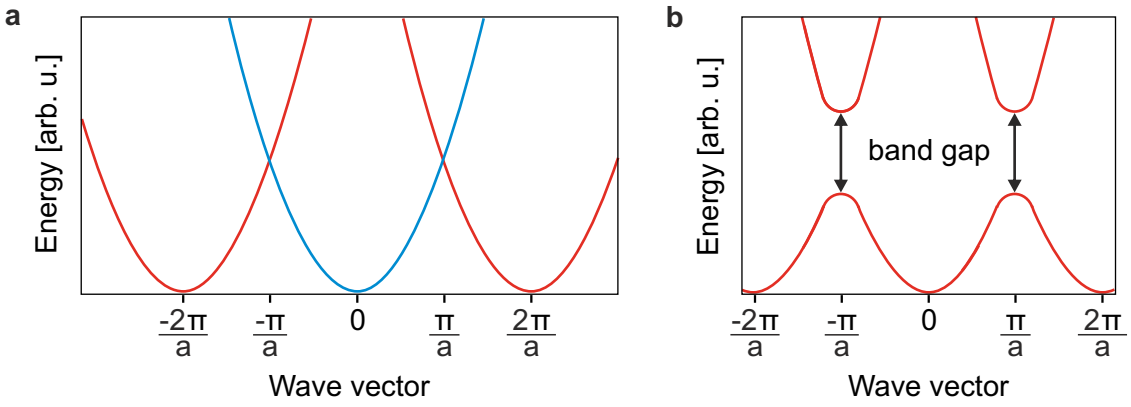

Figure 2.1. Periodic parabolic dispersion of an electron in (a) an empty lattice assuming a lattice constant a resulting in the reciprocal lattice vector being 2π/a and (b) a periodic potential above zero forming band gaps. (a) The blue curve represents the parabolic dispersion of a free electron. Figure adapted.[38]

At the surface of the metal, the periodic potential and the symmetric structure are disrupted. Thus, electronic states distinctive of surfaces occur, namely surface states (SSs) and image potential states (IPSs). In the 1930s, Tamm[39] and Shockley[40] were the first to construct theoretical descriptions of surface states which is why SSs mathematically described by Tamm or Shockley are called Tamm surface states and Shockley surface states, respectively. Tamm SS arise as consequences of asymmetric potentials and the probability for Tamm SSs is higher for narrow-band materials with large interatomic distances. On the contrary, Shockley SSs, which are described by the

nearly free electron model, originate from crossing bands and are more likely to occur for materials with close packed and strong interacting atoms.[41, pp. 253 ff.][42] In contrast to SSs, IPSs emerge from electrons in front of metal surfaces. An electron in front of a metal induces an electric field causing a rearrangement of the charges within the metal in such a way that an image charge inside the metal is formed with the same distance to the surface as the electron in front of the metal. By this means, an electric field perpendicular to the surface is created in vacuum. The attractive Coulomb interaction between the electron and its positive image charge bonds the electron to the surface by an attractive Rydberg-like potential.[43][44]

2.1.2. Organic semiconductors

Whereas electronic devices on the basis of metallic materials are used already for over hundred years,[45] the industrial use of organic semiconductors in electronic applications dates only 20 years back.[5][8] The research on organic compounds regarding their conducting properties dates back to the 1950s when the semiconducting behaviour of small organic molecules was found but with low performance and stability.[8] At the end of the 1970s, a new class of semiconducting polymers was explored that boosted the research on organic materials for electronic applications.[5][46] In 2002, Philips released the first commercial product featuring a display panel based on OLED technology.[5][8] Nowadays, organic molecules are applied in various electronic devices such as OFETs, OLEDs and solar cells offering highly flexible and mechanically robust devices.[47][48]

In general, organic compounds composed of σ-skeletons are non-conductive and thus insulating. However, by introducing conjugated π-systems, the band gap of the material shrinks with lower band gaps for longer conjugated π-systems. In order to get organic semiconductors, the band gap needs to be below 4 eV.[4, pp. V, 1][49, p. 1423]

Especially in the last 30 years, materials and electronic devices based on organic molecules showed high progress.[4, pp. V f.] The major research in the 1990s concerned polycyclic aromatic hydrocarbons such as acenes, conjugated oligomers and polymers, which are composed of repetitive units, and fullerenes.[47] However, also smaller molecules, for example based on dyes and colour pigments, exhibit good semiconducting and device properties such that they are implemented in applications as well.[47]

In contrast to inorganic semiconducting materials, organic semiconductors can be functionalised forming a huge variety to meet different requirements in different applications. The main distinctions between organic and inorganic semiconductors are thereby the intermolecular forces. While in organic materials the molecules interact via weak van-der-Waals interactions, the forces in inorganic materials are stronger.[4, pp. V, 1] Another major difference of organic and inorganic semiconductors concerns the generation and mobility of created charges. For instance, the charges can be generated

by excitation with light. The created positive and negative charges are bound together due to mutual Coulomb interactions. In organic semiconductors, they form correlated electron-hole pairs, referred to as excitons, located on single molecules. This is due to the fact that the Coulomb forces are inversely proportional to the dielectric constant of the medium in which the electron and the hole are situated. For organic semiconductors, the dielectric constant is low (2 - 6). Hence, the distance between the electron and the hole is short and lies in the range of 1 nm while the exciton binding energy is high and lies in the order of 1 eV. Such excitons are called Frenkel excitons. In contrast, the dielectric constant in inorganic semiconductors is high (> 6) generating less bound electron-hole pairs with binding energies in the order of 10 meV and distances in the range of 10 nm called Mott-Wannier excitons.[4, pp. 46, 137] [37, p. 390] [50, pp. 132 f.]

2.1.3. Photochromism

Photochromism is a well-known phenomenon dating back to 1867, when Fritzsche reported the bleaching of a tetracene solution initially coloured orange but losing its colour when exposed to daylight. However, in the dark of night the orange colour returned.[51] [52] Since then, photochromic species have continuously been reported. During the 1960s, photochromic applications were produced with the first product being photochromic glasses which turn dark upon exposure to sunlight. In addition, photochromic materials are used in data storage initially gaining attention in this field with the photochromic micro image technique which reduced a bible containing 1245 pages to an image of about 6 cm^2.[27] [52]

The term photochromism, introduced in 1950 by Hirshberg,[53] is defined as reversible transformation of a chemical species into another chemical species by absorption of electromagnetic radiation. The two chemical species involved have to have different absorption spectra as well as differences in other physical properties, such as dipole moment and geometrical shape for instance.[27] [52] By irradiation, the thermodynamically more stable form is transformed into the photoisomer. For the backswitching, two activations are possible. On the one hand, the backswitching can again be induced photochemically by irradiation with light resulting in the generation of the thermodynamically more stable form. In this case, the photochromism is P-type. On the other hand, the backswitching can be triggered thermally causing T-type photochromism.[52]

If the chemical species performing photochromism consists of a single molecule, it is called molecular photoswitch.[54] Most organic photoswitches exhibit positive photochromism which implies shorter maximum absorption wavelengths for the thermodynamically more stable isomer compared to its photoisomer. In contrast, negative photochromism applies for chemical species with the maximum absorption wavelength of the thermodynamically more stable form being longer than the maximum absorption wavelength of the photoswitched analogue.[52]

Nowadays, photoswitchable materials gain high attention as they can act as so-called smart materials reacting to external stimuli. For smart materials, external stimuli such as mechanical stress, temperature, pH value or electric field can be used to induce macroscopic changes of material properties. However, light clearly represents the most advantageous stimulus as it offers very high spatial and temporal resolution while being sustainable and omnipresent.[27] [55] In this manner, smart photoswitches are qualified for various fields. In addition to the aforementioned fields of sun glasses and data storage, photochromic materials are also applicable in rewritable data storage, light-driven molecular motors, biological systems and storage of solar energy. Especially medical applications are of great interest, such as pharmaceutical active photoswitches, photochromic materials controlling bacterial growth, catalysis and DNA nanotechnologies.[54] [56]- [58] Among various photoswitches advantageous for medical applications, azobenzene derivatives hold great potential as their large molecular structural changes upon photoswitching can induce high activity modulation.[59] [60] Another promising application of photoswitches is their use as molecular solar thermal energy storage which is also referred to as solar thermal battery. Within this process, solar energy induces the formation of the metastable isomer and therefore stores solar energy. This energy can be released afterwards by triggering a heat-releasing thermal conversion to the thermodynamically more stable isomer. An efficient solar thermal battery requires thereby sufficient inertness of the metastable isomer.[61]
To compare the efficiencies of different photoswitchable molecules, the effective cross section σ is a suitable characteristic. It is calculated from the lifetime τ, the photon dose per area and time interval n_p according to equation 2.6.[62]

$$\sigma = \frac{1}{\tau \, n_p} \tag{2.6}$$

By assuming a circular area, n_p is determined using equation 2.7.

$$n_p(t, A) = \frac{P(t)}{E_p \, A} = \frac{P(t) \, \lambda}{h \, c_{vac} \, \pi \, r^2} \tag{2.7}$$

According to equation 2.7, the photon dose P per time t and area A depends on the used wavelength λ defining the photon energy E_p, the speed of light in vacuum c_{vac} and the radius r.[63, p. 32] [64, p. 63, 204] [65, p. 93]

2.2. Spectroscopic methods

In this section, the spectroscopic methods used in this thesis are explained as well as their theoretical background. Starting with the phenomenon of photoemission triggered by one or two photons in section 2.2.1 and section 2.2.2, respectively, which are

both useful tools to investigate electronic states of various materials, temperature-programmed desorption (TPD) is elucidated in section 2.2.3, which is a method to control and ascertain the layer thickness of the investigated samples. Next, section 2.2.4 illustrates how linear optical spectroscopic techniques, such as absorption spectroscopy, can be implemented in order to investigate the dynamics, rate constants, lifetimes and activation energies of chemical processes involving optically active materials. The investigation of excited state dynamics on ultrashort time scales studied by transient absorption (TA) spectroscopy is explained afterwards in section 2.2.5. Lastly, the technique of a scattering scanning near-field optical microscope (s-SNOM) is illustrated in section 2.2.6 which is capable of investigating surface structural and IR optical properties of various samples on the nanometer scale.

2.2.1. One-photon photoemission

Photoemission spectroscopy (PES) is a powerful tool to investigate the electronic structure of various samples, like atoms, molecules, solids and interfaces, and examine both occupied and unoccupied states.[66] PES developed from the photoelectric effect which was first observed by Heinrich Hertz[67] and further investigated by William Hallwachs[68] in 1887. They exposed negatively charged metals to UV radiation and observed a discharge process. This process was dependent on the material and required a minimum threshold frequency.[67][68] Hallwachs discovered that the discharge process was led by emission of negatively charged particles,[68] which were later identified as electrons by Thomson.[69] In 1899, Lenard found that the intensity of the UV light did not change the kinetic energy of the electrons but the amount of them.[70] Those observations can not be explained by classical physics. Thus, the process of photoemission was not fully understood until the concept of quantised light was introduced by Max Planck in 1900 by formulating a universal constant h,[71][72] and Einsteins explanation of the photoelectric effect in 1905 using quantised light particles,[73] for which he was awarded the Nobel prize in 1921.[66]
According to their findings, light particles with the frequency ν transfer their energy into kinetic energy E_{kin} of the electrons e^- of the material as described by equation 2.8. However, the electrons lose some of their kinetic energy in order to leave the sample. This energy loss is characteristic for every material and called work function ϕ.[74]

$$E_{kin}(e^-) \;=\; h\nu \;-\; \phi \tag{2.8}$$

The accuracy of the available instruments at the beginning of the 1900s century was poor, so it took a while for Einstein's equation 2.8 to be proven and to develop spectroscopic methods.[74][75] In the 1950s major instrumental improvements were achieved and two sophisticated spectroscopic methods were developed: ultraviolet photoelec-

tron spectroscopy (UPS) and X-ray photoelectron spectroscopy (XPS).[75]
UPS utilises excitation light in the range of about 10 - 100 eV and therefore probes valence electrons of solids and surfaces.[76] Spicer was the first to publish band gaps and electron affinities in 1958[77] and valence band spectra[78] measured by UPS. Within this energy range, the photoexcited electrons feature a short mean free path of some Ångström which makes UPS a surface sensitive technique capable of probing surface and bulk states.[76][79]-[81]
XPS requires higher energies for excitation. The used X-rays, having an energy of about 0.1 - 5 keV, probe core-level electrons.[82] It is therefore an element specific method. Due to the short mean free path of the photoemitted electrons of about 5 - 50 Å, it is also a surface sensitive technique.[83] XPS was mainly pushed forward by Siegbahn starting in the late 1950s by developing improved analysers which made it possible to determine the chemical composition and chemical shifts due to the chemical environment.[84][85] This method is also used in industry known as electron spectroscopy for chemical analysis (ESCA).[86] For his work on XPS, Siegbahn was awarded the Nobel prize in 1981.[75][87][88]
Both UPS and XPS experiments can only investigate occupied states. In order to examine unoccupied states, inverse photoemission spectroscopy (IPES) was developed originating from bremsstrahlung isochromat spectroscopy (BIS). Therein, an incident electron can decay radiatively into an unoccupied state of the sample emitting a photon whose energy reveals the energy level of the unoccupied state. To scan all unoccupied states, a monochromatic electron beam is used which sweeps through an energy range. Historically, high-energy electrons producing X-rays were used but nowadays the typical energy range is 10 - 40 eV. As the signal level of IPES is about five orders of magnitude smaller than of PES, it took more time to build appropriate devices so that the development of IPES was about one to two decades behind PES.[89]-[91]

2.2.2. Two-photon photoemission

In contrast to the aforementioned one-photon photoemission, two-photon photoemission spectroscopy (2PPE) enables the measurement of occupied as well as unoccupied states in one experiment. Thus, it is a very powerful technique to investigate the full electronic structure of atoms, molecules, solids and interfaces.[92]-[95]
The first photoemission experiments using two excitation beams were carried out in 1977.[96]-[98] Three years later, Rudolf *et al.* used a tunable laser setup in the nanosecond range to carry out one-colour two-photon photoemission spectroscopy (1C-2PPE) experiments. As excitation source, a tunable dye laser was used to generate photons with 2.5 - 3.3 eV energy.[99] In 1988, Schönlein *et al.* conducted the first two-colour two-photon photoemission spectroscopy (2C-2PPE) experiment. For his dichromatic 2PPE experiments, he split the visible femtosecond pulses in two parts with one being

frequency doubled before usage.[100] Lateron, more complicated laser systems were constructed with two different lasers such that the two wavelengths can be chosen individually.[101] The 2PPE setup used in this thesis combines the technique of a tunable laser and frequency doubling in order to generate either a VIS pulse and a UV pulse for 2C-2PPE or UV pulses for 1C-2PPE.

2PPE utilises a pump-probe second order non-linear optical process in which one photon (pump) excites an electron below the Fermi energy E_F and a second photon (probe) excites that electron above the vacuum level E_{vac} (figure 2.2). The excited electron can either originate from an occupied molecular state of an adsorbed molecule or from an electronic state of the substrate. Afterwards, it occupies either a virtual intermediate or an unoccupied molecular state. The lifetime within the aforementioned state must be long enough to absorb another photon. However, a virtual state has no lifetime.[102] Thus, the pump and probe pulse have to be in close temporal proximity and they have to have high intensities as the signal intensities of a second-order process increase quadratically with light intensity.[44][102] By absorbing a second photon, the electron is subsequently excited above the vacuum level and detected by a time-of-flight (TOF) spectrometer for instance. Before being detected, it may occupy an unoccupied adsorbate state above the vacuum level which is called a final state.[103][104]

To distinguish whether a peak arises from an initial, intermediate or final state, the photon energy needs to be varied (figure 2.2) and it is necessary to carry out a slope evaluation by plotting the measured peak energies against the photon energy. Thus, in 1C-2PPE experiments a slope of one indicates unoccupied states while a slope of

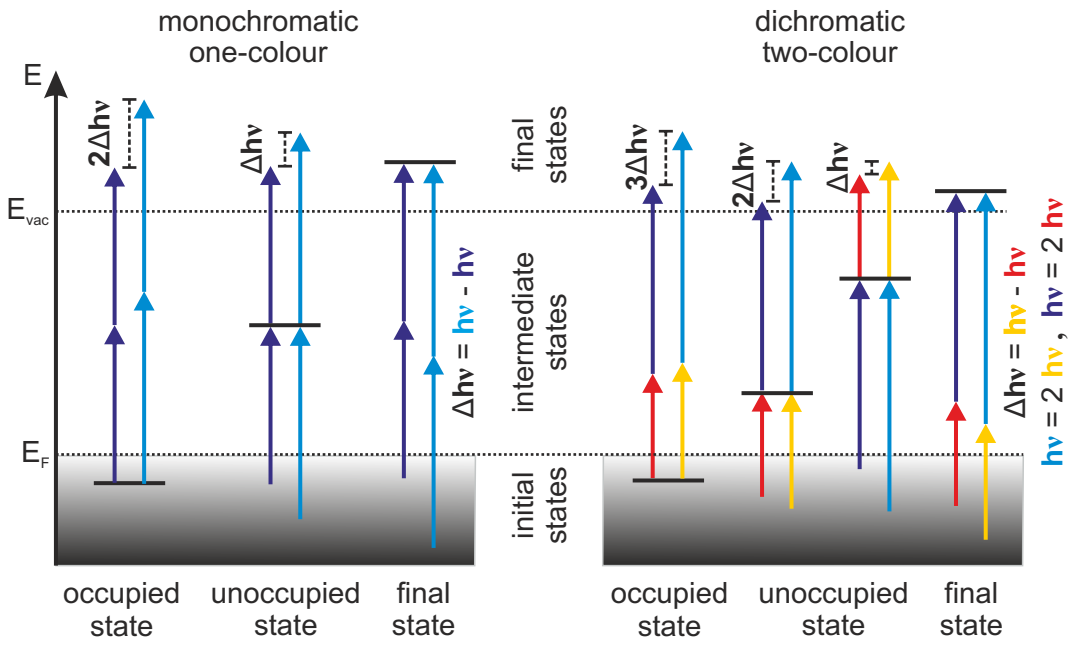

Figure 2.2. Scheme of photon energy dependent 2PPE measurements to assign peaks to occupied, unoccupied and final states according to the kinetic energy of the emitted electrons. Figure adapted.[38]

two reveals occupied states. In contrast, for 2C-2PPE experiments referred to the VIS pulse, the slope of unoccupied states correspond to one or two depending on whether the VIS or UV pulse promotes the electron into the unoccupied state, respectively. A slope of three refers to an occupied state. In monochromatic as well as dichromatic 2PPE experiments, a slope of zero corresponds to a final state. This slope analysis holds true for SS and adsorbate states but not for bulk states which exhibit dispersion along the normal component of the electron wave vector $k_{w\perp}$.[105][106] In general, for detection of an unoccupied adsorbate state, electrons from the substrate can be excited to populate the unoccupied molecular state. This creates a negative ion resonance and the measured energy level is assigned to a transport state. In case of an occupied adsorbate state, one electron of the respective state is excited by two photons above the vacuum level creating a positive ion resonance. Again, the measured energy level is referred to a transport state. In both cases, the molecule gets charged leading to a negative ion and a positive ion, respectively. According to Koopman's theorem, the energies of those single-electron states can also be interpreted as ionisation potential IP and electron affinity EA as the ionisation potential of an occupied state is equal to its negative orbital energy and the electron affinity of an unoccupied state is equal to its negative orbital state, respectively.[107][108, pp. 426 f.] Thus, the transport gap E_{transp} can be determined according to equation 2.9.

$$E_{transp} = IP - EA \tag{2.9}$$

However, with 2PPE an intramolecular electronic excitation is also possible which generates an exciton, e.g. by forming an electron-hole pair. In this case the molecule remains overall neutral. For an intramolecular electronic excitation, a correlated electron-hole pair can be formed resulting in a smaller energy gap. The minimum required excitation energy determining the optical gap E_{opt} can be related to the transport gap according to equation 2.10.

$$E_{opt} = E_{transp} - E_B \tag{2.10}$$

By this means, the exciton binding energy E_B can be identified.[109]
To avoid one-photon processes, which exhibit four orders of magnitude higher cross sections compared to second-order two-photon processes and thus would completely mask signals from the latter, the photon energies are kept smaller than the work function of the investigated system for 2PPE measurements.[44][94] Upon 2PPE experiments, electrons are ejected and thus the sample has to be grounded or held at a constant potential to avoid electrical charging effects. The use of insulating samples is merely possible if the insulating part is kept thin and deposited on a conducting substrate.[102] Along with other photoemission techniques, 2PPE is a surface-sensitive

method since the inelastic mean free pathway of the photo-ejected low-energy electrons is quite short being in the nanometer range or below, depending on the photon energy and the material used.[80][81] If a 2C-2PPE experiment is carried out using a UV and VIS pulse with no time delay between both pulses, one has to keep in mind that also 1C-2PPE processes will happen due to the absorption of two UV photons. This is accounted for by recording mono- and dichromatic data with the same parameters on the same spot and subtracting the monochromatic data from the dichromatic data to obtain the unadulterated 2C-2PPE spectra.
The kinetic energies of the ejected electrons are composed of the initial binding energy E_B with respect to the Fermi energy E_F, the work function and the energies of the two photons $h\nu_1$ and $h\nu_2$ according to equation 2.11.

$$E_{kin} = h\nu_1 + h\nu_2 - \phi + E_B \tag{2.11}$$

The work function can also be expressed as difference between the vacuum level E_{vac} and the Fermi level according to equation 2.12.

$$\phi = E_{vac} - E_F \tag{2.12}$$

Electrons being excited from the Fermi edge require the least energy to be pushed above the vacuum level and hence show the highest kinetic energies (figure 2.3). They appear in the 2PPE spectrum at the Fermi edge position. Electrons possessing the least kinetic energy are located at the secondary edge. A 2PPE spectrum spans over the energy range of the two photons involved and shows peaks arising from occupied and unoccupied substrate or adsorbate states as well as an exponential background. Those peaks result from increased cross sections due to a high density of occupied and unoccupied states. The exponential background arises from secondary electrons being excited by inelastic scattering events.[38][102][110] A common way to display 2PPE spectra is not to refer the data to the measured kinetic energy but to the final state energy E_{Final} which corresponds to the sum of the kinetic energy and the work function according to equation 2.13.

$$E_{Final} - E_F = E_{kin} + \phi \tag{2.13}$$

This beneficial graphic rendition allows to easily read the work function, which is basically the energy of the secondary edge, and the binding energies of the electronic states involved. For occupied states, the sum of the energies of both photons are subtracted from the $E_{Final} - E_F$ energy whereas for unoccupied states the photon energy of the probe are subtracted from the latter in order to depict the electronic structure of the studied system in an energy level diagram with respect to the Fermi energy.[111]

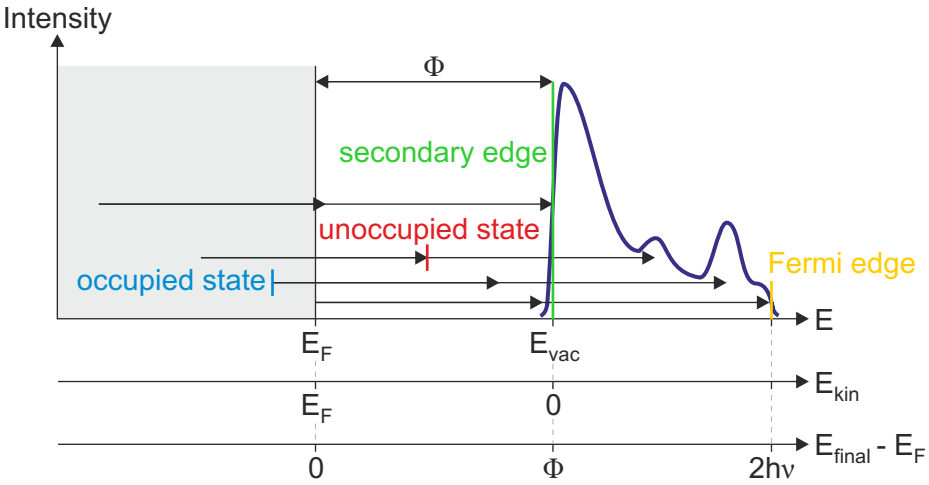

Figure 2.3. Scheme of a typical 2PPE spectrum investigating an adsorbate on a conductive substrate. Electrons of the conductive substrate or of occupied adsorbate states (marked blue) get excited by two photons $h\nu$ and leave the sample via a virtual intermediate state or an unoccupied adsorbate or substrate state (marked red). The 2PPE spectrum starts at the secondary edge and spans to the Fermi edge at $2\ h\nu$. Although the kinetic energy of the electrons is measured, the 2PPE spectrum is usually referred to $E_{Final} - E_F$.

The substrate for 2PPE experiments used in this thesis is Au(111). Being an inert conductive substrate with a homogeneous surface, it is an ideal candidate. Within 2PPE spectra, Au(111) shows features such as *d*-bands, *sp*-band and a Shockley SS. Its work function is around 5.5 eV which changes for adsorbate/Au(111) samples. Those characteristics of the used Au(111) substrate are shown in section 4.1.[102][112]
For 2PPE experiments using femtosecond laser pulses, it is possible to conduct time-resolved two-photon photoemission spectroscopy (TR-2PPE) by implementing a time delay between the two laser pulses. This is achieved by extending the optical pathway of one beam, acting as the probe pulse, by utilising a delay stage. That way, excited state dynamics can be studied on a femtosecond time scale and the respective lifetimes can be extracted. The TR-2PPE intensities include the transient populations N over time according to equation 2.14. The TR-2PPE intensity at a fixed kinetic energy of photoelectrons as a function of pump-probe delay time can be described as cross-correlation XC which is a convolution of the autocorrelation function AC and the population. In turn, the autocorrelation is a convolution of the pump intensity I_1 and the probe intensity I_2.[38][113]

$$XC(t) \propto (AC \cdot N)(t) \propto (I_1 \cdot I_2 \cdot N)(t) \tag{2.14}$$
$$\propto \int_{-\infty}^{\infty}\int_{-\infty}^{\infty} I_1(t_1) \cdot I_2(t_2 - t_1) \cdot N(t_2 - \Delta t)\, dt_1 dt_2$$

With 2PPE techniques, information about band structures and dispersion can be obtained as well. For that purpose, angle-resolved two-photon photoemission spectroscopy (AR-2PPE) is carried out by varying the angle of the substrate and thus changing

the emission angle of the photoemitted electrons in front of the analyser. For periodic structures, as it is the case for the used Au(111) crystal and well-defined adsorbates on top, the electron wave function inside and outside the periodic structure has to phase-match.[114] Hence, the wave vector parallel to the surface $k_{w||}$ is preserved during photoemission and can be calculated according to equation 2.15 where δ represents the emission angle with respect to the surface normal.

$$k_{w||} = \frac{\sqrt{2\, m_e\, E_{kin}}}{\hbar}\, sin(\delta) \tag{2.15}$$

Plotting the kinetic energy as a function of $k_{w||}$ unfolds the dispersion of the respective electronic state. Assuming a free electron like dispersion, the photoelectrons in AR-2PPE exhibit a parabolic dispersion curve which can be fitted to the data using equation 2.16. The energy E_0 at a parallel wave vector of zero as well as the effective mass m^* can thereby be determined.

$$E_B = E_0 + \frac{\hbar^2\, k_{w||}^2}{2\, m^*} \tag{2.16}$$

The effective mass is a parameter for the electrons' ability to move parallel along the surface. This way, the band structure can be mapped.[38] [93] [102] [115]

2.2.3. Temperature-programmed desorption

In order to further characterise the adsorbed species on the substrate, temperature-programmed desorption (TPD) experiments are carried out. TPD measurements are suitable to gain information about the reaction order of desorption, the binding energy, which corresponds to the activation energy for desorption, and the amount of layers of the sample as long as the adsorbed molecules desorb intact.[114, pp. 273 ff.] [116]
In 1948, Apker introduced the flash filament technique. After deposition of tungsten vapor on a ribbon in an ultra-high vacuum (UHV) chamber, he flashed the ribbon with a constant heating rate of 100 K per 10 s which led two times to a pressure increase.[117]
The corresponding spectroscopy is called thermal desorption spectroscopy and is conducted by recording the pressure change with increasing temperature. For accuracy, the temperature rise was held linear later on, which is why the programmed temperature led to the term temperature-programmed desorption.[116] [118]- [121]
Nowadays in a typical TPD spectrum, the temperature, which is linearly increasing with time, is plotted versus intensity of a molecule fragment measured by a quadrupole mass spectrometer (QMS) within a UHV chamber. At a molecule specific temperature, desorption takes place in the order of increasing binding energy of the different species adsorbed on the substrate. In the simplest case for instance, first a multilayer peak is observed resulting from desorbing molecules of higher layers and subsequently the

monolayer (ML) peak is obtained at higher temperatures resulting from desorption of the more strongly bound molecules of the ML directly attached to the substrate (figure 2.4).[109][122][123]

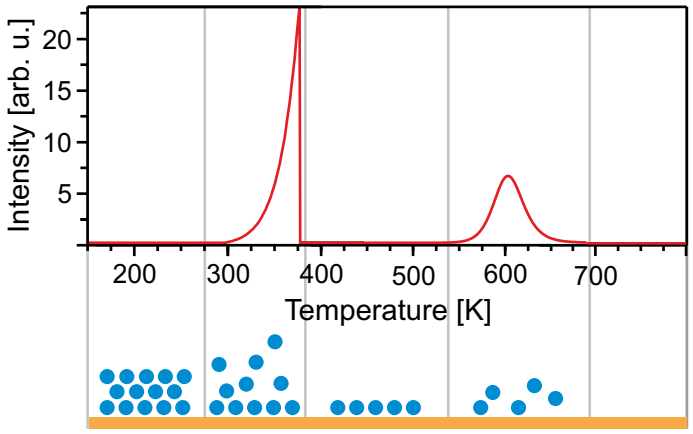

Figure 2.4. Scheme of a TPD spectrum (upper part) and the respective processes on a molecular scale (lower part). By increasing the temperature, first the higher layers get desorbed resulting in a multilayer peak. At higher temperature, the ML, which is more strongly bound to the substrate, desorbs and consequently leads to a ML peak in the TPD spectrum.

The desorption process can be described quantitatively by a kinetic model, which was first done by Smith *et al.* in 1958[119] and put further for different heating rates by Redhead in 1962.[120] When the coverage θ is described by the number of adsorbed molecules N_{ad} divided by the number of available adsorbate places N according to equation 2.17, the rate constant of the desorption process r_{des} is represented by the coverage change over time.

$$\theta = \frac{N_{ad}}{N} \tag{2.17}$$

The rate constant of desorption depends on the rate constant k_{des} and the order of the desorption process n as described in equation 2.18.

$$r_{des} = -\frac{d\theta}{dt} = k_{des}\,\theta^{n} \tag{2.18}$$

The rate constant can be expressed in an Arrhenius term consisting of a constant k_0 and an exponential term depending on the activation energy of desorption E_{des} and the temperature T as well as the universal gas constant R according to equation 2.19.

$$k_{des} = -k_0\, e^{-\frac{E_{des}}{R\,T}} \tag{2.19}$$

With k_0 being the atomic frequency ν_0, one obtains the Polanyi-Wigner equation shown in equation 2.20 which was originally formulated for the number of adsorbed molecules N_{ad} instead of coverage θ.[114, p. 234, pp. 273 ff., p. 498][124, p. 182][125]

$$\frac{d\theta}{dt} = -\nu_0 \, \theta^n \, e^{-\frac{E_{des}}{R\,T}} \tag{2.20}$$

The shape of the TPD spectrum depends on the order of the desorption process (figure 2.5). In a zero-order process, the desorption rate is independent of the initial coverage and therefore the signal increases exponentially having a sharp drop when all molecules are desorbed. With the independence of the desorption rate on the coverage, the maximum temperature increases with higher initial coverage as it takes more time for more molecules to desorb. Usually, the multilayer peak of a TPD spectrum follows a zero-order kinetic.[126]-[128] A first-order desorption process being linearly dependent on the coverage leads to a peak in the TPD spectrum with the maximum temperature being constant for different initial coverage. This kinetic is often observed for ML desorption.[126]-[128] For a recombinative second-order desorption it is necessary for two molecules to meet before desorbing. Hence, the probability for meeting is higher with increasing initial coverage which leads to a decreasing maximum temperature with increasing initial coverage.[114]

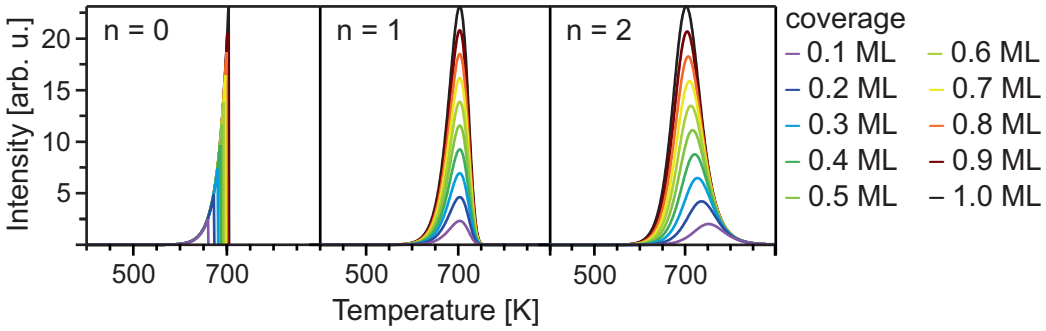

Figure 2.5. Calculated desorption spectra according to the Polanyi-Wigner equation shown in equation 2.20 for the most common orders n = 0, 1, 2 for different initial coverages ranging from θ = 0.1 - 1.0 ML in 0.1 ML steps with an atomic frequency of ν_0 = 10^{-13} s^{-1} and an activation energy for desorption of E_{des} = 2.0 eV. Figure adapted.[122]

In order to solve the Polanyi-Wigner equation shown in equation 2.20 and determine values for v_0, θ, n and E_{des}, several methods have been developed around 1960 by Smith,[119] Ehrlich[129] and Redhead.[120] Those methods lack accuracy as they make assumptions such as coverage independency of v_0 and E_{des}, or assume values for v_0.[116] However, lateral interactions between the adsorbed species may lead to coverage dependent values for v_0, n and E_{des}.[130] In the 1970s, more accurate analyses were carried out such as comparing the experimental data to computational plotted desorption curves.[131] Moreover, the complete analysis was introduced by King *et al.* in which all parameters of the Polanyi-Wigner equation described in equation 2.20 are determined from experimental data.[116][121] The method is still widely used as it provides high accuracy.[130][132]

Within this thesis, the coverage θ is specified in units of MLs. As the intensity I_{QMS}

of the partial pressure of molecule signals measured with a QMS is proportional to the coverage θ,[132] the latter is obtained by integrating TPD spectra in the multilayer range I_{multi} as well as in the monolayer range I_{mono} and calculating the coverage θ according to equation 2.21. This holds true as long as the molecule desorbs intact.[38]

$$\theta \; = \; 1 \; + \; \frac{\int I_{multi}}{\int I_{mono}} \, dT \tag{2.21}$$

If one monolayer is desired, there are two options to prepare the sample. On the one hand, the dosing temperature and time can be estimated by recording different TPD spectra. On the other hand, an excess of adsorbates can be prepared and the multilayer can be removed by heating to a temperature above the multilayer desorption but below the monolayer desorption.

2.2.4. Kinetic linear spectroscopy

In order to describe reaction dynamics, the population evolution of the species involved needs to be determined. For first order reactions like B $\rightarrow$ C, the concentration of species B over time $c_B(t)$ can be described by the rate constant k according to equation 2.22.

$$\frac{\partial c_B(t)}{\partial t} \; = \; - \, k \; c_B(t) \tag{2.22}$$

Integration of equation 2.22 provides the population by multiplying its starting concentration at time zero $c_{B,0}$ with an exponential term according to equation 2.23. By means of equation 2.23 it can be seen that the reaction B $\rightarrow$ C exhibits a monoexponential concentration gradient.

$$c_B(t) \; = \; c_{B,0} \; e^{-k \; t} \tag{2.23}$$

To indicate the lifetime of a species, its characteristic lifetime τ is calculated which corresponds to the reciprocal rate constant as described in equation 2.24. The characteristic lifetime of a species specifies thereby the time after which the starting concentration is declined to 1/e.

$$\tau \; = \; \frac{1}{k} \tag{2.24}$$

The rate constant is temperature dependent and can exactly be determined within the transition state theory and the Eyring equation using statistical thermodynamic concepts. For most reactions, the Eyring equation can be simplified to the Arrhenius equation shown in equation 2.25 and its linearised form described in equation 2.26. Thus, the rate constant depends on a pre-exponential factor k_0, being a measure of

the collision rate, the activation energy E_A and the temperature.

$$k = k_0 - e^{-\frac{E_A}{R\,T}} \tag{2.25}$$

$$ln(k) = -\frac{E_A}{R}\,\frac{1}{T} + ln(k_0) \tag{2.26}$$

In order to determine the activation energy of a chemical process, the rate constant at different temperatures needs to be identified. Using equation 2.26, the activation energy can be extracted from the gradient of a linear plot in which T^{-1} is plotted against $ln(k)$. This plot is called Arrhenius plot.[108, pp. 884 ff., pp. 893 ff., pp. 975 ff.]
The concentration of an optically active material can be identified with the law of Lambert-Beer shown in equation 2.27 which describes the intensity I as a function of the starting intensity I_0, the molar extinction coefficient ϵ being dependent on the wavelength, the concentration c of the absorbing species and the optical path length d.

$$I = I_0\,10^{-\epsilon_\lambda\,c\,d} \tag{2.27}$$

The absorption A of a species is defined according to equation 2.28.

$$A = log\left(\frac{I}{I_0}\right) \tag{2.28}$$

Hence, using equation 2.27 and 2.28, the Lambert-Beer law can be expressed according to equation 2.29.

$$A = \epsilon_\lambda\,c\,d \tag{2.29}$$

The absorption defined in equation 2.29 is also called absorbance or optical density (OD).[108, p. 485] [133, p. 4]
Inserting equation 2.23 in equation 2.29 yields equation 2.30 which allows the determination of the rate constant of an optically active species by fitting a monoexponential fit function to its kinetic absorption data. Beside the rate constant, the lifetime can be determined as well by using equation 2.24.

$$A(t) = \epsilon_\lambda\,d\,c_{B,0}\,e^{-\,k\,t} \tag{2.30}$$

2.2.5. Transient absorption

Transient absorption (TA) spectroscopy is a powerful tool to investigate excited state dynamics. In order to investigate ultrafast processes, femtosecond pulses are needed. At first, a pump pulse holding a specific energy excites the sample. A fraction of elec-

trons, typically in the range of 0.1 % to tens of percentages,[134] gets thereby promoted from the ground state into an excited states. Subsequently, a low intensity broadband probe pulse probes the sample at a specific time delay Δt with respect to the pump pulse. Thus, information about both emissive and non-emissive excited state species are obtained.[135] In 1985, Zewail *at al.* used this technique to describe the bond cleavage in iodine cyanide molecules after excitation in detail, which is completed within 200 fs. For opening up new pathways to study ultrafast dynamics of various processes, he was awarded the Nobel prize in 1999.[136][137]
The information of TA measurements are usually represented as difference absorption spectra ΔA as a function of the wavelength and the time delay Δt of the two laser pulses according to equation 2.31. Therein, the absorption spectra of the excited species are compared to the absorption spectrum of the ground state.

$$\Delta A(\lambda, \Delta t) = -\, log \left(\frac{I(\lambda, \Delta t)^{pump\ on}_{probe}}{I(\lambda, \Delta t)^{pump\ off}_{probe}} \right) \tag{2.31}$$

Three different phenomena contribute to TA data: ground state bleach (GSB), stimulated emission (SE) and excited state absorption (ESA) (figure 2.6).[134][138]

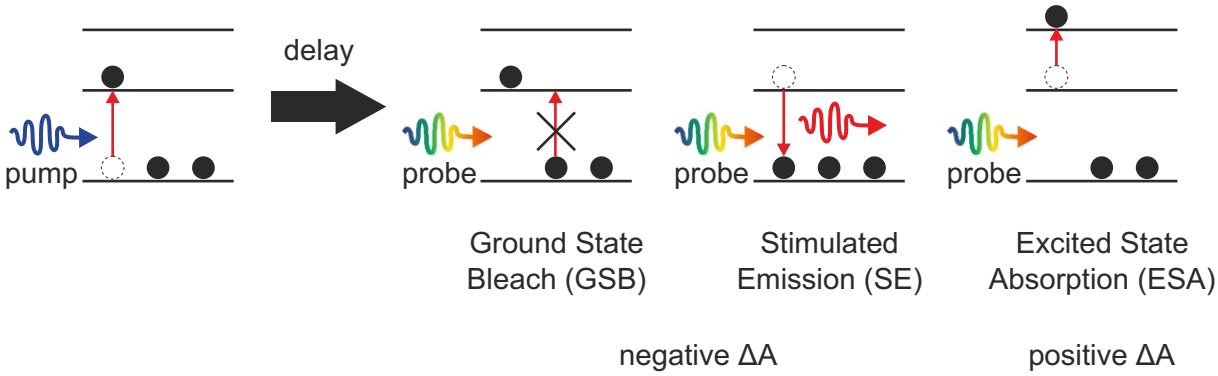

Figure 2.6. Processes contributing to TA experiments. To the difference in absorbance ΔA, GSB adds a negative contribution due to already excited electrons by the pump pulse. SE triggered by incoming photons gives a negative share as well. ESA, however, contributes in a positive way to the TA signal due to further absorption of the excited state.

Following the excitation of the pump pulse, a ratio of molecules is pushed into the excited state. Hence, less molecules are in the ground state compared to the non-excited sample. Consequently, less ground state absorption will take place upon probe interaction which results in an attenuation of absorption and thus leads to a negative signal in the difference absorption spectrum which is called GSB.[134][138]
Another phenomenon in TA spectroscopy is SE. The Einstein coefficient for absorption from the ground state into the excited state as well as the coefficient for stimulated emission from the excited state into the ground state are identical in a two-level system. Hence, SE can be triggered by photons of the probe pulse after population of the

excited state. Therefore, an incident photon matching the energy difference of optically allowed transitions from the excited state to the ground state can induce the emission of a photon of the same energy. The spectral shape of the SE is very similar to the spectral shape of spontaneous emission but can be expanded by longer wavelengths. As the photon produced by SE holds the same direction than the triggering photon, both will be detected resulting in a higher total light intensity and in turn, less difference absorption. The intensity of the probe pulse, however, is kept at a low level such that the excited state population is not considerably affected by SE.[134][138]
For optically allowed transitions, the molecules being in an excited state after pump interaction can be excited further by the probe pulse. This ESA signal can arise from other excited states or new photoproducts. Since the absorption of the excited state represents a novel absorption, the ESA will contribute a positive signal to the difference absorption spectrum. As ultrafast vibrational relaxation may be observed in femtosecond TA experiments, the same electronic species can exhibit different spectra and dynamics in time. Furthermore, absorption of photoproducts may add transient or long-lived components to the TA signal. Such long-lived states are triplet states, charge-separated states and isomerised states for instance.[134][138][139]
GSB, SE and ESA compose the difference absorption spectra (figure 2.7). The multiple contributions can overlay and vibrational progression can be involved as well. For instance, the Stokes shift of chromophores may be small enough for the GSB and the SE to spectrally overlay. This complicates the data analysis.[134]

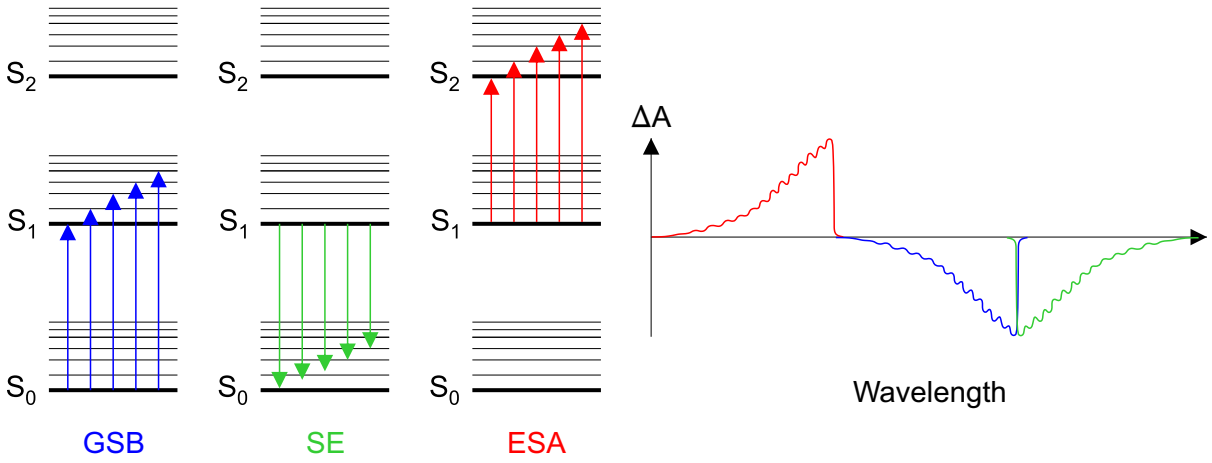

Figure 2.7. Energy level diagrams including S_0, S_1 and S_2 for the processes involved in a TA experiment and how those compose the total TA spectrum. The optically allowed processes GSB, SE and ESA including vibrational progression are shown.

TA data are collected in two-dimensions which is depicted within a 2D plot with, e.g. the pump-probe delay as abscissa and the probe wavelength as ordinate. Mathematically, the difference absorption spectra can be described as the sum of pre-exponential coefficients A_i related to each probe wavelength and the lifetimes τ of the respective

size of the basis expansion i according to equation 2.32.

$$\Delta A(\lambda, \Delta t) \; = \; \sum_{i} \; A_i(\lambda) \; e^{-\frac{\Delta t}{\tau_i}} \tag{2.32}$$

This mathematical expression is the underlying model of global analysis (GA). At the same time, TA recordings can also be depicted as sum of the molar absorptivities ϵ of j observable transient species weighted by their molar concentrations C and the optical path length according to equation 2.33.

$$\Delta A(\lambda, \Delta t) \; = \; \sum_{j} \; \epsilon_j(\lambda) \; C_j(\Delta t) \; d \tag{2.33}$$

From equation 2.33 it can be seen that the time and wavelength dimensions are separable and that the Lambert-Beer law shown in equation 2.27 can be transcribed into matrix notation accordingly.[138] [140]
Using matrix notation, the experimental TA data can be presented as a matrix $\underline{D}$ with l rows corresponding to the number of points along the wavelength axis and m columns corresponding to the number of points along the time axis. Thus, one row represents one spectrum while one column represents one kinetic time trace. In the ideal case, $\underline{D}$ can be written as product of matrix $\underline{C}$, which is of dimensions $l \; \times \; j$ with the time dependent profiles of j components at the l time delay values, and the transposed matrix $\underline{S}^T$, which is of dimensions $j \; \times \; m$ with the transient spectra of the components j measured at m wavelengths, according to equation 2.34.[138]

$$\underline{D} \; = \; \underline{C} \cdot \underline{S}^T \tag{2.34}$$

In order to decompose complex TA data and to determine how many components are present, singular value decomposition (SVD) is carried out. For this, matrix $\underline{D}$ can be described as product of the matrices $\underline{U}$, $\underline{S}$ and $\underline{V}^T$ according to equation 2.35 with the unitary matrix $\underline{U}$, which is sized $l \; \times \; m$ representing the left singular vectors, and the orthonormal matrix $\underline{V}$, which is sized $m \; \times \; m$ representing the right singular vectors. Matrix $\underline{S}$, however, has $l \; \times \; m$ dimensions being zero except for the diagonal elements containing the singular values, which are ordered in terms of their weight.

$$\underline{D} \; = \; \underline{U} \cdot \underline{S} \cdot \underline{V}^T \tag{2.35}$$

Thus, SVD is a kind of noise filter with the first singular values representing the most important components for the spectra and the last ones being noise.[138] [140]- [142]
After determination of the number of components involved, one can start to simultaneously analyse all $\Delta A(\lambda, \; \Delta t)$ spectra by GA. In general, multiwavelength data and their

fitting yields more accurate rate constants and lifetimes compared to slicing the 2D data and fitting monochromatic slices.[143] Using the parametric GA model with the singular values acting as parameters, the TA data are fitted with a sufficient number of monoexponential decays according to equation 2.23. This can be done without knowledge of the underlying reaction mechanism as population dynamics can be specified as the sum of monoexponential decays regardless of the quantity and combination of parallel and sequential pathways present.[143][144] The GA fits a number of non-interacting and parallelly decaying components. The amplitudes of those exponential fits within the global fit provide the decay associated difference spectra. They can be understood as gain or loss of absorption within a determined lifetime. Another way of modelling TA data are a sequential model in which the decay of one component leads to the increase of another component with no branching. As the sequential approach is mathematically interconvertible into a parallel model but not vice versa, fitting a sequential model is preferable. A sequential interpretation of the data yields evolution associated difference spectrum/spectra (EADS) representing the spectral evolution, e.g. the second EADS rises with the first lifetime and decays with the second lifetime. With the sequential approach being the correct reaction model, the EADS represent the species associated difference spectra and hence the EADS depict the difference absorption spectra of the species involved.[138][140][145]
Beside the exponential dynamics, the GA takes the instrument response function (IRF) into account. In fact, the TA data represents a convolution of the sum of exponential decays and the IRF. In general, the IRF is given by the shape of the exciting pulse and the detector response. For pump-probe spectroscopy, the IRF is the convolution of pump and probe pulse. Therefore, it is also called pump-probe artefact. It has a high contribution at short time scales and allows an estimation of the time resolution. In addition, the IRF is wavelength dependent caused by group velocity dispersion (GVD) which can be modelled by a polynomial function within the GA in order to correctly assign the time zero position for each wavelength. Other phenomena which have to be taken into account for GA are coherent artefacts. They can distort the data structure especially at short times. Coherent artefacts, such as two-photon absorption, stimulated Raman amplification and cross-phase modulation, are non-linear effects caused by the simultaneous action of a pump and a probe pulse. Its time profile can be estimated by the IRF.[138][140][146]

2.2.6. Scanning near-field optical microscopy

Scanning near-field optical microscopy is a powerful tool to investigate various samples on a nanometer scale. Hence, scanning near-field optical microscopes (SNOMs) are applied for identification and localisation of organic materials,[147][148] plasmon research[149] and mapping of electronic properties of semiconductors for instance.[150][151]

Optical light microscopy has a long history, starting from planoconvex lenses used in the Arab world in the 11th century as reading stones to magnify manuscripts and the first constructions of microscopes at the end of the 16th century. With Antoni von Leeuwenhoek microscopic techniques gain great attention of natural scientists in the 17th century.[152][153] However, as all optical microscopes utilise light, which is diffracted by passing apertures and lenses due to the wave properties of light, the resolution is limited according to equation 2.36.

$$x = \frac{\lambda}{2\, n_{ri}\, sin(\alpha)} = \frac{\lambda}{2\, NA} \tag{2.36}$$

This limitation is known as Abbe limit since it was discovered by Ernst Abbe and defines the minimal distance x of two point-shaped objects being illuminated which can be resolved. The distance depends on the wavelength of the illuminating light source, the refractive index n_{ri} and the half of the aperture angle α between object and objective with $n_{ri}\, sin(\alpha)$ also being called numerical aperture NA.
Since the numerical aperture is about 1 in most cases, but could go up to 1.5 using high refractive materials, the resolution is limited by the wavelength used and corresponds to about half of the wavelength.[154]-[156]
In order to circumvent the wavelength limitation and resolve structures of some nanometres, other techniques have to be used. One possibility is the application of scanning probe microscopes such as scanning tunneling microscopes (STMs), atomic force microscopes (AFMs) or SNOMs for instance. Binnig and Rohrer invented the first scanning probe microscope, which was the STM, and were awarded the Nobel prize in 1986.[157][158] All scanning probe techniques are based on the interaction of a scanning probe and a sample generating a near-field. Thus, the wavelength limitation discussed above, which is valid for far-field techniques, can be overcome. The resolution for scanning probe methods involving near-field interactions is limited by the geometrical shape of the probing tip.[158] The first SNOM was proposed by Synge[159] in 1928 and realised in 1984 by Pohl *et al.*[160] as well as Lewis *et al.*[161] in parallel.[156] In a SNOM, VIS or IR light is send to the sample creating an evanescent optical near-field. This term describes the non-radiating part of the electromagnetic field, which is bound to the objects surface, in close proximity ($\ll \lambda$) to a light emitter or scatterer, such as illuminated objects. Optical near-fields contain information of small local structures. Disturbing the optical near-fields by a probing tip converts the optical near-field into a propagating wave which can be detected to gain optical information about small structures. The probing tip consists of a metal-coated small tip, which enhances and strongly confines the optical near-field signal at its apex and reflects the signal to the detector. The spatial resolution depends on the tip apex being typically around 20 nm.[156][158][162]
The SNOM used in this thesis is a scattering scanning near-field optical microscope

(s-SNOM) (figure 2.8). It combines a Michelson interferometer for Fourier transform infrared spectroscopy (FTIR) and an AFM unit. The interferometer consists of a broadband IR light source sending its light to a 50:50 beam splitter. Half of the light is reflected onto the tip by several mirrors and finally a parabolic mirror. The other half is transmitted to the reference mirror which translates linearly along the beam path. Next, both parts get reflected to the beam splitter and simultaneously travel to the detector after being focused.[163][164]

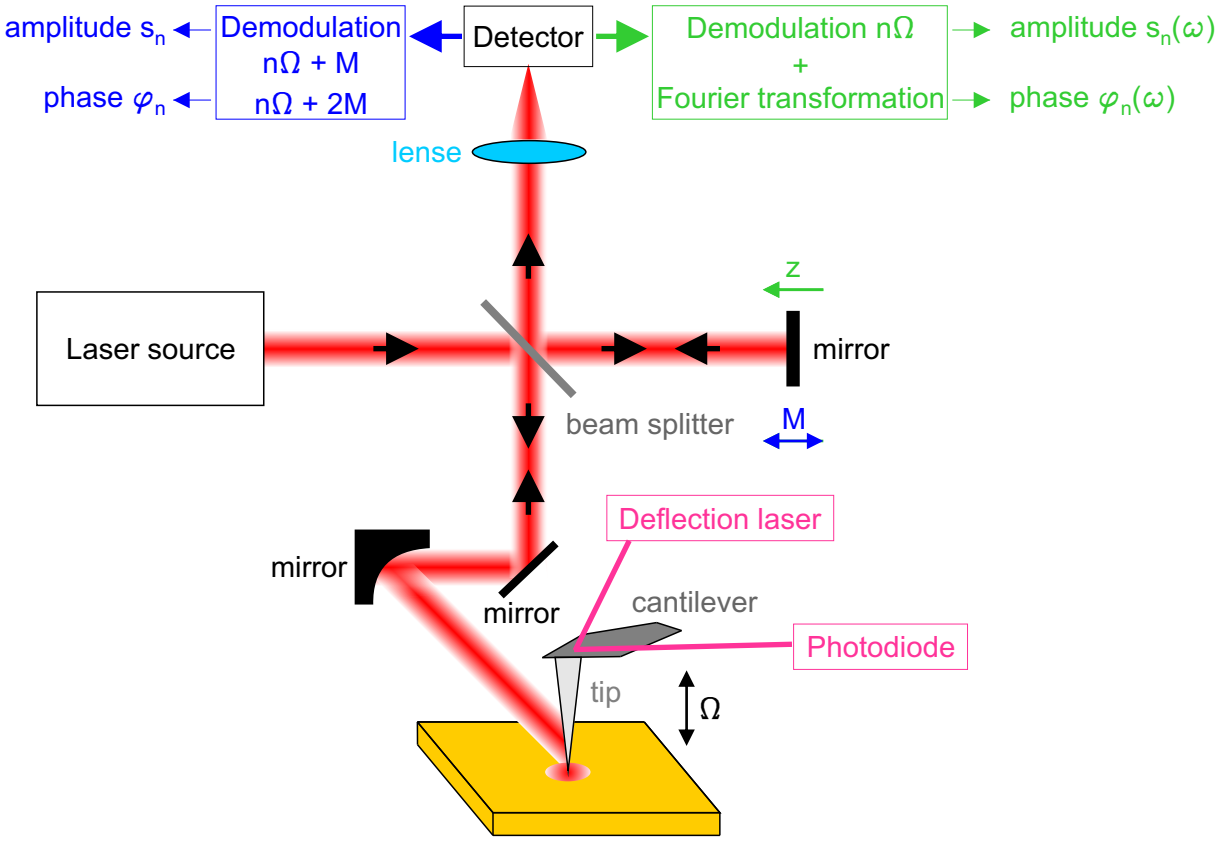

Figure 2.8. Asymmetric Michelson interferometer used in the s-SNOM setup. The laser light is split in two 50:50 partial beams after reaching the beam splitter which directs the transmitting part onto the reference mirror while the reflected part is directed onto the probing tip. The sample illumination happens due to scattering. The backscattered light containing near-field information is merged with the partial beam of the reference arm and both get detected. Within nano-FTIR mode (green), the reference mirror executes a linearly translation z while it oscillates with frequency M in the PsHet mode (blue). In both cases, the near-field amplitude and phase are detected background-free. The tapping AFM unit oscillating with frequency Ω is controlled via the deflection laser which is detected by a photodiode.

The electric field of one wavelength of the incident IR beam E_{in} of the laser source is given by its amplitude $E_{in,0}$, the angular frequency ω, the time, the absolute value of the wave vector and the position z according to equation 2.37.

$$E_{in} = E_{in,0}\, e^{i(\omega t + k_w z)} \tag{2.37}$$

The relation of ω, k_w and wavelength is defined according to equation 2.38.

$$\omega \;=\; k_w \; c_{vac} \;=\; \frac{2\pi}{\lambda} \; c_{vac} \tag{2.38}$$

In general, the intensity of a beam reaching the detector is direct proportional to the square of the absolute value of the electric field. In a Michelson Interferometer, two beams are detected simultaneously which differ in terms of their travel distance z. Both light waves interfere at the detector depending on their phase shift due to the travel distance difference Δz constructively or destructively for each wavelength. For Δz being zero, all wavelengths interfere constructively and the position of the reference mirror is called zero path difference (ZPD).[165, p. 27] The detected intensity I_D of one wavelength is direct proportional to the square of the absolute value of the sum of the partial beams E_1 and E_2 generating the detected electric field E_D according to equation 2.39.

$$I_D \;\propto\; |E_D \; E_D^*| \;=\; |E_1|^2 \; |E_2|^2 \;+\; 2 \, |E_1| \; |E_2| \; cos(k_w \; \Delta z) \tag{2.39}$$

With the intensity of the two partial beams I_1 and I_2 being half of the incident intensity I_0, the detected intensity of each wavelength can be expressed according to equation 2.40.

$$I_D \;=\; I_0 \; (1 \;+\; cos(k_w \; \Delta z)) \tag{2.40}$$

Thus, by changing the position of the reference mirror, the intensity is captured at the detector as a function of Δz in space domain. In order to universalise equation 2.40 to be valid for broadband laser sources, it needs to be integrated over all wavelengths. Next, the detected interferogram is Fourier transformed from the space domain into the frequency domain. According to equation 2.41 this is achieved by integrating over space such that the intensity is obtained as function of light frequency.

$$I_D(\tilde{\nu}) \;=\; \frac{1}{2\pi} \int_{-\infty}^{\infty} I_D(\Delta z) \; cos(k_w \; \Delta z) \; d\Delta z \tag{2.41}$$

Next, a reference spectrum is taken in order eliminate effects such as unsymmetric light sources, residual gas or properties of the detector. Dividing the spectrum of the sample by the reference spectrum thus yields the relative transmission spectrum free of the above mentioned effects. Usually, the frequencies are converted into wavenumbers $\tilde{\nu}$ in order to display IR spectra. In this manner, FTIR provides a precise and fast way to gain absorption spectra of materials.[64, pp. 184 ff., pp. 291 ff., pp. 317 ff.] [166] [167]

The other part of the s-SNOM consists of the AFM unit scanning the sample in tapping mode. The AFM unit is composed of the metal tip, which also acts as probing tip for the

light detection and is mounted on a cantilever, piezo elements and a deflection laser being detected by a photodiode. Within the tapping or intermittent mode, the metal tip including the cantilever oscillates with the tapping frequency Ω close to its resonant frequency allowing one sample contact per period of oscillation. The metal tip interacts with the sample due to van-der-Waals and coulomb interactions. According to attractive or repulsive interactions, the force between tip and sample and thus the tip frequency changes leading to a deflection of the cantilever. This alteration is detected via the deflection laser. Subsequently, the feedback loop controlling the force between tip and sample and hence the tapping frequency is activated which changes the latter enabling a constant tapping frequency. By this means, the topography of the surface is received by the change of the tapping frequency.[162][168]
In order to gain optical information about the sample, it is illuminated due to scattering of the IR light at the probing tip. After interaction of the light with the sample, it is back-scattered onto the tip and directed to the detector. Because of this scattering process, the technique is called scattering or apertureless SNOM in contrast to aperture-type SNOM which utilises a light fibre within the tip to illuminate the sample directly.[158][162]
The electric field of the backscattered light E_{sc} in a s-SNOM can be written as a product of the complex scattering coefficient σ_{sc} and the incident electric field E_{in} according to equation 2.42. The scattering coefficient consists thereby of a scattering amplitude s and a scattering phase φ.

$$E_{sc}(\omega) \;=\; \sigma_{sc}(\omega)\; E_{in}(\omega) \;=\; s(\omega)\; e^{i\varphi(\omega)}\; E_{in}(\omega) \tag{2.42}$$

The imaginary part of the scattering phase is determined exclusively by the local dielectric function and is direct proportional to the effective absorption cross section. Thus, it is linked to the far-field absorption such that the imaginary part of the near-field phase represents the local absorption. In contrast, the amplitude is connected with the real part of the local dielectric function describing the refractive index. Due to the construction of the interferometer incorporating the sample in one of the interferometer arms instead of in front of the detector, as it is the case for many FTIR interferometers, the scattering coefficient and the phase can both be detected. This arrangement is called asymmetric Michelson interferometer.[147][156][169]
For the nanoscale Fourier transform infrared spectroscope (nano-FTIR) mode, the interferometric process is performed as described above. However, E_{sc} not only contains near-field signals but it is rather a sum of the near-field and background scattering with the latter dominating the overall detected intensity. In order to suppress the background scattering, the tip is modulated harmonically with the tapping frequency Ω such that the scattering coefficient due to background scattering σ_{bg} can be considered constant or linearly varying with the tip-sample distance. On the other hand, the signal of the near-

field scattering coefficient σ_{nf} exhibits a non-linear modulation regarding the tip-sample distance as it strongly depends on the interaction of the tip with the sample. In conventional symmetric Michelson interferometers, the detected intensity of higher harmonics $n \geq 2$ of the tapping frequency can be calculated according to equation 2.39 by considering the scattered electric field of 2.42 as a sum of background scattering and near-field interaction yielding equation 2.43.

$$I_D \propto \sigma_{bg,0}\, \sigma^*_{nf,n} + \sigma^*_{bg,0}\, \sigma_{nf,n} \tag{2.43}$$

Hence, even for higher harmonics $n \geq 2$ the higher order near-field scattering coefficient is multiplied with the $n = 0$ background scattering coefficient which is called multiplicative background. However, for asymmetric interferometers as used in nano-FTIR, the near-field and scattering background contributions can be fully separated due to their different modulations in respect of the tapping amplitude as described in equation 2.44. Correspondingly, the detected intensity is direct proportional to the electric field of the partial beam of the reference arm E_{ref} at the ZPD position z_0 and $E_{nf,n}$.

$$I_D(\tilde{\nu}) \propto E_{ref}(d_0)^*\, E_{nf,n} \tag{2.44}$$

This way, in the nano-FTIR mode, samples can be scanned and spectra can be taken using a broadband IR laser.[148][156]

In order to map samples with a monochromatic laser source, which is a useful tool for e.g. excitation of one material in a multi-material sample, the pseudo-heterodyne (PsHet) mode is used. Beside the laser source, there is another difference in the PsHet mode compared to nano-FTIR. The reference mirror oscillates with the frequency M with $M \ll \Omega$. By this means, the detected intensity is direct proportional to the square of the absolute value of the sum of E_{bg}, E_{nf} and E_{ref}. Whereas in nano-FTIR mode signals occur at the detector at the tapping frequency and its higher harmonics, in PsHet mode also sidebands at $n\Omega \pm mM$ with the integer $m \geq 1$ are detected. Using the first $m = 1$ and second $m = 2$ sideband, the near-field amplitude and phase are obtained background-free according to equations 2.45 and 2.46, respectively, with the complex-valued constant f related to the interferometer alignment being directly proportional to $e^{i\,\zeta_{ref}}$ with ζ_{ref} embedding the reference phase offset. The intensities of the higher harmonics are thereby labelled as I_n.

$$s_{nf,n} = 2.16 f \sqrt{I^2_{n,1} + I^2_{n,2}} \tag{2.45}$$

$$\varphi_{nf,n} = arctan\left(\frac{I_{n,2}}{I_{n,1}}\right) + \zeta_{ref} \tag{2.46}$$

If the data is referenced to a reference spectrum, $2.16f$ and ζ_{ref} cancel out. By this means, the near-field amplitude and phase can be calculated free of background only at the detected intensity.[156] [170]

The last measurement mode used in this study is the atomic force microscope infrared (AFM-IR) mode. In contrast to the modes discussed beforehand, it is not operated with a continuous wave (CW) laser but with a pulsed laser. Due to the excitation of the materials, molecular vibrations are induced. By returning to the ground state, part of the vibrational energy is dissipated as heat. Due to subsequent temperature rise, the sample expanses thermally. According to this photothermal transduction, the technique is also called photothermal induced resonance. The thermal expansion is direct proportional to the thermal expansion coefficient of the material. To suppress background signals, the AFM-IR mode is also based on the heterodyne detection discussed above.[168] [171]

3. Experimental Details

Within this chapter, the experimental setups used for the aforementioned and explained experimental techniques are presented. At first, the setup for 2PPE spectroscopy is illustrated in section 3.1, which also includes the setup for TPD experiments. Afterwards, the other used femtosecond pump-probe setup, the TA setup, is explained in section 3.2. Linear optical spectroscopes used for long-term kinetic measurements are elucidated next in section 3.3. At last, the setup of SNOM used in this thesis is demonstrated in section 3.4.

3.1. Two-photon photoemission setup

The setup for 2PPE spectroscopy used in this thesis consists essentially of two parts: the UHV system and the femtosecond laser system. Both systems will be examined in detail in the next sections 3.1.1 and 3.1.2, respectively. In addition, the TOF detection of the photoemitted electrons is of great importance such that the TOF spectrometer will be presented afterwards in section 3.1.3. As the data acquisition of 2PPE experiments taking place in a UHV environment requires well balanced steps which are implemented in a self-written LabView program, the data acquisition will be described in the last section 3.1.4 of this chapter.

3.1.1. UHV chamber and sample preparation

To carry out PES, UHV conditions are required as it is a surface sensitive technique. Thus, the surface has to be clean and not contaminated by residual gas particles which adsorb on the surface of the sample. In addition, the analyser of the photoemission experiments is a TOF spectrometer (section 3.1.3) for which the ejected electrons have to have a free way to the detector without any collision with gas particles.
Hence, experiments and sample preparations are conducted in a UHV chamber with a base pressure of $1 \cdot 10^{-10}$ mbar. The UHV is achieved by a large turbo molecular pump (TPU 520, Balzer) which requires a pre-vacuum obtained by a smaller turbo pump (TPU 071P, Pfeiffer) and a four-stage membrane pump (MD4, Vacuubrand). To maintain the base pressure in the main UHV chamber, the sample transfer system and the evaporator are separated by gate valves which can be closed if the sample transfer system or the evaporator needs to be opened. Both are also pumped down by turbo pumps. In addition, the manipulator is separately pumped out by the pre-pump of the main chambers' turbo pump.
The UHV chamber can be divided into the upper and the lower level (figure 3.1). In the former, the sample preparation takes place. The sample or substrate can be transferred into the main chamber using the transfer rod. It can either be a sample which has been

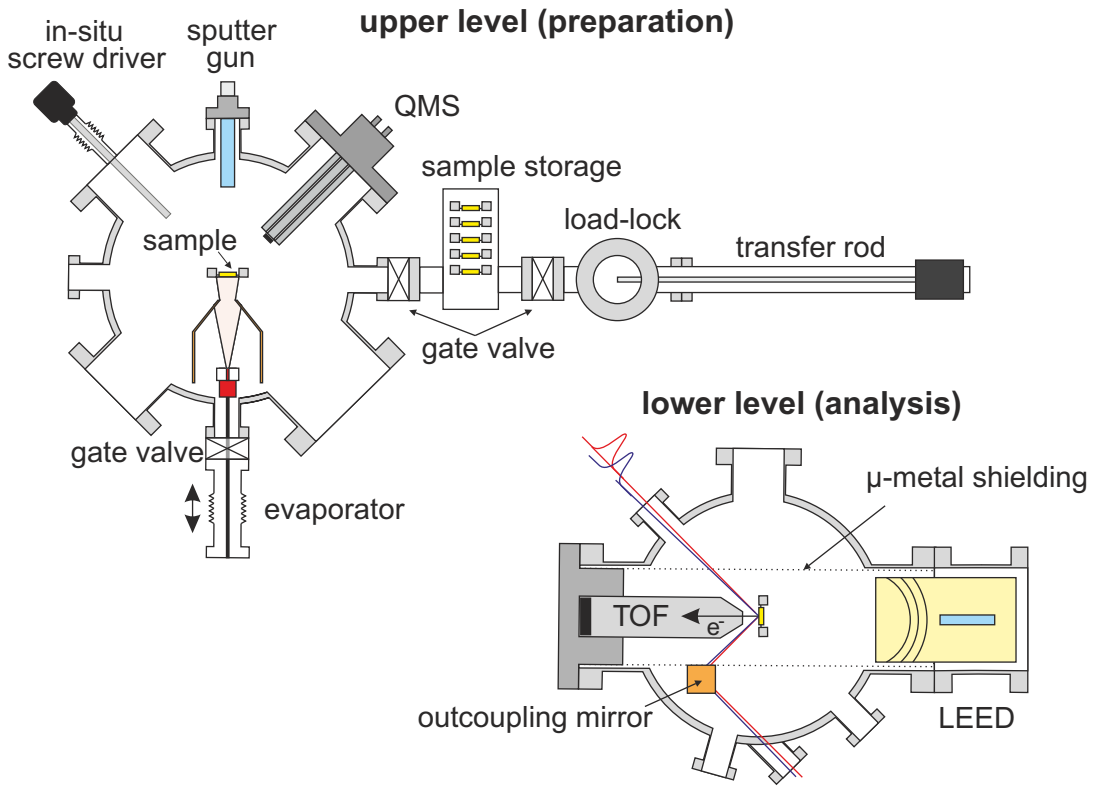

Figure 3.1. Scheme of the UHV Chamber used in this thesis. Sample preparation and TPD measurements are carried out in the upper level while PES measurements are conducted in the lower level. Figure adapted.[172]

prepared outside the chamber and brought in via the load-lock or it can be a sample or substrate which has been stored in the sample storage.

An easy sample or substrate transfer is achieved by the home-built sample holder (figure 3.2). The lower part, which is called sample boat, can easily be transferred using the transfer rod. Next, the sample boat can be fixed to the upper part with the in situ screw driver. The conductive sample or substrate is connected to tantalum wires for resistive heating. Therefore, an electric circuit is required, which is realised with the sample holder as well as the sample boat being divided into a left and right part which are separated by sapphire plates. This way, the sample can be heated to 800 K with a constant heating rate of 1 K s^{-1} by a proportional-integral-derivative (PID) control loop mechanism. The heating is carried out by a temperature controller (340 cryogenic temperature controller, Lake Shore) which also monitors the temperature by a type K thermocouple which is mounted at the back side of the crystal and connected to the temperature controller.

The PID controller uses an algorithm for closed-loop control operation following equation 3.1. For the heater output HO, three parameters, proportional P_{PID}, integral I_{PID} and derivative D_{PID} as well as the error e_{PID}, are necessary to accurately be determined for controlled heating.

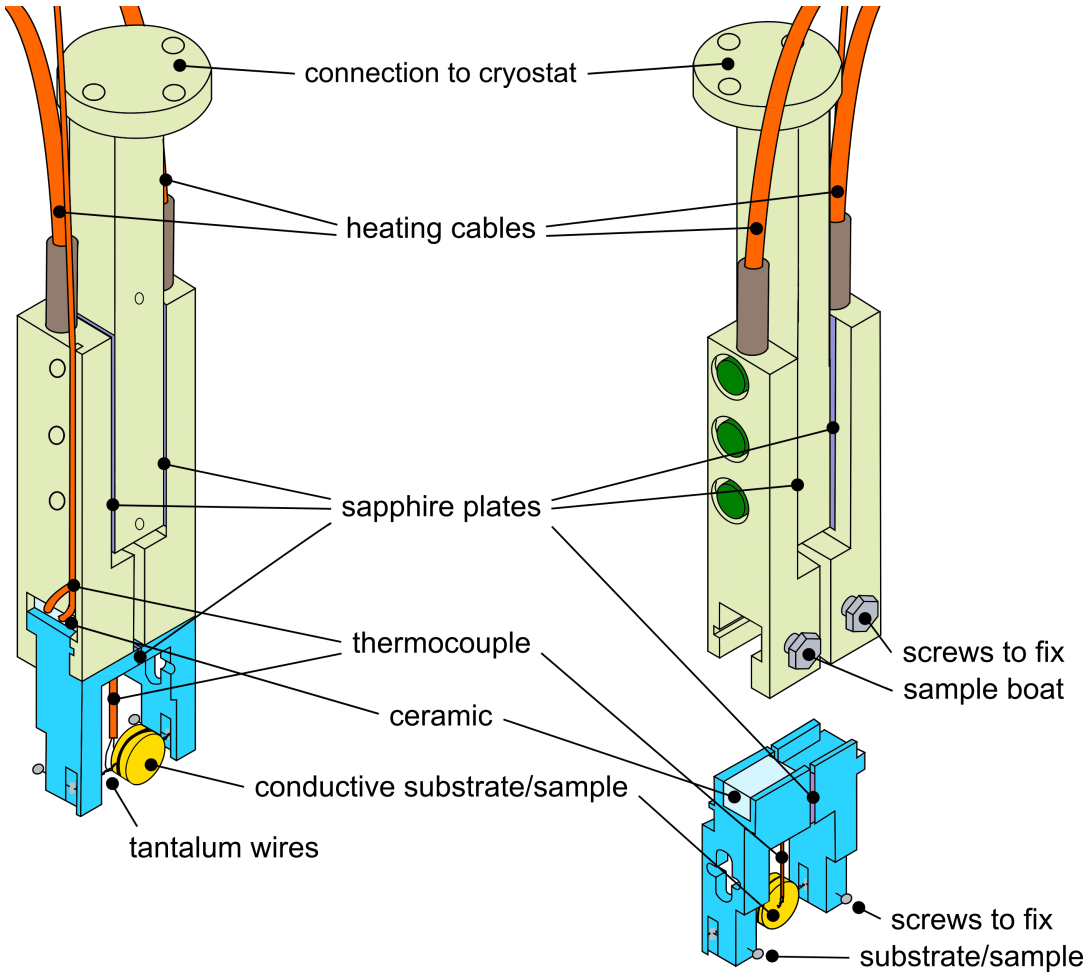

Figure 3.2. Sample holder within the UHV Chamber. The upper part is connected to the cryostat for cooling as well as to a resistive heater for heating for which the sample holder has to be divided into two parts (left and right) which are separated by sapphire plates. The lower part, which is called sample boat, can be exchanged. Figure adapted.[172]

$$HO = P_{PID}\left[e_{PID} + I_{PID}\int e_{PID}\,dt + D_{PID}\frac{de}{dt}\right] \tag{3.1}$$

The error is thereby calculated by subtracting the feedback reading from the set point. The parameters depend on the system to be heated and are influenced not only by the material used but also by the quality of connection of the different materials, e.g. the tantalum wire and the substrate. The proportional term, which is also called gain, mainly defines the velocity for reaching the set point temperature. If its value is too low, the set point temperature cannot be reached. If the P_{PID} value is too high, the actual temperature oscillates for a long period after reaching the set point temperature. The integral term, which is also called reset, controls the error over time such that the heater output stays constant if the set point temperature is reached. If its value is too high, it will cause nearly constant oscillations around the set point temperature. On the other hand, too low values for I_{PID} generate too slow heatings to the set point temperature. The derivative term, which is also called rate, monitors the change of the error

over time. It is important in order to regulate temperature changes in thermally fast systems. It tries to maximise the change in error to reach the set point temperature fast if the actual temperature is far below the set point temperature but slows down the heating if the actual temperature is close to the set point temperature in order not to exceed the latter too much. Therefore, an optimal D_{PID} value causes a fast reaching of the set point temperature with only little overshoot. A too low value causes more oscillations after reaching the set point temperature. If the D_{PID} value is too high, the heating regulation is instable leading to permanent oscillations around the set point temperature.[173][174]

For cooling, the sample holder is linked to a cryostat, which is cooled with liquid nitrogen and usually reaches a sample temperature of 95 K at which all 2PPE measurements conducted in this study were carried out. Once the sample or substrate is fixed on the sample holder, it can be moved along all three axes and it can be turned around the cryostat axis.

In most cases, a sample is brought in situ onto the conductive substrate (figure 3.1). First, the substrate has to be cleaned in a three step cleaning process in order to get a clean and smooth surface. Therefore, the substrate crystal is heated to 800 K with a constant heating rate of 1 K s^{-1} (figure 3.3) and all devices attached to the main UHV chamber, namely the sputter gun, the QMS and the low energy electron diffraction (LEED) screen, are turned on in order to remove adsorbed particles. Next, the crystal is sputtered with Ar^+ ions at an angle of 45° with an ion acceleration voltage of 1.5 kV and a background pressure of 2 - 3 · 10^{-6} mbar for 5 min. Lastly, the substrate crystal is thermally annealed at 800 K for 30 min to recover a high quality crystalline structure and surface.

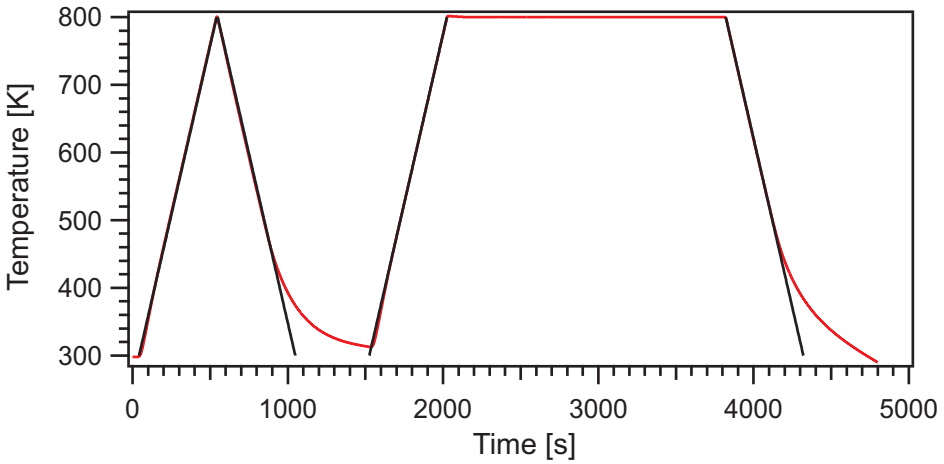

Figure 3.3. Temperature over time for the sputtering and annealing process in order to clean the substrate (red line). The heating and cooling rate is 1 K s^{-1} (black lines).

To vaporise the sample onto the substrate, the latter is turned perpendicular to the evaporator. The evaporator consists of a Knudsen cell evaporator (TCE-BSC, Kentax)

in which three samples can be stored. The dosing is controlled by the temperature of the cell and the dosing time. The other cells can be water cooled such that only one cell is heated and one sample is evaporated on the substrate.
A successful dosing is controlled via TPD (section 2.2.3) for which a QMS (QMG 112A, Balzer) with a mass-to-charge range of m/z = 1 - 200 is used to detect different mass fragments. In addition, TPDs should be carried out after laser measurements to monitor possible changes upon irradiation.
After preparation, the sample is brought to the lower level, which is shrouded by a µ-metal shielding (figure 3.1). The sample is brought closely in front of the conical TOF spectrometer. It is oriented perpendicular to the TOF spectrometer and the incoming laser beams are hitting the sample at an angle of 45°. The laser pulses are passing an MgF_2 window to get into the UHV chamber. The MgF_2 window is constantly highly transmissive in the UV, VIS and near-infrared (NIR) region.[175] In order not to falsify photoemission measurements, the UHV chamber is mounted on the vibration-isolation optical table. For further surface analysis, a LEED (reverse view RVL 900, Fisons Instruments) is also integrated in the µ-metal shielding.

3.1.2. Laser system

To carry out time-resolved photoelectron spectroscopy, beside the UHV system explained above, a femtosecond laser system is needed (figure 3.4). Therefore, a solid state CW neodymium-doped yttrium-aluminium-garnet (Nd:YAG, Verdi V18, Coherent) laser is used to pump a titanium sapphire oscillator (Ti:Sa, Mira Seed, Coherent) as well as a regenerative amplifier (RegA 9050, Coherent). The pump wavelength is 532 nm which is obtained by frequency doubling of the Nd:YAG output of 1064 nm within the Verdi V18.[176, p. 7-2f] The pump intensity of 18 W is split such that about one third pumps the Ti:Sa laser and around two third the RegA. The Ti:Sa oscillator produces pulses in the femtosecond range using the Kerr-lens mode-locking effect.[177, p. 329][178, pp. 2-3] The wavelength can be varied but is kept at 800 nm with a repetition rate of 76 MHz.[178, pp. 2-6] The temporal full width at half maximum (FWHM) is around 57 fs and the spectral FWHM around 32 nm. Those pulses are prolate in time within the stretcher to avoid damage of optical components and are amplified in the RegA afterwards. The regenerative amplifier intensifies the pulse energies from the nJ range to the µJ range. The repetition rate decreases to 300 kHz.[179, p. 3][180] Thereafter, the 800 nm pulses ($h\nu$ = 1.55 eV) are compressed in the compressor to gain an FWHM of 24 nm and 57 fs.
Those output pulses can now be used for photoelectron spectroscopy. In order to study direct photoemission, UPS measurements are carried out, for which the pulses are frequency doubled twice using two β-barium borate (BBO) crystals[181, p. 256f] to obtain pulses of 200 nm ($h\nu$ = 6.2 eV). For 2PPE measurements, the wavelength can

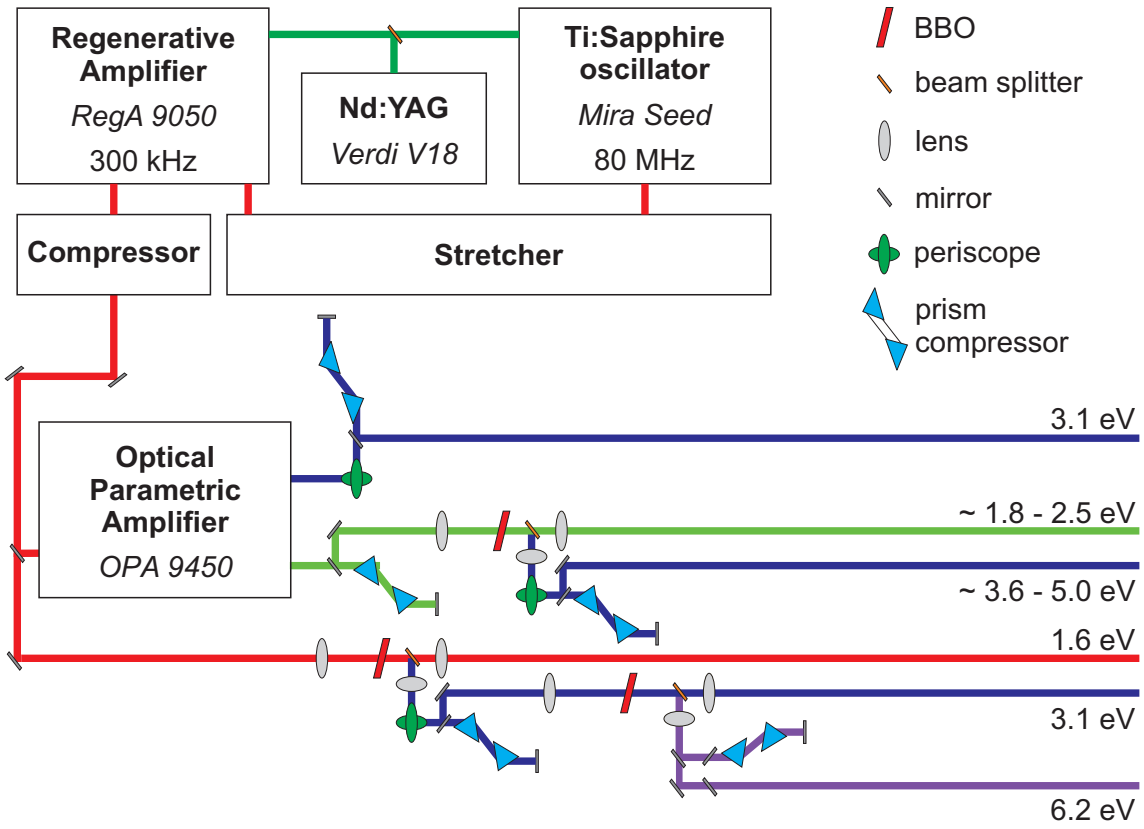

Figure 3.4. PES laser setup used in this thesis. Ultrashort laser pulses are generated in a Ti:Sapphire oscillator which is pumped by a Nd:YAG laser. After amplification by a regenerative amplifier, the wavelength can be varied by an optical parametric amplifier and frequency doubling BBO crystals. Figure adapted.[111]

be varied in a large range within an optical parametric amplifier (OPA 9450, Coherent) which converts the IR pulses into the VIS region with wavelengths varying from 1.8 - 2.5 eV (700 - 500 nm).[182] Those VIS light pulses can be frequency doubled using a BBO crystal[181, p. 256f] to additionally gain pulses in the UV region ranging from 3.6 - 5.0 eV (350 - 250 nm). In addition, an output of 3.1 eV (400 nm) is generated within the OPA.[182] Thus, 1C-2PPE is performed using the UV beam generated by frequency doubling after the OPA. In contrast, 2C-2PPE is carried out using the OPA VIS output and the frequency doubled UV beam. This leads to the restriction $h\nu_1 = \frac{1}{2} h\nu_2$ for all dichromatic measurements unless the 3.1 eV output is used.

To avoid temporal expansion of the pulses due to GVD while passing several optics on the laser table before reaching the sample, prism compressors are used. The geometric alignment and the dispersion within the prism material leads to a negative dispersion which counteracts the temporal broadening.[183] A motorised delay stage is used for the VIS and the 3.1 eV beam to vary the beam pathway in order to conduct TR-2PPE experiments.

The laser pulses are p-polarised when incident on the sample. The time-averaged power is around 0.5 - 2 mW for the UV beam after passing the BBO crystal and the

respective beam splitter as well as 4 - 7 mW for the VIS beam after passing the OPA. The spectral resolution of the incident beams is about 0.03 eV (figure 3.5**a**). The time resolution on the sample can be determined by the cross-correlation of the two incident laser beams. The pulse shape can be measured precisely using a correlation technique.[184, pp. 263 ff.] For pulsed signals, the second order correlation function $A_{XC}(t)$ of the two laser pulses with the intensity $I_1(t)$ and $I_2(t)$ has to be used according to equation 3.2 since the first order correlation function measured by a detector without spacial resolution and a time resolution greater than the delay time Δt provides a signal which is independent of Δt and the pulse shape $I(t)$.

$$A_{XC}(t) \;=\; \frac{\langle I_1(t)\; I_2(t\;+\;\Delta t)\rangle}{\langle I_1(t)\; I_2(t)\rangle} \tag{3.2}$$

To measure $A_{XC}(t)$, the signal of a non-linear process is needed which is fulfilled by 2PPE. In order not to distort the pulse shape of the signal by the lifetime of the pumped state, a short-lived state compared to the laser pulse duration has to be addressed. Therefore, the SS of Au(111) is commonly used which has a lifetime of around 27 fs.[185] Another requirement for the calculation of $A_{XC}(t)$ is that the two laser pulses share the same intensity shape. This is also given in the used setup as both laser pulses are generated by the same source and have a similarly long way on the laser table with one prism compressor each. This leads to the second order correlation function $A_{XC}(t)$ according to equation 3.3.

$$A_{XC}(t) \;=\; \frac{\langle I(t)\; I(t\;+\;\Delta t)\rangle}{\langle I^2(t)\rangle} \tag{3.3}$$

Assuming the laser pulses $I_{1,2}(t)$ to be Gaussian shaped as described in equation 3.4, $A_{XC}(t)$ possesses a Gaussian shape, too, as shown in equation 3.5.

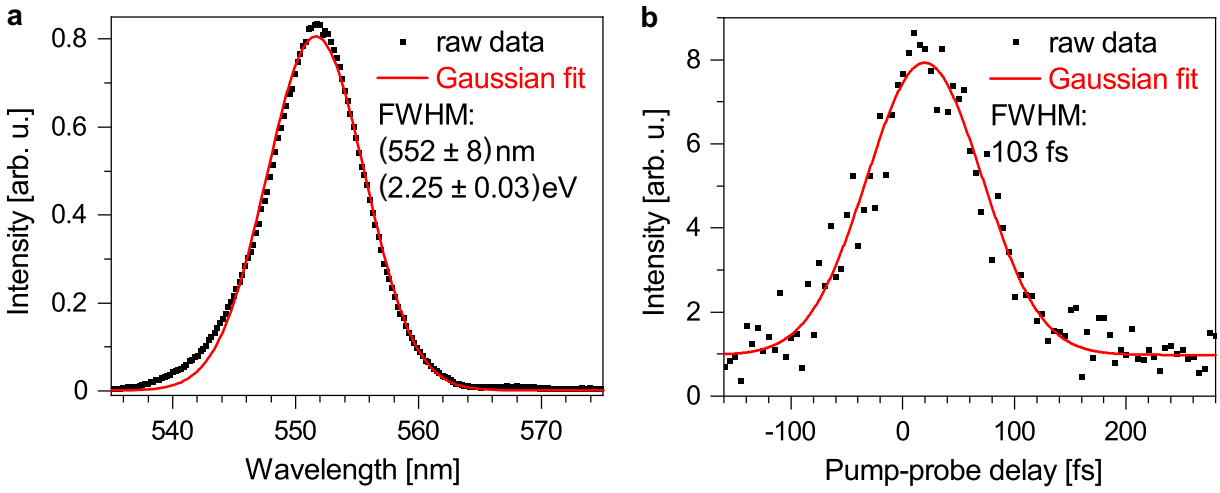

Figure 3.5. Beam characteristics of the 2PPE setup. (a) spectral and (b) temporal resolution, characterised by the autocorrelation signal measured on the substrate.

$$I(t) \;=\; I_0\, e^{-\frac{(2\sqrt{ln(2)})^2\, t^2}{\Delta T_p^2}} \tag{3.4}$$

$$A_{XC}(t) \;=\; A_0\, e^{-\frac{(2\sqrt{ln(2)})^2\, t^2}{\Delta \tau^2}} \tag{3.5}$$

The FWHM of the laser pulses ΔT_p is coupled to the FWHM of the correlation function $\Delta\tau$ according to equation 3.6 which can be used to identify the FWHM of the laser pulses $I_{1,2}(t)$ from the measured cross-correlation signal after fitting a Gaussian peak and determining its FWHM.[184, pp. 263 ff.][186, p. 107]

$$\Delta T_p \;=\; \sqrt{2}\,\Delta\tau \tag{3.6}$$

For the setup used in this thesis, the temporal resolution on the sample within the 2PPE setup is about 73 fs for the single pulses referring to an autocorrelation signal with a FWHM of 103 fs (figure 3.5**b**). The spot diameter of the laser beam ranges between 50 - 100 µm.[38][111]

3.1.3. Time of flight spectrometer

To analyse the photoemitted electrons, a TOF spectrometer is used (figure 3.6). The home-build spectrometer is constructed to properly fit to the UHV chamber of the 2PPE experiment. It has a conical tip near the sample such that the laser beams excite the sample at an angle of 45° with the thereby ejected electron having a minimal way to the TOF spectrometer. The acceptance angle of the spectrometer is 6° which should

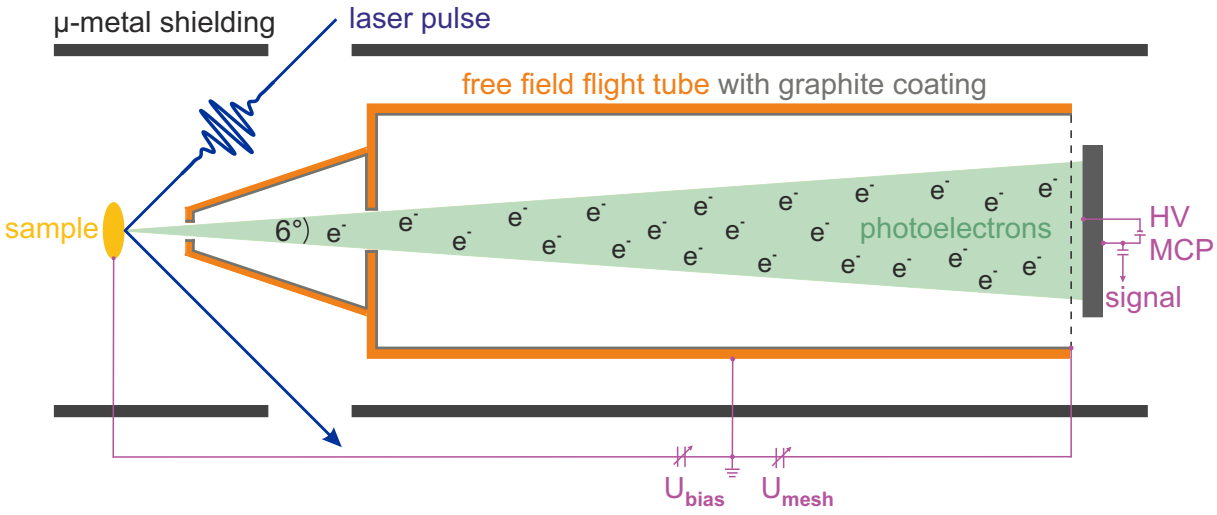

Figure 3.6. Scheme of the TOF spectrometer. The generated photoelectrons pass a graphite coated field free flight tube made of UHV compatible copper and a mesh before hitting the microchannel plates (MCPs) which generates the signal. The spectrometer is surrounded by a µ-metal shielding to protect it from external magnetic fields.

be kept in mind for AR-2PPE. The TOF tube is made up of UHV compatible copper for electrical shielding whose inside is covered with graphite to obtain a smooth surface and a homogeneous work function. In addition, the spectrometer is encircled by a µ-metal to protect its inside from external magnetic fields. The shielding is necessary to avoid deceleration, acceleration and deviations from the initial trajectory of the photoemitted electrons. At the end of the field free drift tube, a mesh is fixed which prevents penetration of the tube by external electric fields. A microchannel plate (MCP) stack having a high voltage of 2.4 - 2.7 keV applied is mounted closely to the end of the drift tube. Thus, the photoemitted electrons get accelerated to the MCPs where they create a cascade of secondary electrons which lead to a voltage drop as detected signal. Knowing the length l_{tube} of the field free drift tube of 210 mm, the mass of the ejected electrons m_e and their travel time t after ejection of the sample at time zero t_0, the kinetic energy E_{kin} can be determined (equation 3.7).[63, p. 14f]

$$E_{kin} = \frac{1}{2} m_e \left(\frac{l_{tube}}{t - t_0} \right)^2 \tag{3.7}$$

However, this analysis of the kinetic energy of the ejected electrons implies some simplifications. First, the electrons do not only pass the field free flight tube but also a short distance between the surface of the sample and the conical tip of the tube as well as a short distance between the mesh and the MCP stacks in which they are accelerated by the MCPs. These lengths are two orders of magnitude shorter in comparison to the tube length and thus can be neglected. Another important point is the difference of the work functions $\Delta\Phi$ of the sample and the spectrometer. Due to the graphite coating of the copper tube, its work function Φ_{TOF} is (4.36 ± 0.02) eV.[187] In most cases, the work function of the sample Φ_{sample} differs as well as the Fermi level and the vacuum level. Hence, the TOF and the sample are electrically connected which leads to a levelling of the Fermi levels (figure 3.7). The difference in work function leads to a cut-off of the measured spectrum if $\Phi_{sample} < \Phi_{TOF}$. Thus, a bias voltage U_{bias} is applied which compensates the difference in work function such that the complete spectrum is recorded. However, by electrically connecting the sample and the tube and applying a voltage, an electric field is created which can influence the measurements. It can mainly be compensated by the applied bias voltage as well. In order to avoid falsifications, the bias voltage should be chosen such that the slowest electrons just reach the detector. This holds true not only for $\Phi_{sample} < \Phi_{TOF}$ but also for $\Phi_{sample} > \Phi_{TOF}$. The aforementioned assumptions are corroborated by bias series in which spectra with different bias voltages are recorded with the secondary edge shifting properly with the difference in the applied bias voltages.[102] [188] [172]

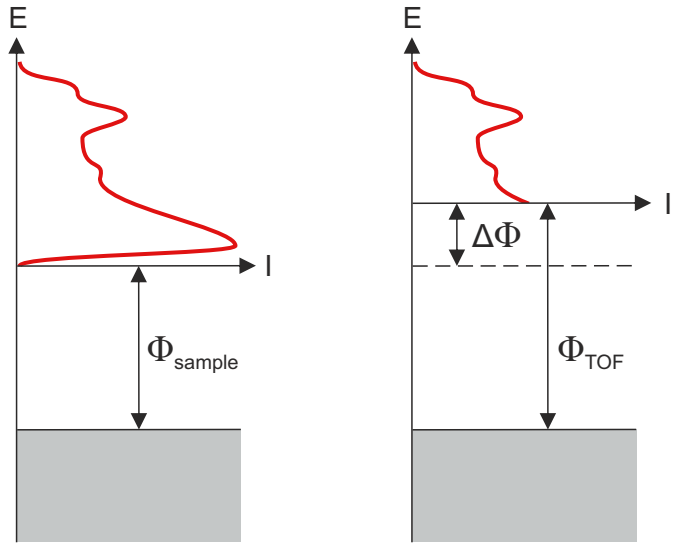

Figure 3.7. Cut-off of the spectrum due to the difference in work function of the sample and the analyser. Both have been electrically connected which leads to an adjustment of the Fermi level.

3.1.4. Data acquisition

The signal of the photoemitted electrons, which is generated by voltage drops within the MCPs caused by the secondary electron cascade, is further processed to gain a photoemission spectrum (figure 3.8). Therefore, it is enlarged by a preamplifier (VT120A Fast Timing Preamplifier, Ortec) which is basically a bipolar transistor. The amplified signals are further processed in a constant fraction discriminator (2126, Cranberra) to accurately define a time and an amplitude of the signal which may was inaccurate beforehand because of statistical fluctuations. Next, it is handled by a multiple event time digitizer (P7887, FAST ComTec) which is used as a 4 GHz TOF multiscaler. It sweeps the time domain and sorts the stop events send by the TOF spectrometer into a matrix of 8192 bins with a binwidth of 0.25 ns.
The trigger signal to start a sweep is generated by a reference photodiode at the output of the RegA. Before it reaches the multiple event time digitizer, it first passes a constant fraction discriminator (2126, Canberra) to compensate for statistical fluctuations in time. However, according to equation 3.7, the start signal t_0 is the time when the laser pulse excites the electron. As the RegA output pulse needs to pass the optical table first, a time offset has to be added. This time offset t_0 of 8 ns and 13 ns for 2PPE and UPS measurements, respectively, is experimentally determined by conducting bias series and changing t_0 to the value at which the secondary edge shifts properly with the difference in the applied bias voltage.
The travel time of the photoemitted electrons determined with the multiple event time digitizer is forwarded to a computer. The computer was constructed within this thesis to match the latest LabVIEW Software and meet high computational performance while

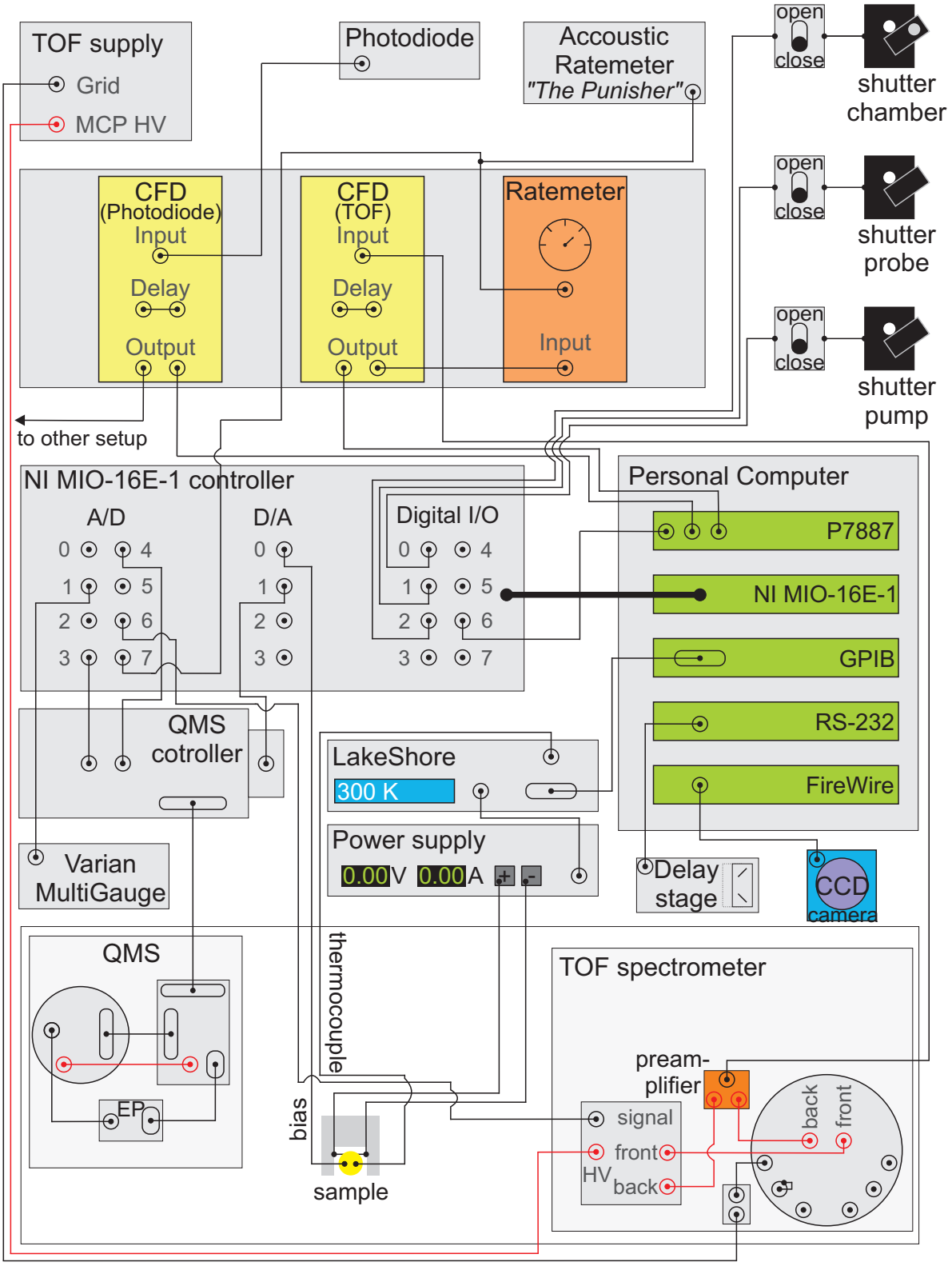

Figure 3.8. Connection diagram of the setup used in this thesis. The circuitry is needed to execute the optical and mass spectra recording and to process the TOF as well as the CCD signal. Figure redrawn and adapted.[102]

still be compatible to the devices linked with it. The computer has a Asus P10S-X mainboard with four peripheral component interconnect (PCI) slots to connect the

multiple event time digitizer P7887, a multifunctional input/output device for data acquisition (DAQ) (MIO-16E-1, National Instruments NI), a general purpose interface bus (GPIB) and a PCI expansion card for a FireWire connector. The computer is equipped with an Intel i5-7500 central processing unit (CPU) with 3.4 GHz and two 8 GB DDR4-2400 UDIMM random-access memory (RAM) modules. As a hard drive, the MX500 solid state drive (SSD) was chosen as SSD cards achieve higher reading and writing speeds than normal hard drives. The graphic board Radeon R5 230 (Sapphire) was chosen which can operate two monitors at once. The operating software is Windows 10 Professional.[189]

The signal from the multiple event time digitizer can be read out with a self-written LabVIEW program called FAST_sTOF version 11.7 executed by LabVIEW 2018 (NI). This new version of the FAST_sTOF program was written within this thesis on the basis of the self-written LabVIEW program FAST_sTOF version 9c using LabVIEW 7.1 from 2004 operated with Windows XP. The computer was updated to the newest operating system which was Windows 2010 after the old computer broke due to a power failure. As LabVIEW 7.1 is not compatible with newer windows versions than Windows XP,[190] which is obsolete nowadays, the most recent and therefore safest Windows version and a more recent LabVIEW version being compatible with this operating system and available in the research group was chosen. However, the old program FAST_sTOF version 9c is not compatible with LabVIEW 2018. Programs written in LabVIEW in general are composed of virtual instruments (VIs). Several VIs of the old program are not running with LabVIEW 2018 and had to be changed.[189][191] Particularly, the VIs for data acquisition were dramatically changed in terms of their architecture. In the old program running with LabVIEW 7.1, traditional NI-DAQ-VIs were used which were discontinued in 2009 after six years of transition in which traditional NI-DAQ-VIs were offered as well as their replacement NI-DAQmx.[192]-[194]

The link of the LabVIEW program to the MCDWIN software (FAST ComTec) controlling the P7887 card is realised by subvi-files from FAST ComTec which were slightly modified. The signal has to be transferred from the time domain to the energy domain which is done by the LabVIEW program. Thus, the intensity plotted on the ordinate is rescaled according to equation 3.8 while the kinetic energy plotted on the abscissa is calculated by equation 3.7.

$$\frac{dN}{dE_{kin}} = \frac{dN}{dt}\,\frac{dt}{dE_{kin}} = \frac{dN}{dt}\left|\frac{dE_{kin}}{dt}\right|^{-1} = \frac{dN}{dt}\,\frac{(t\,-\,t_0)^3}{m_e\,l^2} \tag{3.8}$$

Furthermore, the FAST_sTOF LabVIEW program can control the MCDWIN software by starting new measurements and defining their parameters, such as DAQ time.

To link the self-written LabVIEW program to the further required devices, the multifunctional input/output device MIO-16E-1 is needed which features an analog-to-digital

converter A/D, a digital-to-analogue converter D/A and a digital input/output I/O part (figure 3.8). For 2PPE measurements, the bias voltage is set within the LabVIEW program FAST_sTOF and applied on the sample via the digital I/O part of the DAQ card MIO-16E-1. For 2C-2PPE experiments, three spectra are conducted (pump and probe pulse, pump only and probe only) for which two shutters controlled by the digital I/O part of the DAQ card are used. To ensure no falsification of the spectra due to a slow shutter movement, a short waiting time is added after sending the signal open or close to the shutter before recording a spectrum. In addition, the digital I/O part of the DAQ card controls a mirror in front of the coupling window of the UHV chamber which is used to reflect the laser beams onto a charge-coupled device (CCD) camera (DMK 21F04, The Imaging Source) to check the spatial overlap of the two laser beams. Therefore, the distance between the mirror and the camera has to be equal to the distance between the mirror and the sample. The camera is connected to the computer by a FireWire plugged in a PCI card and it is operated by the manufacturers software (IC Capture 2.4, The Imaging Source). The CCD camera is also used to determine the spot size of the laser beams. Furthermore, the camera can be put in front of another window of the UHV chamber in order to control the positioning of the sample in front of the TOF spectrometer.
For TR-2PPE measurements, the delay time of the two laser beams is varied by changing the path length of the VIS laser beam using a motorised precision positioning linear delay stage (M-505.4DG for the VIS OPA output, M-510.12 for the 3.1 eV output, Servocontroller C-862.00, all from Physik Instrumente PI). The controller of the stage is linked to the computer by a recommended standard (RS) RS-232 interface. The stages can be operated with the LabVIEW program FAST_sTOF via LabVIEW subvifiles controlling the software of the stage (NetMove420, PI). To avoid adulteration of a time-resolved measurement, the recording is stopped while the stage is moving and a short waiting time is added before the recording is continued.
Furthermore, there is a second self-written LabVIEW program called Universal_SH version 02_1. It is written to control pressure and temperature, to set temperature and heating rate as well as to perform QMS experiments. This version was written within this thesis. Just as the FAST_sTOF program, the old version 01 of Universal_SH LabVIEW program was used with LabVIEW 7.1 on an computer running with Windows XP as the operating system. By changing to the newer computer with Windows 10 and LabVIEW 2018, the Universal_SH version 01 program was not working due to compatibility problems and had to be reprogrammed.[189][191]
To monitor the pressure inside the main chamber, the LabVIEW program is linked to an ion gauge (Multi-Gauge Controller, Varian) via the A/D part of the MIO-16E-1 card. Its analogue signal (1 - 10 V) being proportional to the measured value is converted into a pressure unit within the LabVIEW program. For monitoring the temperature of

the sample, both self-written LabVIEW programs are linked to a temperature controller (340 Temperature Controller, LakeShore) via a GPIB PCI plug-in card. The temperature controller is additionally controlling a power supply (SM 35 - 45, Delta Elektronica) for resistive heating of the sample via a type K thermocouple. The heating is implemented by a PID control loop mechanism for precise heating with a defined heating rate within the Universal_SH program. The PID parameters are entered in the Universal_SH LabVIEW program and forwarded to the temperature controller and the power supply. The standard PID parameters are 15, 15 and 15, respectively, which results in a constant heating rate of 1 K s^{-1}.
For QMS experiments, the analogue signal of the QMS (1 - 10 V) is read out at the A/D part of the DAQ card and transformed into the proper unit. This way, e.g. residual gas analysis can be conducted by scanning the mass-to-charge ratio. In addition, by heating while monitoring specific mass-to-charge ratios with the QMS device, TPD measurements are carried out. To set the mass-to-charge range and the resolution for the former and the mass-to-charge ratios for the latter, the LabVIEW program Universal_SH is communicating with the QMS via the D/A part of the MIO-16E-1 card.
Following the data acquisition, the data are analysed with the program Igor Pro 6.37.

3.2. Transient absorption setup

For TA measurements, a regenerative titanium sapphire amplified laser system is used in order to produce femtosecond pulses (Astrella, Coherent, figure 3.9). The 90 fs pulses are centred around 800 nm and hold an energy of 1.6 mJ with a repetition rate of 4 kHz. Subsequently, the laser pulse is divided into two parts with a 60:40 beam splitter of which one part having about 0.65 mJ is directed into a collinear optical parametric amplifier (TOPAS PRIME, Light Conversion) to generate the femtosecond pump pulses. The computer controlled optical parametric amplifier can tune the wavelength continuously from UV to NIR from about 189 nm - 20 µm to set the desired wavelength. After passing a chopper with 2 kHz repetition rate, the excitation pulse is focused onto the sample within a commercially available setup (HELIOS Fire System, Ultrafast Systems). The second part of the fundamental beam having an energy of around 0.1 mJ enters the commercially available setup directly and is sent to a mechanical delay stage which enables a minimum time step size of 2.8 fs allowing a resolution of 14 fs and delay times up to 8 ns. Afterwards, the fundamental beam is directed onto a calcium fluoride, sapphire or YAG crystal which generates a linearly polarised white light continuum in the UV, VIS or NIR region, respectively. The white light continuum emerges from self-phase modulation and covers a total range of 330 - 1600 nm. Following, the white light continuum is collimated and focused on the sample as well. The polarisation between the two beams hold an angle of 54.7°, which is called magic angle, in order to

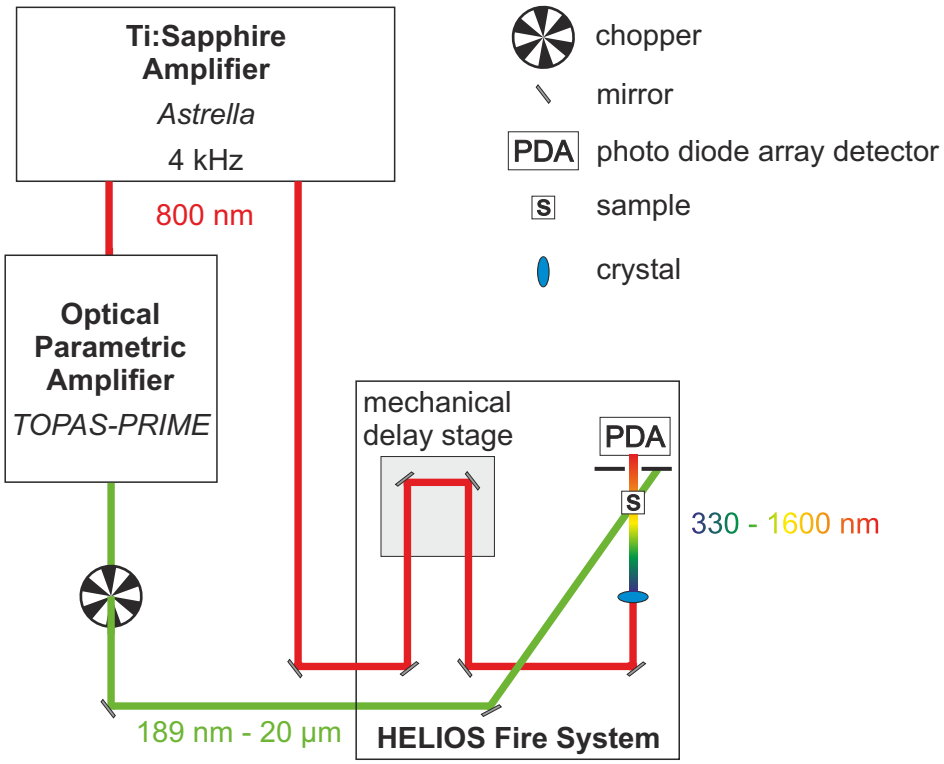

Figure 3.9. TA setup. The fundamental femtosecond pulses are generated within a titanium sapphire amplified laser system and are sent to an optical parametric amplifier in order to generate the pump pulse and to a delay stage and a sapphire crystal in order to generate the white light continuum probe pulse.

eliminate molecular structural changes and rotational diffusion contributions and thus only measure the pure population dynamics.[195][196] The spot diameter at the sample is around 300 µm and the autocorrelation is about 130 fs.[146][197][198] The sample is fixed in a sample holder suitable for cuvettes or thin films. To minimise photodegradation of light sensitive samples, the sample holder is movable.

In order to ensure integrity of the samples, their steady state spectra before and after the TA measurements are checked and unaltered TA scans are validated by comparing each single scan to the previous one.

After data acquisition with the Helios 16.1 software, the analysis is performed with the open-source program Glotaran version 1.5.1.[199] First, all TA data are background subtracted and the scattering of the excitation pulse is removed before data analysis. The spectral window is set such that extreme noise found at the edges of the spectra are cut off. The analysis is carried out by applying a GA with positive rate constants and a sequential model. Long-lived states and photoproducts exhibiting much longer lifetimes than the experiment are included in global fits by introducing a component with much longer lifetime compared to the duration of the experiment which adds a constant offset over the whole experimental period of about 8 ns.[134][139] In Glotaran, this can be achieved by fixing the rate constant of one component to a very small rate, e.g. 1000 s^{-1} and accordingly apply a long lifetime of 1 ms in this case.[200] On the

contrary, short-lived components with lifetimes below the resolution of the laser setup are labelled with < 0.2 ps. Their EADS are not shown as they cannot be separated from the pump-probe artefacts.
The errors of the determined lifetimes constitute of an experimental error of 160 fs due to the autocorrelation of the approximately 100 fs broad pulses and the fitting error added by Gaussian error propagation. The shown TA traces are prepared with the Matlab Code speAnalysis version 1.1 written by Ture Hinrichsen of the university of Cambridge used in Matlab R2019a as no dispersion correction can be carried out with the analysis program Glotaran. Within the program speAnalysis, the background and dispersion correction are carried out. Subsequently, all data are plotted with OriginPro 2020b to create all shown figures.

3.3. Linear optical spectroscopes

Steady state UV/VIS spectroscopic measurements are recorded by two different spectrometers (V-770, Jasco or UV-2600, Shimadzu). Solutions are measured using a standard cuvette with 10 mm optical pathway. Films are spin coated or drop cast on plasma cleaned quartz glass substrates having a size of 25.4 $\times$ 25.4 $\times$ 0.2 mm^3.
For the temperature-controlled kinetic UV/VIS measurements an Agilent 8453 spectrometer (Agilent) is used with a USP-203-A cooling unit (Unisoku). The measurements are conducted under inert gas atmosphere using quartz cuvettes with 10 mm optical pathway. The integration time was kept at 500 ms for all experiments. The solutions are constantly stirred to guarantee homogeneous samples and kinetics. Before starting a kinetic measurement series, steady state conditions are ensured by subsequent measurements until no changes are observed.
For steady state and kinetic IR investigations, FTIR is used. The FTIR spectrometer (Tensor 27, Bruker) is equipped with a silicon carbide heating element to produce a broadband IR light. For steady state measurements on films in transmission mode, the IR is directed into a microscope (Hyperion 1000, Bruker). Afterwards, the beam is focused through an aperture, which defines the spot size, onto the sample. The sample is put on a computer controlled table such that the measurement position can be changed automatically. The FTIR spectrometer, the microscope and the measurement chamber of the microscope are purged with dry air to avoid atmospheric absorptions. The IR light is subsequently analysed by a nitrogen cooled mercury cadmium telluride (MCT) detector.
In order to conduct kinetic measurements in solution, the IR beam is directed into a measuring cell (Aquaspec, Bruker) within the FTIR spectrometer. The calcium fluoride measuring cell has an optical pathway of about 7 µm. The solution can be injected into the flow-through system which includes a filter prior to the transmission cell. Within the

measurement chamber, a light emitting diode (LED) possessing a maximum emission intensity at 594 nm is placed and its light is sent into the measuring cell using a mirror. The whole FTIR spectrometer including the measurement chamber are purged with dry air to avoid atmospheric absorptions. After transmission through the measuring cell, the IR beam is analysed with a nitrogen cooled MCT detector. Before starting a kinetic measurement series, steady state conditions are ensured by subsequent measurements until no changes are observed. Afterwards, a kinetic series is started with an integration time of 6 s.
All data obtained by linear optical spectroscopes are further analysed with the software Origin Pro 2020b.

3.4. Scanning near-field optical microscope

In order to gain information about the near-field, an s-SNOM (neaSNOM, neaspec) is used (figure 3.10). The sample chamber with the AFM unit is located in its centre. The metal-coated tip is typically coated with a platinum iridium alloy and exhibits a radius of about 25 nm which determines the resolution. The AFM is operated in intermittent contact mode with a tapping amplitude held slightly below the resonant frequency

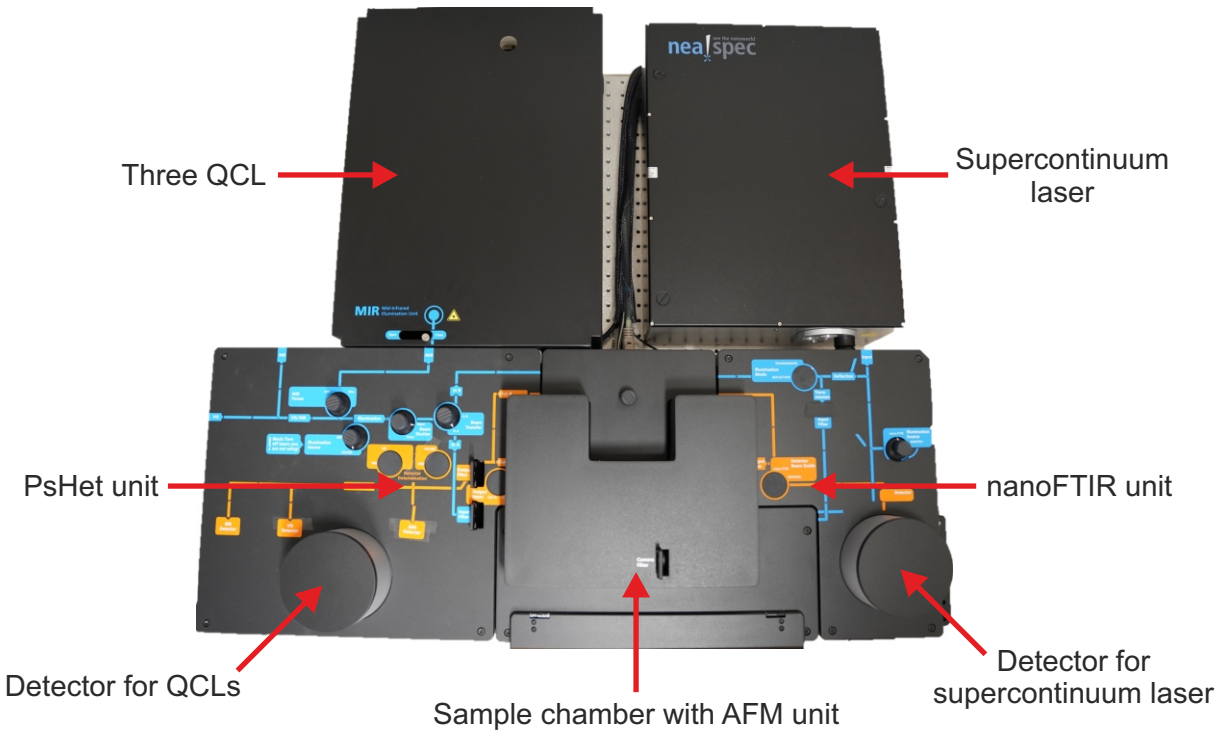

Figure 3.10. s-SNOM setup with three different operation modes. For the nano-FTIR mode, the broadband laser, the optics and the detector can be found on the right-hand side whereas the three monochromatic QCLs, the optics and the detector for the PsHet mode are located at the left-hand side. The QCLs can be operated in pulsed mode as well allowing to use the AFM-IR mode.

which is typically around 10 - 100 nm. The position of the cantilever is monitored by a deflection laser. The nano-FTIR unit can be found on the right-hand side with the supercontinuum laser (FF dichro design midIR_11031, TOPTICA Photonics AG) being at the back. It features a tunable broadband output in the range of 700 - 2250 cm^{-1} from which five continuous emission regions of a range of greater than 500 cm^{-1} can be selected. The FTIR unit of the nano-FTIR mode allows a spectral resolution of up to 3.2 cm^{-1}. The nitrogen cooled MCT detector is mounted at the front. The PsHet unit is located on the opposite side. Three quantum cascade laser (QCL) (MIRcat-2300, DRS Daylight solutions) are at the back of the left-hand side which allow the selection of a specific wavelength with a wavelength accuracy of $\leq$ 1 cm^{-1} within the software. The wavelength can be tuned continuously within a range of about 1065 - 1731 cm^{-1} for CW operation needed for the PsHet mode and around 1077 - 1810 cm^{-1} for pulsed operation needed for the AFM-IR mode, respectively. For pulsed operation, the repetition rate is 100 kHz with a pulse width of 500 ns. The spot diameter is below 2.5 mm. The nitrogen cooled MCT detector can be found at the front.[163] [164]
After data acquisition using the software neaSCAN from neaspec, the 2D data are analysed with the open-source software Gwyddion 2.58. The IR spectra of different laser wavelength regions were merged using the Matlab code NearfieldDataEvaluation written by Christian Huck from the university of Heidelberg. For further data analysis, all spectral data are analysed and plotted using the program Origin Pro 2020b.

4. 6,13-Diazapentacene on Au(111)

Acenes are important small organic semiconducting molecules with great potential for applications in organic electronic devices. Since acenes and their derivatives exhibit promising electronic properties, they are incorporated in various electronic devices such as OFETs, solar cells and OLEDs. The outstanding acene pentacene, consisting of five linearly fused aromatic rings, is the benchmark for thin-film devices. Diverse pentacene derivates are implemented in devices to increase their performance according to the specific device requirements.[24] [201]

For example, aryl substituted pentacene derivatives are used for red OLEDs which show quantum efficiencies close to the theoretical maximum.[202] [203]

For photovoltaic devices, pentacene has also proven itself as powerful material. Because the triplet state T_1 is at about half of the energy of the singlet state S_1, the process of singlet fission occurs. Hence, absorption of one photon, promoting a pentacene molecule into the S_1 state, generates two T_1 states on two pentacene molecules upon depopulation of S_1. Thus, one photon creates two charge carriers. By this means, the maximum power conversion efficiency of about 34 % determined by the Shockley-Queisser limit can be overcome to design solar cells with pentacene exhibiting up to 129 % external quantum efficiency.[24] [204] [205]

Pentacene and its derivatives are widely used for OFETs. High charge carrier mobility as well as mechanical flexibility are important properties which make those materials promising candidates. Hole mobilities greater than 5.5 $cm^2\ V^{-1}\ s^{-1}$ for pentacene[22] and 20 $cm^2\ V^{-1}\ s^{-1}$ for the pentacene derivative rubrene[23] have been achieved. However, for OFET materials, many material properties beside the ones already mentioned influence the device performance such as crystallinity, stability, bulk structure and interface structure.[20] [24] [25] [206] [207]

Up to now, many p-type organic semiconductors have been studied which exhibit hole transport properties. However, n-type organic semiconductors with good electron transport properties are rare. Thus, pentacene derivatives revealing n-type properties are of great interest. One way to gain n-type organic semiconductors is the introduction of electron withdrawing groups in pentacene or its derivatives. However, functionalising those molecules with halogens or cyanide groups give rise to distortion of the planar acene structure which influences the carrier transport properties negatively. Substitution of carbon atoms of the molecular acene backbone with nitrogen atoms in contrast generate n-type semiconductors still owing a planar fashion such that excellent n-type OFET materials can be created.[24] [26]

The N-substituted pentacene derivative studied in this thesis is 6,13-diazapentacene (DAP) (figure 4.1). It features a pyrazine ring in its centre which increases the electron affinity and has been implemented in maser (microwave analogue of the laser)[208]

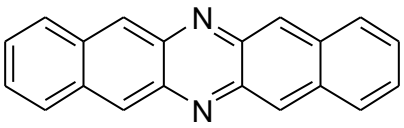

6,13-Diazapentacene
(DAP)

Figure 4.1. Structural formula of the studied pentacene derivative DAP.

and OFETs[209] for instance. With pentacene being a p-type semiconductor, the energy of the lowest unoccupied molecular orbital (LUMO) needs to be lowered to enable electron injection and obtain an n-type derivative. DAP holds an outstanding position as it has ambivalent character and can potentially be used as p- or n-type semiconductor.[26][210][211] On the one hand DAP and pentacene hold similarities such as the planar molecular geometry and the singlet-triplet gap allowing singlet fission. On the other hand, the local electronic structure of DAP distincts strongly from pentacene due to the presence of the nitrogen atoms.[206][212]
Since the energy alignment at the metal/organic interface and the electronic structure of the molecular film of the small organic semiconductor as well as its change at different layer thicknesses are key factors in device performance, those properties of DAP and the model electrode material gold Au(111) will be studied in the following.[20][209] First, the Au(111) metal substrate is characterised first in section 4.1 while the adsorption and desorption properties as well as the layer thicknesses of DAP are addressed in section 4.2. Finally, the electronic structure of DAP on Au(111) is analysed in section 4.3.

4.1. Characterisation of the Au(111) metal substrate

In order to study the metal/organic interface, which plays a crucial role in device performance,[20] gold is chosen as a model electrode material. Thus, experiments in this chapter are carried out with gold functioning as substrate. More precisely, a single crystal of Au(111) was used. The characteristics of the noble metal single crystal Au(111) are high stability, low reactivity and hence little substrate-adsorbate interaction which makes Au(111) a perfect electrode model material.[213]
Au(111) crystallises in a face-centered cubic (fcc) lattice in the bulk. However, at the close-packed (111) surface reconstruction takes place which makes gold unique compared to all other fcc metals. A large percentage of the surface can still be associated with the fcc lattice but it is superimposed by hexagonal-close packed (hcp) regions. This surface reconstruction structure is called herringbone structure.[213][214]
The Au(111) crystal in this study features the literature known characteristics (section 2.2.2). The *d*-bands and an *sp*-band, detected at high photon energies, are observed as well as a Shockley SS close to the Fermi edge (figure 4.2**a**).

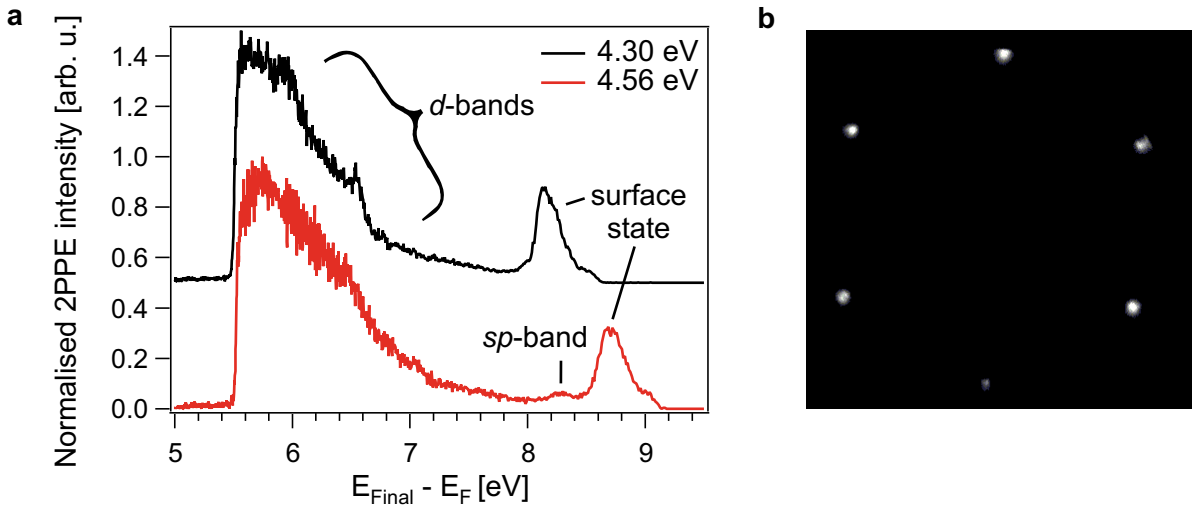

Figure 4.2. Characterisation of the used Au(111) substrate. (a) 1C-2PPE spectra at different photon energies revealing a work function of 5.5 eV as well as signals due to *d*-bands, *sp*-band and the SS. (b) LEED pattern of the substrate surface.

Those states exhibit dispersion which can be measured by AR-2PPE (figure 4.3). While the slope analysis of the SS provides a slope of two which refers to an occupied state, no slope analysis of the *d*-bands and the *sp*-band can be performed since those bulk states exhibit dispersion along the normal component of the electron wave vector $k_\perp$. The intense and narrow SS signal indicates a highly ordered reconstructed Au(111) surface and holds a binding energy of (0.42 ± 0.05) eV below E_F in line with the literature (error calculation see equation A.1 - A.3 appendix A).[215] The work function is (5.50 ± 0.05) eV in accordance with the literature.[102][112] The LEED pattern of the Au(111) crystal indicates a herringbone reconstruction of the Au(111) surface (figure 4.2**b**).[216] In summary, the Au(111) crystal used in this thesis shows the expected

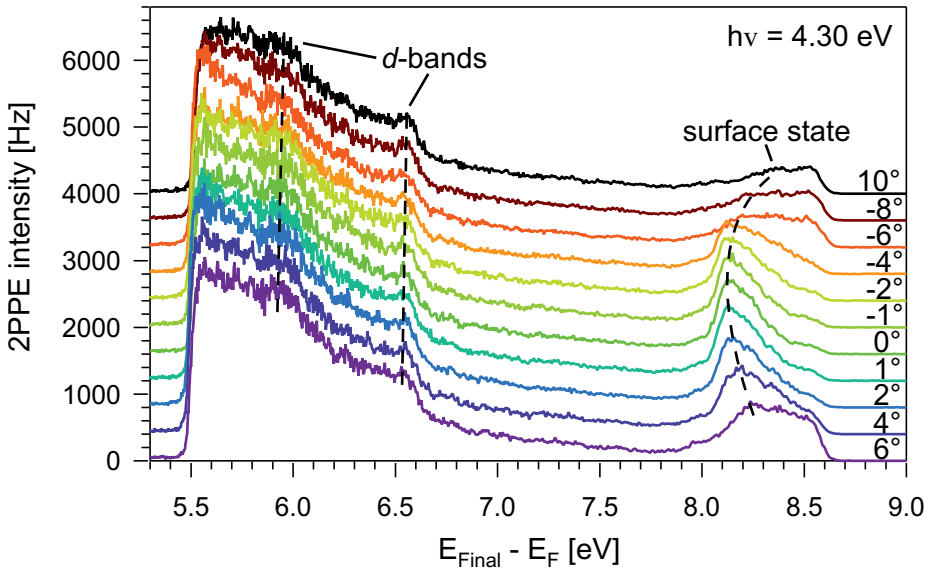

Figure 4.3. AR-2PPE of Au(111) revealing the dispersion of the *d*-bands and the SS.

features, which prove a clean and highly ordered metal surface, and is well prepared by the applied procedure (section 3.1.1).

4.2. Adsorption and desorption properties of DAP/Au(111)

Next, the molecular packing of DAP (synthesised by Hilmar Reiss, Bunz research group, organic chemistry department of the Ruprecht-Karls-Universität Heidelberg) as well as its adsorption and desorption properties on Au(111) are investigated. After preparing the Au(111) substrate (section 3.1.1), the substrate was held at 300 K to ensure good adhesion for DAP deposition. The evaporation process was realised by heating DAP to 463 K within the effusion cell. Subsequently, the evaporator was opened to deposit DAP on the Au(111) surface for about 125 s to obtain a three monolayer thick adsorbate layer for instance. For lower coverages, the evaporation time was shortened whereas longer dosing times were applied for higher coverages.
To ensure integrity of the DAP molecules upon evaporation, electron impact ionisation mass spectrometry (mass spectrometry facility, organic chemistry department of the Ruprecht-Karls-Universität Heidelberg) was carried out on the DAP samples before and after heating in the effusion cell. Both mass spectra are identical and consist of signals which can all be related to fragments of the DAP molecule (figure 4.4). This indicates no decomposition upon evaporation. The four mass-to-charge ratios 76.05, 102.07, 126.06 and 140.08 m/z (marked in figure 4.4) represent the characteristic fragments $C_6H_4^+$, $C_8H_6^+$, $C_{10}H_6^+$ and half of the molecule $C_{10}H_6N^+$, respectively.

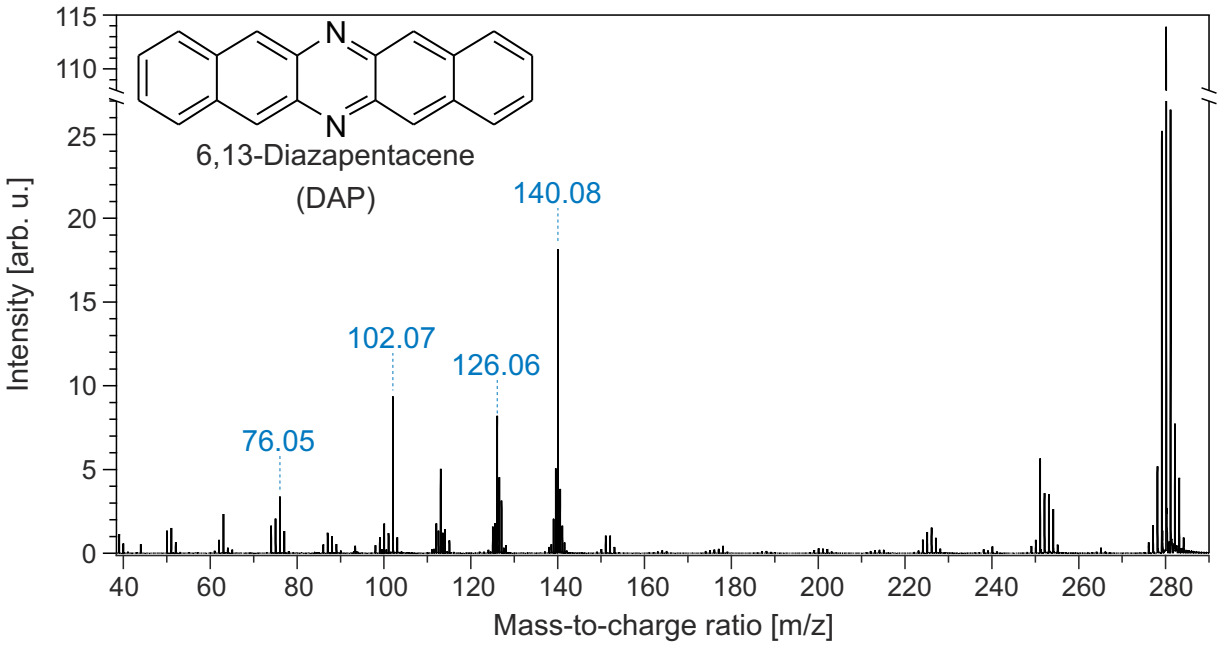

Figure 4.4. Mass spectrum of DAP with its molecular structure shown in the inset and the marked mass-to-charge ratios 76.05, 102.07, 126.06 and 140.08 m/z corresponding to the fragments $C_6H_4^+$, $C_8H_6^+$, $C_{10}H_6^+$ and $C_{10}H_6N^+$, respectively.

Those characteristic fragments are also monitored during TPD experiments. TPD spectra of DAP reveal three features denominated with α_1, α_2 and α_3 located at 365 - 395 K depending on the coverage, 435 K and 450 - 670 K, respectively (figure 4.5). The former signal exhibits zero-order desorption characteristics, indicating a molecular desorption independent of the coverage, and shows no saturation even for higher coverages. Therefore, α_1 is attributed to the multilayer desorption. The second feature α_2 can be assigned to a more densely packed compressed phase, as reported for other aromatic organic compounds, such as pentacene, on coinage metal surfaces.[123][132][217] The third feature α_3 describes submonolayer desorption with its tail structure being characteristic for acenes.[217] The first ML is determined as sum of the saturated peaks α_2 and α_3. In order to determine the coverage according to equation 2.21, the sum of the saturated signals α_2 and α_3 is integrated forming $\int I_{mono}$ and α_1 is integrated forming $\int I_{multi}$. In case of a saturated monolayer, the integral of the compressed phase and the tail corresponds to 0.5 ML, respectively. Furthermore, as the shape and the coverage determination of each fragment is identical (figure 4.5**a**), an intact desorption can be assigned. In addition, the intact multilayer desorption indicates a successful evaporation and adsorption of intact DAP molecules in the first place.

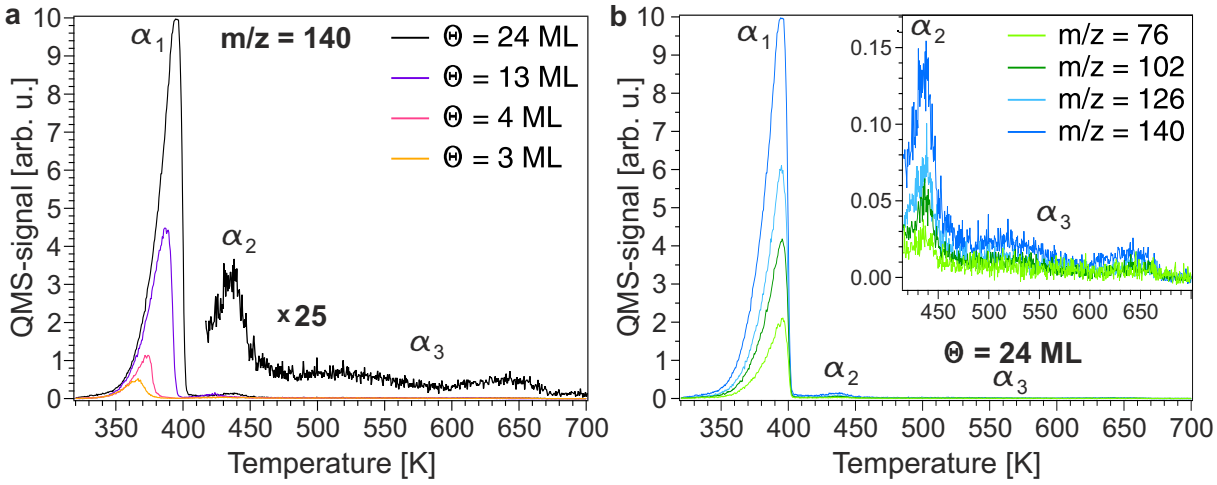

Figure 4.5. TPD spectra of DAP adsorbed on Au(111) by applying a heating rate of 1 K s^{-1}. (a) Different initial coverages monitoring the ionic fragment with m/z = 140 and (b) different ionic fragments at an initial coverage of 24 ML are shown revealing a zero-order desorption and a sub-monolayer tail typical for acenes.

Comparing the TPD results of DAP with the literature reported pentacene TPDs, both resemble each other in their shapes. The α_1, α_2 and α_3 features of pentacene are located at about 390 K, 420 K and 460 - 750 K, respectively. Thus, the compressed phase of DAP is more strongly bound to the Au(111) surface compared to pentacene, whereas the submonolayer tail of DAP is shorter and weaker bound. Both adsorbed molecules show a compressed phase and a tail-shaped signal forming the monolayer. Interest-

ingly, in both cases the integral of the compressed phase is about 0.5 ML for a saturated monolayer regime. STM studies on monolayer and submonolayer pentacene layers on Au(111) reveal long-range interactions between the pentacene molecules such that the first half of the monolayer consists of pentacene molecules keeping long distances. Adsorption of additional pentacene molecules within the gaps between the already attached pentacene molecules reduces the pentacene-pentacene distance generating the stronger bound compressed phase.[122][218] The TPD data of DAP suggests a similar mechanism for the adsorption of DAP on Au(111).

4.3. Electronic structure of DAP on Au(111)

To study the electronic structure of DAP and its energy level alignment in close contact to a metal electrode, 2PPE experiments are carried out. At first, 1C-2PPE spectra of DAP on Au(111) are compared (figure 4.6). Different DAP coverages are thereby analysed while applying the same photon energy in the experiments. At submonolayer coverage the spectrum is dominated by metal states such as *d*-bands and the SS. However, due to adsorption of DAP the SS is shifted from (-0.42 ± 0.05) eV to (-0.18 ± 0.05) eV below the Fermi level (SS'). Molecular features are obtained at coverages above 1 ML. At 1.3 ML, the peaks arising from metal states are overlaid by molecular states apart from the shifted SS located at (-0.22 ± 0.05) eV below the Fermi level. Shifted SS towards and even above the Fermi energy due to adsorption of molecules have been reported previously.[219][220] Four distinct signals are observed which can be related to their original states in the following analysis. The shifted SS

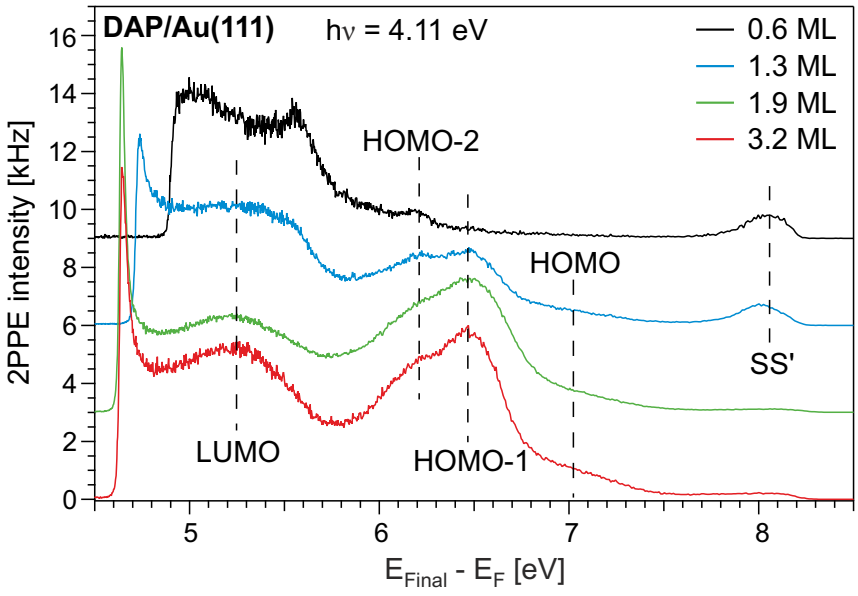

Figure 4.6. 1C-2PPE (hν = 4.11 eV) spectra of DAP at different coverages. Molecular states arise at a coverage of 1 ML which broaden at higher coverages while each signal is still distinguishable even at high coverage. Figure adapted.[109]

disappears and the molecular features get more pronounced by increasing the coverage further to 1.9 ML. At a coverage of 3.2 ML, the molecular states are more intense. Remarkably, the molecular features exhibit no significant broadening at higher coverages. For irregular structures within the multilayer, the molecule-molecule interaction changes which influences the energy levels leading to slightly different energies. This results in peak broadening of 2PPE spectra. As no broadening for high coverages is observed, the adsorption of DAP on Au(111) leads to highly regular structured multilayers. This is supported by high-resolution electron energy loss spectroscopy (HREELS) data which show that DAP molecules adsorb on Au(111) in a planar fashion with the molecular backbone oriented parallel to the substrate surface. This is valid for both the mono- and multilayer.[109]

In addition, a shift of the work function can be observed with increasing coverage. The work function of gold is reduced from (5.50 ± 0.05) eV to (4.90 ± 0.05) eV for a DAP coverage of 0.6 ML. A higher coverage of 1.3 ML further decreases the work function to (4.71 ± 0.04) eV. For coverages of 1.9 ML and higher, the work function stays constant at (4.62 ± 0.05) eV.

To analyse the origin of the peaks observed in the coverage dependent 2PPE data, photon energy dependent measurements were carried out (figure 4.7**a**). As a coverage, 3 ML was chosen as this coverage gives distinct molecular features. The photon energy was varied between 4.00 eV and 4.50 eV in about 0.10 eV steps. For a photon energy of 4.00 eV, four signals are obtained with $E_{Final} - E_F$ energies of (5.18 ± 0.12), (5.98 ± 0.12), (6.27 ± 0.11) and (6.75 ± 0.20) eV. Those signals also compose the 2PPE spectra applying photon energies of 4.11 and 4.21 eV with those peaks being shifted towards higher energies for higher photon energies. For the 2PPE data of the higher photon energies 4.31 and 4.40 eV, an additional feature is observed located at (4.96 ± 0.04) eV for 4.31 eV and (5.07 ± 0.05) eV for 4.40 eV, respectively. The peaks get less pronounced at higher photon energies which may be due to lower cross sections. Furthermore, at 4.40 eV beside the molecular states a *d*-band feature of the metal substrate is present. To get more insight into the molecular state contributing to the 2PPE data at higher photon energies, an additional measurement at 4.50 eV was carried out (figure A.1 appendix A). The signal of interest could be fitted to the data, however, not all states observed at other photon energies could be distinguished. With the fitted signals of the photon energy dependent 1C-2PPE measurements, a slope evaluation is carried out (figure 4.7**b**) to assign the observed peaks to initial, intermediate and final electronic states (figure 2.2). Three signals feature a slope of about two corresponding to initially occupied molecular states. Utilising a molecular picture, the states can be assigned to the highest occupied molecular orbital (HOMO), HOMO-1 and HOMO-2 at (-1.27 ± 0.11), (-1.72 ± 0.07) and (-2.03 ± 0.10) eV with respect to the Fermi energy of Au(111), respectively. The other

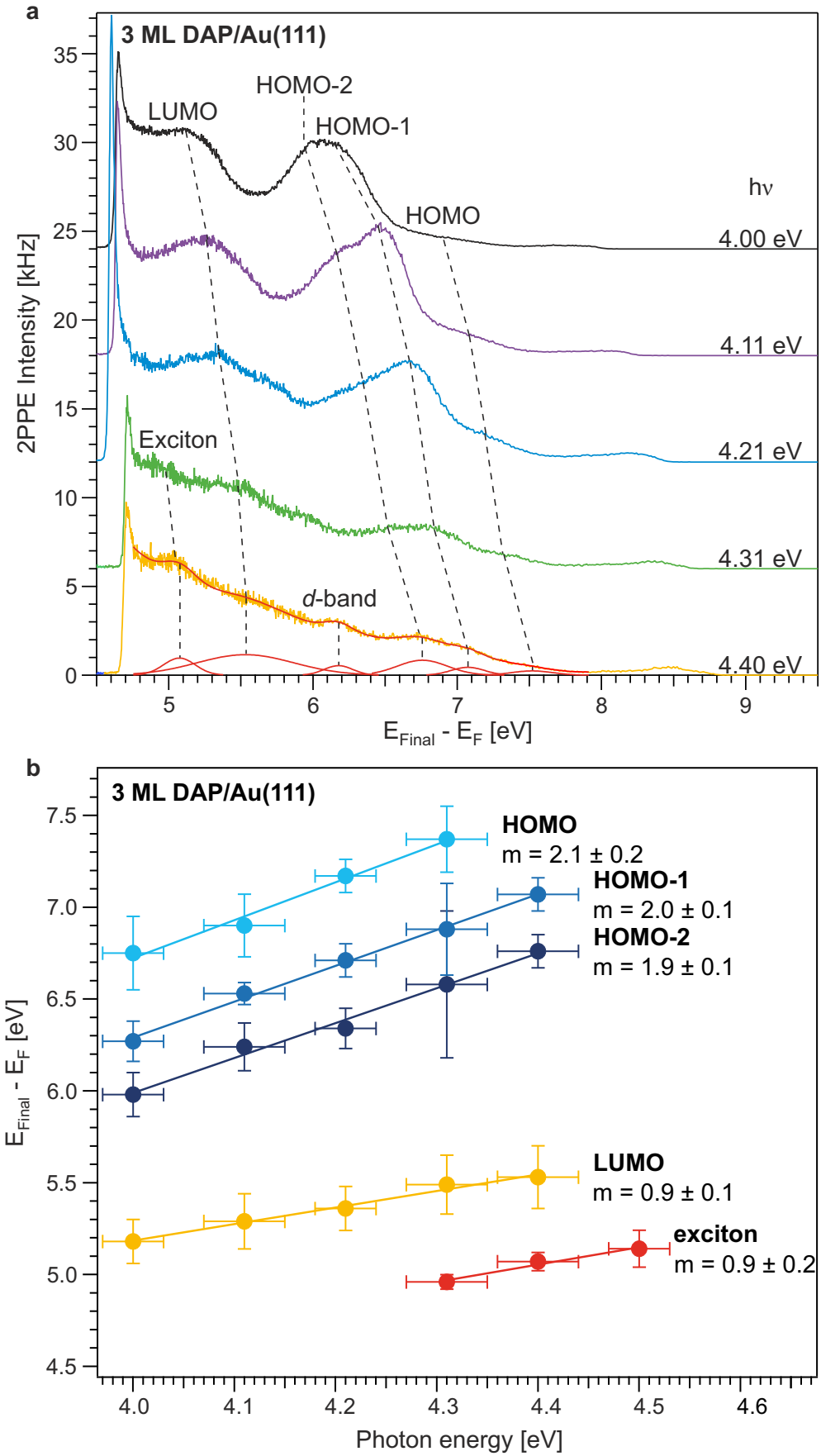

Figure 4.7. (a) 1C-2PPE spectra of DAP with identified signals fitted as Gaussian peaks shown in red. (b) Plotting their energies against the photon energy allows the assignment to molecular states. Figure adapted.[109]

two signals exhibit a slope of about one and thus correspond to intermediate unoccupied molecular states. Within the molecular picture, this states can be assigned to the LUMO located at (1.16 ± 0.07) eV and the exciton at (0.65 ± 0.05) eV with respect to the Fermi level. After identifying the origin of the detected molecular states, an energy level diagram of the electronic states of a three ML thick layer of DAP on Au(111) can be drawn with the energy levels presented with respect to the Fermi energy (figure 4.8). Within the energy level diagram, E_{Bind} represents the binding energies of the occupied states whereas E_i denotes the energy levels of the intermediate states. The fundamental gap, referring to the transport gap, can be calculated using the Koopman's theorem according to equation 2.9 yielding a fundamental gap of (2.43 ± 0.13) eV. In addition, the optical gap and the exciton binding energy can be determined with re-

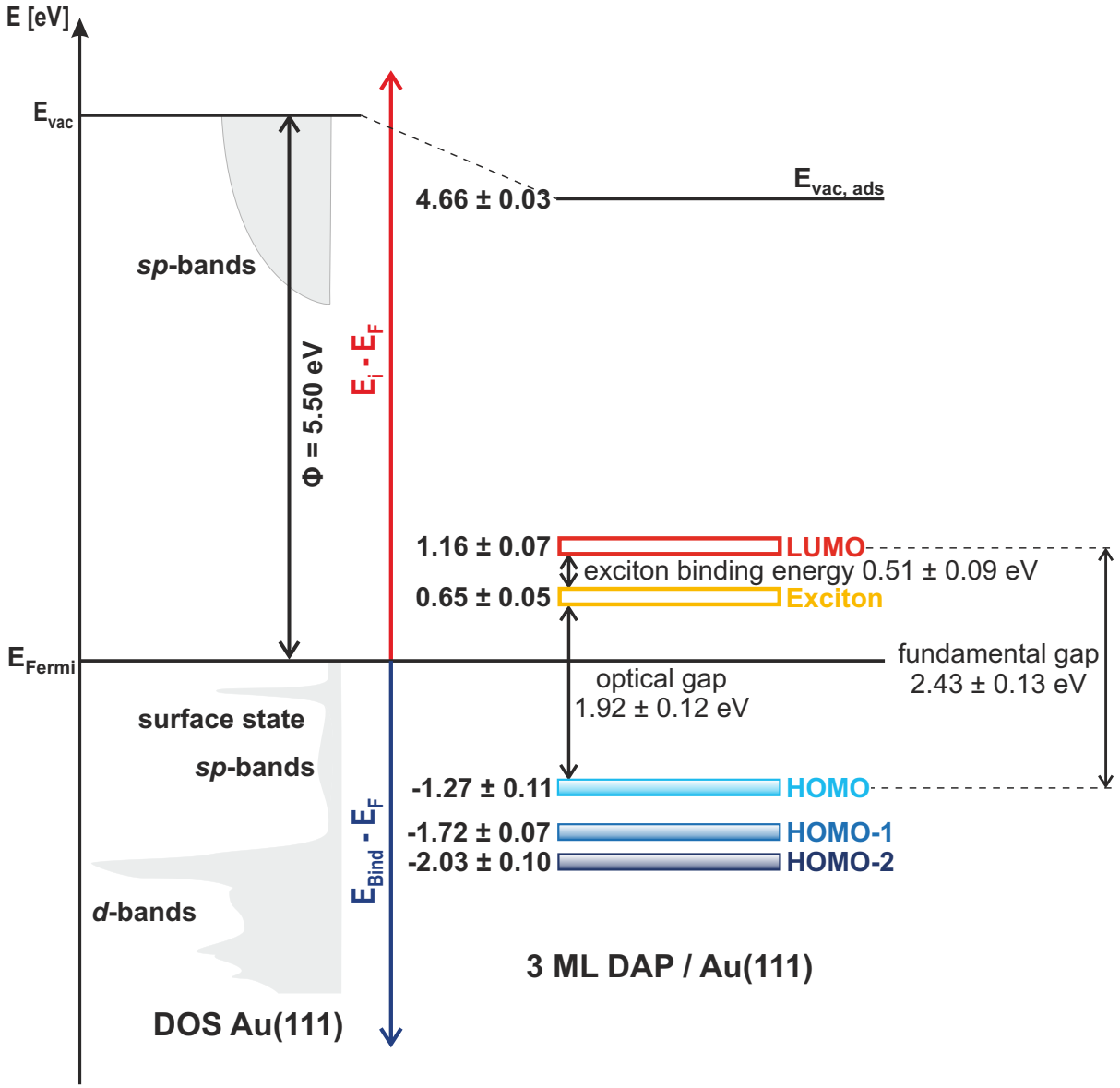

Figure 4.8. Energy level diagram of the molecular states of a 3 ML thick layer DAP on Au(111) detected by 2PPE.

spect to equation 2.10 resulting in an optical gap of (1.92 ± 0.12) eV and an exciton binding energy of (0.51 ± 0.09) eV.
2C-2PPE and UPS measurements revealed a poor cross section of DAP on Au(111) for several coverages. For instance, 2C-2PPE spectra only show two signals at low DAP coverages which vanished for higher coverages (figure A.2 appendix A). Those states exhibit dispersion with one state being an initial and the other state being an intermediate state according to the slope evaluation (figure A.3 appendix A). They can be attributed to the shifted SS and IPS, respectively. Hence, no molecular signals could be detected in 2C-2PPE such that no TR-2PPE experiments could be carried out due to poor cross sections.
Comparing the optical gap of (1.92 ± 0.12) eV determined by 1C-2PPE experiments with the optical gap of 2 eV identified in HREELS and UV/VIS measurements in a chloroform solution,[109] both gaps agree within their errors. Thus, the adsorbate-substrate and the adsorbate-adsorbate interactions are quite weak such that the Au(111) metal surface exerts weak influence on the electronic states of adsorbed DAP molecules and relatively poor intermolecular forces between the DAP molecules are present compared to the DAP molecules in chloroform solution.
By comparing DAP with its parent polycyclic aromatic hydrocarbon compound, the optical gap of pentacene amounts to 2.1 eV for both, thin films adsorbed on Au(111) and in solution.[109] Hence, the optical gap is reduced by 0.10 eV by introducing two nitrogen atoms at the centre. This can be explained by the increased electronegativity resulting in stabilised valence molecular orbitals. In addition, the exciton binding energy of DAP of (0.51 ± 0.09) eV is in agreement to the calculated exciton binding energy of pentacene of 0.55 eV such that both compounds form correlated electron-hole pairs referred to as Frenkel excitons which are common for organic semiconductors (section 2.1.2).[109][221]

5. Orthogonal photoswitches

Nowadays, not only simple electronic devices are needed but smart materials reacting to external stimuli with light being the most beneficial stimulus. However, as systems get more complex, multiple photoresponsive materials within one device are needed which are independently addressable. The research concerning orthogonally, meaning independently, photoadressable chemicals started at the beginning of the millennial with a publication from Bochet regarding irreversible wavelength-selective cleavage of two photolabile protecting groups.[222] Since then, numerous applications with orthogonal photoadressability have been invented in various fields such as lithography,[30] nanoparticle self-assembly,[223] supramolecular patterned surfaces,[224] DNA nanotechnology,[56] and regulation of enzyme activity.[225] However, there are still issues to be solved especially in terms of selectivity.[29][224][226]

A well-known class of photochromic materials are azobenzenes[227][228] which have already been successfully implemented in several orthogonal multiresponsive systems.[56][223][224][226] Azobenzene consists of a nitrogen-nitrogen double bond with each nitrogen being attached to one phenyl ring, respectively. Azobenzene derivatives feature an azobenzene core with different substituents on the phenyl rings (e.g. figure 5.1 with the Boltzmann constant k_B).

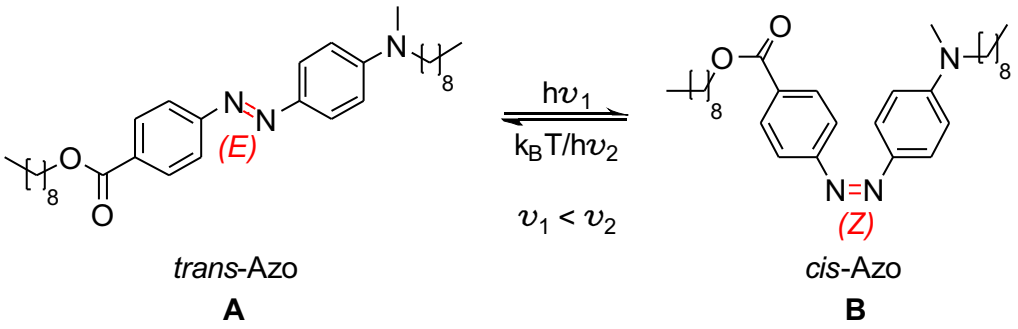

Figure 5.1. Reversible photoswitching of the studied azobenzene derivative (Azo).

Upon irradiation with light, azobenzenes can change their double bond configuration from the thermodynamically more stable trans-isomer to the metastable cis-isomer and vice versa. This microscopic variation leads to macroscopic changes especially in volume and shape as the material bends.[228] The backswitching is either induced photochemically or thermally such that azobenzenes belong to P- and T-type photochromic compounds. The switching process occurs on an ultrafast femto- to picosecond time scale with the exact mechanism being still under debate as the mechanism also depends on the exact structure of the derivative and the environment. Proposed mechanisms are rotation, inversion, concerted inversion and inversion-assisted rotation.[228]-[230]

Azobenzene exhibits a broad absorption in the UV range due to the $\pi \rightarrow \pi^*$ excitation from $S_0 \rightarrow S_2$ as well as a weak absorption in the VIS range representing the $n \rightarrow \pi^*$ transition from $S_0 \rightarrow S_1$. Upon excitation with UV light, the trans-to-cis (*E*-to-*Z*) isomerisation is induced and the former absorption band decreases while the latter increases in intensity. For photoinduced backswitching, the VIS band is addressed. This way, azobenzene covers a big range of the visible spectrum. By introducing substituents, the absorption bands shift. For push-pull azobenzene derivatives, which feature an electron withdrawing group on one phenyl ring and an electron donating group on the other phenyl ring, the $\pi \rightarrow \pi^*$ band is strongly red-shifted while the $n \rightarrow \pi^*$ transition stays nearly unaffected generating nearly degenerate $S_0 \rightarrow S_2$ and $S_0 \rightarrow S_1$ transitions both in the VIS region.[228] [231]

After excitation to the S_2 state, ultrafast $S_2 \rightarrow S_1$ conical intersection takes place in azobenzene and its derivatives within about 50 fs for azobenzene (figure 5.2).[139] Subsequently, the movement of the wavepacket out of the Franck-Condon region is observed happening in around 450 fs for azobenzene. Next, conical intersection takes place from $S_1 \rightarrow S_0$ followed by vibrational relaxation to the ground state with lifetimes in azobenzene of about 2.5 and 9 ps, respectively.[139] In contrast, for azobenzene derivatives, mostly only three time constants are observed in the order of below 0.2 ps, 0.4 - 1.5 ps and 5 - 20 ps. Most explanations of the observed lifetimes attribute the short time constant to either $S_2 \rightarrow S_1$ internal conversion or the movement of the wavepacket out of the Franck-Condon region, the lifetime of around 0.4 - 1.5 ps to the $S_1 \rightarrow S_0$ conical intersection and the longest time constant to vibrational cooling within S_0. This

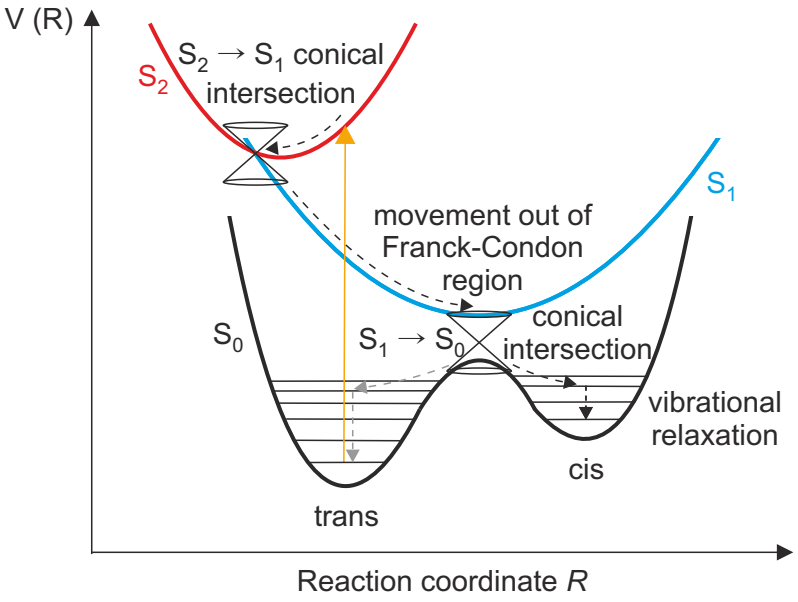

Figure 5.2. General excitation scheme of trans-to-cis isomerisation of azobenzene derivatives upon $S_0 \rightarrow S_2$ excitation. After excitation, the population reaches the S_1 and next the S_0 state through conical intersections, respectively. Not only the desired cis-isomers are thereby created but also trans-isomers.

excited state dynamics hold true for both, trans-to-cis and cis-to-trans isomerisation. By $S_0 \rightarrow S_1$ excitation essentially the same decay paths apply beside the $S_2 \rightarrow S_1$ step.[232]-[228]

For the study of two orthogonal photoswitches presented in this thesis, the push-pull and negatively photochromic azobenzene derivative nonyl-(*E*)-4-((4-(methyl(nonyl)amino)phenyl)diazenyl)-benzoate (Azo) (figure 5.1) was chosen showing steady state absorption in a spectral window of about 340 - 550 nm (section 5.2). Thus, for an orthogonal multiresponsive mixture, the second photoswitch has to absorb in the red region of the VIS spectrum.

A suitable class of photoswitches are thus donor-acceptor Stenhouse adducts which have initially been isolated and investigated by Stenhouse in 1850.[238][239] However, those adducts have been researched for their negative photochromic properties and high fatigue resistance just in the last decade.[240] All donor-acceptor Stenhouse adducts feature a triene with a carbonyl group attached at the first carbon atom, a hydroxyl group fixed at the third carbon atom and a nitrogen atom at the end with the carbonyl group mostly being part of a ring system (figure 5.3). The amine group acts as an electron donor while the carbonyl group operates as electron acceptor.

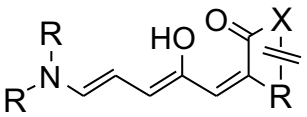

Figure 5.3. General scaffold of donor-acceptor Stenhouse adducts with R being any rest and X being an electron withdrawing group.

The switching process of this class of photochromic systems occurs upon excitation with light while the backswitching is initialised thermally, thus exhibiting T-type photochromism (e.g. figure 5.4). Upon absorption of a photon, *Z*-to-*E* isomerisation of the middle C-C double bond occurs. Secondly, a C3-C4 bond rotation takes place to create the required spatial proximity for the following thermal conrotatory 4π-electrocyclisation. With this ring closing reaction, the initially coloured compound turns colourless. Lastly, proton transfer occurs to gain the zwitterionic product.[241]-[243]

The numerous derivatives of this class can be divided in three generations. The first generation feature either a Meldrum's or barbituric acid as acceptor and an alkyl amine as donor resulting in thermal equilibria in favour of the linear isomer but with limited solvent compatibility. The second generation comprises aniline derivatives instead of alkyl amines which extends the solvent compatibility and increases the tunability of the absorption spectra into the red region but yields poor thermodynamic equilibrium between open and closed form. Finally, the third generation introduces strong electron withdrawing groups as electron acceptors combining the advantages of the first and second generation.[241][242]

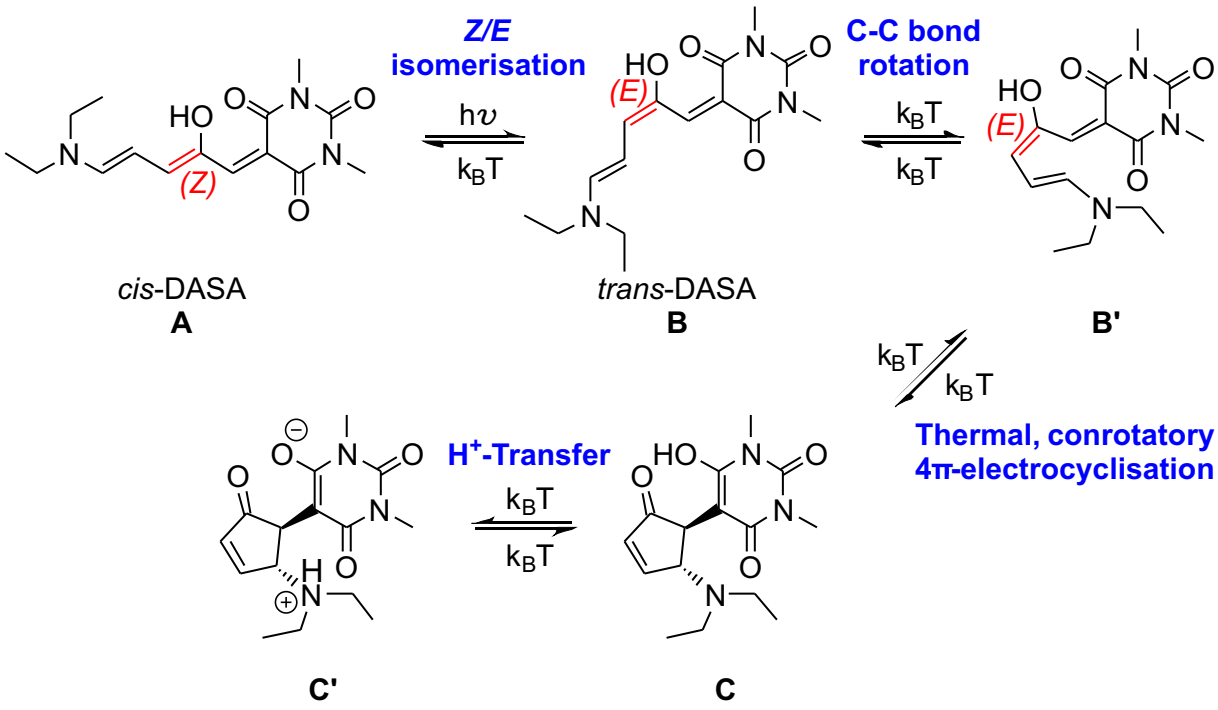

Figure 5.4. Reversible switching mechanism of the studied donor-acceptor Stenhouse adduct DASA including all relevant isomeric structures.

Although this class of photochromic compounds has a short history, donor-acceptor Stenhouse adducts have been successfully implemented in various applications such as photothermal actuators,[244] deadhesion initiator,[245] organocatalyst recycling and micellar disassembly for cargo delivery.[246] Especially their dramatic change in solubility upon switching is utilised.[246] In addition, they have been implemented in orthogonal multiresponsive systems as phase-transfer tag[226] and they have been proven as suitable candidates for information storage and photolithography.[29] One main reason for the boost of this rather new photochromic class is its absorption in the long wavelength region of the VIS spectrum as most well-known other classes of photoswitches absorb in the UV range and in the blue region of the VIS spectrum.[226][240][247]
In this work, a derivative of the first generation is used as a thermal equilibrium in favour of the open form is appreciated and no further redshift of the absorption spectrum is needed to independently address both used photoswitches. In fact, an additional wavelength inducing simultaneous switching beside orthogonal addressing both photoswitches opens more possibilities, such that a sufficient spectral overlap is desired. Thus, the donor-acceptor Stenhouse adduct 5-((2*Z*,4*E*)-5-(diethylamino)-2-hydroxypenta-2,4-dien-1-ylidene)-1,3-dimethylpyrimidine-2,4,6(1*H*,3*H*,5*H*)-trione (DASA) was chosen (figure 5.4) absorbing in a spectral range of about 450 - 620 nm (section 5.2).
In addition to their advantageous spectral properties, both photoswitches can be 3D printed within a liquid crystal matrix.[28] By this means, smart 4D devices can be fabricated with the fourth dimension being the response in time upon light exposure acting

as external stimulus. Also known as additive manufacturing, such 4D printed devices pave the way for new smart materials in fields such as (micro)robotic and biomedical applications.[28][248]
Following, the sample preparations of Azo, DASA and Azo+DASA in different environments are given in section 5.1 and the respective steady state UV/VIS spectra are discussed in section 5.2. Afterwards, the ultrafast excited state dynamics upon photoswitching both molecular switches as well as their 1:1 molar mixture are studied in different environments in section 5.3 to account for influences and interactions of the environment and the photoresponsive molecules on each other. The dynamics on longer time scales are researched in the following sections with special attention on influences and interactions of the photoswitches on each other as well as environmental impacts. The kinetics are thereby investigated by means of temperature dependent kinetic UV/VIS spectroscopy in section 5.4 whereby effective cross sections, lifetimes and activation energies are determined while the kinetics of the closed DASA isomers are studied in section 5.5 via IR kinetic spectroscopy. Lastly, the results of all measurements are summarised in section 5.6.

5.1. Sample preparation

Azo and DASA (synthesised by Li-Yun Hsu,[28] Blasco research group, organic chemistry department of the Ruprecht-Karls-Universität Heidelberg) as well as their molar 1:1 mixture Azo+DASA were investigated in solution using toluene (Tol) and acetonitrile (MeCN) as non-polar and polar solvent, respectively, as well as in thin films both neat and as polymethyl methacrylate (PMMA) blend. All preparation steps were done under yellow light conditions or in the dark to prevent photobleaching.
For the measurements in solution, Azo was dissolved in Tol and MeCN at concentrations suitable for the particular experiment. For the TA measurements using cuvettes with an optical pathway of 0.5 mm and the UV/VIS experiments conducted with cuvettes with an optical pathway of 10 mm, an optical density of around 1 is targeted. Thus, Azo (1.3 mg, 2 µmol) was dissolved in Tol or MeCN (4.000 ml) for the TA experiments. To ensure a complete dissolution of the photoswitch, the mixture was vortexed (vortex mixer 7-2020, Gemmy Industrial Corp.) for about 1 minute. In contrast, for the UV/VIS measurements, a stock solution of Azo (1.3 mg, 2.0 µmol) in Tol or MeCN (650 µl) was prepared and sonicated (Sonorex, RK 255 H, Bandelin electronic) for 11 minutes to guarantee solvation. Next, part of the stock solution (30 µl) was further diluted with solvent (3.000 ml).
For both thin films of Azo, neat and PMMA blend, an optical density of around 1 is desired. For the neat films a solution was prepared by dissolving Azo (3.7 mg, 5.7 µmol) in dichloromethane (DCM) (2.000 ml) with the assistance of 1 minute vortexing. Then,

the neat films were prepared by drop casting part of the latter solution (35 µl) on pre-heated 1 × 1 × 0.5 mm^3 sapphire substrates at 40 °C which had been plasma cleaned by a plasma hand tool (piezobrush PZ2, relyon-plasma) for about 1 minute beforehand. Afterwards, the films were dried in vacuo (10^{-3} mbar) overnight. The Azo-PMMA blends were prepared under cleanroom conditions. The 25.4 × 25.4 × 0.2 mm^3 quartz substrates were plasma cleaned (MARCH CS 1701 Reactive Ion Etching system, Nordson Electronics Solutions) for minimum 5 minutes before usage. The solutions for spin coating were prepared by dissolving Azo (20.0 mg, 30,9 µmol) with PMMA (1600.0 mg, 106.7 µmol) in DCM (4.000 ml) and subsequent sonication of the mixture for 11 minutes. Afterwards, part of the solution (335 µl) was spin coated (500 rpm, 45 s). The films were stored in vacuo (10^{-3} mbar) for 12 days before usage.
The solutions and films containing DASA were prepared accordingly with the same optical densities required. For the TA measurements in Tol and MeCN, DASA (1.0 mg, 3.3 µmol) was dissolved in the respective solvent (1.000 ml) as stock solution which was vortexed for about 1 minute to ensure solvation. Subsequently, part of the stock solution (315 µl) was further diluted by adding solvent (3.685 ml). For UV/VIS measurements, also the above mentioned stock solution was used but sonicated for 11 minutes to guarantee complete solvation. In the next step, part of the stock solution (20 µl) was further diluted with solvent (3.000 ml). For IR measurements DASA (1 mg, 3.3 µl) was added to Tol or MeCN (200 µl) with the help of 11 minutes of sonication.
For the neat DASA films, DASA (1.0 mg, 3.3 µmol) was dissolved in DCM (1615 µl) and vortexed for around 1 minute. Next, part of this solution (100 µl) was further diluted with DCM (600 µl). Part of the latter solution (35 µl) was drop cast on pre-heated 1 × 1 × 0.5 mm^3 sapphire substrates at 40 °C. The substrates had been plasma cleaned by a plasma hand tool for about 1 minute previously. In contrast, the PMMA blends were fabricated on minimum 5 minutes plasma cleaned 25.4 × 25.4 × 0.2 mm^3 quartz substrates under clean room conditions. DASA (4.0 mg, 13.0 µmol) as well as PMMA (1600.0 mg, 106.7 µmol) were subsequently dissolved in DCM (4.000 ml). After 11 minutes sonication, part of the solution (340 µl) was spin coated (1500 rpm, 45 s). The films were dried in vacuo (10^{-3} mbar) for 12 days before usage.
The equimolar mixtures of Azo and DASA were prepared correspondingly. For the TA measurements in Tol and MeCN, a DASA stock solution was prepared by dissolving DASA (1.0 mg, 3.3 µmol) in Tol or MeCN (1.000 ml). After about 1 minute vortexing, part of the solution (616 µl) was added to a mixture of Azo (1.3 mg, 2.0 µmol) in the respective solvent (3385 µl) and the mixture was vortexed for around 1 minute. Following, the 1:1 mixture was diluted by removing part of the solution (2.040 µl) and adding solvent (2.040 µl). For UV/VIS measurements, an Azo and DASA stock solution was prepared by dissolving Azo (1.3 mg, 2.0 µmol) in Tol or MeCN (650 µl) and DASA (1.0 mg, 3.3 µmol) in the same solvent (1.000 ml), respectively. After 11 minutes of

sonication of each solution, part of the DASA stock solution (20 µl) and part of the Azo stock solution (21 µl) was mixed and diluted by adding solvent (2980 µl).
The 1:1 Azo+DASA PMMA blends were fabricated on 25.4 × 25.4 × 0.2 mm^3 quartz substrates which had been plasma cleaned for minimum of 5 minutes. Azo (8.4 mg, 13.0 µmol), DASA (4.0 mg, 13.0 µmol) and PMMA (1600.0 mg, 106.7 µmol) were dissolved in DCM (4.000 ml) and sonicated for 11 minutes. Subsequently, the thin films were prepared by spin coating (1500 rpm, 45 s) part of the latter solution (340 µl).
All solvents used were Uvasol grade and all used chemicals were purchased from Merck. The glass substrates with a transparent window of 220 - 250 nm were bought from AdValue Technology while the used cuvettes transparent from 190 - 2700 nm were acquired from Starna Scientific GmbH.

5.2. Steady state absorption

In the next step, the steady state absorptions of the prepared samples are analysed. Azo shows a broad absorption band in the VIS region (figure 5.5). This band may embody both $\pi \rightarrow \pi^*$ and $n \rightarrow \pi^*$ transition as they can spectrally overlap due to the push-pull system. Comparing the spectra in solution, Azo exhibits positive solvatochromism by shifting its absorption maximum from 437 nm in Tol to 447 nm in MeCN (figure 5.5**a**). The bathochromic shift upon increasing solvent polarity is thereby mainly due to non-specific solute-solvent interactions, such as dispersion and dipolar effects, with a contribution of specific solute-solvent interactions, such as hydrogen bondings.[249][250] Upon excitation with e.g. an LED having its maximum wavelength at 434 nm, the broad VIS band decreases in intensity whereas a blue-shifted peak arises due to the formation of

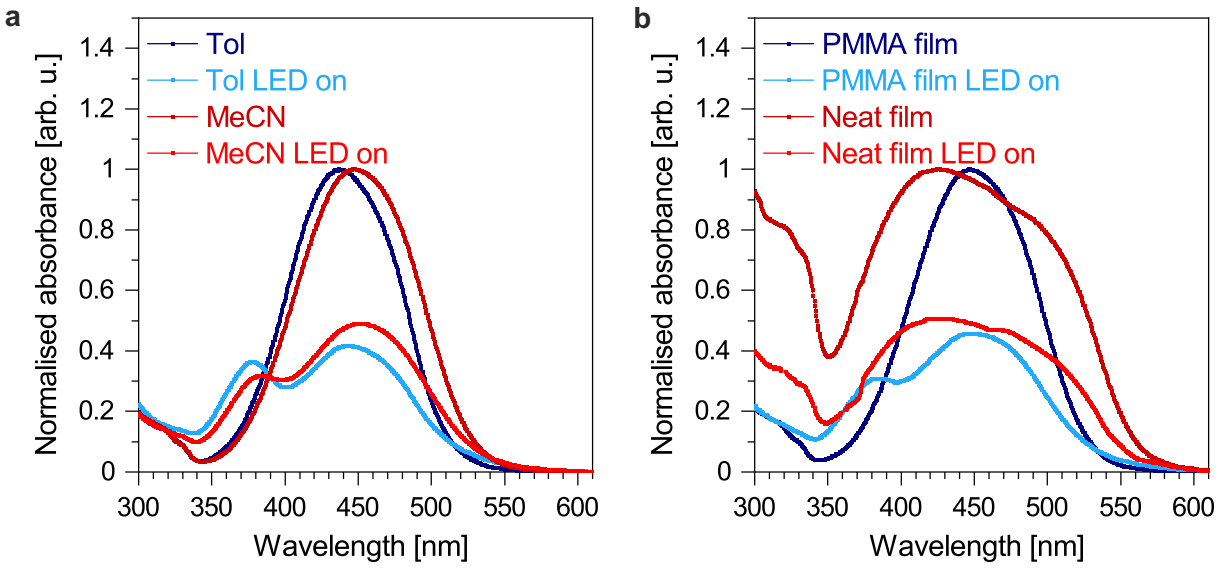

Figure 5.5. Absorption spectra of Azo before and during illumination with an LED having its maximum wavelength at 434 nm inducing the trans-to-cis isomerisation in (a) solution using Tol and MeCN as solvent and (b) in solid state as neat film and PMMA blend.

Z-Azo in both solvents (UV/VIS spectra of all used LEDs in figure B.1). By using different solvents the environmental influence on the switching behaviour and dynamics can be studied. However, as materials in most devices are in solid state,[251]-[254] films were also fabricated.

Therefore, neat films and PMMA blends are investigated (figure 5.5**b**). The neat films show broad absorption thereby covering a range of about 340 - 600 nm which makes it difficult to combine it with another photochromic compound while maintaining orthogonal addressability in the VIS range. Furthermore, the broadened absorption is a consequence of a statistical mixture of H- and J-type aggregates[255] making the analysis complicated on account of the number of different species present. Hence, a PMMA blend was fabricated as the presence of PMMA separates the Azo molecules such that intermolecular interactions are reduced. In fact, by using an Azo-PMMA blend, the absorption spectrum resembles the spectrum of Azo in MeCN maintaining both the maximum absorption wavelength and the FWHM.

In contrast, DASA shows negative solvatochromism by shifting the absorption maximum from 570 mn in Tol to 549 nm in MeCN (figure 5.6**a**). The general trend of a hypsochromic shift by increasing the solvents' polarity for aprotic solvents was also found in literature for donor-acceptor Stenhouse adducts.[256] Upon irradiation with an LED possessing maximal intensity at a wavelength of 594 nm for the measurements in Tol and 560 nm in MeCN, respectively, the absorption peak decreases to a minimum while an additional red-shifted shoulder around 620 nm is observed in the Tol solution. This absorption is attributed to the linear *E*-isomer.[256]

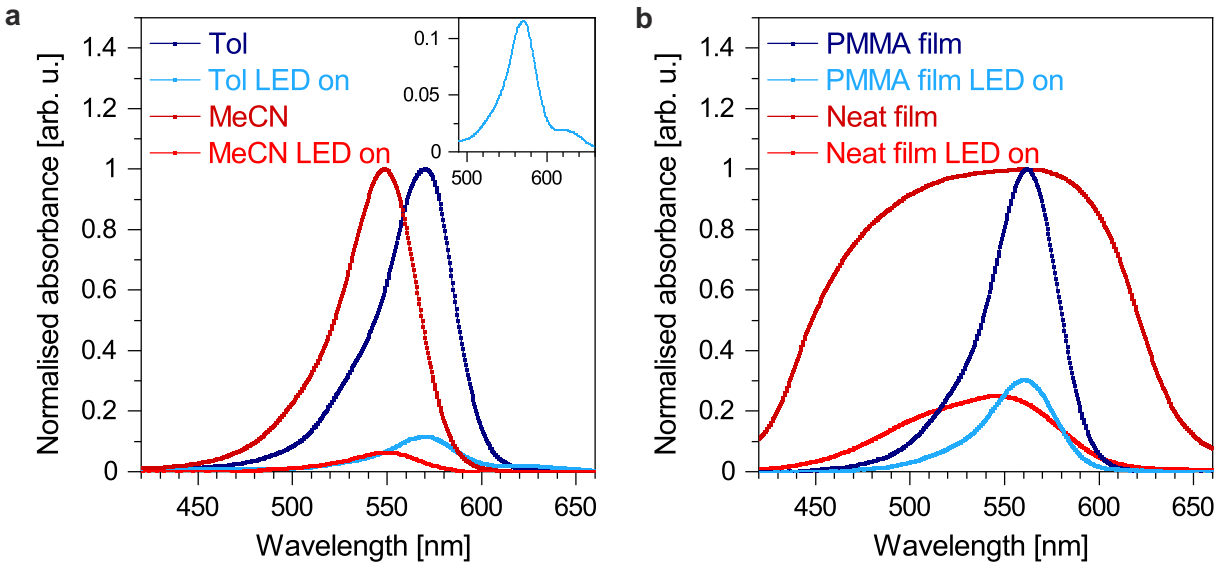

Figure 5.6. Absorption spectra of DASA before and during illumination with an LED leading to trans-to-cis isomerisation in (a) solution using Tol and MeCN as solvents and (b) in solid state as neat film and PMMA blend. (a) The inset shows the enlarged illuminated DASA spectrum in Tol with the shoulder observed at 620 nm. The maximum wavelength of the LED is at 594 nm for measurements in Tol and films while it is at 560 nm for the measurement in MeCN.

Also, thin films of DASA were fabricated both neat and as PMMA blend (figure 5.6**b**). The neat DASA films exhibit extreme broadening with an absorption range of around 380 - 700 nm. The broad absorption is due to the formation of a statistical mixture consisting of H- and J-type aggregates.[255] Thus, the analysis of a neat DASA film is challenging as multiple species are present. Furthermore, as nearly the whole VIS spectrum is covered by DASA absorption, an orthogonal mixture can hardly be achieved when the excitations are meant to be in the VIS range. To circumvent this problem, PMMA blends were prepared which exhibit a smaller absorption band since the intermolecular interaction between the individual DASA molecules is prohibited by the presence of PMMA. The absorption maximum of the DASA-PMMA blend lies between the maximum found in Tol and MeCN solution at 562 nm. The FWHM of the DASA-PMMA blend is slightly smaller compared to the absorption spectra in solution.
Comparing the spectra of Azo and DASA in Tol, MeCN and the PMMA-blend, it is evident that both molecules can be addressed independently as their spectra only overlap slightly around 510 nm. Beside the orthogonal addressability, both molecules can be excited simultaneously due to their small spectral overlap. Thus, a multiresponsive system consisting of a mixture of Azo and DASA can be created providing highly smart responses by light stimulation.
The steady state absorption spectra of molar 1:1 mixtures of Azo+DASA reveal no additional signals but represent the sum of the absorption spectra of the single components (figures 5.7 and B.2 appendix B). Comparing the spectra in their different environments, the absorption spectra narrow in the order of Tol, PMMA and MeCN as a consequence of the redshift of Azo and the simultaneous blueshift of DASA. In addition, the absorption cross section of Azo decreases in the order of Tol, PMMA and MeCN resulting in lower peak intensities.

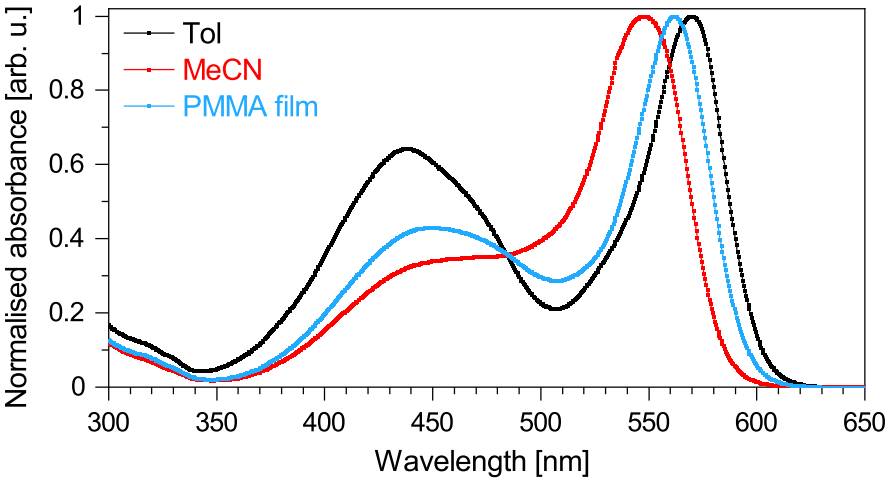

Figure 5.7. Absorption spectra of 1:1 molar DASA+Azo mixtures as Tol solution, MeCN solution and PMMA blend film.

5.3. Transient absorption measurements

In order to study the switching dynamics of Azo, DASA and their 1:1 molar mixture, TA measurements with resolution in the femtosecond range are utilised for the excited state dynamics on an ultrafast time scale. In addition to the mutual influence and interaction of both photoswitches, the environmental impact is examined by preparing a non-polar and polar solution utilising Tol and MeCN, respectively, as well as thin films. PMMA blends are investigated as the neat films show additional signals due to aggregate formation. Furthermore, DASA neat films are not stable under light irradiation, even when encapsulated. The PMMA blends however, show no additional signals and are stable under irradiation if moved as it is the case in the following TA experiments. The solutions were studied in a cuvette with 0.5 mm optical pathway using a flow cell applying a flow speed of 2 ml per minute to prevent photobleaching. Both, the cuvettes and the film substrates are made of quartz being fully transparent in the studied spectral window. For measurements conducted in solution, an excitation energy of 220 - 420 nJ was applied in order to obtain a good signal-to-noise ratio with no photodegradation. However, for thin films containing DASA, the power had to be reduced to 10 - 40 nJ to prevent degradation. To exclude photobleaching, the integrity of the samples was monitored (section 3.2).
On the ultrafast time scale, the photoinduced trans-to-cis and cis-to-trans isomerisation of Azo as well as the *Z*-to-*E* isomerisation of DASA is observed. Thus, isomer **A** and **B** of both photoswitches (figure 5.1 and 5.4) as well as the involved excited states are investigated in the following sections. First, a non-polar liquid environment is chosen in section 5.3.1. Next, the polarity of the surrounding is increased in section 5.3.2. Lastly, the excited state dynamics are analysed in thin film in section 5.3.3 and the results are compared in section 5.3.4.

5.3.1. Non-polar solutions using toluene

Hereafter, the excited state dynamics upon orthogonally switching Azo with light using a wavelength of 431 nm (trans-to-cis), orthogonally backswitching of Azo using a wavelength of 379 nm (cis-to-trans), orthogonally switching DASA with light using a wavelength of 582 nm (*Z*-to-*E*) and simultaneously switching Azo (trans-to-cis) and DASA (*Z*-to-*E*) using a wavelength of 506 nm are examined. The independent addressability of the photoswitches is indicated by the steady state absorption spectra (figures 5.5 and 5.6). Additionally, it was ensured by taking TA data of non-switched and switched DASA samples excited with 431 and 379 nm as well as non-switched and switched Azo samples excited with 582 nm revealing no features beside the time zero dispersion and in some cases artefacts due to the LED used to generate the switched species (UV/VIS spectra of all used LEDs in figure B.1 appendix B). Furthermore, TA

test measurements with Azo and the LED for DASA switching turned on as well as test measurements with DASA and the LED for Azo switching turned on were conducted. In some cases, artefacts due to the LED are observed which was accounted for in the measurements studying Azo switching when switched DASA is present and studying DASA switching when switched Azo is present.

Switching Azo orthogonally

The TA data of Azo in Tol excited by light using a wavelength of 431 nm is composed of five signals (figure 5.8**a**). One negative feature at around 440 nm represents the GSB as it resembles the steady state absorption but being narrowed at early times due to the presence of positive features at its short and long wavelength side. With increasing time delay, however, the positive signals decay and the GSB broadens such that the latter holds the spectral width of the steady state absorption. The GSB decays with

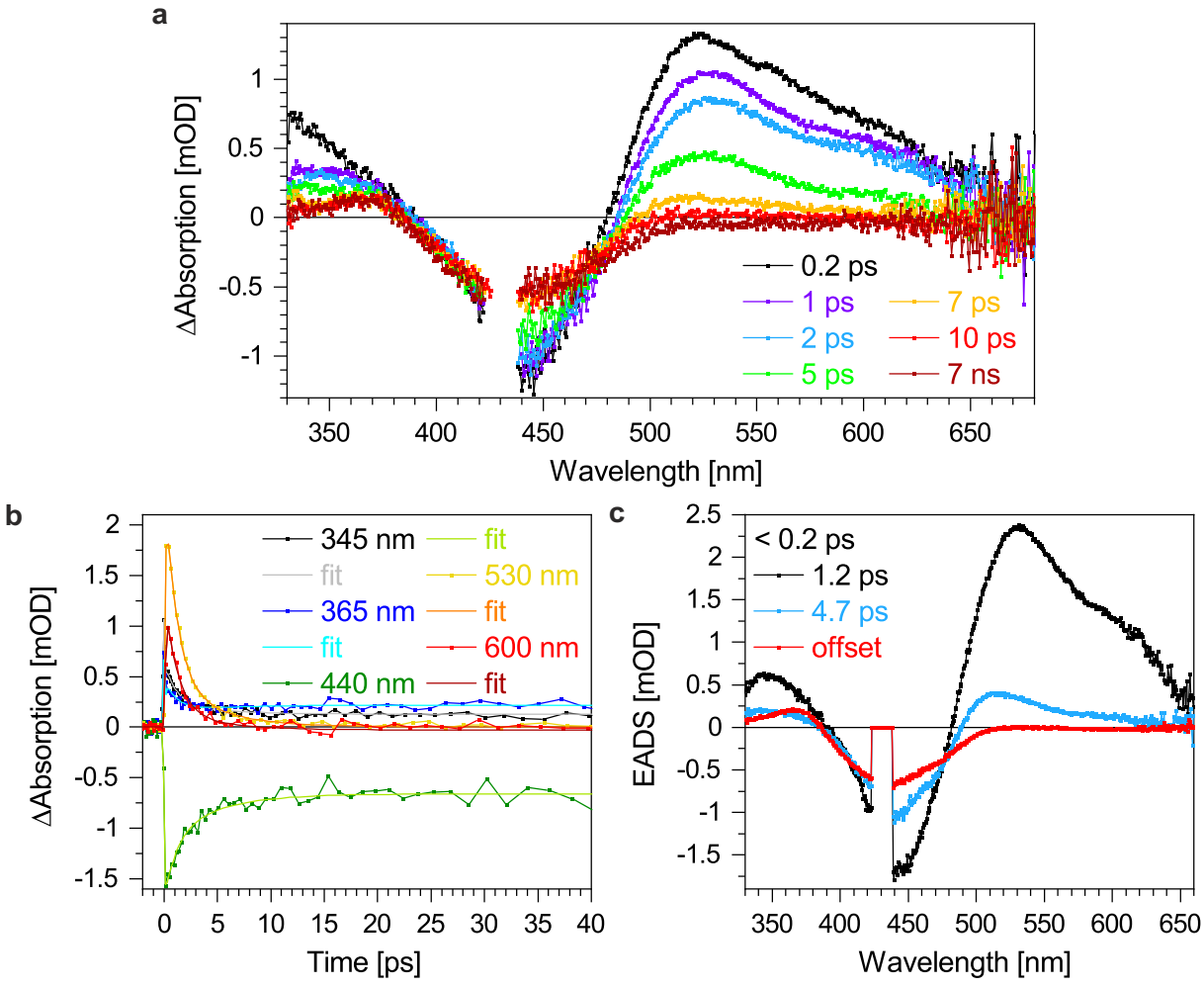

Figure 5.8. TA data of Azo in Tol excited with light of a wavelength of 431 nm. (a) Chosen time traces, (b) selected wavelength traces with corresponding fits and (c) EADS as well as their time constants obtained by GA. The EADS of the short time constant being below the resolution of the laser setup is not shown since this EADS is not separable from the pump-probe artefact.

about 22 ps to a constant level below zero. The constant offset reveals that not all excited *trans*-Azo molecules return to the *trans*-Azo ground state within the experimental measurement period of about 8 ns. The other TA signals are positive corresponding to four ESAs with two being in the UV region and two being red-shifted compared to the GSB. The ESAs are located at around 345, 365, 530 and 600 nm. The latter two decay within about 25 and 35 ps, respectively. The ESA at around 345 nm decays within 27 ps while the ESA at around 365 nm decays to a minimum in about 4 ps and subsequently slightly increases until reaching a constant value at about 30 ps. Interestingly, the ESAs at around 530 and 600 nm exhibit a short rise within the first 0.1 - 0.2 ps before reaching their maximum intensity.
Analysing the TA data by GA (figure 5.8**b**) yields three time constants τ_i of (< 0.2 ± 0.2), (1.2 ± 0.2) and (4.7 ± 0.2) ps as well as an offset (figure 5.8**c**). Taking a look at the EADS, the signal initially located at about 530 nm undergoes a blueshift. Comparing the results to other push-pull azobenzene derivatives, the red-shifted ESAs compared to the GSB can be assigned. Thus, the vibrationally excited S_1 state is represented by the ESA at around 600 nm and the hot *trans*-isomer ground state by the ESA at about 530 nm.[229][233][234][257] The short rise time of the aforementioned ESAs fit to those results as the rise time can be attributed to the decay of $S_2 \rightarrow S_1$.[233] The ESA in the UV region located at around 345 nm, however, is harder to assign as the transient absorption profiles in the UV region may consist of several components.[257] The ESA at about 365 nm, which does not decay to zero as the other ESAs, is attributed to the absorption of *cis*-Azo. This is supported by the spectral overlap, especially at the short wavelength side, of the steady state absorption spectra of switched Azo to the TA data at late times and the EADS of the offset. Thus, the *cis*-Azo isomer is successfully generated upon photoswitching and is stable forming a constant signal contributing to the TA data as an offset. Comparing the determined lifetimes to azobenzene and its derivatives as elucidated at the beginning of this chapter, $S_2 \rightarrow S_1$ conical intersection or internal conversion takes place as well as the movement of the wavepacket out of the Franck-Condon region towards the conical intersection of $S_1 \rightarrow S_0$ on an ultrafast time scale. The excitation to the S_2 is thereby confirmed by quantum chemical calculations.[258] One of the aforementioned processes is described by the time constant of below 0.2 ps. The lifetime of 1.2 ps is related to the decay of the S_1 state to the S_0 state via conical intersection. The desired *cis*-Azo is thereby created but also *trans*-Azo. Next, vibrational relaxation within the ground state occurs on a time scale of 4.7 ps. The successful switching of *trans*-Azo to *cis*-Azo is accounted for by the offset generating negative and positive features in the corresponding EADS, respectively.
If DASA is added to a solution of Azo in Tol such that a 1:1 molecular ratio of Azo to DASA is obtained, the TA data is generally unaltered (figure 5.9**a**). Again, five signals are observed with the negative feature at around 440 nm representing the GSB

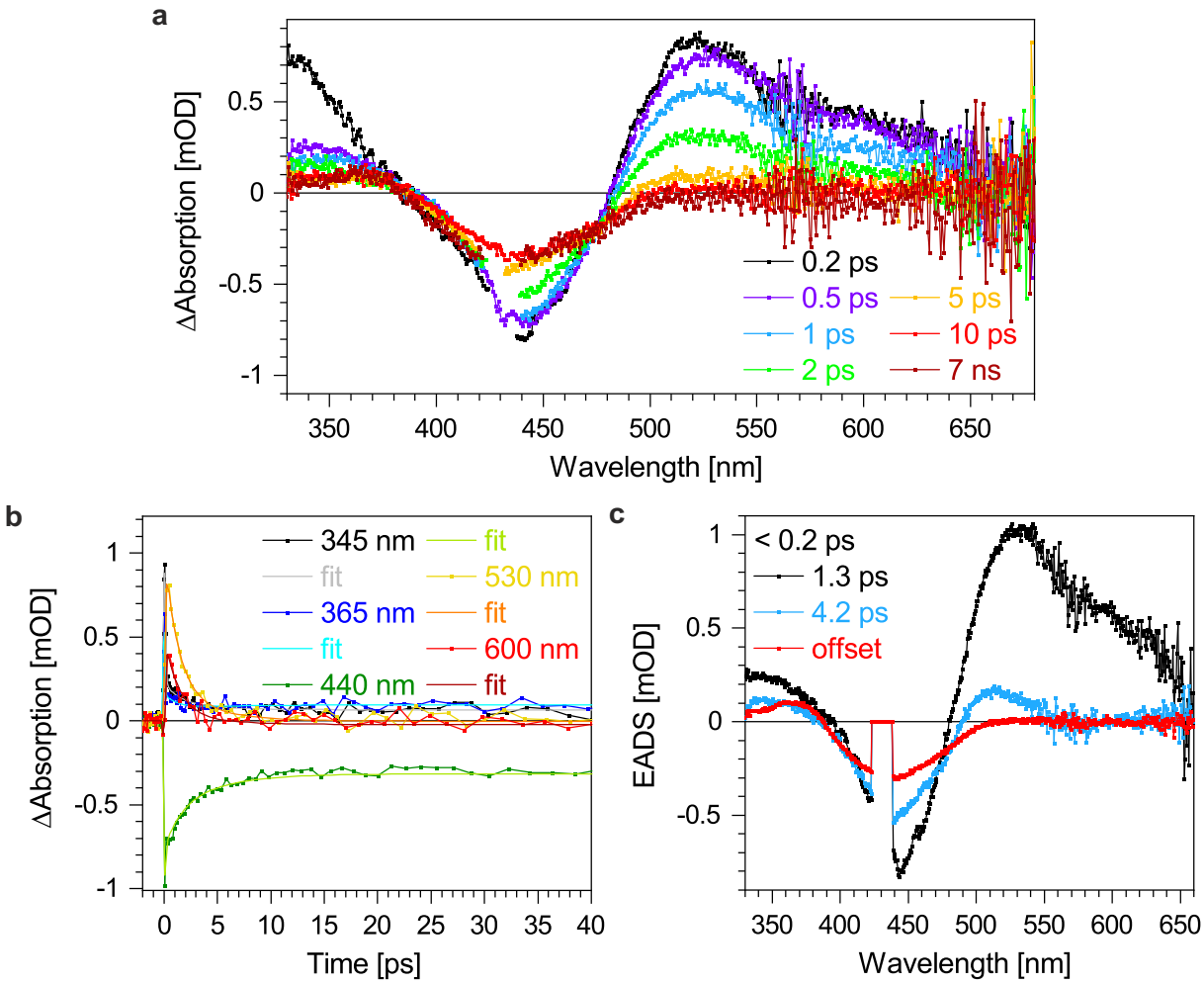

Figure 5.9. TA data of Azo in Tol excited with light of a wavelength of 431 nm while DASA is present. (a) Chosen time traces, (b) selected wavelength traces with corresponding fits and (c) EADS as well as their time constants obtained by GA. The EADS of the short time constant being below the resolution of the laser setup is not shown since this EADS is not separable from the pump-probe artefact.

and four positive signals at about 345, 365, 530 and 600 nm. The latter two exhibit a short rise time before reaching their maximum while the ESA located at around 365 nm quickly reaches a minimum but slightly increases later on before reaching its constant positive offset. The GSB decreases but stops at a constant level as some molecules are successfully switched from the trans- to the cis-isomer upon the TA experiment forming the ESA at about 365 nm.

GA (figure 5.9**b**) reveals three lifetimes τ_i of (< 0.2 ± 0.2), (1.3 ± 0.2) and (4.2 ± 0.3) ps as well as an offset (figure 5.9**c**). Compared to pure Azo in Tol (figure 5.8), all time constants are unaltered within their respective error limits beside the longest time component decreasing by 0.5 ps. Hence, the excited state dynamics remain the same with the vibrational cooling being accelerated by the presence of DASA.

To investigate possible interactions and influences of both photoswitches further, a 1:1 molar mixture of Azo and DASA in Tol is excited while illuminated by an LED having

its maximum wavelength at 594 nm in order to switch the DASA compound (*Z*-to-*E*). To ensure a photostationary state of DASA, the mixture is illuminated several minutes before running the TA experiment as well as during the measurement. According to prior steady state absorption spectra of DASA in Tol, by mimicking the geometric conditions of the TA measurement, roughly 80 % of DASA is in the closed-form during the TA experiment (figure B.3**a** appendix B).

The TA data of a 1:1 molar mixture of Azo and DASA switched by the illumination of an LED in Tol (figure 5.10**a**) resembles the data of the pure Azo and the 1:1 molar mixture of Azo and DASA without LED illumination (figures 5.8 and 5.9). The GSB is observed as negative feature at about 440 nm and four ESAs located at around 345, 365, 530 and 600 nm are detected. The latter exhibits a short rise time before reaching its maximum while the ESA at about 365 nm slightly increases to a constant positive offset after passing a minimum. The GSB reaches a constant offset as well after decay-

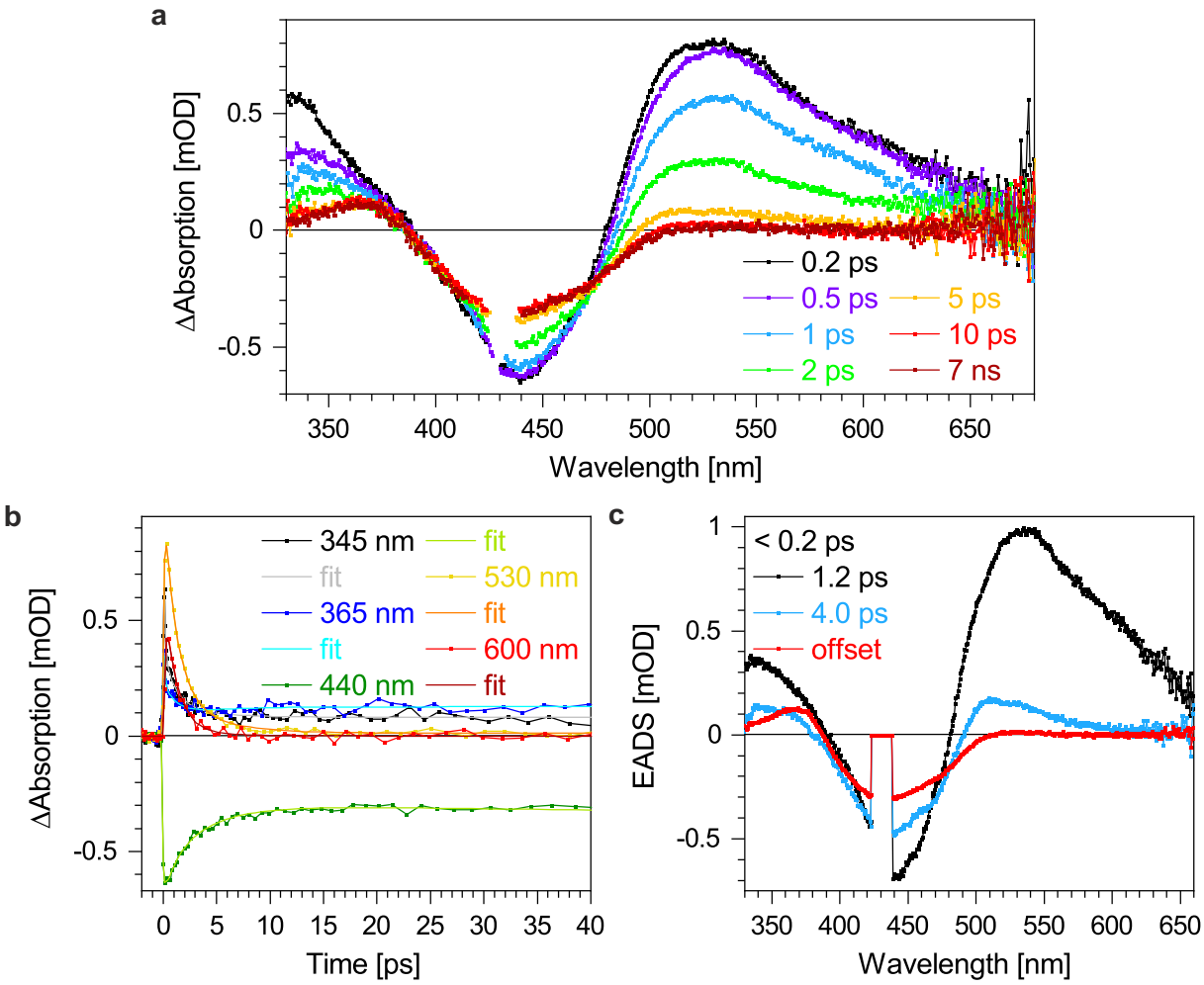

Figure 5.10. TA data of Azo in Tol excited with light of a wavelength of 431 nm while switched DASA is present due to irradiation with an LED with maximum intensity at 594 nm. (a) Chosen time traces, (b) selected wavelength traces with corresponding fits and (c) EADS as well as their time constants obtained by GA. The EADS of the short time constant being below the resolution of the laser setup is not shown since this EADS is not separable from the pump-probe artefact.

ing. However, the GSB decays to a negative signal since molecules are successfully switched from trans to cis.
A GA of the data (figure 5.10**b**) yields time constants τ_i of (< 0.2 ± 0.2), (1.2 ± 0.2) and (4.0 ± 0.2) ps as well as an offset (figure 5.10**c**). The lifetimes are within their error limits in accordance to the measurements of pure Azo and the 1:1 molar mixture Azo and DASA beside the longest lifetime (figures 5.8 and 5.9). Therefore, the same excited state dynamics after excitation take place. The vibrational cooling described by the longest time constant, however, is the same as in the non-switched DASA and Azo mixture within the error limit but decreased by 0.5 ps compared to pure Azo in Tol.

Backswitching Azo photochemically

Since the trans-to-cis isomerisation of Azo was studied in the previous section, the photochemical backswitching of Azo, meaning the cis-to-trans isomerisation, is addressed within this section. Therefore, an Azo in Tol solution was illuminated with an LED having its maximum wavelength at 409 nm to produce *cis*-Azo while having no overlap with the DASA absorption. This solution is referred to as *cis*-Azo solution in the following. Mimicking the geometric situation of the TA measurements, the amount of *cis*-Azo was estimated to be about 60 % (figure B.4**a** appendix B).
Exciting *cis*-Azo in Tol with light of a wavelength of 379 nm to induce backswitching from cis to trans, several features are observed (figure 5.11**a**). At early times, two negative features located at around 375 and 442 nm are obtained. Comparing the spectral positions to the absorption features of Azo (figure 5.5), the negative signals are attributed to the GSBs of *cis*-Azo and *trans*-Azo, respectively. The GSB at around 368 nm decays within about 11 ps to a constant offset pointing out that *cis*-Azo was successfully switched to the trans state which is stable for longer than the experimental period of around 8 ns. The GSB of the *trans*-Azo being initially present decays to zero within about 1.5 ps. In addition, four positive ESAs are present. The ESA in the UV region at around 338 nm resembles the ESA found in the trans-to-cis switching at about 345 nm. The slight change in spectral position is due to the GSB at around 370 nm which narrows the ESA at its long wavelength side. Thus, a similar origin of the feature compared to the trans-to-cis switching process is obvious. The 338 nm trace decays within about 44 ps to a negative value since simultaneously the ESA decays to zero and the GSB broadens towards longer delay times and thereby also covers 338 nm. Similar to the TA data of the trans-to-cis switching, two ESAs located at around 530 and 600 nm occur with the former exhibiting a hypsochromic shift upon increasing time delay due to the decay of the latter. Both ESAs decay to about zero in around 41 and 47 ps, respectively. The ESA located at around 403 nm at 0.3 ps bathochromically shifts at longer delay times to its final value at about 433 nm which is reached in around 25 ps. The positive offset indicates the successful generation of the photoproduct *trans*-Azo.

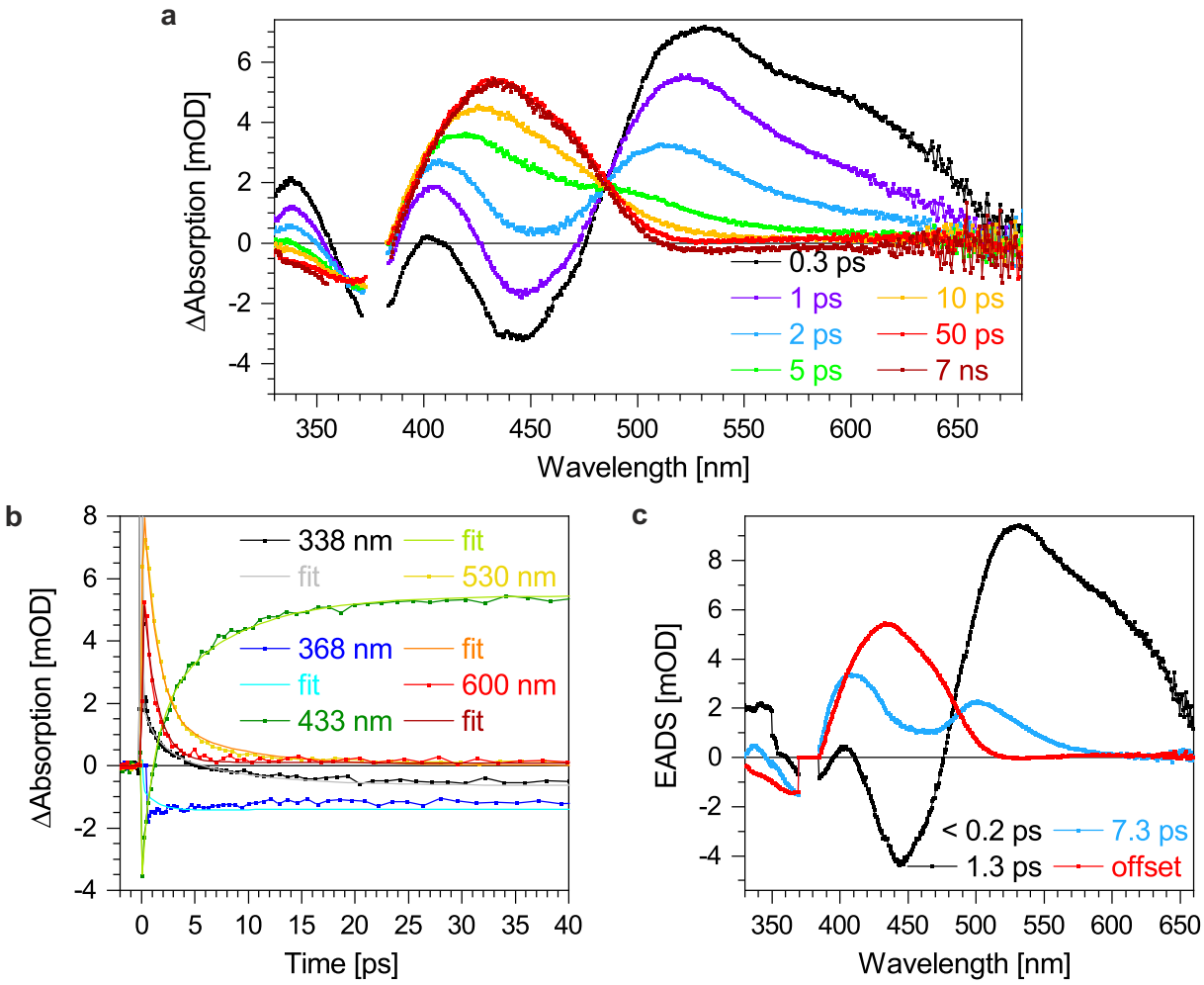

Figure 5.11. TA data of Azo in Tol excited with light of a wavelength of 379 nm to induce backswitching (cis-to-trans). (a) Chosen time traces, (b) selected wavelength traces with corresponding fits and (c) EADS as well as their time constants obtained by GA. The EADS of the short time constant being below the resolution of the laser setup is not shown since this EADS is not separable from the pump-probe artefact.

GA (figure 5.11**b**) describes the TA data by three time constants τ_i of (< 0.2 ± 0.2), (1.3 ± 0.2) and (7.3 ± 0.2) ps as well as an offset (figure 5.11**c**). Comparing the obtained lifetimes and EADS to the results of trans-to-cis photoisomerisation, one gets a complete picture of the excited state dynamics after excitation with 379 nm corresponding to the $\pi \rightarrow \pi^*$ excitation as confirmed by quantum chemical calculations.[258] First, the $S_2 \rightarrow S_1$ conical intersection or the movement of the wavepacket out of the Franck-Condon region occurs described by the time constant of below 0.2 ps. Next, $S_1 \rightarrow S_0$ conical intersection takes place on a time scale of 1.3 ps. Lastly, vibrational relaxation happens with a lifetime of 7.3 ps. This is in line with photoisomerisation of *cis*-azobenzene and its derivatives studied in literature.[237] [259] [260] Hence, the ESAs located at around 530 and 600 nm are attributed to the vibrationally excited ground state of the trans-isomer and the S_1 state, respectively. The UV ESA is again hard to assign as it may consist of several signals. The ESA initially located at 403 nm refers to

the absorption of the *trans*-Azo photoproduct. Since the latter ESA overlaps spectrally with the GSB of initially present *trans*-Azo, it emerges from the short wavelength side of the peak and undergoes a redshift such that the ESA at late times resembles the steady state absorption of *trans*-Azo. Interestingly, an isosbestic point at about 485 nm is observed indicating that all molecules in the vibrationally excited ground state exhibiting ESA at around 530 nm decay to the *trans*-Azo photoproduct absorbing at about 433 nm.

In the next step, the influence of DASA upon backswitching Azo is studied. Therefore, a 1:1 molar ratio of Azo and DASA was prepared in Tol before generating *cis*-Azo by LED illumination and starting the TA experiment. Again, the TA data reveals several excited states involved upon excitation (figure 5.12**a**). In total, four positive and two negative features are visible. Three ESAs located at around 338, 530 and 600 nm represent involved excited transition states decaying within the experiment. The negative

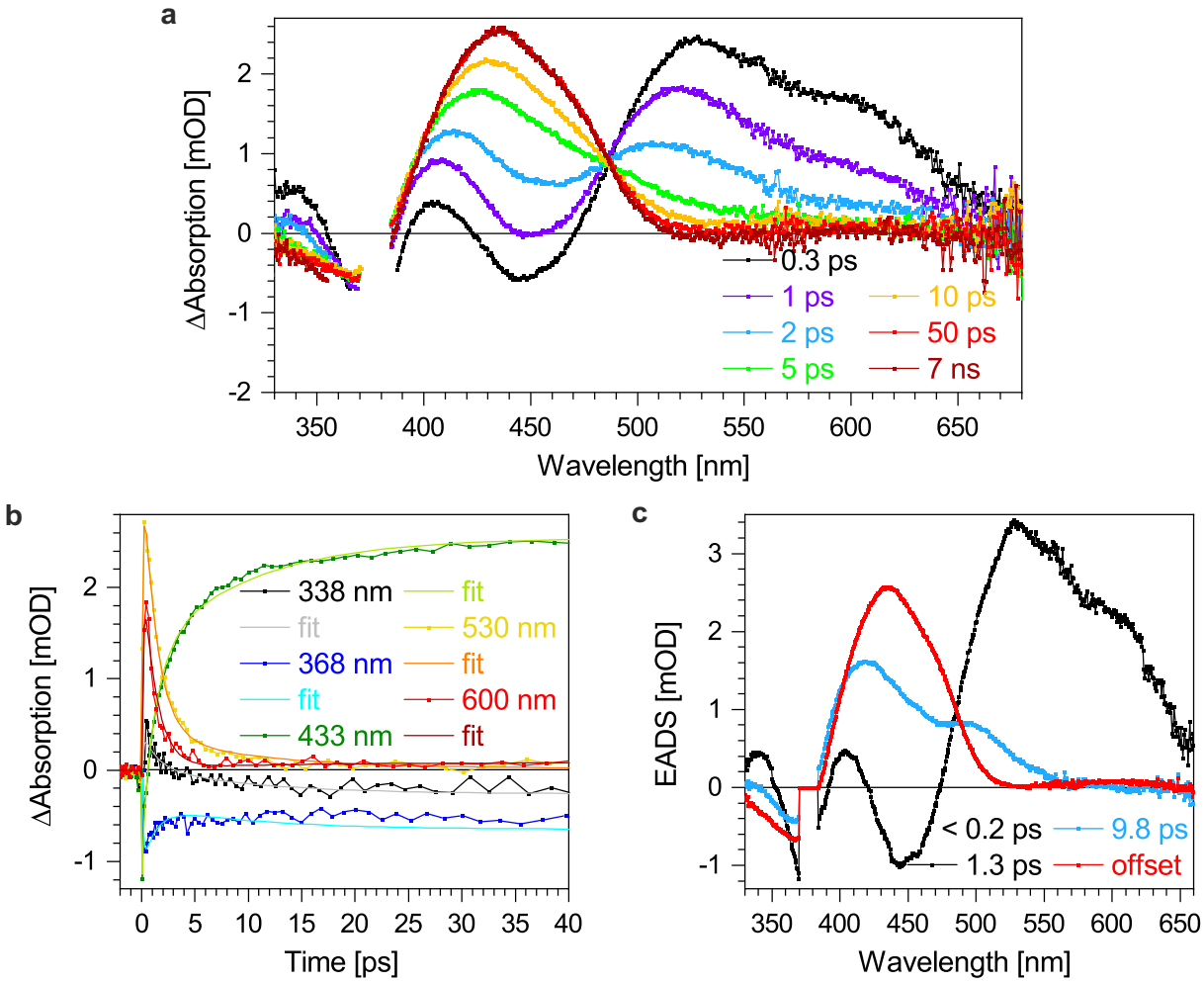

Figure 5.12. TA data of Azo in Tol excited with light of a wavelength of 379 nm to induce backswitching while DASA is present. (a) Chosen time traces, (b) selected wavelength traces with corresponding fits and (c) EADS as well as their time constants obtained by GA. The EADS of the short time constant being below the resolution of the laser setup is not shown since this EADS is not separable from the pump-probe artefact.

GSBs of the present cis and trans species are observed at about 368 and 444 nm, respectively. The latter GSB decays rapidly to zero while the GSB assigned to the *cis*-Azo decays to a constant negative value because part of the molecules are successfully photoswitched to the trans isomer showing ESA at around 405 - 435 nm. The ESA of the photoproduct exhibits a redshift as it spectrally overlaps with the vanishing negative signal at about 444 nm until it stays constant within the experimental measurement period of about 8 ns. Moreover, the ESAs located at around 530 and 433 nm exhibit an isosbestic point at about 585 nm indicating interconversion of both states.
The excited state dynamics are described by a global fit (figure 5.12**b**) yielding three time constants τ_i of (< 0.2 ± 0.2), (1.3 ± 0.2) and (9.8 ± 0.3) ps as well as an offset (figure 5.12**c**). Hence, the excited state dynamics after photoexcitation are unchanged compared to the pure Azo solution as the time constants and EADSs are equal apart from the longest time component (figure 5.11). Vibrational relaxation is slowed down by 2.5 ps in the present Azo+DASA mixture.
To investigate the influence of the closed zwitterionic DASA isomer **C'** on the photoswitching of *cis*-Azo, a 1:1 molar mixture of Azo and DASA in Tol was prepared. Beside the illumination with an LED, having its maximum wavelength at about 409 nm to produce *cis*-Azo, the solution was additionally illuminated with an LED with maximum intensity at around 594 nm to generate switched DASA (figure B.3**a** appendix B). The features of this mixture obtained by TA measurement (figure 5.13**a**) resemble the former outcomes. Again, two negative GSBs at about 368 and 444 nm are observed at early times representing the *cis*- and initial *trans*-Azo, respectively. Whereas the latter signal decays rapidly to zero, the former decays to a constant negative offset as part of the molecules are successfully switched to the trans-photoproduct being stable during the experimental period. The ESAs located at around 330, 530 and 600 nm are assigned to excited intermediate states decaying with increasing delay time. The ESA initially detected at around 404 nm bathochromically shifts towards about 435 nm upon increasing time delay due to the spectral overlap of the vanishing negative feature located at around 444 nm. The constant positive offset at about 435 nm represents the *trans*-Azo photoproduct.
GA (figure 5.13**b**) provides three time constant τ_i of (< 0.2 ± 0.2), (1.4 ± 0.2) and (7.9 ± 0.2) ps as well as an offset (figure 5.13**c**). Since the lifetimes and EADS resemble the results of pure Azo and non-switched DASA+Azo photochemical backswitching (figures 5.11 and 5.12), the relaxation pathways remain unaltered. However, the vibrational cooling described by the longest time constant is increased by 0.6 ps in the present mixture compared to pure Azo in Tol due to the presence of DASA.

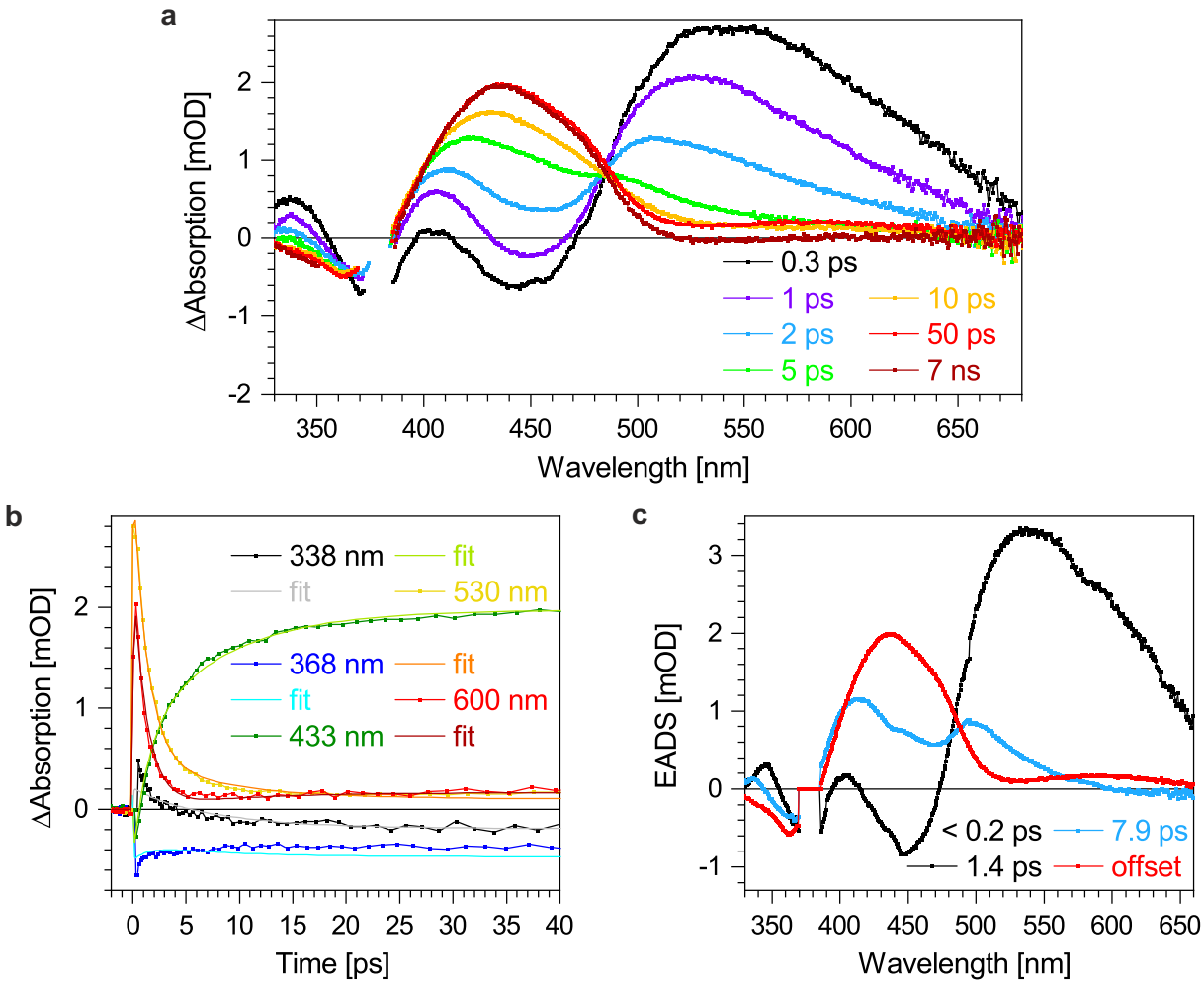

Figure 5.13. TA data of Azo in Tol excited with light of a wavelength of 379 nm to induce backswitching while switched DASA is present due to irradiation with a LED with maximum intensity at 594 nm. (a) Chosen time traces, (b) selected wavelength traces with corresponding fits and (c) EADS as well as their time constants obtained by GA. The EADS of the short time constant being below the resolution of the laser setup is not shown since this EADS is not separable from the pump-probe artefact.

Switching DASA orthogonally

Although the photoswitchable molecules Azo and DASA are very different, their switching mechanism on the femtosecond time scale both contain *E*/*Z* isomerisation. In case of DASA, *Z*/*E* isomerisation takes place upon excitation with light.

By exciting DASA in the aprotic non-polar solvent Tol, a couple of signals are observed (figure 5.14**a**). At early times, a broad negative signal at about 570 nm and a positive feature at higher energies located around 447 nm is obtained. The negative feature consists of the GSB as it spectrally overlaps with the steady state absorption (figure 5.6) and an SE constituting the shoulder at longer wavelengths. By comparing the steady state absorption with the negative TA feature in detail, the GSB is narrower compared to the steady state absorption as the latter shows a more pronounced shoulder on its short wavelength side due to vibrational progression.[261][262] The GSB located at

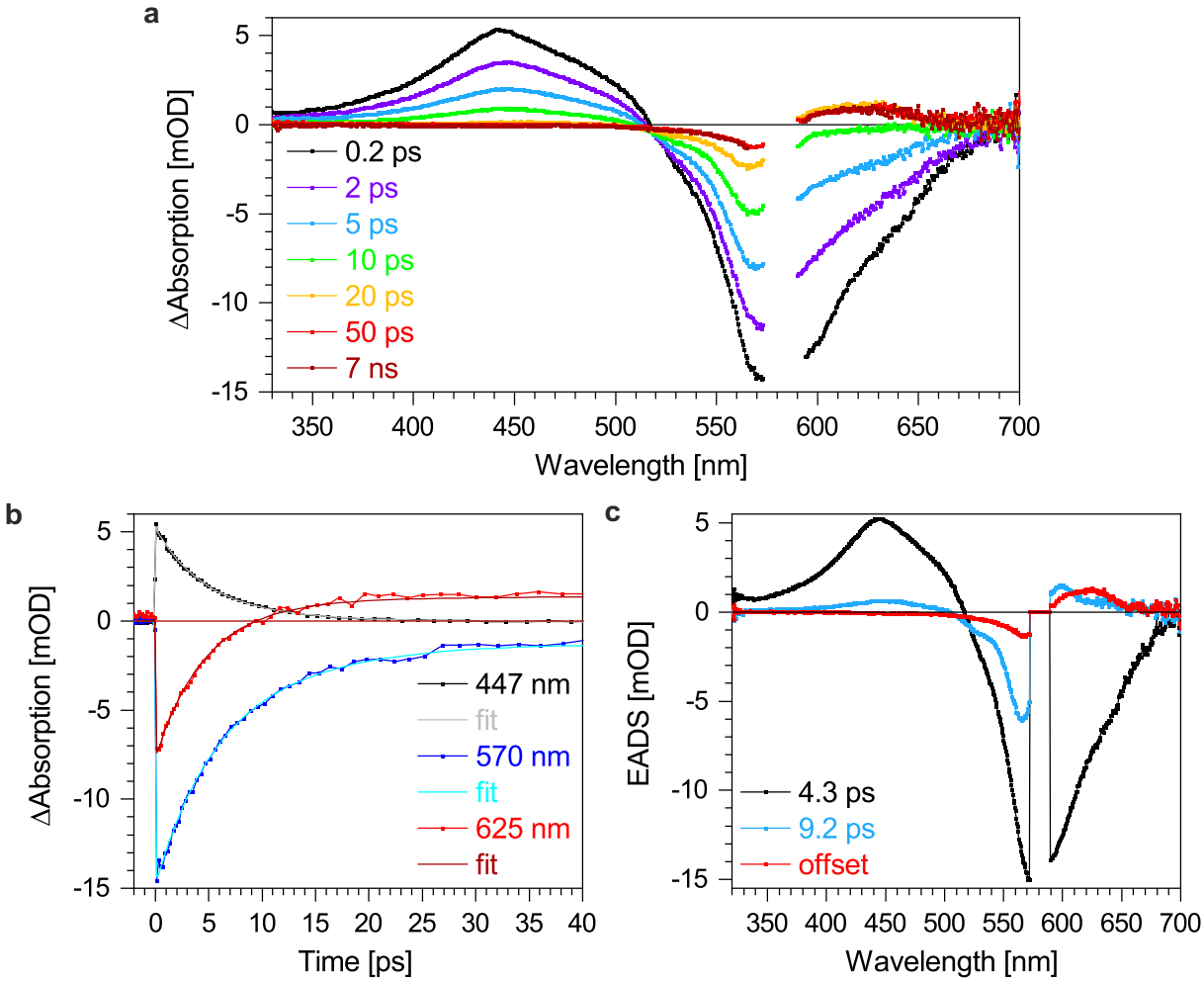

Figure 5.14. TA data of DASA in Tol excited with light of a wavelength of 582 nm to induce *Z*-to-*E* isomerisation. (a) Chosen time traces, (b) selected wavelength traces with corresponding fits and (c) EADS as well as their time constants obtained by GA.

about 570 nm decays within 55 ps to a constant level whereas the SE at around 625 nm reaches zero within 10 ps. As both overlapping negative signals decay with different time constants, the maximum of the negative feature undergoes a small blueshift upon increasing time delay. Since the GSB does not decay to zero but to a constant negative offset, part of the molecules are promoted into another state being stable within the experimental period of about 8 ns. The positive ESA located at around 447 nm decays within about 51 ps to zero. At later times, a positive ESA emerges at longer wavelengths compared to the GSB at about 625 nm. After 42 ps it reaches its final positive value representing the absorption of the photoproduct *E*-DASA. This is confirmed by spectral identity of the positive ESA with the transient absorption band in UV/VIS absorption experiments upon switching DASA with an LED identified as absorption of the *E*-DASA.[247]

Description of the TA data by GA (figure 5.14**b**) results in two time constants τ_i of (4.3 ± 0.2) and (9.2 ± 0.2) ps as well as an offset (figure 5.14**c**). Upon excitation, the molecules get excited to S_1 as indicated by theoretical calculations.[261][262] Thus, the

blue-shifted ESA represents the S_1 state. Upon decay of the latter ESA, *trans*-DASA is formed as indicated by the positive peak at around 600 nm of the EADS of 9.5 ps. Next, vibrational relaxation leads to a redshift of the ESA of about 20 nm. The observed excited state dynamics are in accordance with excited state dynamics of literature known donor-acceptor-Stenhouse-adducts.[256] [263]

Following, the interaction and influence of Azo on the excited state dynamics and switching behaviour of DASA in Tol is studied. Therefore, a 1:1 molar mixture of Azo and DASA in Tol was prepared. The TA data upon switching DASA while Azo is present (figure 5.15**a**) looks similar to the pure DASA solution (figure 5.14). At early times, a broad negative and positive signal occurs. The negative signal is composed of the GSB at around 570 nm and SE making up the long-wavelength shoulder of the negative signal. In addition, a broad positive ESA appears at about 447 nm. Upon increasing time delay, the GSB and the SE decrease in their intensity and simultaneously a new ESA located at around 625 nm is obtained at later times. Hence, the maximum intens-

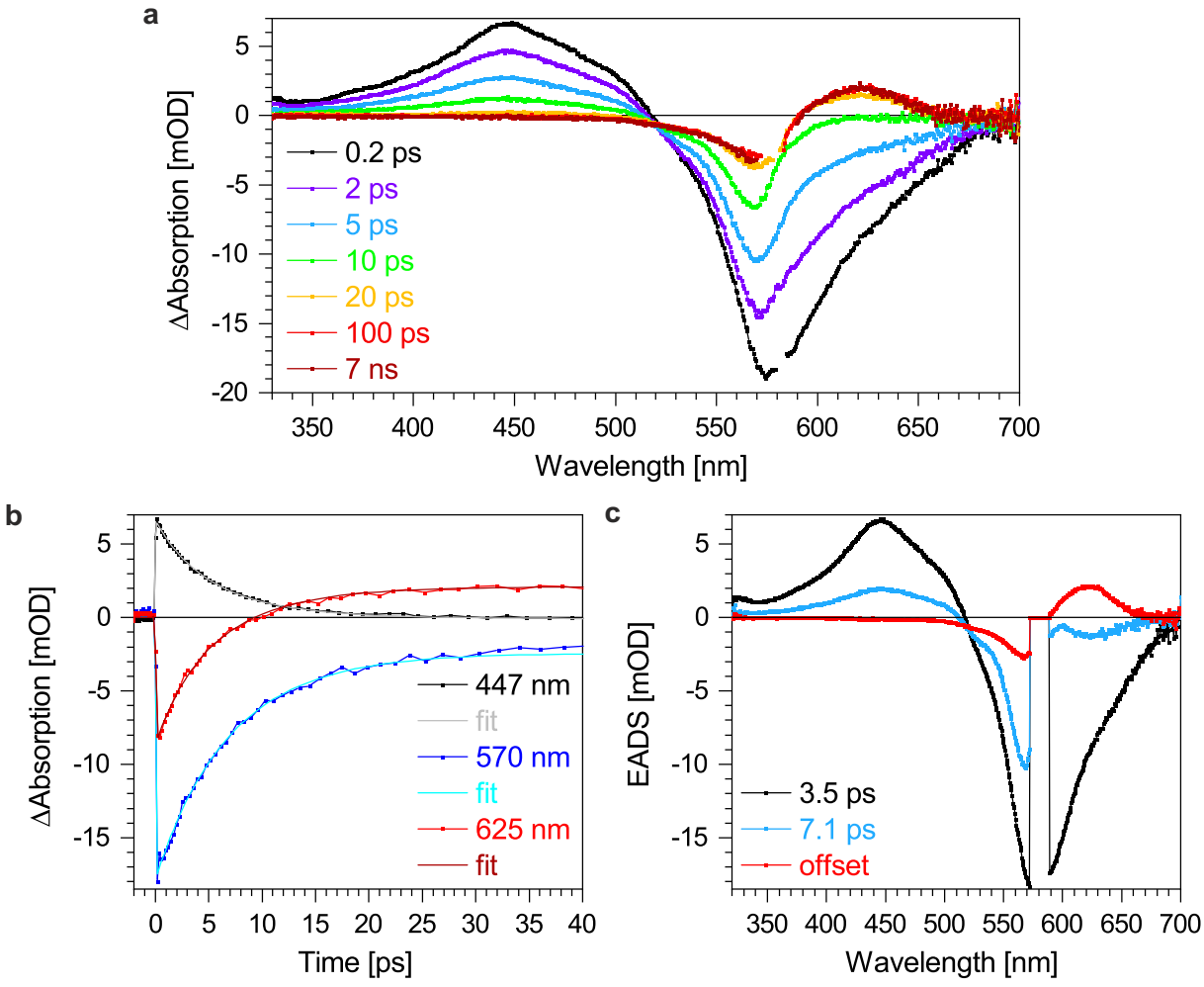

Figure 5.15. TA data of DASA in Tol excited with light of a wavelength of 582 nm while Azo is present. (a) Chosen time traces, (b) selected wavelength traces with corresponding fits and (c) EADS as well as their time constants obtained by GA.

ity of the GSB follows a slight blueshift with increasing time delay. The ESA at about 447 nm decreases to zero with increasing time delay. At the end of the experiment, the GSB decays to a constant negative signal indicating successful switching of *Z*-DASA to its structural isomer *E*-DASA which is represented by the ESA at about 625 nm. The absorption of *E*-DASA adds a constant offset to the TA data since the photoproduct is stable much longer than the experimental period of about 8 ns.
A global fit of the TA data (figure 5.15**b**) results in two lifetimes τ_i of (3.5 ± 0.2) and (7.1 ± 0.2) ps as well as an offset (figure 5.15**c**). Comparing the time constants to the outcomes of pure DASA solution (figure 5.14), they shorten by 0.8 and 2.1 ps, respectively. The EADS look similar beside a minor difference in the EADS of the second time component (blue curves in figures 5.14**c** and 5.15**c**). In pure DASA, a positive peak around 600 nm represents the photoproduct in its electronic ground state but in higher vibrational states. When Azo is present this signal trace is also found at about 600 nm but still at negative $\triangle$A values. Despite minor changes in the time constants and EADS, the overall excited state dynamics upon photoswitching DASA remain unchanged.
Next, the interaction and influences of *cis*-Azo on the switching properties of DASA are studied. Therefore, a 1:1 molar mixture of Azo and DASA was prepared in Tol. To generate the switched Azo species in a photostationary state, the solution was illuminated several minutes prior to the experiment as well as during the experiment with an LED having its maximum wavelength at around 409 nm to induce Azo switching resulting in about 60 % *cis*-Azo (figure B.4**a** appendix B).
The TA data upon switching DASA while *cis*-Azo is present (figure 5.16**a**) reveal only small changes compared to the other DASA switching experiments (figures 5.14 and 5.15). At early times, an ESA at around 447 nm is observed as well as two negative signals composing of the GSB located at about 570 nm and the SE identified as a clear long-wavelength shoulder at around 625 nm. Upon increasing time delay, the ESA and the SE decay to zero. The GSB decays to a constant negative offset while exhibiting a small blueshift due to the decay of the SE. At later times, a positive ESA band is obtained at about 625 nm. The GSB and the latter ESA stay at a constant negative and positive value, respectively, which indicates the successful switching of *Z*-DASA to *E*-DASA.
By GA (figure 5.16**b**), two time constants τ_i of (3.3 ± 0.2) and (7.3 ± 0.2) ps as well as an offset (figure 5.16**c**) are identified. The lifetimes are within their error limits identical to the outcomes of switching DASA with non-switched Azo present (figure 5.16). Also the EADS feature the same signals. Hence, the same excited state dynamics exist.

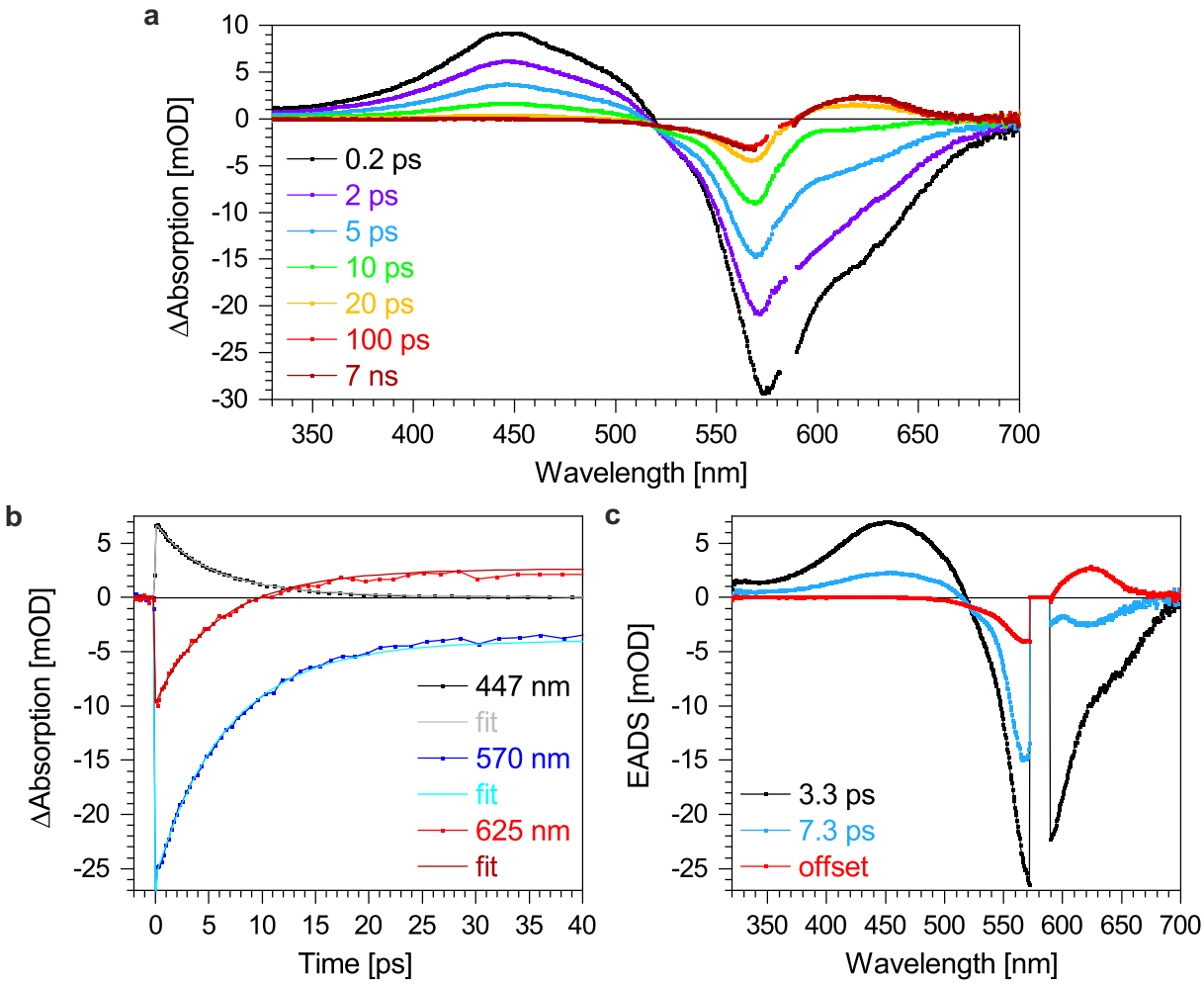

Figure 5.16. TA data of DASA in Tol excited with light of a wavelength of 582 nm while switched Azo is present due to irradiation with an LED with maximum intensity at a wavelength of 409 nm. (a) Chosen time traces, (b) selected wavelength traces with corresponding fits and (c) EADS as well as their time constants obtained by GA.

Switching Azo and DASA simultaneously

The last measurement series in Tol aims at the interaction of the photoswitches when both are addressed simultaneously by photoexcitation with 506 nm (isomerisation of *trans*-Azo to *cis*-Azo and *Z*-DASA to *E*-DASA). Since the excitation energy has to be varied, the single photoswitches have to be characterised first.

To begin with, the Azo switching dynamics upon excitation with 506 nm are studied (figure 5.17**a**). In the TA data, a broad negative feature assigned to GSB at about 450 nm occurs at early times. Simultaneously, four positive ESAs emerge around 345, 385, 537 and 600 nm. With increasing time delay, the latter two ESAs decay in about 24 and 20 ps, respectively. As the decay times of the overlapping signals differ, the maximum intensity of the signal at around 530 nm undergoes a blueshift. In contrast, the ESA in the UV region at around 345 nm decays within 28 ps while the feature initially located at about 385 nm hypsochromically shifts towards 365 nm and reaches

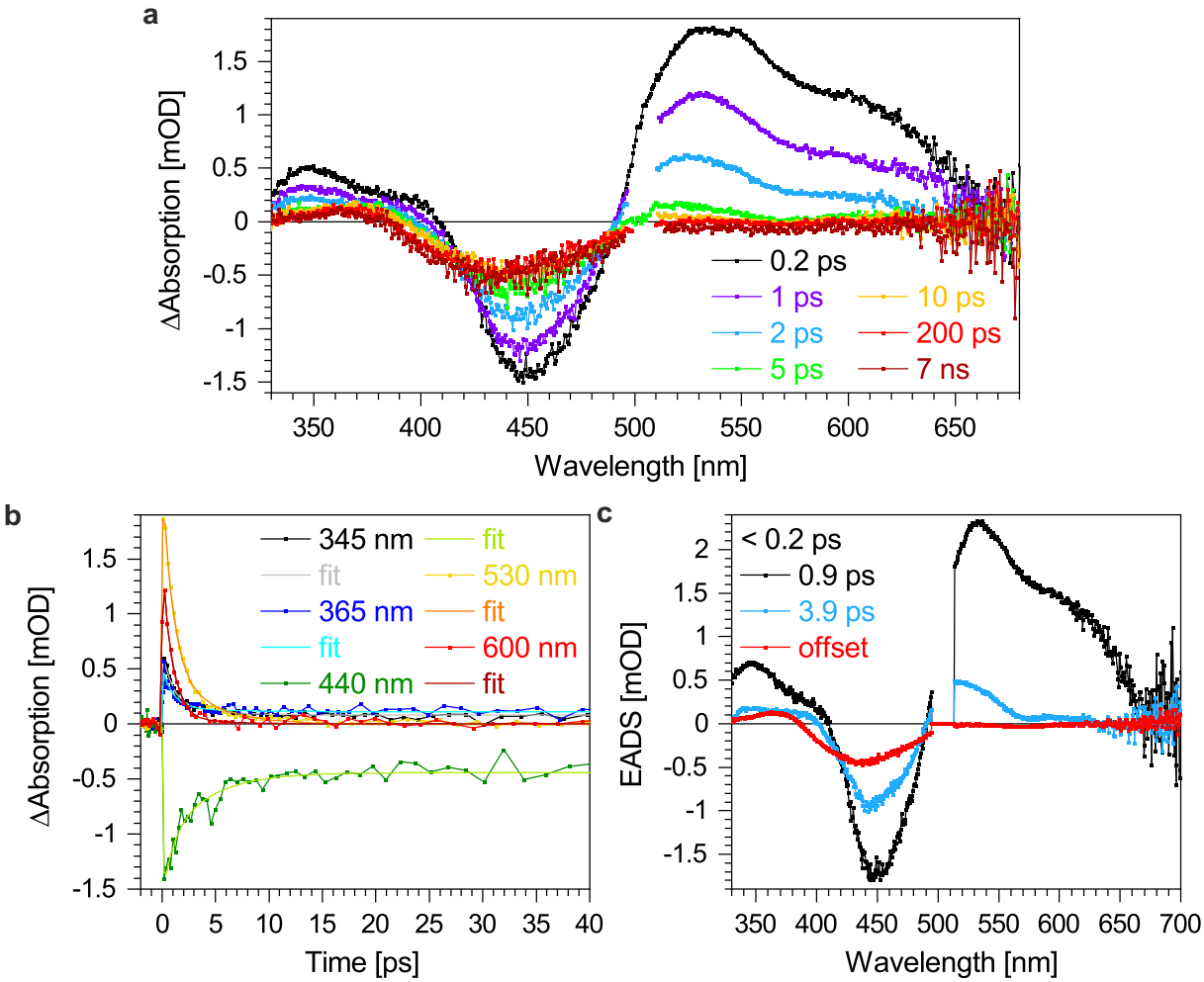

Figure 5.17. TA data of Azo in Tol excited with light of a wavelength of 506 nm. (a) Chosen time traces, (b) selected wavelength traces with corresponding fits and (c) EADS as well as their time constants obtained by GA. The EADS of the short time constant being below the resolution of the laser setup is not shown since this EADS is not separable from the pump-probe artefact.

a maximum intensity after ca. 17 ps. The spectral shift is thereby due to the decay of overlapping signals. This holds also true for the GSB which shifts with increasing time delay towards approximately 440 nm and broadens. The GSB also decays not to zero but to a constant negative offset reached after around 55 ps. The offset signals indicate successful switching of *trans*-Azo, represented by the GSB, to *cis*-Azo, being stable longer than the experimental period of about 8 ns as depicted by the absorption at about 365 nm.

GA of the data (figure 5.17**b**) yields three time constants τ_i of (< 0.2 ± 0.2), (0.9 ± 0.2) and (3.9 ± 0.2) ps as well as an offset (figure 5.17**c**). Comparing the lifetimes and EADS determined, the excited state dynamics after excitation to S_2 as for orthogonally switching Azo applies (paragraph Switching Azo orthogonally, this section). The S_1 population is thereby represented by its absorption at around 600 nm and the trans-isomer in the electronic ground state but in higher vibrational levels is observed by the ESA at around 530 nm. The successful switching is witnessed by the remaining GSB

of *trans*-Azo and the absorption of the photoproduct *cis*-Azo at around 365 nm which are assigned by the spectral identity with the steady state absorption of both isomers (figure 5.5). The ESA at around 345 nm is harder to assign since different components can contribute in this spectral region.

In comparison with the trans-to-cis isomerisation by excitation with 431 nm (figure 5.8), the spectral features remain overall unaltered. However, all signals are slightly bathochromically shifted at early times for the excitation with 506 nm. In addition, the last two steps are slightly accelerated by 506 nm excitation in comparison with 431 nm excitation such that the time constants shorten by 0.3 and 0.8 ps, respectively.

Next, the excited state dynamics of DASA in Tol upon excitation with 506 nm are studied via TA measurements (figure 5.18**a**). At early times, a broad symmetric positive feature at around 447 nm occurs. At longer wavelengths, a negative feature holding an asymmetric shape appears with its maximum located at about 570 nm. This negative feature consists of two overlapping signals which is the GSB identified by its spectral

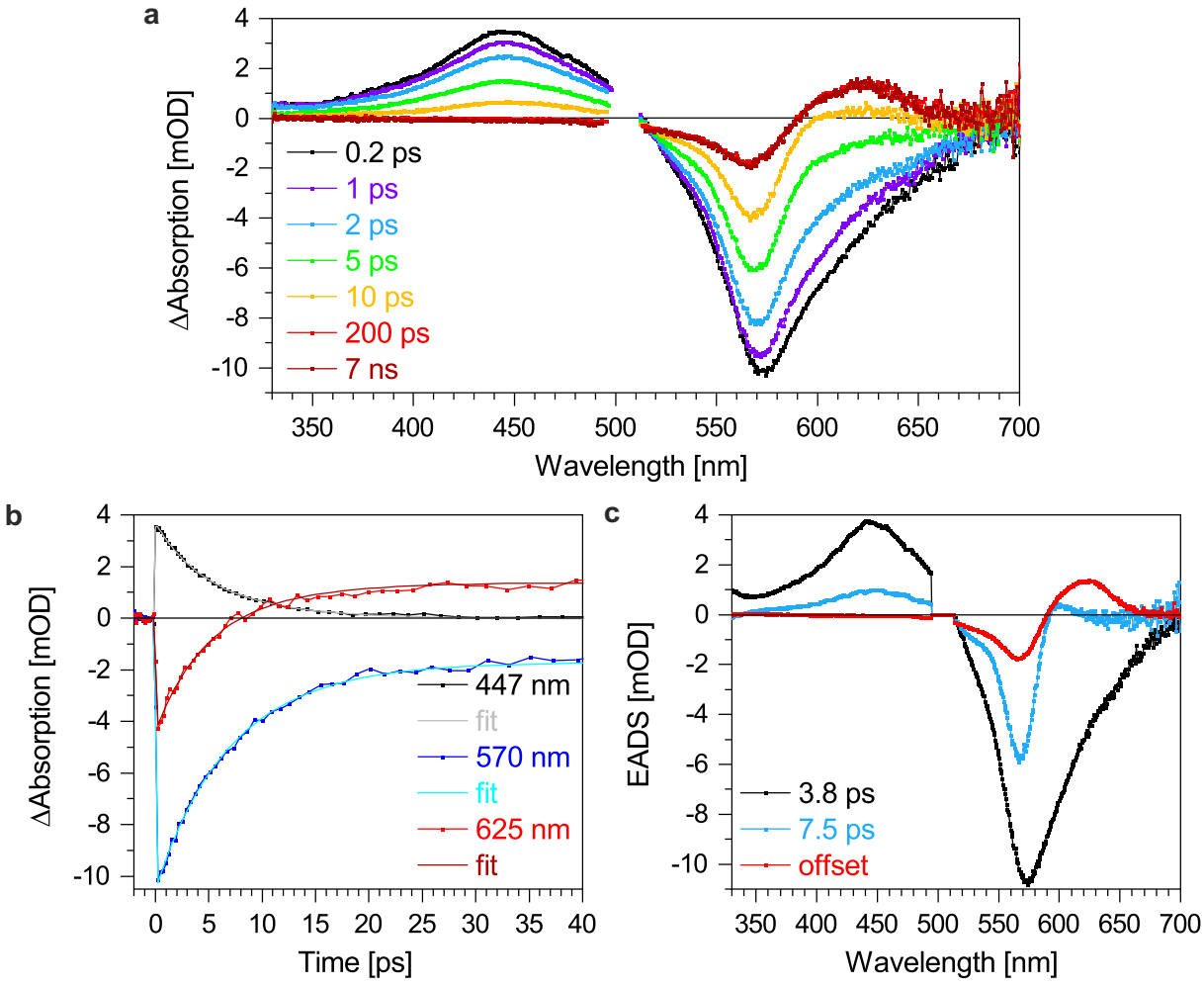

Figure 5.18. TA data of DASA in Tol excited with light of a wavelength of 506 nm. (a) Chosen time traces, (b) selected wavelength traces with corresponding fits and (c) EADS as well as their time constants obtained by GA.

identity with the steady state absorption of DASA (figure 5.6) and a red-shifted SE. With increasing time delay, all three signals decay with the ESA and SE decaying to zero within around 50 and 8 ps, respectively. On the contrary, the GSB decays to a constant negative offset which is reached after about 70 ps. Since the overlapping GSB and the SE decay with different time constants, the maximum of the GSB undergoes a blueshift towards around 565 nm with increasing time delay. At later times, a positive ESA emerges at about 625 nm approaching its maximum intensity after around 60 ps. The constant positive and negative offsets show the formation of the *E*-DASA photoproduct being stable much longer than the experimental period of about 8 ns.
GA of the TA data (figure 5.18**b**) results in two time constants τ_i of (3.8 ± 0.2) and (7.5 ± 0.2) ps as well as an offset (figure 5.18**c**). Comparing the determined time constants and EADS to the results upon addressing DASA with the orthogonal switching wavelength, the same excited state dynamics upon photoexcitation to S_1 happen (paragraph Switching DASA orthogonally, this section). The S_1 state is thereby witnessed by its absorption at around 447 nm. The ESA at about 600 nm found in the blue EADS refers to the *E*-DASA photoproduct in the electronic ground state but in higher vibrational levels with the absorption shifting to 625 nm after vibrational relaxation.
Comparing the results to the *Z*-to-*E* isomerisation of DASA in Tol but excited with 582 nm (figure 5.14), no significant changes in the spectral shape and dynamics are observed. However, the excited state dynamics are accelerated using higher energy light to induce switching. Thus, the lifetimes by excitation with 506 nm are shortened by 0.5 and 1.7 ps, respectively.
Finally, the excited state dynamics and interactions of a 1:1 molar ratio of Azo and DASA in Tol are investigated when both are switched simultaneously (figure 5.19**a**). At early times, several signals are observed. The short-wavelength region of the spectrum is dominated by a positive ESA of symmetric spectral shape located at about 447 nm. At longer wavelengths, an asymmetric shaped negative feature at around 570 nm is observed which bears two close features. Comparing the spectral range with the steady state absorption spectra of Azo and DASA (figures 5.5 and 5.6), the signal at about 570 nm can be identified as the GSB of DASA and thus, the bathochromically shifted signal as SE. With increasing time delay, the ESA in the short-wavelength region decays within around 12 ps to zero while the SE approaches zero in about 8 ps. The GSB decreases to a constant negative offset reached after around 60 ps. Due to the different decay times of the overlapping GSB and SE, the maximum position of the GSB undergoes a hypsochromic shift with the maximum intensity at later times found at about 565 nm. At later times, three new signals emerge with two positive features located at around 365 and 625 nm as well as one negative feature found at about 440 nm. The ESA at about 365 nm reaches its maximum intensity at around 52 ps while the ESA located at around 625 nm obtains its maximum after about 60 ps. The negative

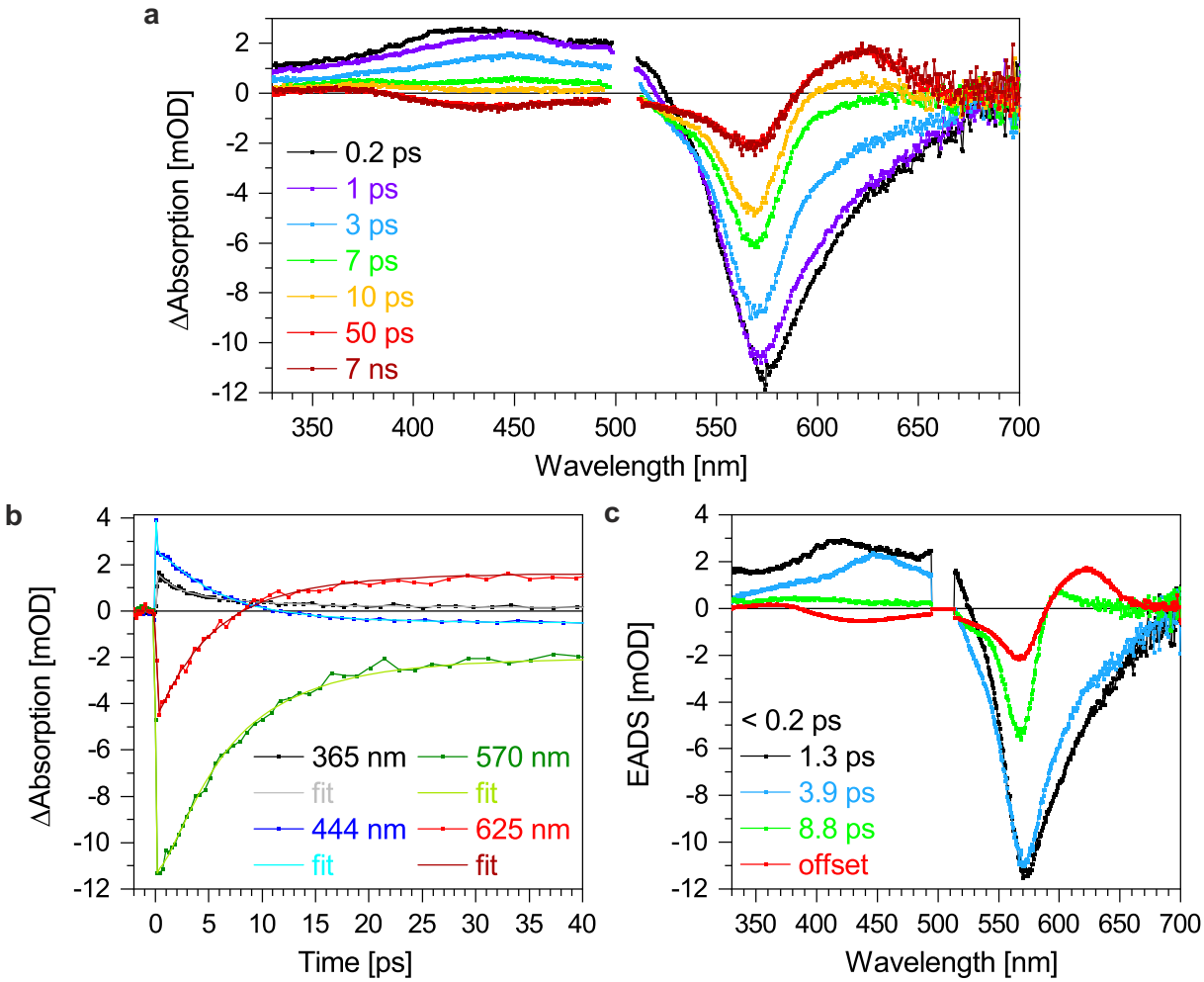

Figure 5.19. TA data of Azo and DASA in Tol simultaneously excited with light of a wavelength of 506 nm. (a) Chosen time traces, (b) selected wavelength traces with corresponding fits and (c) EADS as well as their time constants obtained by GA. The EADS of the short time constant being below the resolution of the laser setup is not shown since this EADS is not separable from the pump-probe artefact.

feature at about 440 nm identified as GSB of Azo by comparison with the steady state absorption spectra of the involved molecules (figures 5.5 and 5.6) reaches a constant negative offset after around 70 ps. Hence, the data reveal four constant offsets with two negative and two positive features indicating two successful switching processes of *trans*-Azo to *cis*-Azo and *Z*-DASA to *E*-DASA creating two photoproducts being stable much longer than the experimental period of about 8 ns.

Fitting the TA data with a global fit (figure 5.19**b**), four time constants τ_i of (< 0.2 ± 0.2), (0.9 ± 0.2), (3.9 ± 0.2) and (8.8 ± 0.2) ps as well as an offset are obtained (figure 5.19**c**). Furthermore, several features are present in the EADS. In order to elucidate the excited state dynamics, it is necessary to compare the spectral features and lifetimes with the data of the single components (figures 5.17 and 5.18). By doing so, a clear picture emerges.

The signals at early times, namely the ESA at about 447 nm as well as the GSB and the SE located at around 570 nm, can be related to the DASA switching process. It

may seems puzzling that no Azo signature is observed at early times. However, one has to keep in mind that the Azo and DASA mixture was holds a 1:1 molar ratio to maximise possible interactions. However, by comparing the intensities of the single photoswitches, the Azo signals are clearly less intense than the DASA features (figure 5.17 and 5.18). Thus, the DASA signals henpeck the spectrally overlapping Azo features at early times. At later times, the absorption of DASA molecules in the S_1 state found at around 447 nm decay and the formation of the photoproduct *E*-DASA is witnessed by its absorption at around 625 nm. With increasing time delay and decreasing intensity, however, the GSB of *trans*-Azo and the ESA of the photoproduct *cis*-Azo are observed once their intensities in the relevant spectral windows are higher compared to the DASA signals. The same holds true for the determined EADS which consist of Azo and DASA features. In summary, all obtained spectral signatures can be attributed to the single photoswitches with no additional features noticed. Having a glance at the found lifetimes, they can be attributed to the single photoswitches as well. The shortest two time constants of below 0.2 ps and 1.3 ps are clearly related to the Azo excited state dynamics with the second lifetime being slightly extended by 0.4 ps in comparison with the pure Azo solution. The third time constant of 3.9 ps is assigned to both photoswitches as both exhibit this lifetime within the experimental error. The fourth time constant is attributed to DASA switching also being increased by 1.3 ps in comparison to the pure DASA solution. Hence, both photoswitches show independent photoswitching with the same excited state dynamics present.

5.3.2. Polar solutions using acetonitrile

In contrast to the aforementioned measurements, the non-polar solvent Tol is substituted by the aprotic polar solvent MeCN in the following section. Changing the environment and especially the polarity may have a huge impact on the switching properties and the underlying excited state dynamics.[264] [265]

Since Azo shows positive solvatochromism (figure 5.5) and DASA exhibits negative solvatochromism (figure 5.6) causing a spectral narrowing of the absorption of their mixture (figure 5.7), the excitation wavelengths have to be adapted. Thus, photoswitching of Azo is induced by excitation with light of a wavelength of 415 nm (trans-to-cis) while light of a wavelength of 379 nm is used for backswitching (cis-to-trans). DASA photoswitching is stimulated by light using a wavelength of 582 nm (*Z*-to-*E*) and photoswitching of both molecular switches is excited by 510 nm light (*trans*-Azo to *cis*-Azo and *Z*-DASA to *E*-DASA). Orthogonal switching is verified by photoexciting Azo with 582 nm and DASA with 379 and 415 nm, both in the non-switched and switched state, resulting in no TA signal beside the pump-probe dispersion and in some cases artefacts due to the LED generating the switched species (UV/VIS spectra of all used LEDs in figure B.1 appendix B). Moreover, TA test measurements were performed by switch-

ing Azo while the LED inducing switching of DASA and switching DASA while the LED inducing switching of Azo were turned on. In some cases, the LED caused artefacts which was accounted for in the measurements investigating the switching of Azo when switched DASA is present and the switching of DASA when switched Azo is present.

Switching Azo orthogonally

Several negative and positive signals are observed in the TA data when exciting Azo in MeCN with 415 nm to induce photoswitching (figure 5.20**a**). The negative feature located at around 450 nm represents the GSB as it resembles the steady state absorption (figure 5.5). At early times, the GSB is narrowed compared to the steady state absorption due to ESAs at its short and long wavelength side. At later times with decaying ESAs, the GSB broadens such that the spectral shape of the GSB equals the spectral width of the steady state absorption. The GSB decays within 21 ps to a constant neg-

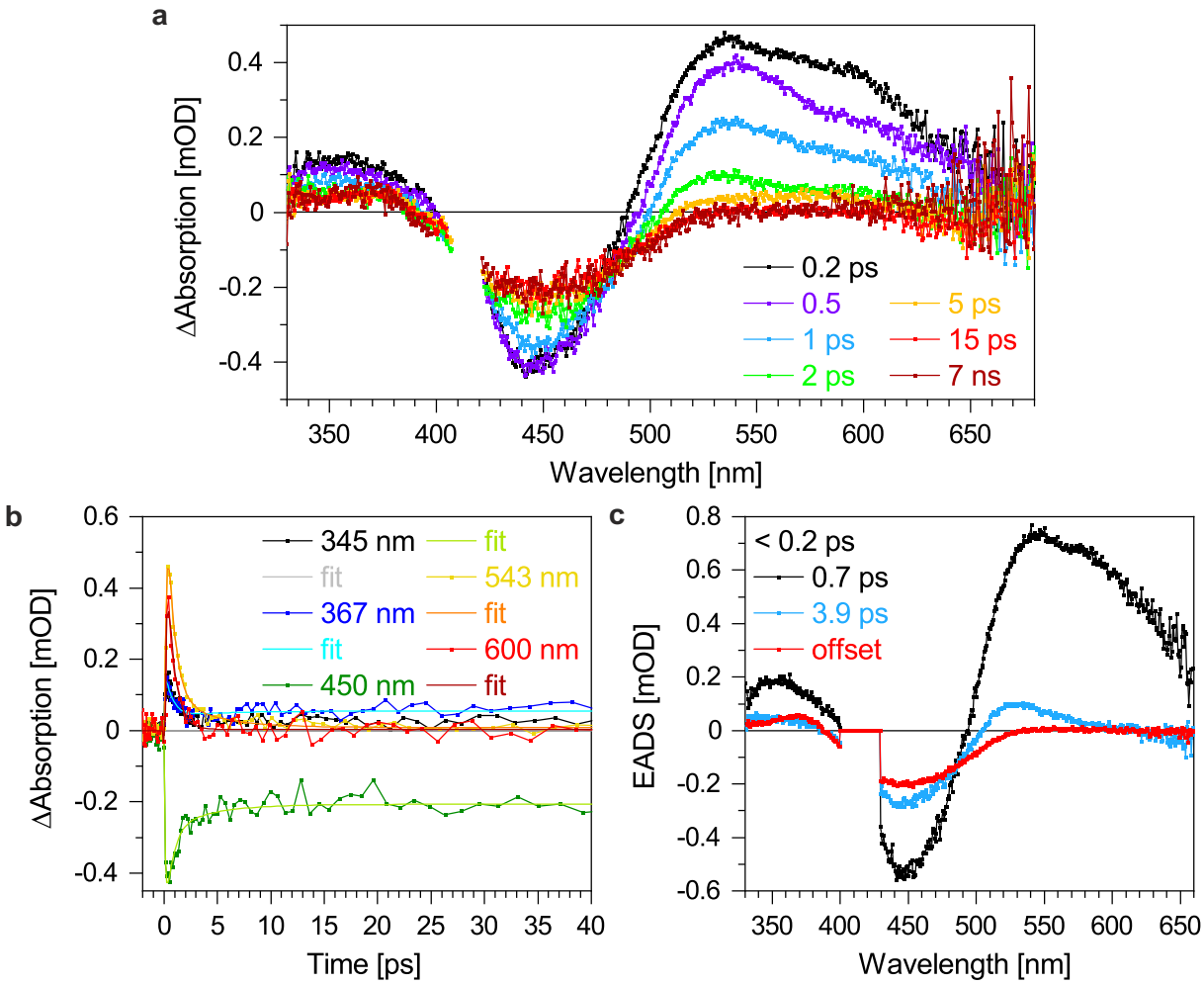

Figure 5.20. TA data of Azo in MeCN excited with light of a wavelength of 415 nm. (a) Chosen time traces, (b) selected wavelength traces with corresponding fits and (c) EADS as well as their time constants obtained by GA. The EADS of the short time constant being below the resolution of the laser setup is not shown since this EADS is not separable from the pump-probe artefact.

ative offset as not all excited molecules return to the *trans*-Azo ground state within the ca. 8 ns experimental delay time. Beside the negative signal, four positive ESAs are present at early times with two being in the UV range and two being red-shifted compared to the GSB. The ESAs are at about 345, 367, 543 and 600 nm. The latter two ESAs decay within about 27 and 5 ps, respectively, while the ESA located at around 345 nm decays within around 19 ps. The behaviour of the ESA at about 367 nm is different as the signal decays within ca. 3 ps to a minimum and slightly rises to a constant positive offset which is reached in around 17 ps. This ESA is attributed to *cis*-Azo successfully generated upon photoswitching. The assignment is validated by the spectral overlap, particularly at the short-wavelength side, of the ESA and the steady state absorption feature caused by photoswitching (figure 5.5). The *cis*-isomer is stable much longer than the experimental period of about 8 ns as the signal constitutes a constant offset to the data.

GA (figure 5.20**b**) results in three time constants τ_i of (< 0.2 ± 0.2), (0.7 ± 0.2) and (3.9 ± 0.2) ps as well as an offset (figure 5.20**c**). The lifetimes fit to the excited state dynamics found in Tol (section 5.3.1, detailed description in paragraph Switching Azo orthogonally). Hence, after excitation to S_2 conical intersection from $S_2 \rightarrow S_1$ takes place in below 0.2 ps with the absorption of the S_1 state observed at about 600 nm. Next, the S_0 state is populated within 0.7 ps witnessed by the ESA at approximately 543 nm caused by *trans*-Azo but in higher vibrational levels. Lastly, vibrational relaxation occurs in 3.9 ps to form the photoproduct *cis*-Azo in its electronic and vibrational ground state absorbing at about 367 nm.

Comparing the results with the outcomes of switching Azo in the non-polar solvent Tol (figure 5.8), the excited state dynamics upon photoswitching remain the same. However, the photoswitching is accelerated in MeCN manifesting in a decrease of 0.5 and 0.8 ps from 1.2 and 4.7 ps in Tol to 0.7 and 3.9 ps in MeCN, respectively. In addition, spectral shifts occur as a consequence of increased polarity of the environment. In general, all signals exhibit a bathochromic shift with some signals being only slightly affected but others being shifted by about 13 nm.

By adding DASA in a 1:1 molar fashion to Azo, the general signals found in the TA data upon photoswitching remain the same (figure 5.21**a**). Four positive signals, attributed to ESAs located at around 345, 367, 543 and 600 nm are found as well as a negative signal at about 450 nm. The latter refers to the GSB decaying not to zero but to a constant negative offset as part of the molecules are successfully photoswitched from *trans*-Azo to *cis*-Azo exhibiting an ESA at around 367 nm which adds as constant offset to the data.

Applying a GA to the TA data (figure 5.21**b**), time constants τ_i of (< 0.2 ± 0.2), (0.8 ± 0.2) and (3.3 ± 0.2) ps as well as an offset are obtained (figure 5.21**c**). Hence, the overall excited state dynamics upon photoswitching Azo remain unaltered but the time con-

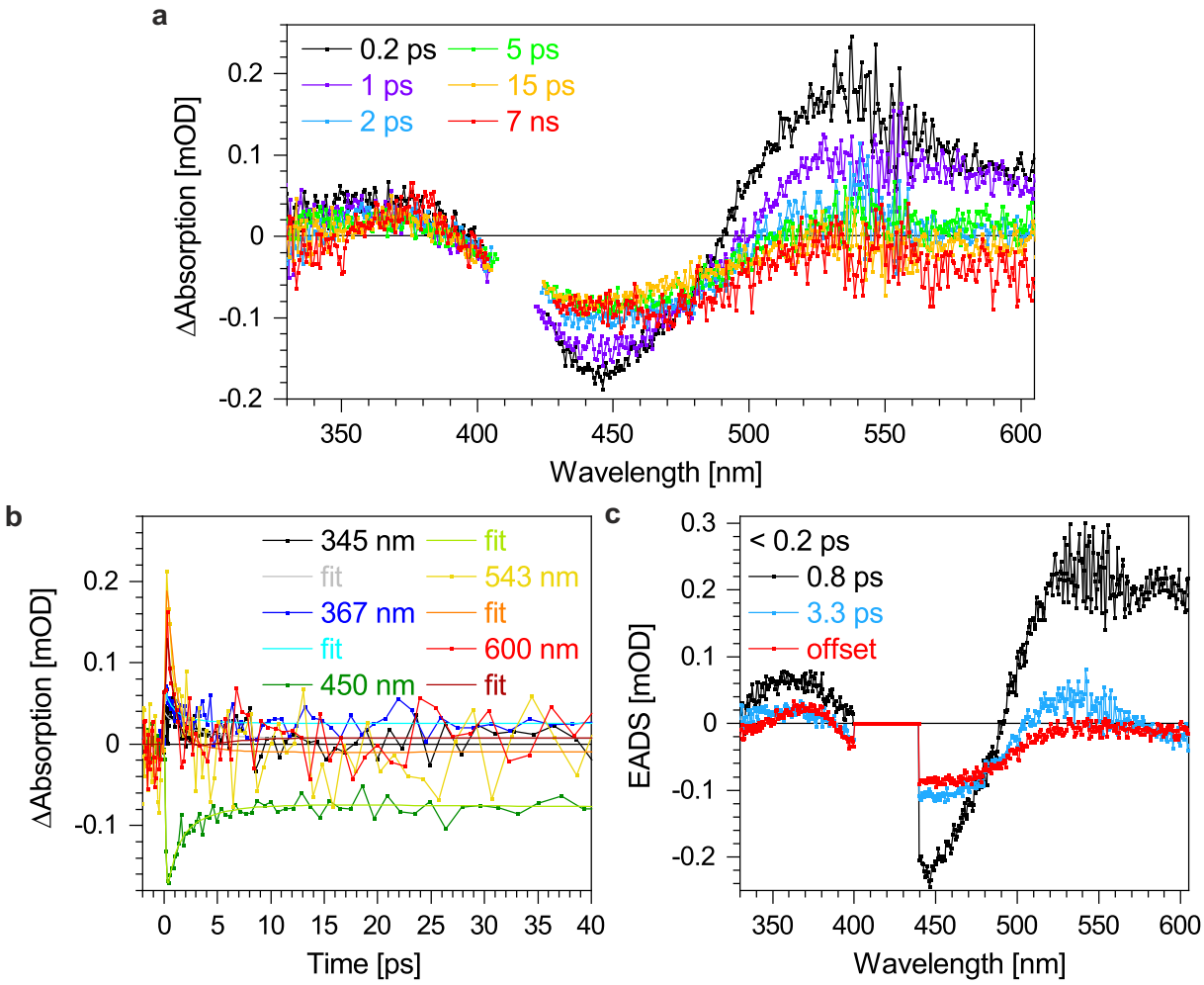

Figure 5.21. TA data of Azo in MeCN excited with light of a wavelength of 415 nm while DASA is present. (a) Chosen time traces, (b) selected wavelength traces with corresponding fits and (c) EADS as well as their time constants obtained by GA. The EADS of the short time constant being below the resolution of the laser setup is not shown since this EADS is not separable from the pump-probe artefact.

stant of the vibrational cooling is shortened in the presence of DASA by 0.5 ps compared to pure Azo in MeCN.

In the next step, the interaction and influence of switched DASA on the switching properties of Azo are studied. Therefore, an LED with maximum intensity at a wavelength of around 594 nm is used to promote DASA into its closed state. However, the cross section is smaller compared to switching in Tol such that about 5 % of DASA in MeCN is converted into the closed isomer **C'** (figure B.3**b** appendix B). Nevertheless, it could have an impact on the switching behaviour of Azo.

Hence, the mixture was illuminated several minutes before the TA experiment and the illumination was also kept on during the measurement to ensure a photostationary state. The TA data reveals that five signals are present of which the negative signal at around 450 nm refers to the GSB while the four positive features located at about 345, 367, 543 and 600 nm represent ESAs (figure 5.22**a**). Within some picoseconds,

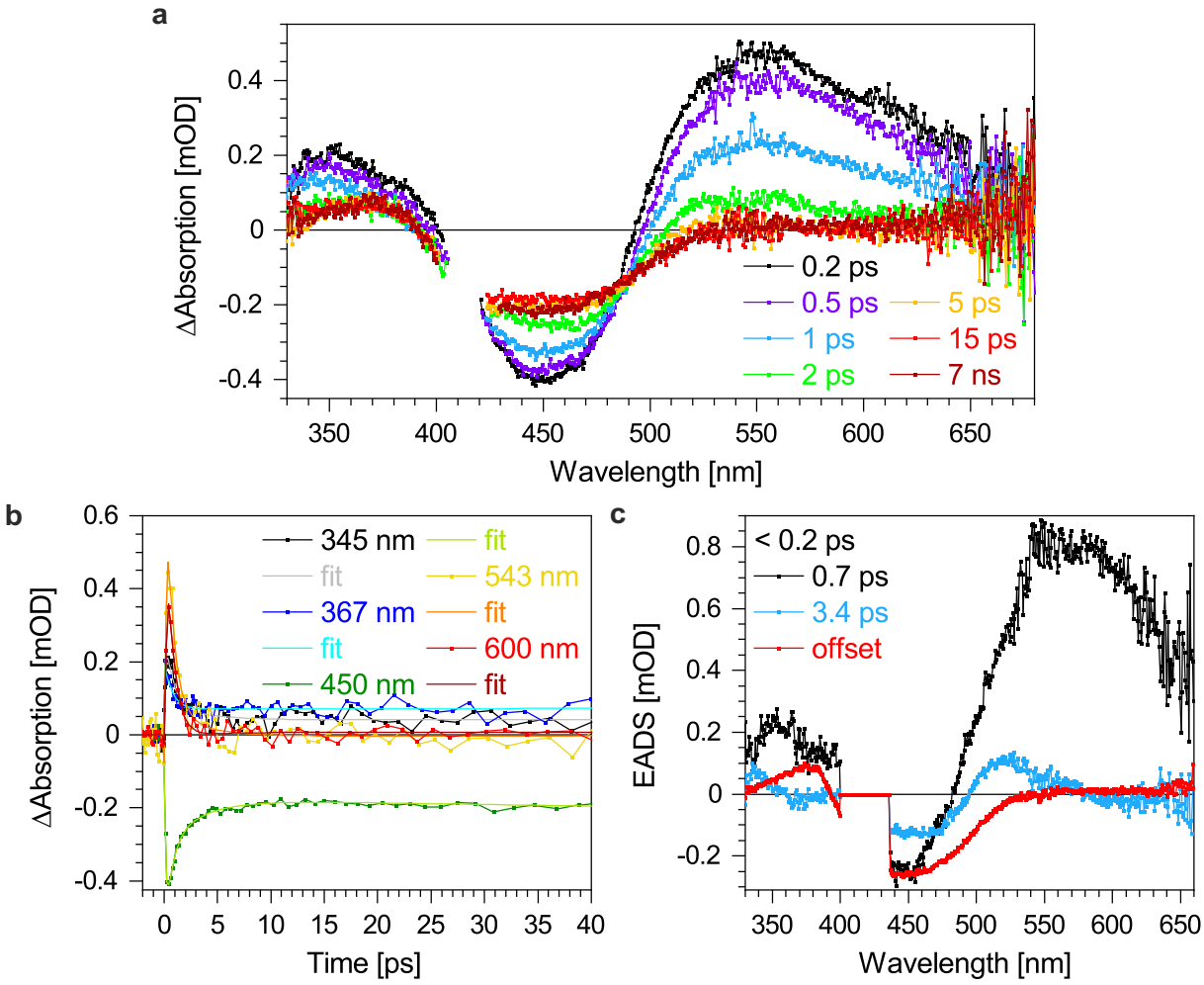

Figure 5.22. TA data of Azo in MeCN excited with light of a wavelength of 415 nm while switched DASA is present due to irradiation with an LED with maximum intensity at a wavelength of 594 nm. (a) Chosen time traces, (b) selected wavelength traces with corresponding fits and (c) EADS as well as their time constants obtained by GA. The EADS of the short time constant being below the resolution of the laser setup is not shown since this EADS is not separable from the pump-probe artefact.

all signals decay to their final value with the GSB staying at a constant negative ΔA indicating that a specific amount of molecules is switched to the cis isomer exhibiting an ESA at around 367 nm.

GA describes the TA data (figure 5.22**b**) with three time constants τ_i of (< 0.2 ± 0.2), (0.7 ± 0.2) and (3.4 ± 0.2) ps as well as an offset (figure 5.22**c**). Thus, the excited state dynamics are similar to the prior TA experiment (figure 5.21) with no changes due to the presence of 5 % *E*-DASA.

Backswitching Azo photochemically

In turn, the photochemical backswitching to induce cis-to-trans isomerisation of Azo in MeCN provides four positive and two negative signals (figure 5.23**a**). Prior to the TA experiment, the *cis*-Azo solution in MeCN was prepared by LED illumination prior

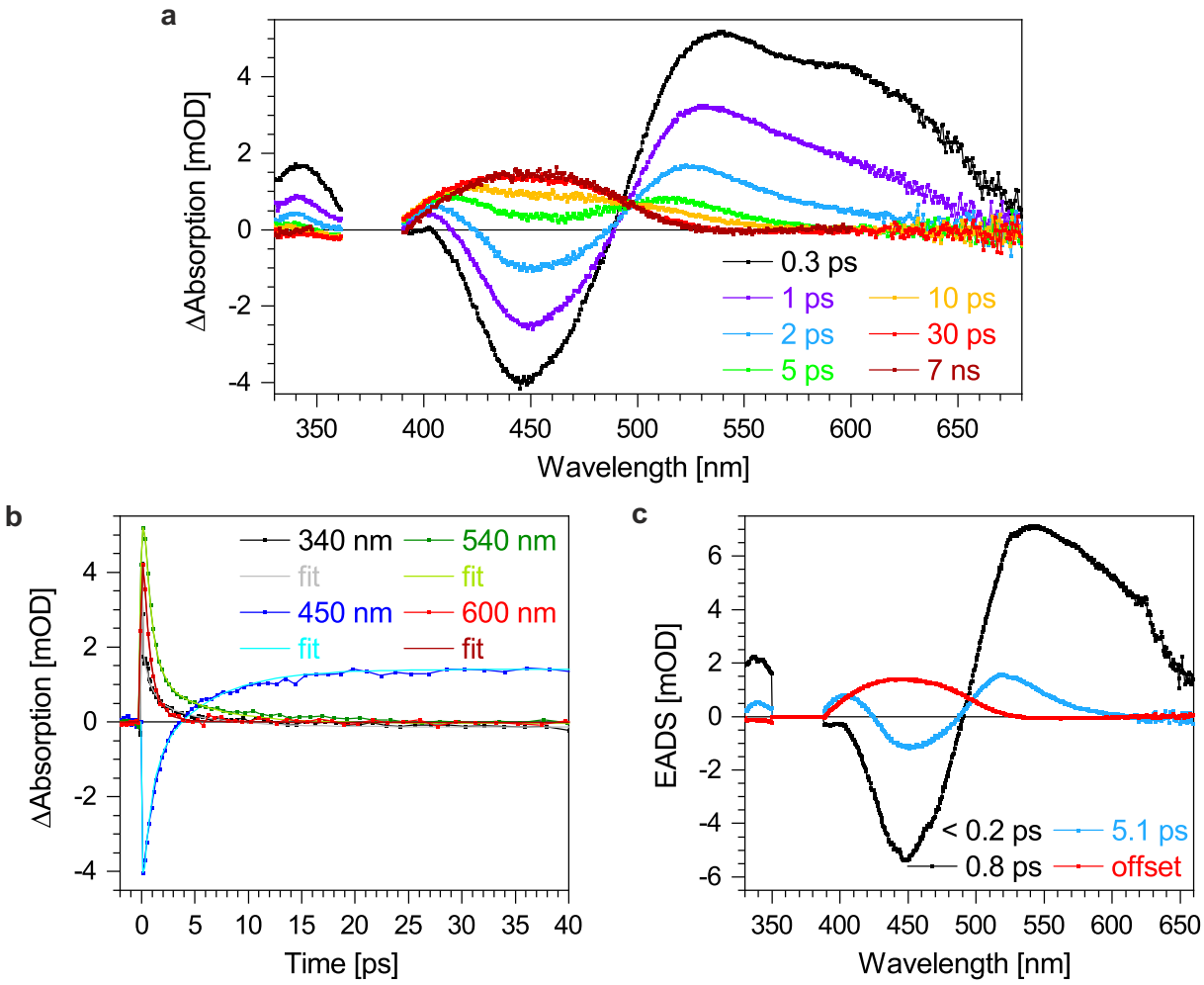

Figure 5.23. TA data of Azo in MeCN excited with light of a wavelength of 379 nm to induce backswitching (cis-to-trans). (a) Chosen time traces, (b) selected wavelength traces with corresponding fits and (c) EADS as well as their time constants obtained by GA. The EADS of the short time constant being below the resolution of the laser setup is not shown since this EADS is not separable from the pump-probe artefact.

and during the TA measurement to maintain a photostationary state with the maximum intensity of the LED being at about 409 nm. In MeCN, the cross section is smaller such that by mimicking the geometric conditions of the TA experiment, 25 % of the Azo molecules are switched to the cis-isomer according to UV/VIS experiments (figure B.4**b** appendix B).

In the TA data, the negative features located at around 370 and 445 nm refer to bleaching of the ground states of *cis*-Azo and initially present *trans*-Azo, respectively. The GSB at about 370 nm is observed at its short-wavelength side but the main part is cut off due to huge scattering of the pump pulse overlapping with the GSB.

The excitation wavelength was shortened by 20 nm to 359 nm in another TA experiment to check whether the huge scattering is due to a resonant frequency. However, this did not increase the data quality but even more data points had to be cut off due to scattering of the pump pulse.

As indicated by the traces of long delay times (figure 5.23), the GSB of *cis*-Azo decays not to zero but stops at a constant negative offset as part of the molecules do not return to the initial ground state within the experimental period of around 8 ns. The GSB located at the ground state absorption of *trans*-Azo decays to zero within 4 ps. Three ESAs are observed at early times located at around 340, 540 and 600 nm which decay to zero in about 29, 30 and 28 ps, respectively. The ESA at around 540 nm undergoes a blueshift with increasing time delay due to the decay of the ESA at about 600 nm. The third ESA emerges at early times on the short-wavelength side of the negative feature at around 445 nm and undergoes a bathochromic shift from 402 to 450 nm during its rise due to the simultaneous decay of the negative signal. It reaches a positive final value at 33 ps staying constant over the whole remaining experimental period. Hence, this absorption represents the absorption of the photoproduct *trans*-Azo.
According to GA (figure 5.23**b**), the TA data is described by three time constants τ_i of (< 0.2 ± 0.2), (0.8 ± 0.2) and (5.1 ± 0.2) ps as well as an offset (figure 5.23**c**). Comparing the outcomes of the GA to the results of Azo backswitching in Tol (paragraph Backswitching Azo photochemically, section 5.3.1), the dynamics and species involved remain the same such that the same sequence after S_2 excitation applies. Thus, the ESA located at about 600 nm refers to the S_1 state populated in below 0.2 ps through conical intersection. The electronic ground state is reached via conical intersection within 0.8 ps but in higher vibrational levels with *trans*-Azo absorbing at around 530 nm. The final absorption at about 450 nm occurs after vibrational relaxation with a time constant of 5.1 ps. An isosbestic point at around 497 nm indicates complete conversion of vibrationally excited *trans*-Azo to *trans*-Azo in its electronic and vibrational ground state. Summarised, *cis*-Azo was switched to *trans*-Azo which is confirmed by the signals composing the offset, namely the GSB of the Azo molecules not returning to the cis-state thus resulting in a negative GSB at about 370 nm and the ESA of the trans photoproduct absorbing at around 450 nm. The negative signal at early times at about 445 nm is due to incomplete trans-to-cis conversion prior to the experiment.
In contrast to Tol, the $S_1 \rightarrow S_0$ conical intersection and the vibrational relaxation in MeCN is accelerated by 0.5 and 2.2 ps, respectively.
Conducting the same experiment but with a 1:1 molar mixture of Azo and DASA in MeCN, it is harder to identify all signals (figure 5.24**a**). The GSB of *trans*-Azo, present due to incomplete trans-to-cis isomerisation prior to the experiment, is found at about 445 nm. The negative GSB of the cis-isomer located at around 370 nm is adumbrated at its short-wavelength side but its main part is cut off due to huge pump scattering. Three ESAs are easily identified at about 340, 540 and 600 nm. The ESA representing absorption of the photogenerated *trans*-Azo starts to emerge at around 400 nm at early times. Subsequently, it undergoes a redshift due to the decay of the negative signal at its long-wavelength side. At later times, it stops to shift at about 450 nm and exhibits a

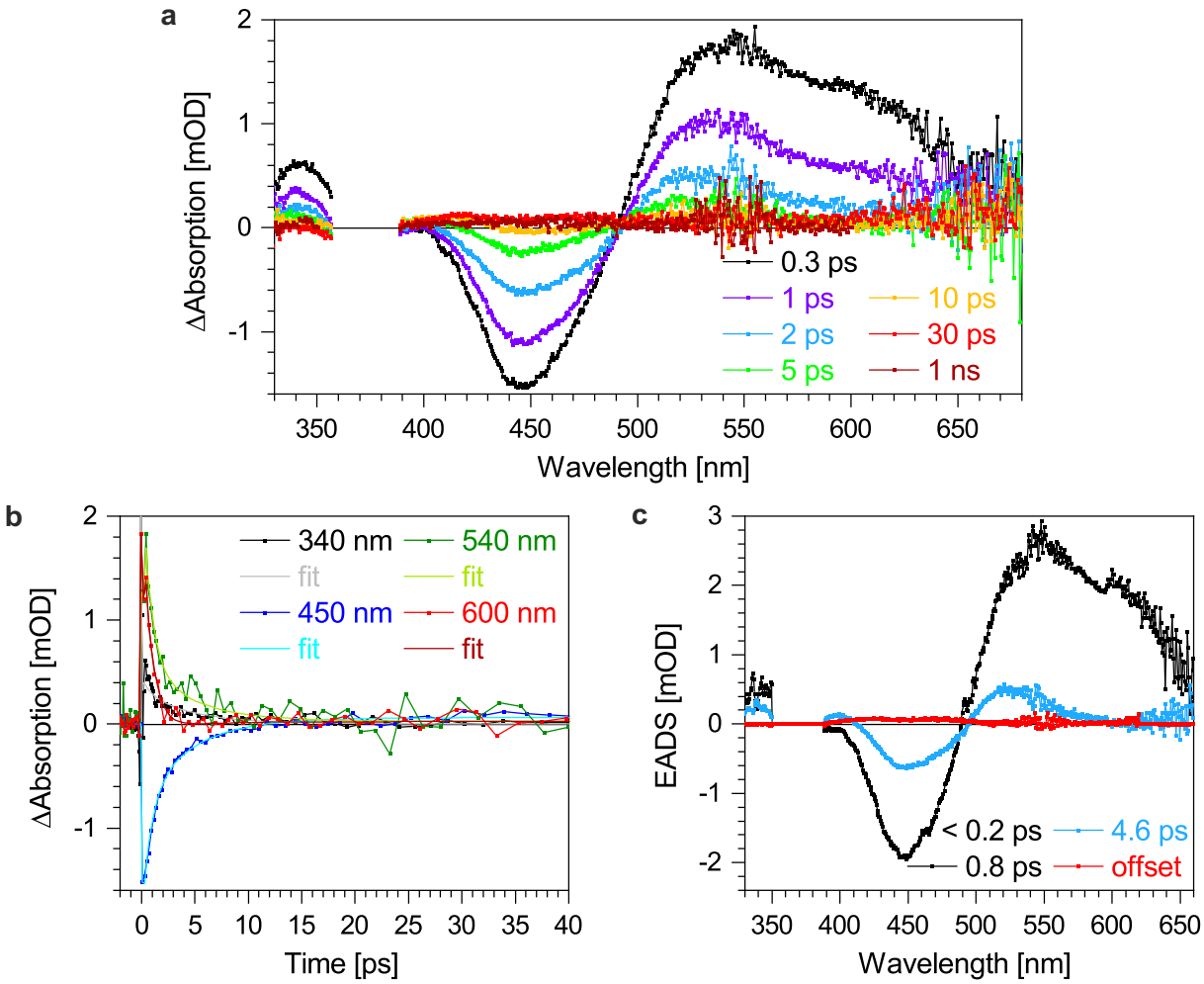

Figure 5.24. TA data of Azo in MeCN excited with light of a wavelength of 379 nm to induce backswitching while DASA is present. (a) Chosen time traces, (b) selected wavelength traces with corresponding fits and (c) EADS as well as their time constants obtained by GA. The EADS of the short time constant being below the resolution of the laser setup is not shown since this EADS is not separable from the pump-probe artefact.

positive signal since part of the cis-molecules are switched to the trans-isomer. However, the signal is little indicating a bad cross section for the backswitching in MeCN. GA (figure 5.24**b**) yields time constants τ_i of (< 0.2 ± 0.2), (0.8 ± 0.2) and (4.6 ± 0.2) ps as well as an offset (figure 5.24**a**). Comparing the results to the findings of photoswitching *cis*-Azo in MeCN without DASA (figure 5.23), the excited state dynamics upon photoexcitation stay unaltered and the lifetimes are the same except for the vibrational cooling shortened by 0.5 ps.

Next, the influence of switched DASA molecules in their closed-isomer structure **C'** on the switching behaviour of *cis*-Azo in MeCN was investigated. However, the pump laser beam, the LED for switching Azo radiating around 409 nm as well as the LED to induce DASA photoswitching having its maximum wavelength at 594 nm produced extreme scattering such that the data cannot be analysed. The same holds true for a control experiment without DASA being present in the mixture. However, due to the former

results, no change in excited state dynamics are expected compared to the *cis*-Azo and DASA mixture in MeCN.

Switching DASA orthogonally

Following, the switching properties and excited state dynamics of the *Z*-to-*E* (cis-to-trans) photoisomerisation of DASA in the aprotic polar solvent MeCN are investigated. At early times, two broad features are seen in the TA data (figure 5.25**a**). The positive signal located at around 445 nm is allocated to an ESA decaying to zero in about 38 ps. The broad negative signal, however, consists of two signals. On the one hand, GSB is observed at around 548 nm. This signal decays within about 60 ps to a constant negative offset. On the other hand, SE at around 602 nm decays to zero in about 8 ps. Due to the decay of the SE, the maximum of the GSB exhibits a hypsochromic shift. Interestingly, the GSB at early times is narrower compared to the steady state absorption but at later times, the spectral distribution matches. At later times, a positive

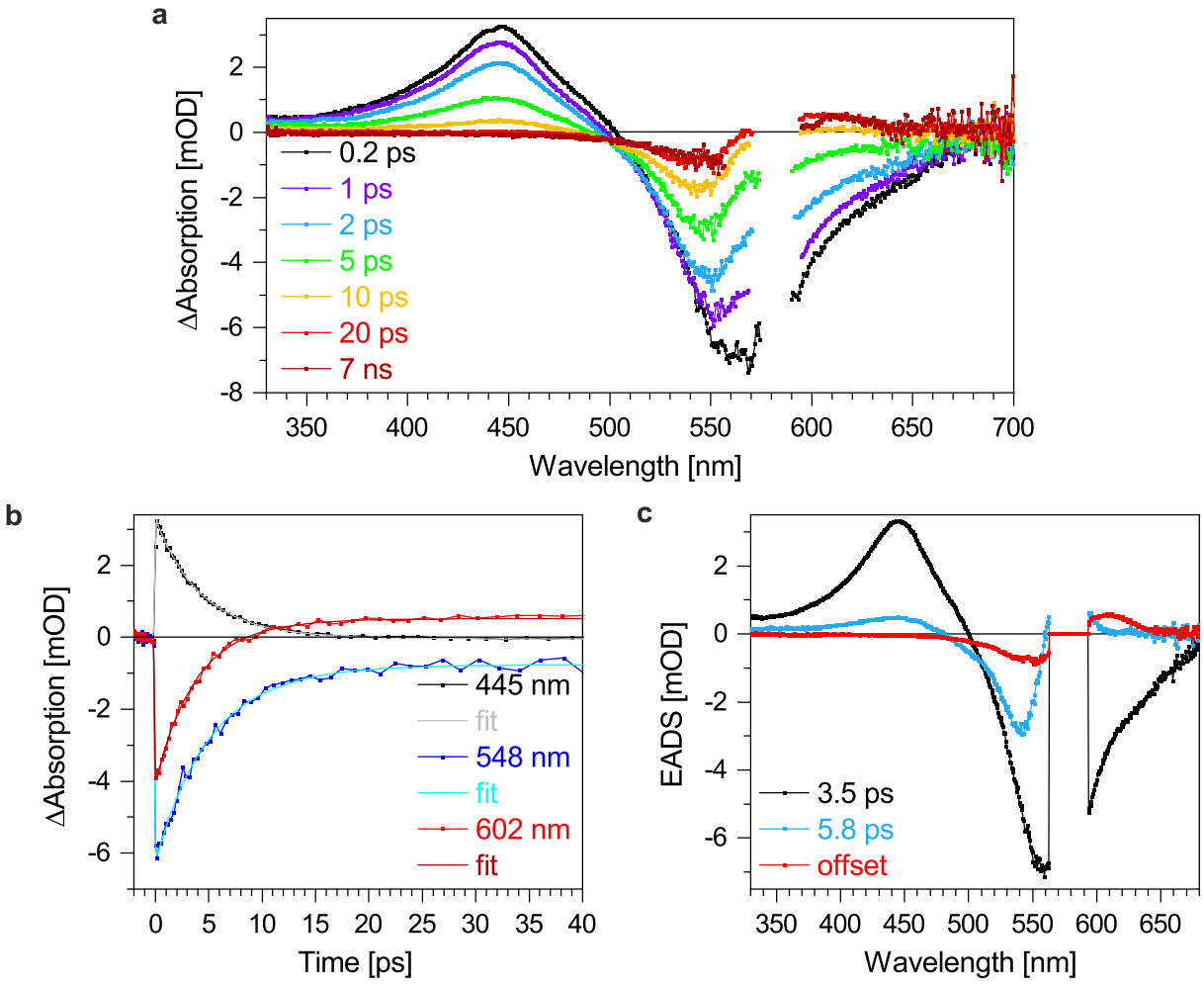

Figure 5.25. TA data of DASA in MeCN excited with light of a wavelength of 582 nm. (a) Chosen time traces, (b) selected wavelength traces with corresponding fits and (c) EADS as well as their time constants obtained by GA.

ESA arises at around 602 nm reaching a constant positive offset at about 42 ps. At the end of the experimental period of around 8 ns, part of the GSB as well as the red-shifted ESA remains. This reveals that part of the molecules is successfully switched from the *Z* ground state, absorbing at about 548 nm, to the *E* ground state, absorbing at around 602 nm. The remaining ESA can be identified as the photoproduct since its spectral position is only slightly shifted compared to the spectrum of *E*-DASA in Tol due to solvatochromism (figure 5.6).
GA (figure 5.25**b**) yields two lifetimes τ_i of (3.5 ± 0.2) and (5.8 ± 0.2) ps as well as an offset (figure 5.25**c**). The findings of photoswitching DASA in MeCN are similar to the excitation dynamics in the non-polar solvent Tol (section 5.3.1, detailed description in paragraph Switching DASA orthogonally). Hence, the S_1 state is observed by the ESA at about 445 nm which is depopulated generating *E*-DASA in the electronic ground state but in higher vibrational levels absorbing at around 575 nm as seen in the blue EADS. Due to vibrational cooling, the aforementioned signal undergoes a redshift to about 602 nm.
In comparison with the outcomes of the same experiment in Tol, the general signals, EADS and time constants remain similar. However, the latter are accelerated in MeCN by 0.8 and 3.4 ps, respectively. In addition, all signals are blue-shifted up to 22 nm due to negative solvatochromism.
By conducting a TA experiment with a 1:1 molar ratio of Azo and DASA in MeCN, the influence of Azo on switching DASA is studied (figure 5.26**a**). The TA data at early times contain a broad positive and negative signal. The positive signal at about 445 nm represents the ESA of the excited state. The negative signal consists of the GSB at around 548 nm and the SE being red-shifted compared to the GSB. With increasing time delay, the ESA and the SE decay to zero while the GSB undergoes a blueshift and decays to a constant negative ΔA value indicating that part of the molecules do not return to the initial state during the experimental period of about 8 ns. At later times, a new positive ESA emerges at around 602 nm. It reaches a constant offset representing the absorption of the *E*-DASA photoproduct.
The TA data is fitted by GA (figure 5.26**b**) resulting in two time constants τ_i of (3.3 ± 0.2) and (5.3 ± 0.2) ps as well as an offset (figure 5.26**c**). By contrasting the lifetimes and EADS with the findings of switching DASA without Azo being present (figure 5.25), the signal traces and excited state dynamics are unaltered but the second lifetime decreases by 0.5 ps when Azo is present.

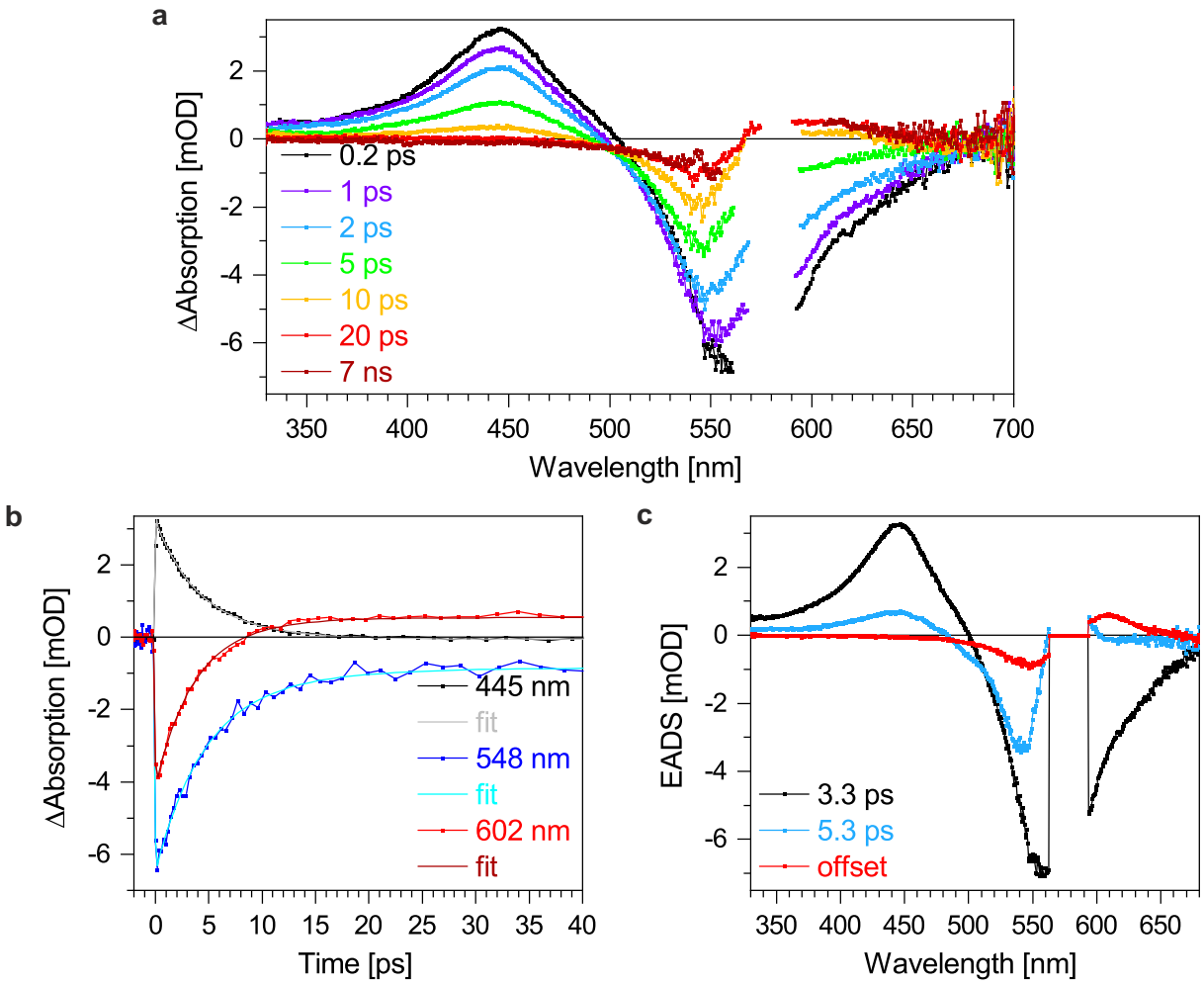

Figure 5.26. TA data of DASA in MeCN excited with light of a wavelength of 582 nm while Azo is present. (a) Chosen time traces, (b) selected wavelength traces with corresponding fits and (c) EADS as well as their time constants obtained by GA.

To complete the study about the excited state dynamics of DASA in MeCN, the influence of switched Azo is explored by TA measurements (figure 5.27**a**). To generate switched *cis*-Azo, the mixture is illuminated with an LED several minutes prior as well as during the experiment to maintain a photostationary state of Azo. With the geometric conditions in the TA setup, 25 % *cis*-Azo is formed (figure B.4 appendix B). The TA data upon switching DASA compose of a broad positive signal at around 445 nm and a broad negative feature at longer wavelengths at early times. The negative signal actually consists of two signals of which one represents the GSB located at about 548 nm and a red-shifted SE. Upon increasing time delay, the ESA and the SE signal decay to zero. Simultaneously, the GSB decays but stops at a constant negative offset while undergoing a hypsochromic shift. The offset indicates successful switching of *Z*-DASA as part of the molecules do not return to the initial ground state. At later times, a positive ESA band arises at around 602 nm which is related to the absorption of the *E*-DASA photoproduct. As signalised by the constant positive offset, the photoproduct is stable longer than the experimental period of about 8 ns.

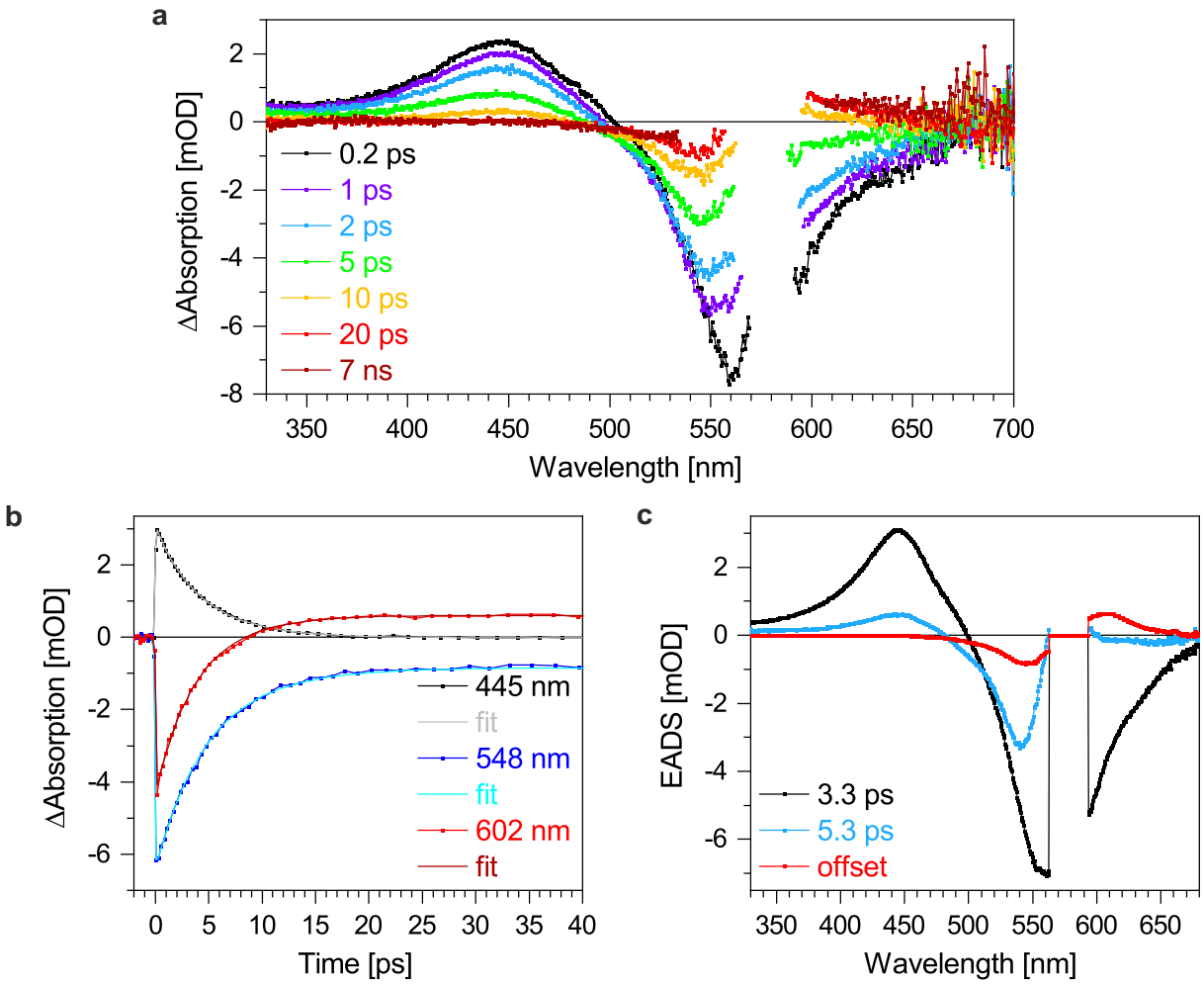

Figure 5.27. TA data of DASA in MeCN excited with light of a wavelength of 582 nm while switched Azo is present due to irradiation with an LED with maximum intensity at 409 nm. (a) Chosen time traces, (b) selected wavelength traces with corresponding fits and (c) EADS as well as their time constants obtained by GA.

The TA map is described with a global fit (figure 5.27**b**) resulting in two time constants τ_i of (3.3 ± 0.2) and (5.3 ± 0.2) ps as well as an offset (figure 5.27**c**). Hence, the lifetimes and EADS resemble the outcomes of the photoswitching of DASA in the presence of non-switched Azo (figure 5.26) resulting in the same excited state dynamics.

Switching Azo and DASA simultaneously

In order to finalise the studies on the switching behaviour of Azo and DASA in the aprotic polar solvent MeCN, simultaneous excitation of both photoswitches is left to research (*trans*-Azo to *cis*-Azo and *Z*-DASA to *E*-DASA). At first, the single photoswitches have to be measured in order to account for changes due to the different excitation wavelength.

Starting with Azo, several signals are present in the TA data upon switching with 510 nm light (figure 5.28**a**). At early times, the negative GSB occurs at about 450 nm. In ad-

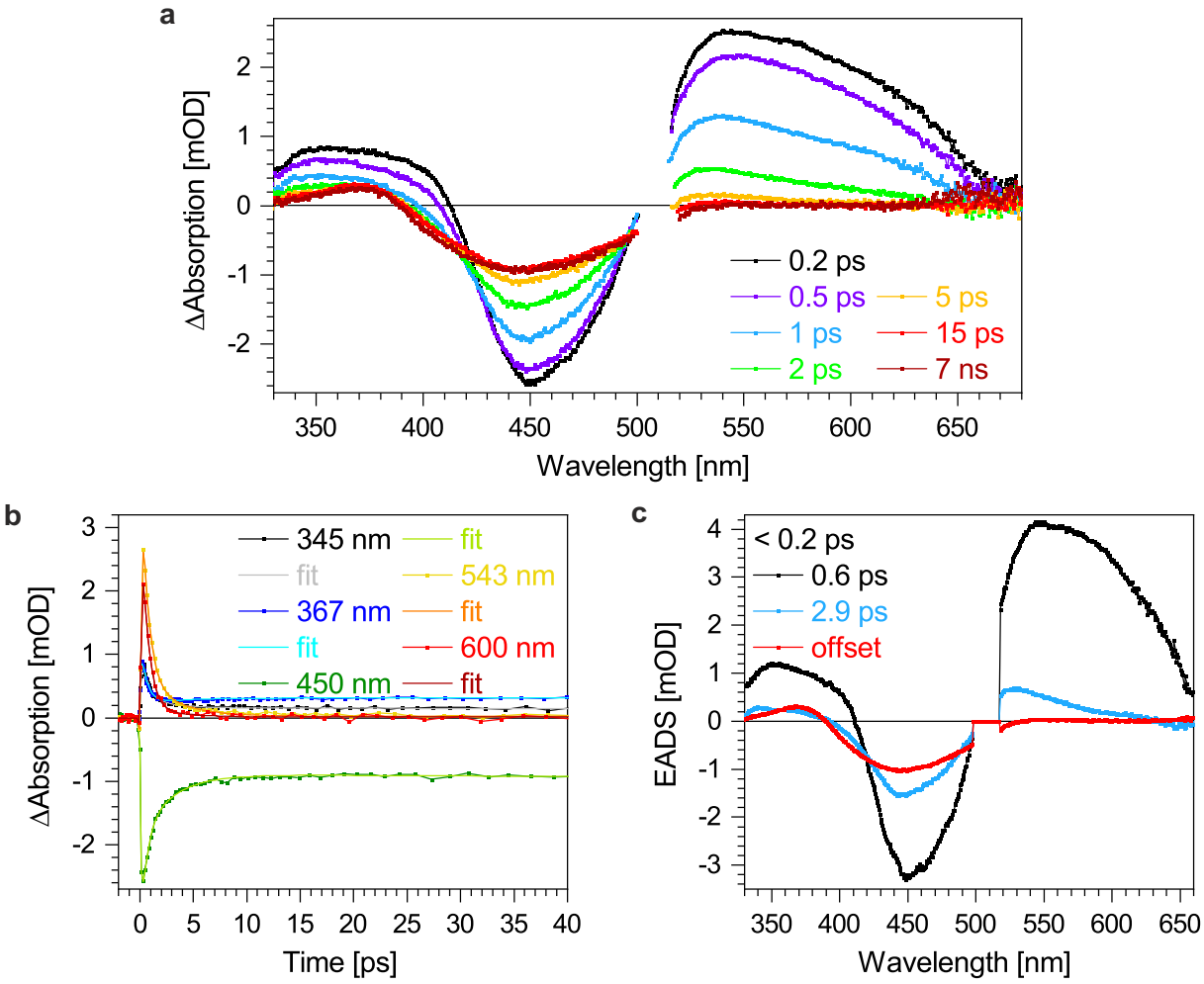

Figure 5.28. TA data of Azo in MeCN excited with light of a wavelength of 510 nm. (a) Chosen time traces, (b) selected wavelength traces with corresponding fits and (c) EADS as well as their time constants obtained by GA. The EADS of the short time constant being below the resolution of the laser setup is not shown since this EADS is not separable from the pump-probe artefact.

dition, four positive features located at around 345, 385, 543 and 600 nm emerge. As the two former and the two latter spectrally overlap, respectively, their exact spectral positions are difficult to determine. Having a closer look at the ESAs in the short-wavelength region, the trace at about 345 nm decays to zero within around 16 ps while the ESA at about 385 nm decays to a constant positive offset and simultaneously undergoes a blueshift towards around 367 nm. Due to the spectral overlap and the different decay times, the hypsochromic shift takes place. Analysing the trace at 367 nm, it reaches a minimum after about 3 ps and rises afterwards to a constant positive level which is reached after around 17 ps. Coincidently, the two ESAs located at about 543 and 600 nm decay in around 17 and 13 ps, respectively. Similar to the UV ESAs, the maximum of the ESA at about 543 nm hypsochromically shifts on account of the different lifetimes of the spectrally overlapping signals. The GSB in contrast, decays to a constant negative offset met after around 20 ps. Additionally, the GSB undergoes a slight blueshift and broadens due to the decay of the spectrally overlapping ESAs.

GA of the data (figure 5.28**b**) results in three time constants τ_i of (< 0.2 ± 0.2), (0.6 ± 0.2) and (2.9 ± 0.2) ps as well as an offset (figure 5.28**c**). Hence, the lifetimes and the obtained EADS fit to the excited state dynamics of Azo addressed orthogonally such that the same sequence after $\pi \rightarrow \pi^*$ takes place (paragraph Switching Azo orthogonally, this section). Hence, the S_1 state and the reached vibrationally excited ground state of *trans*-Azo are represented by their absorptions at around 600 and 543 nm, respectively. The remaining GSB of *trans*-Azo and the absorption of the photogenerated *cis*-Azo at about 367 nm display successful switching with the photoproduct being stable much longer than the experimental period of about 8 ns as indicated by the constant offset.
Comparing the received outcomes to the same trans-to-cis isomerisation but induced by 431 nm light, the signals at early times are slightly shifted towards longer wavelengths and the overlapping spectral features are harder to distinguish for the excitation with 510 nm. Furthermore, the second and third time constant is accelerated by 0.1 and 1.0 ps, respectively, by the latter excitation wavelength.
The TA data upon switching DASA in MeCN with 510 nm feature several signatures (figure 5.29**a**). At early times, an ESA at around 445 nm is observed which decays within about 37 ps to zero. At longer wavelengths, two negative features are obtained at around 548 and 583 nm with the former being identified as the GSB as in accordance with steady state absorption of *Z*-DASA (figure 5.6) and hence the latter is attributed to SE. While the GSB decays to a constant negative offset within about 44 ps, the SE decays to zero in around 8 ps. Due to the spectral overlap and the different lifetimes, the maximum position of the GSB undergoes a small hypsochromic shift with increasing time delay. At later times, an additional ESA appears first with its maximum pointing at around 580 nm and a long tail towards longer wavelengths. Later on, it exhibits a bathochromic shift to reach its final maximum intensity at around 602 nm. It reaches a positive constant value after about 32 ps. The negative and positive offset represent the successful switching of *Z*-DASA to *E*-DASA with the photoproduct being stable much longer than the experimental period of about 8 ns.
A GA of the present TA data (figure 5.29**b**) reveals two time constants τ_i of (4.1 ± 0.2) and (6.7 ± 0.2) ps as well as an offset (figure 5.29**c**). By comparing the determined lifetimes and EADS to the dynamics upon orthogonally addressing DASA (figure 5.25), the same excited state dynamics upon photoswitching apply (section 5.3.2, detailed description in paragraph Switching DASA orthogonally, section 5.3.1). Hence, the S_1 state populated upon photoexcitation is represented by the ESA at around 445 nm. The photoproduct *E*-DASA in its electronic ground state is observed first in higher vibrational levels by the peak located at about 575 nm in the blue EADS while the absorption shifts to about 602 nm after vibrational relaxation.
Drawing a comparison between the *Z*-to-*E* isomerisation of DASA in MeCN induced by 510 nm and 582 nm, the isomerisation is decelerated in the present case of excit-

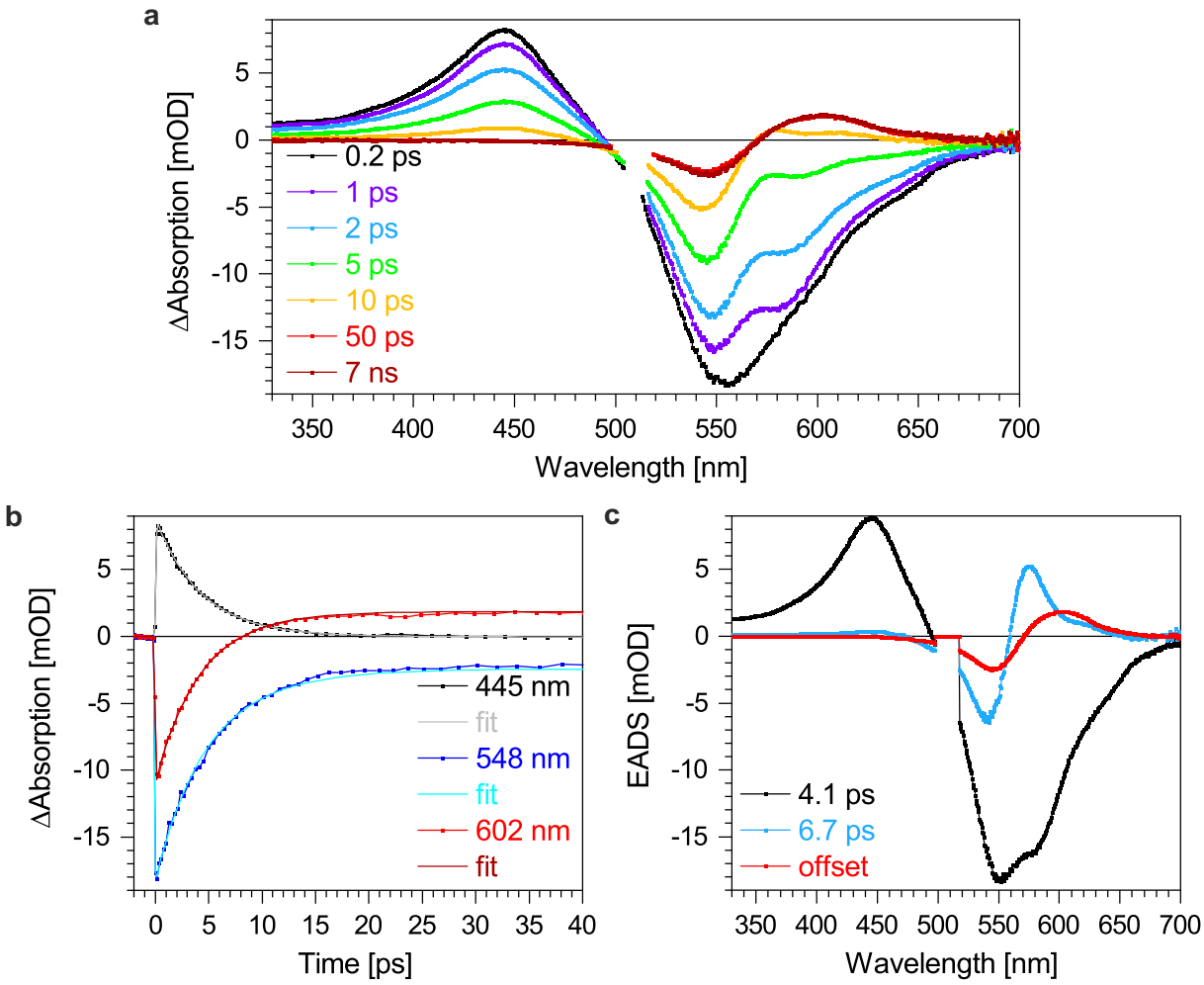

Figure 5.29. TA data of DASA in MeCN excited with light of a wavelength of 510 nm. (a) Chosen time traces, (b) selected wavelength traces with corresponding fits and (c) EADS as well as their time constants obtained by GA.

ing with 510 nm. More precisely, both time constants are extended by 0.6 and 0.9 ps, respectively.

To resolve the question about influences and interactions of Azo and DASA if both are excited simultaneously in a polar environment, a respective TA measurement was carried out with a 1:1 molar ratio of both photoswitches. The TA data comprise several features (figure 5.30**a**). At early times, the short-wavelength range of the spectrum is dominated by an ESA at about 445 nm. In the remaining part of the spectrum, however, two overlapping negative signals are observed at around 548 and 585 nm. According to steady state absorption measurements of *Z*-DASA (figure 5.6), the former is attributed to the GSB such that the latter is assigned to SE. With increasing pump-probe time delay, the ESA decays to zero in about 15 ps while the same process takes around 8 ps for the SE. In contrast, the GSB decays not to zero but stops at a constant negative value reached after about 42 ps while simultaneously slightly shifting to longer wavelengths. At later times, an emerging ESA dominates the spectrum. It first appears at around 580 nm exhibiting a long-wavelength tail. With increasing time delay, it shifts

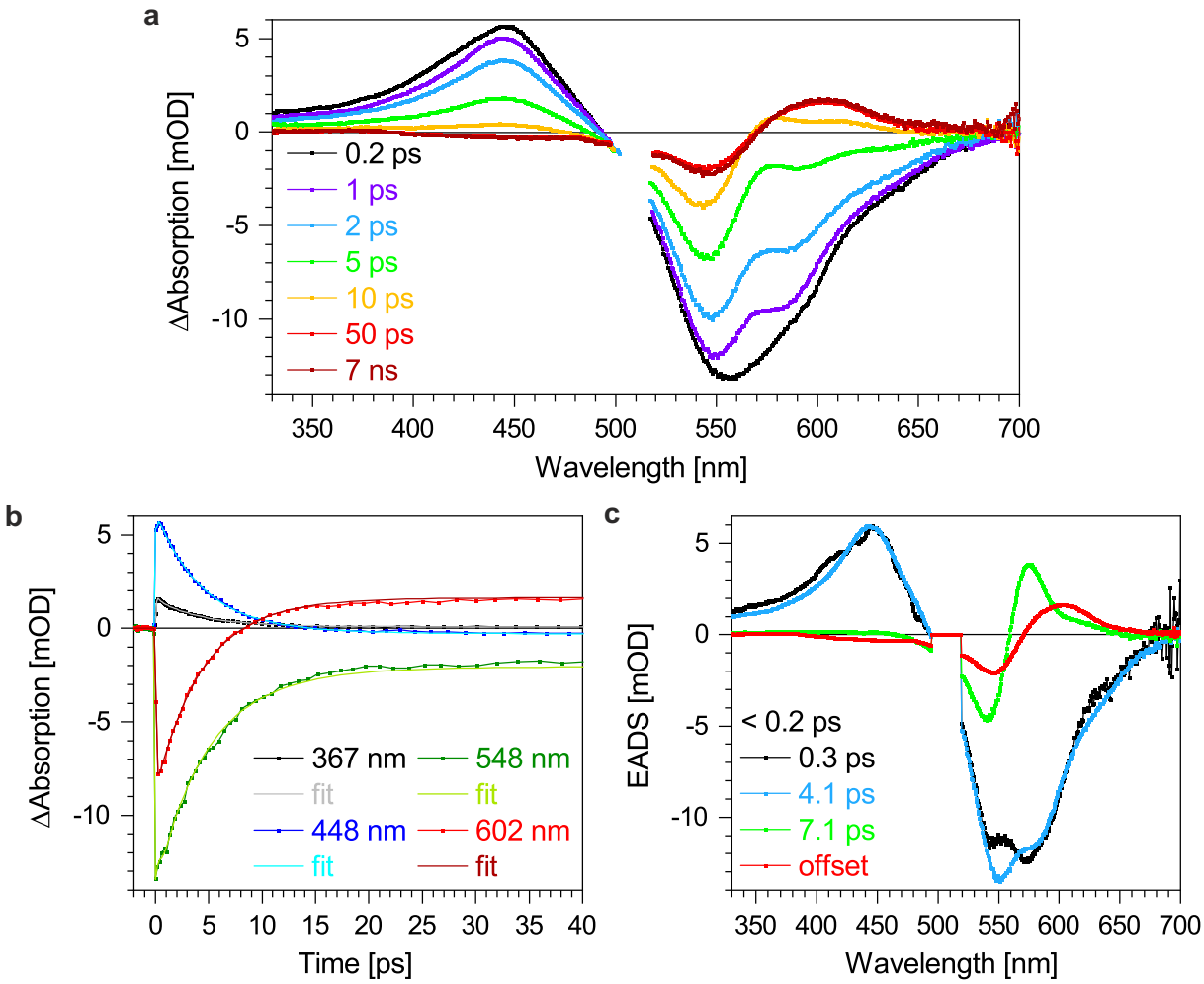

Figure 5.30. TA data of Azo and DASA in MeCN simultaneously excited with light of a wavelength of 510 nm. (a) Chosen time traces, (b) selected wavelength traces with corresponding fits and (c) EADS as well as their time constants obtained by GA. The EADS of the short time constant being below the resolution of the laser setup is not shown since this EADS is not separable from the pump-probe artefact.

its maximum position to around 602 nm and adopts a symmetric shape both attained at about 35 ps. Furthermore, two new features in the blue and UV region appear albeit with low intensity. On the one hand, a negative feature appears at around 450 nm reaching a negative offset at about 38 ps. This signal is assigned to the GSB of Azo since it agrees with the steady state absorption of *trans*-Azo (figure 5.5). On the other hand, a positive signature at around 367 nm emerges. This ESA reaches a positive constant value in about 35 ps. After the experimental period of about 8 ns, two ESAs and two GSBs remain indicating the successful generation of the two photoproducts *cis*-Azo and *E*-DASA being stable much longer than the experimental duration of about 8 ns.

GA of the TA data (figure 5.30**b**) results in four time constants τ_i of (< 0.2 ± 0.2), (0.3 ± 0.2), (4.1 ± 0.2) and (7.1 ± 0.2) ps as well as an offset (figure 5.30**c**). In order to understand the excited state dynamics of the mixture of both switching molecules, a

comparison of the spectral features and lifetimes to the to the outcomes of the single photoswitches is required (figure 5.28 and 5.29). This way, the current data can be understand in detail.
The three signatures dominating the spectra at early times, namely the ESA at around 445 nm, the GSB at about 548 nm and the SE located at around 585 nm, are clearly related to the DASA *Z*-to-*E* isomerisation. The fact that no signal at early times can be attributed to Azo and its excited state dynamics is explained by the overlapping nature of the low intensity signals. Since the TA data of single Azo (figure 5.28) shows much less pronounced signals than the respective measurement of DASA (figure 5.29), the DASA features are dominating the spectra since the ratio of Azo and DASA molecules was not set to get the most distinguishable signals but to 1:1 molar as the focus lies on intermolecular interactions which should be maximised at an equimolar ratio. With increasing time delay, the ESA of DASA in the S_1 state at about 445 nm decays and the formation of the *E*-DASA photoisomer is confirmed first by the absorption of the vibrationally excited photoproduct at around 585 nm and later by the ESA of *E*-DASA in its vibrational and electronic ground state at about 602 nm. As the dominating DASA signals in the short-wavelength region decay, the less pronounced Azo features get visible. Thus, the remaining GSB of *trans*-Azo and the ESA of the photogenerated *cis*-Azo is observed at around 450 and 367 nm, respectively. Taking the determined time constants into account, they can be attributed to the single switching procedures. The two shortest time constants are assigned to the Azo switching process with the latter being slightly accelerated by 0.3 ps in comparison to exciting pure Azo in MeCN with the same excitation energy. The third lifetime of 4.1 ps is attributed to the DASA switching process since it is identical with the time constant found for switching a respective pure DASA solution. Lastly, the longest lifetime is assigned to the DASA switching as well because it only slightly differs from the time constant found in a respective pure DASA solution being slightly increased in the present case by 0.4 ps. Hence, the only missing time constant found for the single photoswitches is 2.9 ps related to the Azo vibrational relaxation. Since this process shows the smallest contribution in the TA data of switching Azo and since the Azo signals are little in intensity compared to DASA, this process contributes only to a minor degree to the presented TA data such that this process is drowned by the DASA processes and not observable. In summary, no additional or changed features were obtained such that the same excited state dynamics for Azo+DASA switching apply as for the pure compounds (detailed descriptions in paragraphs Switching Azo orthogonally and Switching DASA orthogonally, section 5.3.1).

5.3.3. Thin films using PMMA blends

Although measurements in solution are suitable to study environmental influences such as the polarity, thin film samples are of high interest since they are more close to im-

plementations as most applications are in solid state.[11][28][266] Thus, the excitation dynamics of thin films are studied in this section as they can differ from the results in solution.[265] As films, PMMA blends are investigated which show absorption spectra of about the same width as the spectra in solution. In contrast, neat films exhibit broad absorption making orthogonal addressability difficult. The steady state absorption spectra of the photoswitches and their mixture are spectrally shifted compared to the spectra in solution (figures 5.5, 5.6 and 5.7). Hence, the excitations wavelengths had to be adapted. In PMMA blend films, Azo switching was induced by light using a wavelength of 431 nm (trans-to-cis) while backswitching was achieved by excitation with light using a wavelength of 369 nm (cis-to-trans). In contrast, light of a wavelength of 585 nm stimulated photoswitching of DASA (*Z*-to-*E*) and 515 nm light was utilised to initiate simultaneous switching of both photoswitches (*trans*-Azo to *cis*-Azo and *Z*-DASA to *E*-DASA). The independent addressability was checked by additionally photoexciting non-switched and switched Azo with 585 nm as well as non-switched and switched DASA with 369 and 431 nm resulting in no signals beside the wavelength dependent time zero position (section 2.2.5). In order to generate the switched species, an LED was turned on (UV/VIS spectra of all used LEDs in figure B.1 appendix B). Furthermore, TA test measurements were conducted with Azo and the LED for DASA switching turned on as well as with DASA and the LED for Azo switching turned on to account for artefacts.

Switching Azo orthogonally

After excitation with light of a wavelength of 431 nm to induce photoswitching of Azo (trans-to-cis) embedded in a PMMA matrix, several excitation dynamics are obtained (figure 5.31**a**). The negative feature at around 440 nm is referred to as the GSB as its position is close to the steady state absorption (figure 5.5). However, due to the presence of positive ESAs next to it, the negative GSB is narrowed. With increasing time delay, the red-shifted ESA decays and the blue-shifted ESA increases so that the GSB broadens towards longer wavelengths but narrows towards shorter wavelengths. The GSB decays within about 90 ps to a constant negative offset revealing that some of the molecules do not return to the initial ground state within the experimental period of about 8 ns. Two ESAs are located at longer wavelengths compared to the GSB at around 543 and 600 nm. Upon increasing time delay, the ESA at around 543 nm exhibits a hypsochromic shift. The ESAs located at around 543 and 600 nm decay in approximately 85 and 72 ps, respectively, to a slightly positive value. In contrast, the ESAs in the UV region located at around 340 and 370 nm decay within 77 and 4 ps, respectively. The latter, however, slightly increases afterwards to reach a constant positive value at about 89 ps. This ESA at around 370 nm represents the absorption of the photoproduct *cis*-Azo which stays constant within the experimental period.

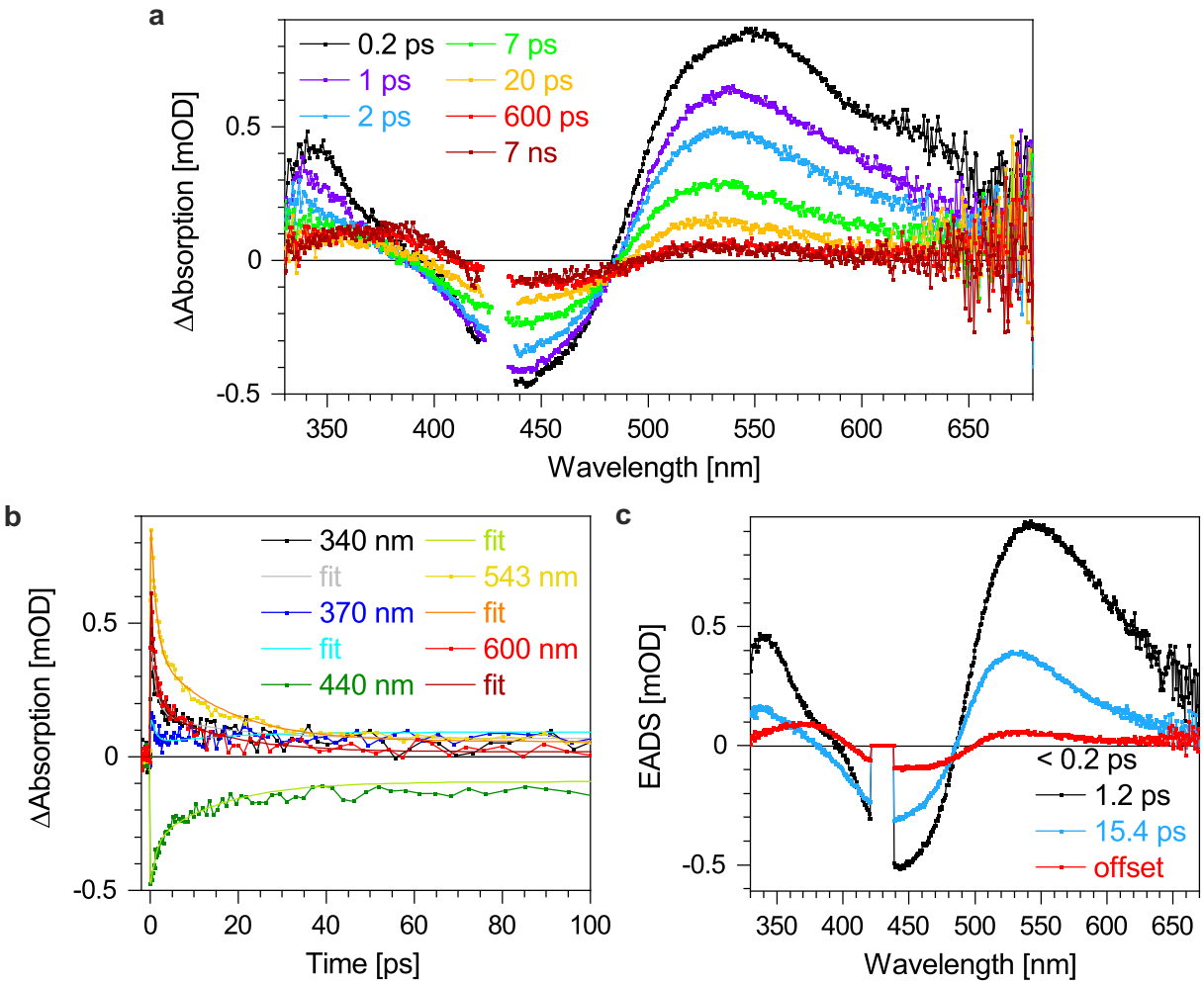

Figure 5.31. TA data of an Azo film as PMMA blend excited with light of a wavelength of 431 nm. (a) Chosen time traces, (b) selected wavelength traces with corresponding fits and (c) EADS as well as their time constants obtained by GA. The EADS of the short time constant being below the resolution of the laser setup is not shown since this EADS is not separable from the pump-probe artefact.

The TA data is described by a GA (figure 5.31**b**) using three time constants τ_i of (< 0.2 ± 0.2), (1.2 ± 0.2) and (15.4 ± 0.2) ps as well as an offset (figure 5.31**c**). The lifetimes and spectral features fit to the excited state dynamics of Azo in Tol and MeCN after excitation to S_2 (sections 5.3.1 and 5.3.2, detailed description in paragraph Switching Azo orthogonally section 5.3.1). The S_1 state is reached in below 0.2 ps and witnessed by the ESA located at about 600 nm. The electronic ground state is observed by the ESAs at around 543 and 370 nm caused by vibrationally excited *trans*-Azo and by *cis*-Azo after vibrational relaxation, respectively. The small positive feature persisting at longer wavelengths than 500 nm indicates that the photoswitching is still ongoing.

Comparing the results of the PMMA blend to the findings in solution, the dynamics of the $S_1 \rightarrow S_0$ conical intersection are similar to the Tol solution. However, the vibrational cooling occurs on a much longer time scale with a lifetime increased by 10.7 and

11.5 ps compared to the solutions in Tol and MeCN, respectively. Furthermore, small spectral shifts of the absorption bands in the PMMA blend are found compared to the data in solution.

Preparing a thin film consisting of a 1:1 molar ratio of Azo and DASA as PMMA blend, the changes of photoswitching Azo due to the presence of DASA are elucidated (figure 5.32**a**). Similar to the pure Azo-PMMA-blend, four positive signals located at about 340, 370, 543 and 600 nm are observed as well as a negative feature at around 440 nm. The latter is referred to as the GSB while the ESA located at about 370 nm signalise the absorption of the photoproduct *cis*-Azo.

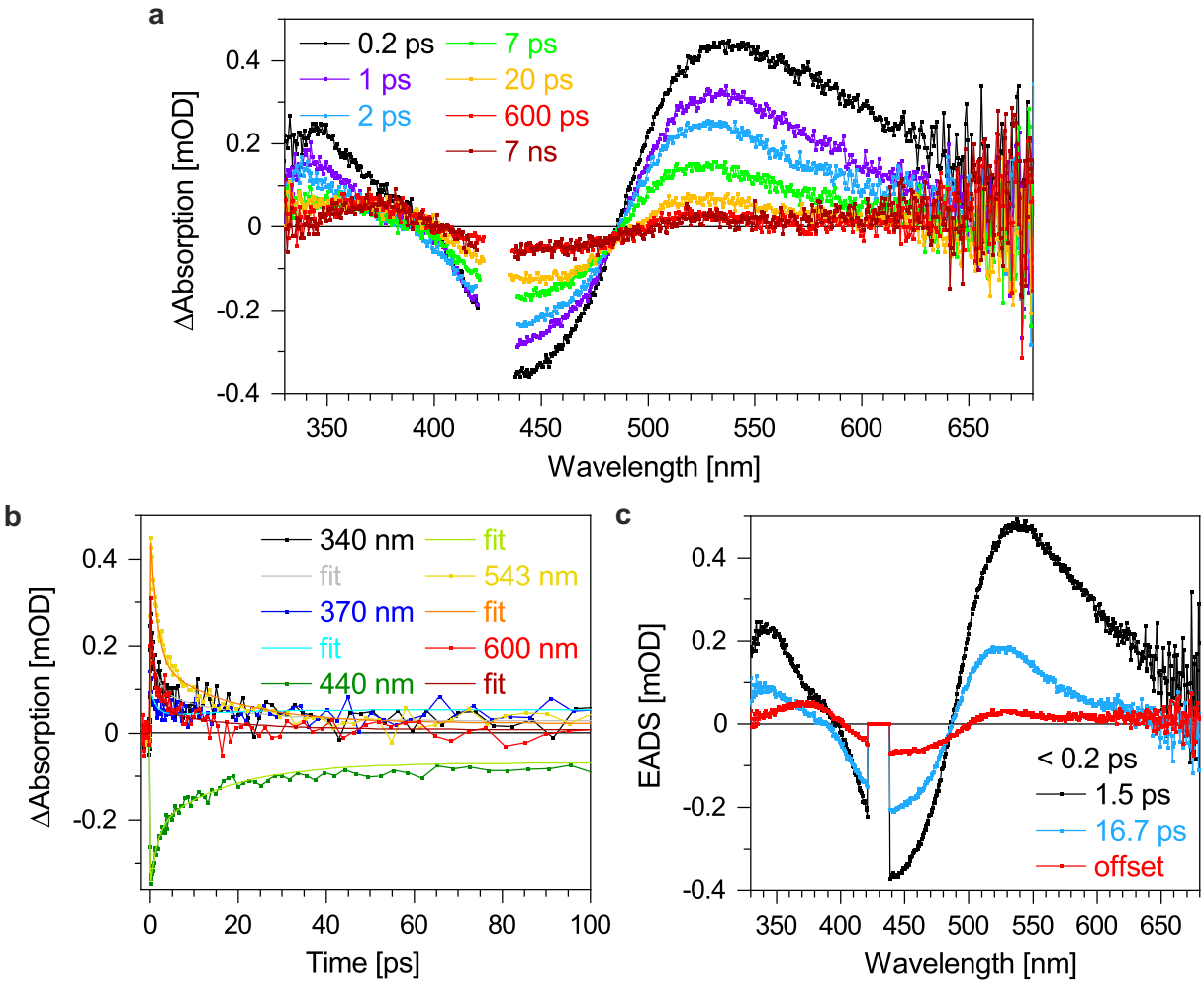

Figure 5.32. TA data of an Azo film as PMMA blend excited with light of a wavelength of 431 nm while DASA is present. (a) Chosen time traces, (b) selected wavelength traces with corresponding fits and (c) EADS as well as their time constants obtained by GA. The EADS of the short time constant being below the resolution of the laser setup is not shown since this EADS is not separable from the pump-probe artefact.

GA (figure 5.32**b**) yields EADS similar to the Azo film in a PMMA matrix (figure 5.31) and provides time constants τ_i of (< 0.2 ± 0.2), (1.5 ± 0.2) and (16.7 ± 0.4) ps as well as an offset (figure 5.32**c**). Thus, the overall excited state dynamics remain unaltered with the latter time constants being increased by 0.3 and 1.3 ps. Hence, the addition

of DASA may decelerates the $S_1 \rightarrow S_0$ conical intersection and slows down the vibrational relaxation.

In order to enlighten possible interactions and influences of the closed zwitterionic DASA isomer **C'** on the switching properties of Azo, a thin film of a 1:1 molar ratio of Azo and DASA was investigated as PMMA blend. Therefore, an additional LED with maximum intensity at 594 nm was used to induce switching of DASA. The percentage of switched DASA cannot be determined as the films have to be moved during illumination to prevent photobleaching which is possible in the TA setup but not in the UV/VIS spectrometer. To generate closed DASA isomers **C'** in a photostationary state, the thin film was illuminated several minutes before and during the TA experiment.

At a first glance, the dynamics and spectral features (figure 5.33**a**) resemble the findings of the identical experiment without LED illumination (figure 5.32). Five signals,

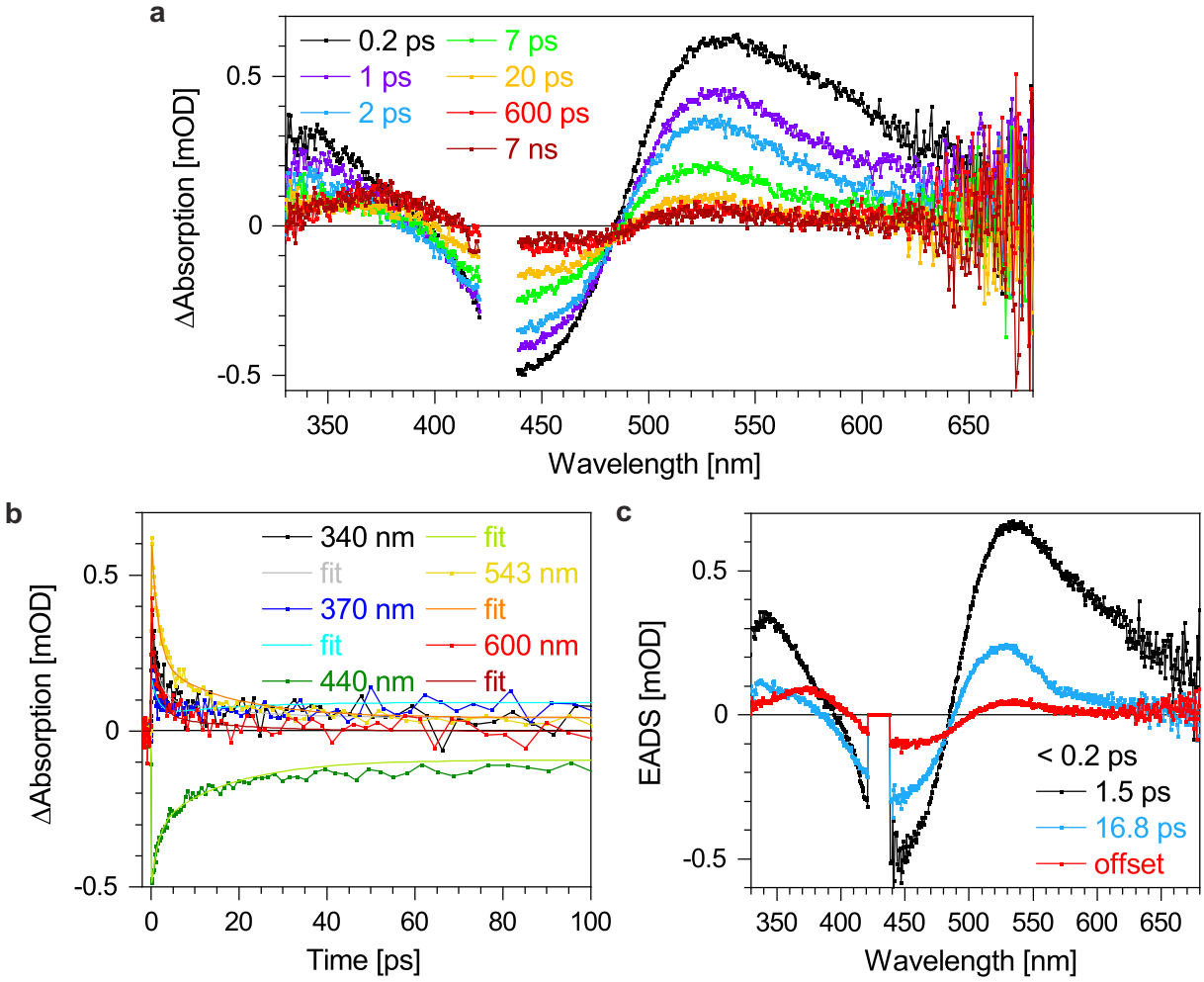

Figure 5.33. TA data of an Azo film as PMMA blend excited with light of a wavelength of 431 nm while switched DASA is present due to irradiation with an LED with maximum intensity at 594 nm. (a) Chosen time traces, (b) selected wavelength traces with corresponding fits and (c) EADS as well as their time constants obtained by GA. The EADS of the short time constant being below the resolution of the laser setup is not shown since this EADS is not separable from the pump-probe artefact.

located at about 340, 370, 440, 543 and 600 nm are detected. Beside the negative signal at around 440 nm, all other signals are positive. The former represents the GSB while the latter are ESAs. Indicated by the offset, a fraction of *trans*-Azo does not return to the initial ground state within the experimental period of around 8 ns resulting in a remaining GSB at about 440 nm. Instead, the photoproduct *cis*-Azo is formed absorbing at around 370 nm. The latter feature stays constant within the experimental period as well as a small positive feature above 500 nm.
GA (figure 5.33**b**) results in three time constants τ_i of (< 0.2 ± 0.2), (1.5 ± 0.2) and (16.8 ± 0.4) ps as well as an offset (figure 5.33**c**). Thus, the excited state dynamics are identical to the findings of the non-switched Azo-DASA-PMMA blend (figure 5.32) such that the same decay pathways apply.

Backswitching Azo photochemically

After studying the trans-to-cis photoisomerisation of Azo as PMMA blend thin film, the respective back reaction is investigated (cis-to-trans). Therefore, *cis*-Azo is generated by illumination with an LED holding its maximum intensity at about 409 nm. Mimicking the geometric conditions of the TA setup within an UV/VIS setup, around 50 % of the Azo molecules are in the cis-configuration (figure B.4**c** appendix B). The sample is illuminated several minutes prior to the experiment as well as during the TA measurement to ensure a photostationary state.
The TA data shows several signals (figure 5.34**a**). Since not only the desired *cis*-Azo is present at the start of the experiment but also *trans*-Azo in the photostationary state achieved by LED illumination, both are excited by the 369 nm pump pulse leading to two negative GSBs at early times at around 377 and 440 nm, respectively. In addition, three positive ESAs are observed at early times at about 335, 530 and 600 nm. With increasing time delay, the aforementioned ESAs decay within about 1140, 1560 and 1040 ps, respectively. As the overlapping ESAs at around 530 and 600 nm possess different lifetimes, the maximum intensity of the positive feature shifts towards shorter wavelengths. The GSB of *cis*-Azo decreases in its intensity but stops at a constant level while the GSB of the trans-isomer decays within about 1 ps to zero. At later times, a positive ESA emerges in the blue region of the spectrum. Due to the simultaneous rise of the latter and the decay of the spectrally overlapping GSB of *trans*-Azo, the ESA undergoes a redshift from ca. 408 to 425 nm with increasing time delay. After about 1415 ps, the ESA finally reaches its maximum intensity at around 425 nm. Furthermore, the GSB of *cis*-Azo shifts towards shorter wavelengths with increasing time delay reaching a final value of around 362 nm after approximately 1245 ps. The spectral change is due to the concurrent decay of the UV ESA and the rise of the ESA in the blue region which both spectrally overlap with the GSB. At later times, the GSB of *cis*-Azo remains as well as the positive ESA at about 425 nm indicating successful

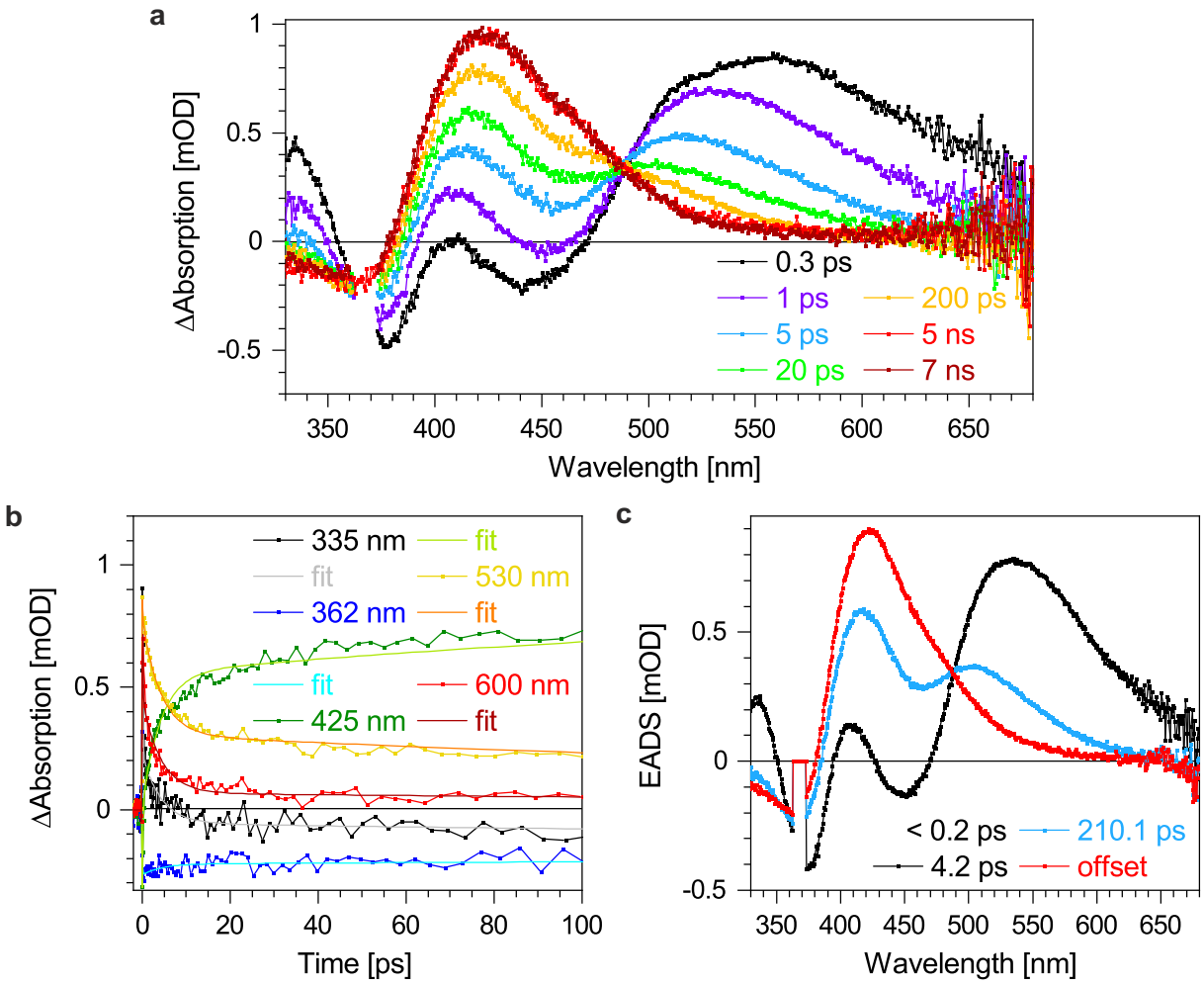

Figure 5.34. TA data of an Azo film as PMMA blend excited with light of a wavelength of 369 nm to induce backswitching. (a) Chosen time traces, (b) selected wavelength traces with corresponding fits and (c) EADS as well as their time constants obtained by GA. The EADS of the short time constant being below the resolution of the laser setup is not shown since this EADS is not separable from the pump-probe artefact.

switching of part of *cis*-Azo to its trans form. This is confirmed by the spectral position of the features if compared to steady state absorption of both species (figure 5.5). Interestingly, there is an isosbestic point at around 488 nm.

GA of the data (figure 5.34**b**) reveals three time constants τ_i of (< 0.2 ± 0.2), (4.2 ± 0.2) and (210.1 ± 1.9) ps as well as an offset (figure 5.34**c**). According to the amount of time constants and the spectral features, the same excited state dynamics upon photoexcitation of Azo to S_2 in Tol and MeCN apply (sections 5.3.1 and 5.3.2, detailed description in paragraph Switching Azo orthogonally section 5.3.1). Hence, the S_1 populated through $S_2 \rightarrow S_1$ conical intersection in below 0.2 ps shows ESA at about 600 nm. The electronic ground state reached through conical intersection within about 4.2 ps is witnessed by the ESAs at about 530 and 425 nm caused by *trans*-Azo in higher vibrational levels and after vibrational cooling, respectively, with the vibrational relaxation described by the time constant of around 210 ps. However, the shape and

spectral position of the absorption of the photoproduct *trans*-Azo at about 425 nm is striking. Since *trans*-Azo was already present before the switching experiment in the photostationary state stimulated by the LED, the absorption of *trans*-Azo in the ground state is observed as GSB at around 440 nm. Thus, the absorption of the photoproduct *trans*-Azo generated upon excitation is expected to have the same spectral position and shape. Indeed the signal shifts with increasing time delay towards the GSB but stops at around 425 nm. In addition, the signal features an asymmetric shape with a long tail towards lower energies.
Comparing the findings with the results obtained in solution, the second and third time constant is extended in solid state by 2.9 and 202.8 ps compared to Tol solution as well as by 3.8 and 205.0 ps compared to MeCN solution, respectively. The spectral features are similar such that the same excited state dynamics apply. However, this is not true for the third lifetime and the ESA related to the photoproduct *trans*-Azo. The time constant is two orders of magnitude larger and the asymmetric spectral shape is not found in solution. In fact, the solution data shows the ESA at longer time delays at the same spectral position as the GSB of *trans*-Azo as expected. Due to the stiffness and the steric hindrance of the environment in a solid film compared to solution, processes may take longer. In addition, the demand for space increases upon cis-to-trans isomerisation of Azo. However, since the vibrational cooling is slowed down by two orders of magnitude with a spectral position indicating that the majority of the molecules are not in the ground state at the end of the experiment, the electrons may be trapped in another state with slightly higher energy than the ground state.[267][268] Film formation can induce trap states within the bandgap which are not present in solutions.[269][270] By the presence of a trap state near the ground state with a long lifetime, the long time constant and the spectral shape of the ESA at about 425 nm can be explained.
Next, the influence of DASA on the backswitching behaviour of Azo in thin film is studied. Therefore, the same TA experiment was conducted but with an equimolar mixture of Azo and DASA.
This way, similar features are obtained (figure 5.35**a**). At early times, two negative signals located at about 375 and 435 nm are observed. Those GSBs represent *cis*-Azo and *trans*-Azo, respectively, being excited by the pump pulse. In addition, three positive signals at around 335, 530 and 600 nm occur. With increasing time delay, the ESAs decay to zero. Due to the spectral overlap of the latter two positive features and their different time constants, the maximum intensity shifts towards shorter wavelengths. While the weakly pronounced GSB of *trans*-Azo decays rapidly to zero, the GSB of *cis*-Azo decays to a constant negative value. Simultaneously, it shifts towards shorter wavelengths due to the coincident decay of the ESA in the UV region and the rise of the long-wavelength ESA which both slightly spectrally overlap with the GSB of *cis*-Azo. This long-wavelength ESA emerges at later times at about 410 nm and bathochromic-

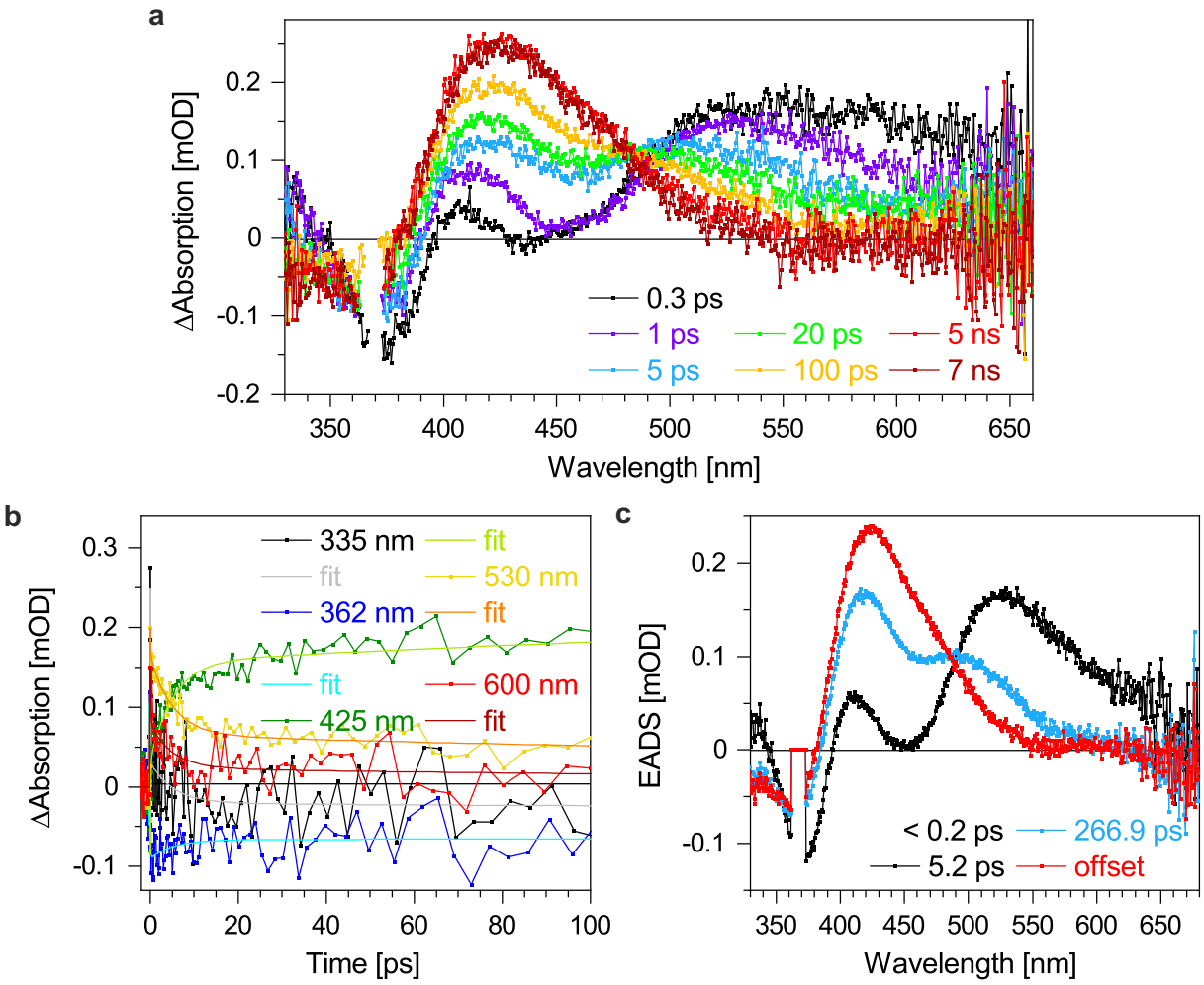

Figure 5.35. TA data of an Azo film as PMMA blend excited with light of a wavelength of 369 nm to induce backswitching while DASA is present. (a) Chosen time traces, (b) selected wavelength traces with corresponding fits and (c) EADS as well as their time constants obtained by GA. The EADS of the short time constant being below the resolution of the laser setup is not shown since this EADS is not separable from the pump-probe artefact.

ally shifts with increasing delay time to reach its final energetic position at around 425 nm. At the end of the experiment, the remaining GSB of *cis*-Azo at about 362 nm and the asymmetric ESA at around 425 nm indicate successful switching with the photoproduct *trans*-Azo being stable much longer than the experimental period of about 8 ns.

Analysis of the TA data by a global fit (figure 5.35**b**) results in three time constants τ_i of (< 0.2 ± 0.2), (5.2 ± 0.2) and (266.9 ± 8.4) ps as well as an offset (figure 5.35**c**). As the determined lifetimes and spectral signatures resemble the ones found in Azo-PMMA-blends (figure 5.34), the same excited state dynamics apply. In contrast, the second and third lifetime is extended by 1.0 and 56.8 ps, respectively, such that the conical intersection of $S_1 \rightarrow S_0$ and the vibrational relaxation take longer in the mixture.

To gain a full picture of the influences of DASA on the switching properties of Azo in a PMMA blend film, the interaction of switched DASA in its closed isomeric structure **C'**

is investigated. For that purpose, an Azo-DASA-PMMA blend film holding a 1:1 molar ratio of the photoswitches was illuminated several minutes prior and during the TA experiment to ensure a photostationary state with two LEDs with maximum intensities at about 409 nm and 594 nm to generate switched Azo and DASA, respectively (figure B.4 appendix B).

The TA data of the subsequently excited sample containing *cis*-Azo and *E*-DASA reveals several signals (figure 5.36**a**). At early times, the GSB located at about 375 nm representing the excited *cis*-Azo is observed. Only a slight negative feature at around 447 nm is obtained at very early times which is caused by excitation of *trans*-Azo being initially present due to the photostationary state achieved by the LED. On account of excited state intermediates, three ESAs occur at about 335, 530 and 600 nm. With increasing time delay, all above listed signals decay to zero beside the GSB of *cis*-Azo

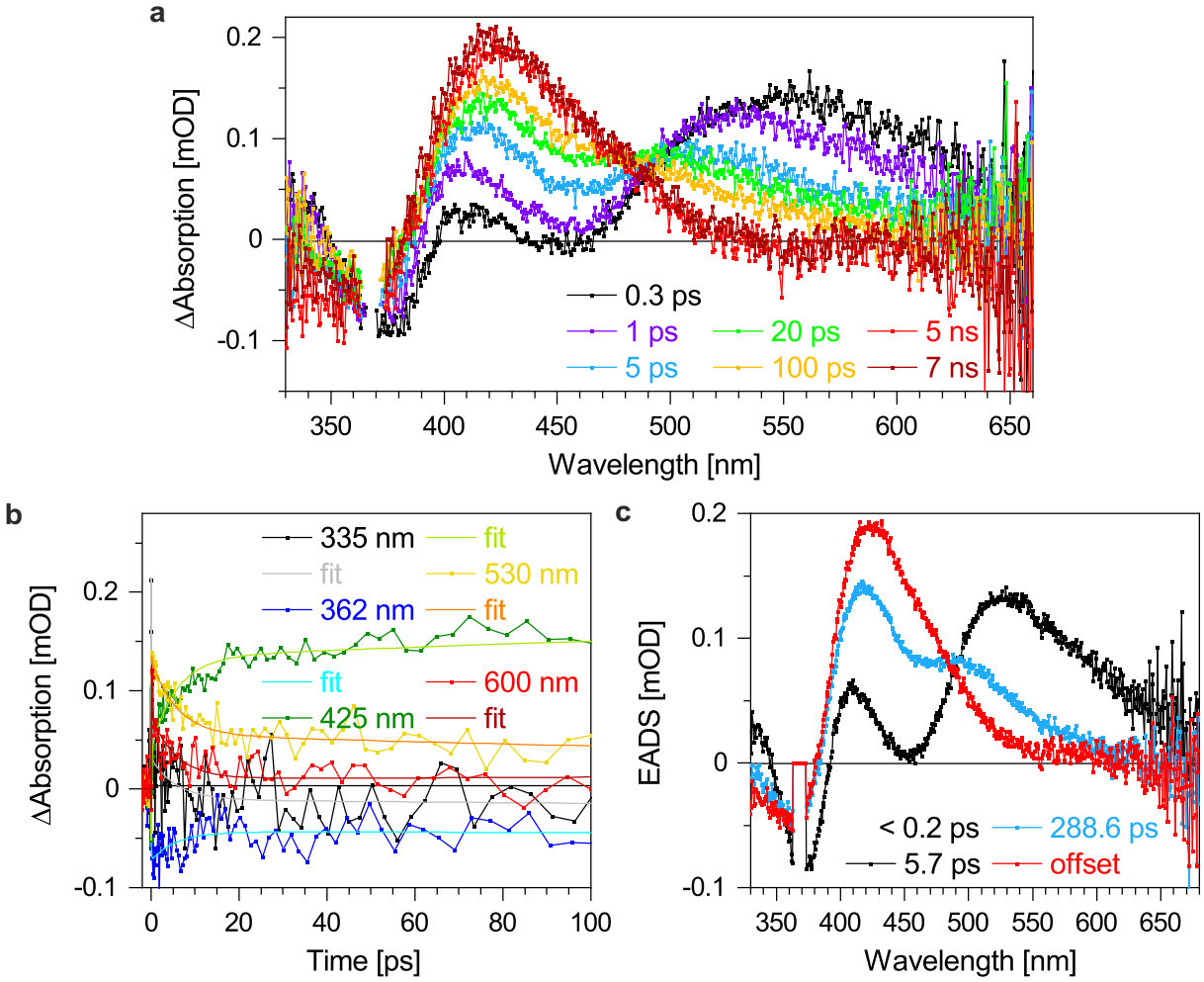

Figure 5.36. TA data of an Azo film as PMMA blend excited with light of a wavelength of 369 nm to induce backswitching while switched DASA is present due to irradiation with an LED holding a maximum intensity at 594 nm. (a) Chosen time traces, (b) selected wavelength traces with corresponding fits and (c) EADS as well as their time constants obtained by GA. The EADS of the short time constant being below the resolution of the laser setup is not shown since this EADS is not separable from the pump-probe artefact.

which stops at a constant negative value. In addition, a positive ESA initially located at around 410 nm emerges exhibiting a bathochromic shift upon increasing time delay. At later times, this signal holds a positive constant value located at around 425 nm. The offsets in the data display successful switching of *cis*-Azo represented by the negative feature to its trans-isomer embodied by the positive signature. Furthermore, an isosbestic point at about 488 nm is observed.
GA of the data (figure 5.36**b**) yields three time constants τ_i of (< 0.2 ± 0.2), (5.7 ± 0.2) and (288.6 ± 10.4) ps as well as an offset (figure 5.36**c**). Contrasting the lifetimes and EADS with the results of the other Azo films (figures 5.34 and 5.35), the same excited state dynamics upon photoexcitation take place. However, the second and third step is slightly decelerated by 0.5 and 21.7 ps, respectively, compared to the analogous experiment with only non-switched DASA present.

Switching DASA orthogonally

The experimental data measured by TA upon switching DASA as thin PMMA blend film show several features (figure 5.37**a**). At early times, a broad symmetric positive feature in the blue region of the VIS spectrum occurs as well as a red-shifted asymmetric negative feature. The positive feature at around 450 nm is assigned to an ESA. The negative feature, however, consists of two spectrally overlapping features. The GSB is located at about 562 nm identified as GSB due to the spectral overlap with the steady state absorption (figure 5.6). However, the GSB is narrower compared to the steady state absorption since the former shows a less pronounced shoulder at its short-wavelength side with the shoulder caused by vibrational progression. The red-shifted shoulder of the negative TA signal represents the SE. The ESA decays within about 410 ps to zero while the SE at around 615 nm signal reaches zero in about 232 ps. The GSB decays within around 405 ps to a constant negative offset. With increasing delay time, the GSB shifts its maximum intensity towards shorter wavelengths. At later times, a low intensity ESA located at about 615 nm is recognised. It reaches its positive offset in around 382 ps. Thus, at later times, the remaining GSB forms a negative offset while the low intensity ESA provides a positive offset. This suggests that part of the molecules are successfully switched from the initial *Z*-isomer to the *E*-isomer. The newly created photoproduct absorbing at about 615 nm is identified as *E*-DASA because its absorption resembles the absorption found in solutions (figure 5.6).
GA of the TA data (figure 5.37**b**) reveals two time constants τ_i of (5.5 ± 0.2) and (64.6 ± 0.3) ps as well as an offset (figure 5.37**c**). In order to study the excited state dynamics after excitation, a comparison to the results in solution provides insight (sections 5.3.1 and 5.3.2).

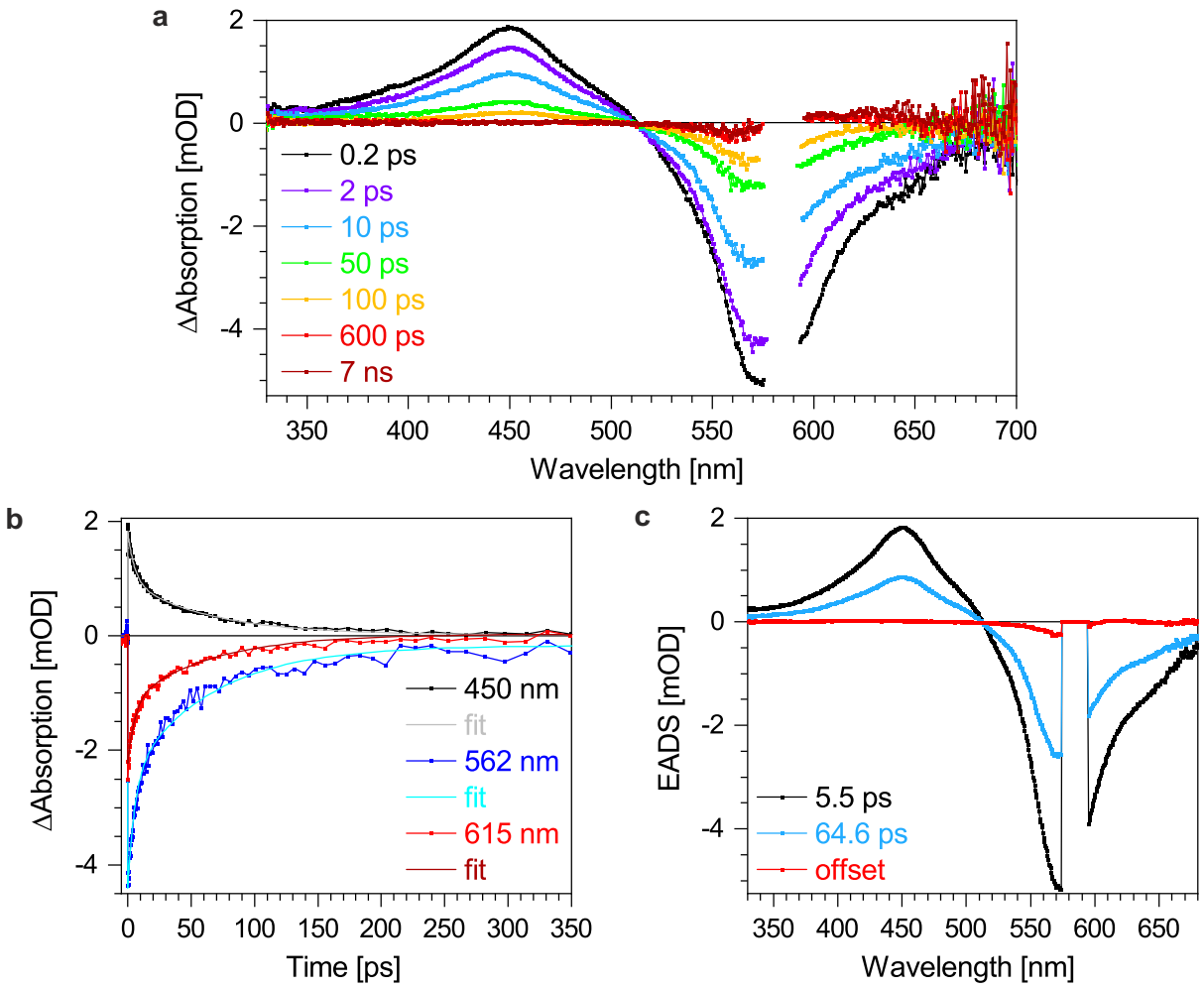

Figure 5.37. TA data of a DASA film as PMMA blend excited with light of a wavelength of 585 nm. (a) Chosen time traces, (b) selected wavelength traces with corresponding fits and (c) EADS as well as their time constants obtained by GA.

Comparing the time constants, all lifetimes are extended in solid state by 1.2 and 55.4 ps as well as 2.0 and 58.8 ps compared to the solutions in Tol and MeCN, respectively. The EADS of the shortest time constant and the offset in the PMMA matrix resemble the findings of the solutions. However, the EADS of the offset reveals less photoswitching. The EADS of the second time constant differs from the results in solutions (blue curves). Whereas the respective EADS in solution show the rise of the photoproduct in higher vibrational levels as peaks at around 600 and 575 nm for Tol and MeCN, respectively, the thin film data shows no peak in that spectral window. However, as the intensity of the photoproduct indicated by the offset is quite weak, also a low intensity of the signal of *E*-DASA in higher vibrational levels is expected. Since the latter absorption spectrally overlaps with the more intense SE, it is may not observable due to its low intensity. Apart from that, the EADS and time constants are in accordance such that the same excited state dynamics apply (detailed description in paragraph Switching DASA orthogonally section 5.3.1).

Thus, after excitation to S_1, witnessed by the ESA at about 450 nm, the population

propagates to S_0 with absorption of electrons in the electronic ground state in higher vibrational levels barely observed due to the weak intensity and spectral overlap with the SE. The latter absorption of the *E*-DASA photoproduct is observed at around 615 nm. The excited state dynamics, especially the vibrational cooling, take thereby place on a longer time scale compared to the measurements in solution. This is caused by the stiff environment in the solid PMMA matrix impeding the free motion of the molecules. In order to investigate the interaction and influence of Azo on the switching behaviour of DASA in thin film, an Azo-DASA-PMMA blend was fabricated holding an equimolar ratio of Azo and DASA. Upon excitation of DASA, two broad features are observed in the TA data at early times (figure 5.38**a**). The positive feature is located at about 450 nm and decays to zero with increasing time delay. The negative feature, on the other hand, is of asymmetric shape as it consists of two overlapping signals. The GSB, identified by spectral overlap with the steady state absorption (figure 5.6), is situated at around 562 nm while the long-wavelength shoulder of the negative feature repres-

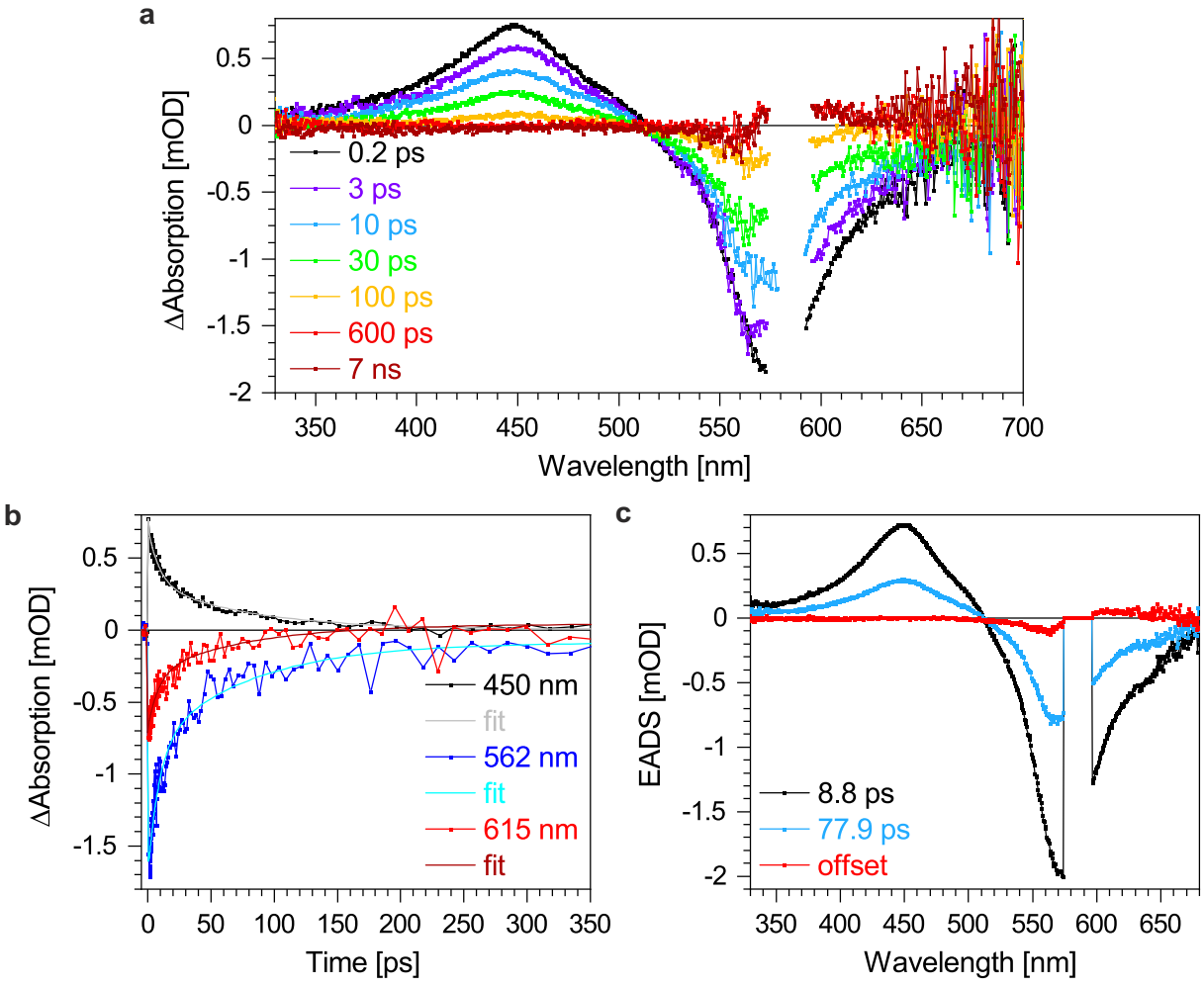

Figure 5.38. TA data of a DASA film as PMMA blend excited with light of a wavelength of 585 nm while Azo is present. (a) Chosen time traces, (b) selected wavelength traces with corresponding fits and (c) EADS as well as their time constants obtained by GA.

ents SE. Upon increasing time delay, both signals decay with the GSB decaying to a constant negative $\triangle$A value while the SE decays to zero. Due to the different lifetimes, the maximum of the negative feature undergoes a blueshift with increasing time delay. At later times, a new positive ESA of low intensity located at about 615 nm occurs. That positive feature stays constant over the experimental period of about 8 ns indicating the formation of the photoproduct *E*-DASA which is stable for the whole experimental duration with the remaining GSB revealing that not all molecules return to the initial ground state.
The excitation dynamics are described by a global fit (figure 5.38**b**) resulting in two time constants τ_i of (8.8 ± 0.2) and (77.9 ± 0.7) ps as well as an offset (figure 5.38**c**). Hence, the excited state dynamics upon photoswitching are unaltered compared to a DASA-PMMA blend as the time constants and EADS are similar (figure 5.37). However, the lifetimes are extended by 3.3 and 13.3 ps, respectively, indicating slower excited state dynamics when Azo is present.
Next, the influence of *cis*-Azo on the switching mechanism and excited state dynamics of DASA as PMMA blend thin film is studied. Therefore, a 1:1 molar ratio of Azo and DASA is prepared in a PMMA matrix and switched Azo is generated by illumination with an LED having its maximum wavelength at around 409 nm several minutes before the experiment as well as during the measurement to ensure a photostationary state. This way, about 50 % Azo molecules are in the cis state (figure B.4 appendix B).
Upon excitation of the thin film to induce DASA switching, two distinct features are obtained at early times (figure 5.39**a**). On the one hand, a broad positive signal at around 450 nm is observed. On the other hand, a negative feature at longer wavelengths arises. The latter consists of the GSB at about 562 nm in accordance with the steady state absorption (figure 5.6) and an overlapping SE at longer wavelengths. With increasing time delay, the ESA and SE decay to zero while the GSB decays to a small negative offset. Simultaneously, the maximum of the negative feature undergoes a hypsochromic shift due to the different decay times of both negative signals. At later times, a new positive ESA with low intensity occurs at around 615 nm identified as absorption of *E*-DASA as confirmed by the spectral position compared to the steady state absorptions (figure 5.6). The remaining signals at the end of the experiment, depicted as offset, indicate successful switching of *Z*-DASA to *E*-DASA with the photoproduct being stable longer than the experimental period of about 8 ns.
GA (figure 5.39**b**) reveals two time constants τ_i of (5.8 ± 0.2) and (50.7 ± 0.4) ps as well as an offset (figure 5.39**c**). Hence, the lifetimes and EADS are in accordance with the previous results such that the same excitation dynamics apply (detailed description in paragraph Switching DASA orthogonally section 5.3.1). However, the dynamics are accelerated since the time constants are shortened by 3.1 and 27.2 ps, respectively, compared to the same blend but without switching Azo.

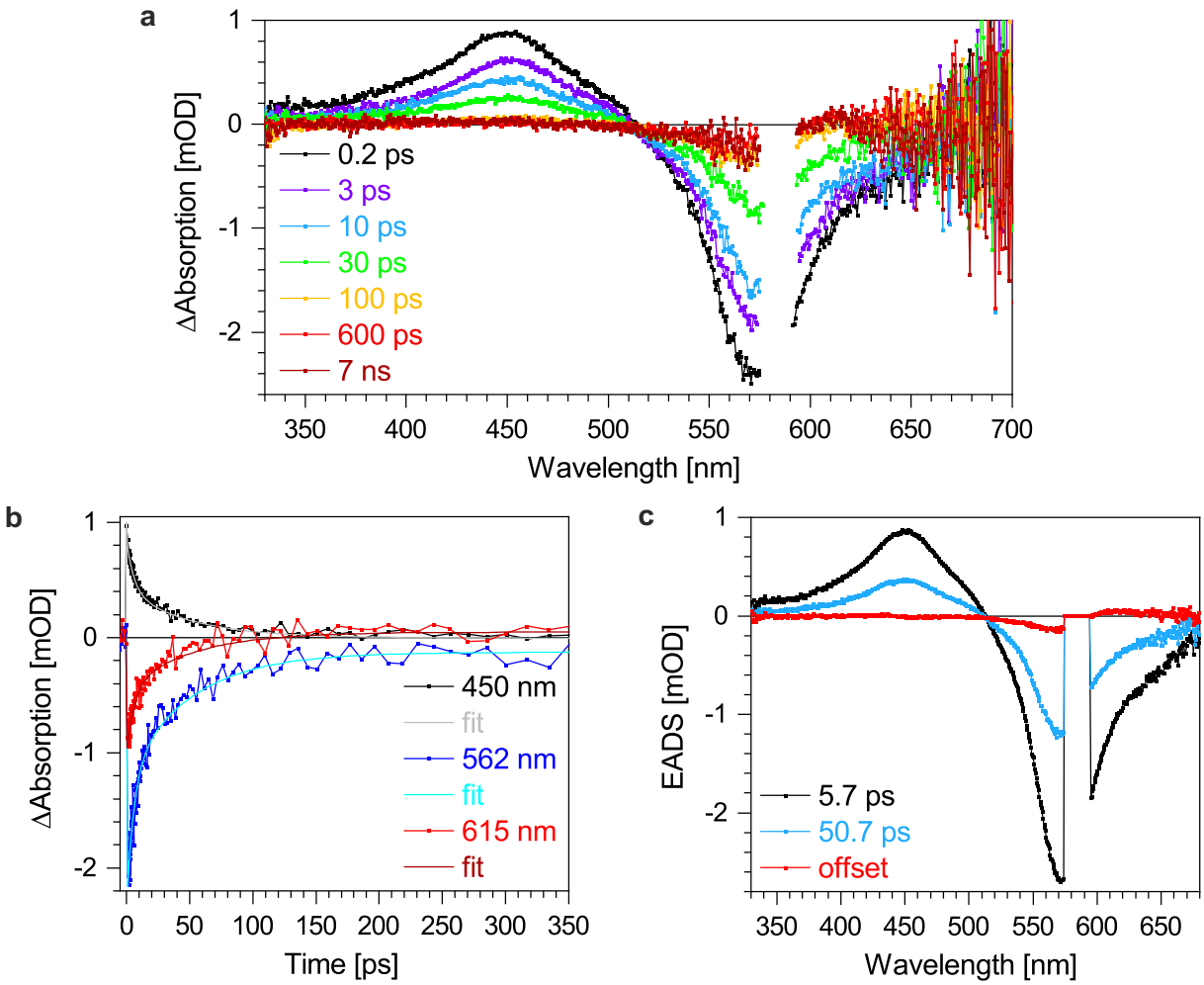

Figure 5.39. TA data of a DASA film as PMMA blend excited with light of a wavelength of 585 nm while switched Azo is present due to irradiation with an LED with maximum intensity at 409 nm. (a) Chosen time traces, (b) selected wavelength traces with corresponding fits and (c) EADS as well as their time constants obtained by GA.

Switching Azo and DASA simultaneously

To finally complete the excited state investigations, the interactions and influences of Azo and DASA on each other in a PMMA blend film are studied if both photoswitches are addressed simultaneously (*trans*-Azo to *cis*-Azo and *Z*-DASA to *E*-DASA). Therefore, the single components have to be studied first to allocate all signals and changes to their correct origin.

To begin with, the excited state dynamics upon switching Azo are investigated for trans-to-cis isomerisation induced by illumination with light of a wavelength of 515 nm. Several features are present in the TA data (figure 5.40**a**). At early times, two ESAs in the short-wavelength region appear at about 345 and 402 nm. In addition, a negative feature identified as GSB is observed around 468 nm. Furthermore, two overlapping ESAs at about 558 and 600 nm are found. With increasing pump-probe time delay, the ESA in the UV region decays to zero within around 146 ps. The ESA at about 402 nm,

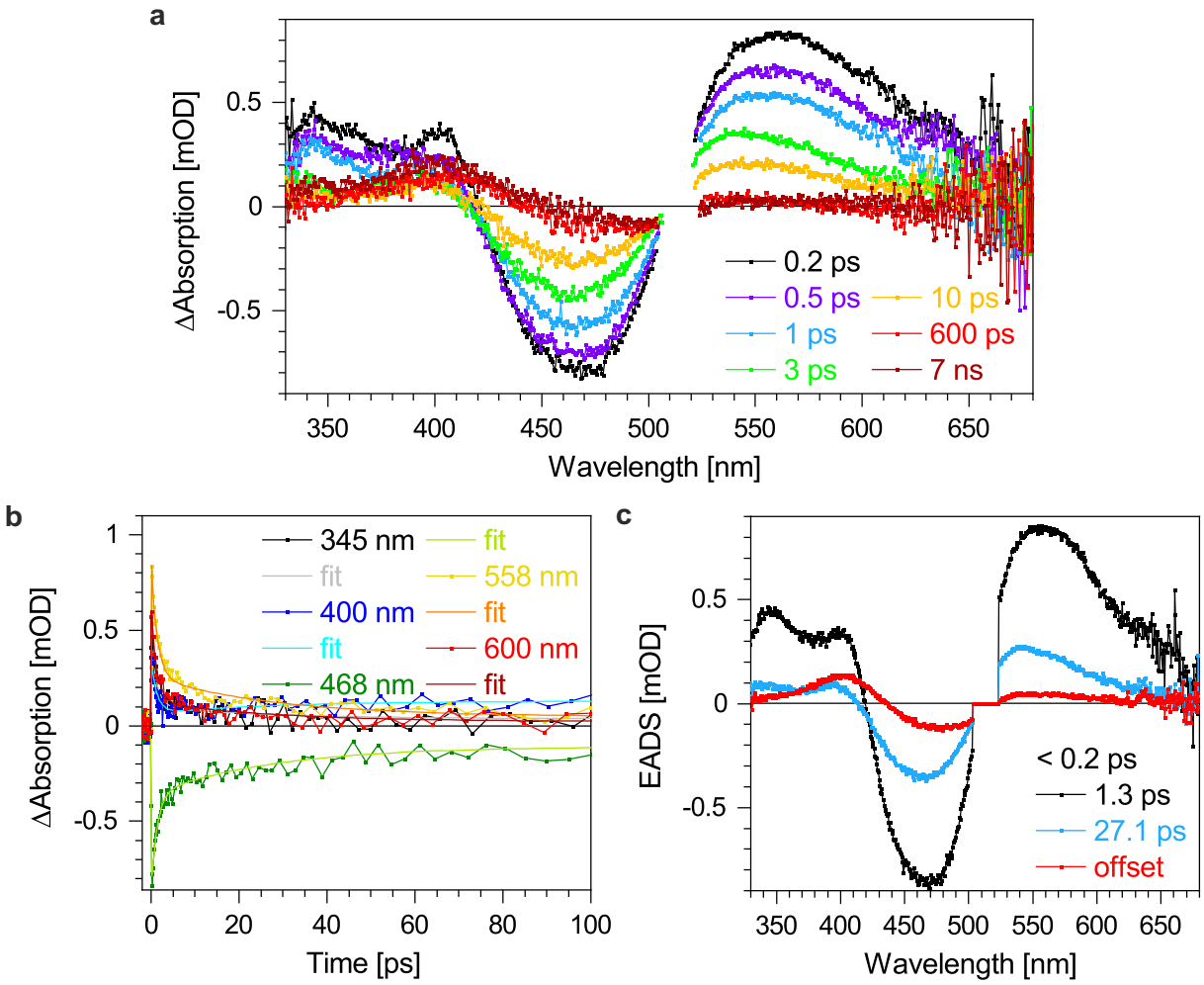

Figure 5.40. TA data of an Azo film as PMMA blend excited with light of a wavelength of 515 nm. (a) Chosen time traces, (b) selected wavelength traces with corresponding fits and (c) EADS as well as their time constants obtained by GA. The EADS of the short time constant being below the resolution of the laser setup is not shown since this EADS is not separable from the pump-probe artefact.

however, decreases to a minimum within around 6 ps and subsequently slightly rises to a constant positive value reached in about 140 ps. Along that way, it undergoes a slight hypsochromic shift. The GSB decreases in its intensity but to a constant negative offset which takes about 160 ps. Meanwhile, the ESAs located at around 558 and 600 nm decay to zero within about 167 and 128 ps, respectively. Since the determination of the maximum is difficult due to the overlapping nature of both ESAs, the maximum of the former was defined by the maximum of the first shown EADS. As an offset, a remaining GSB and a positive ESA of the photoproduct *cis*-Azo contribute to the data. This indicates the successful switching of *trans*-Azo to *cis*-Azo with the latter being much longer stable than the experimental period of about 8 ns. As the ESA broadens with increasing time delay, the GSB in turn shifts its maximum position to longer wavelengths.

Analysing the data with a global fit (figure 5.40**b**), three time constants τ_i of ($< 0.2 \pm 0.2$),

(1.3 ± 0.2) and (27.1 ± 0.5) ps as well as an offset arise as a result along with their respective EADS (figure 5.40**c**). Judging the findings in the light of switching Azo orthogonally, the excited state dynamics are unchanged with the sequence happening after photoexcitation to S_2 (paragraph Switching Azo orthogonally, this section; detailed description in paragraph Switching Azo orthogonally section 5.3.1). The S_1 state is thereby represented by its absorption at around 600 nm. In contrast, the electronic ground state of *trans*-Azo in higher vibrational levels is indicated by the ESA located at around 558 nm while the photoproduct *cis*-Azo absorbs at about 400 nm after vibrational relaxation.

In comparison with the outcomes of the same switching process but induced with 431 nm, all features are bathochromically shifted when excited with 515 nm. In addition, the vibrational relaxation is slowed down by 11.7 ps in the current case.

Next, the excited state dynamics upon exciting DASA as thin PMMA blend film with 515 nm are studied (figure 5.41**a**). At early times, a positive feature located at about

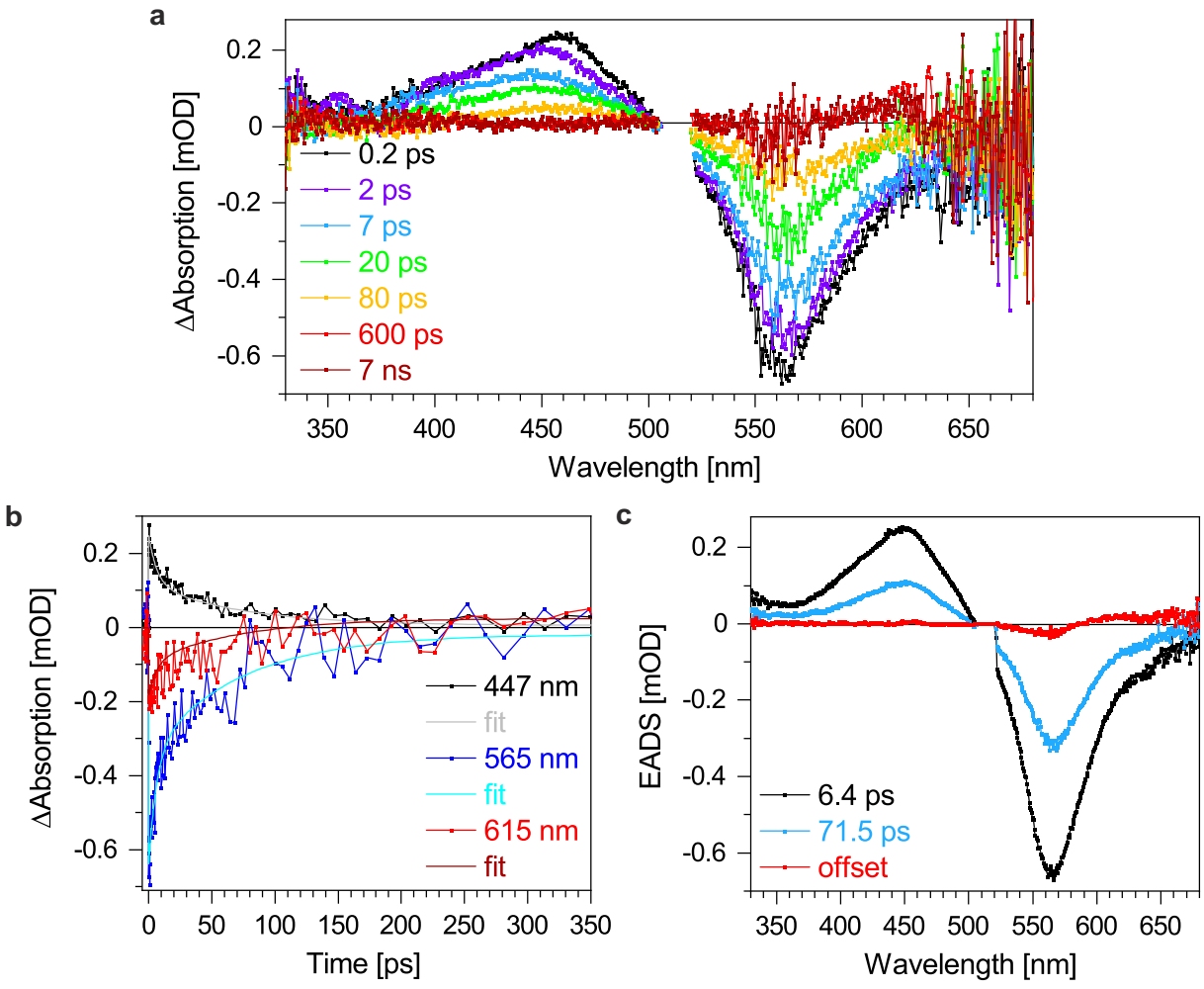

Figure 5.41. TA data of a DASA film as PMMA blend excited with light of a wavelength of 515 nm. (a) Chosen time traces, (b) selected wavelength traces with corresponding fits and (c) EADS as well as their time constants obtained by GA.

447 nm is observed as well as an negative feature at longer wavelengths. Having a closer look, the negative signature consists of two closely overlapping signals of which the GSB is located at around 565 nm while the SE is slightly red-shifted. With increasing time delay, the ESA and the SE decay to zero within about 445 and 126 ps, respectively. The GSB decays as well but to a constant negative offset in around 517 ps. At later times, a new ESA emerges located at around 615 nm reaching a constant positive offset reached after about 425 ps. In general, the signal-to-noise ratio is poor such that the latter ESA showing low intensity is hard to identify.
With a GA (figure 5.41**b**), the TA data can be described by two time constants τ_i of (6.4 ± 0.2) and (71.5 ± 0.6) ps as well as an offset along with their respective EADS (figure 5.41**c**). Thus, the lifetimes and identified spectral signatures fit to the excited state dynamics found for orthogonal excitation and in solution (detailed description in paragraph Switching DASA orthogonally section 5.3.1). Accordingly, after excitation to S_1 its absorption is observed as ESA located at around 450 nm whereas the photoproduct *E*-DASA absorbs at around 615 nm. The remaining GSB and ESA indicate successful photoswitching. The constant offsets are thereby best observed in the respective EADS since the data is quite noisy considering the low intensity signals.
In comparison with the *Z*-to-*E* photoisomerisation of DASA as thin film but excited with light using a wavelength of 585 nm, the general spectral features and EADS are in agreement. However, the signals exhibit a small hypsochromic shift for the current data, especially in the region of the GSB and SE at early times. Considering the time constants, the switching upon excitation with 515 nm is slightly decelerated compared to the usage of 585 nm light as reflected by extended lifetimes in the present case by 0.9 and 6.9 ps, respectively.
In the final TA measurement in this study, the excited state dynamics of Azo and DASA upon simultaneous excitation with light using a wavelength of 515 nm as PMMA blend film holding an equimolar ratio of the photoswitches are investigated (figure 5.42**a**). At early times, a broad positive ESA is observed in the blue region of the spectrum with its maximum located at around 447 nm. At shorter wavelengths, a high noise value may hint towards underlying signals. Furthermore, a broad negative feature at about 565 nm arises with a second signal at its long-wavelength side. By comparison of the TA data with the steady state absorption of both photoswitches (figures 5.5 and 5.6), the signature at around 565 nm is allocated to the GSB of *Z*-DASA and the bathochromically shifted signal is attributed to SE of DASA. With increasing pump-probe delay, the ESA and the SE decay within about 380 and 87 ps to zero, respectively. On the contrary, the GSB decays to a constant negative offset reached after around 400 ps. At later times, a new ESA emerges at around 615 nm which gains intensity until a pump-probe delay of about 495 ps is reached. From there on, it stays at a constant positive level. In the short-wavelength region of the spectrum, a slight rise is

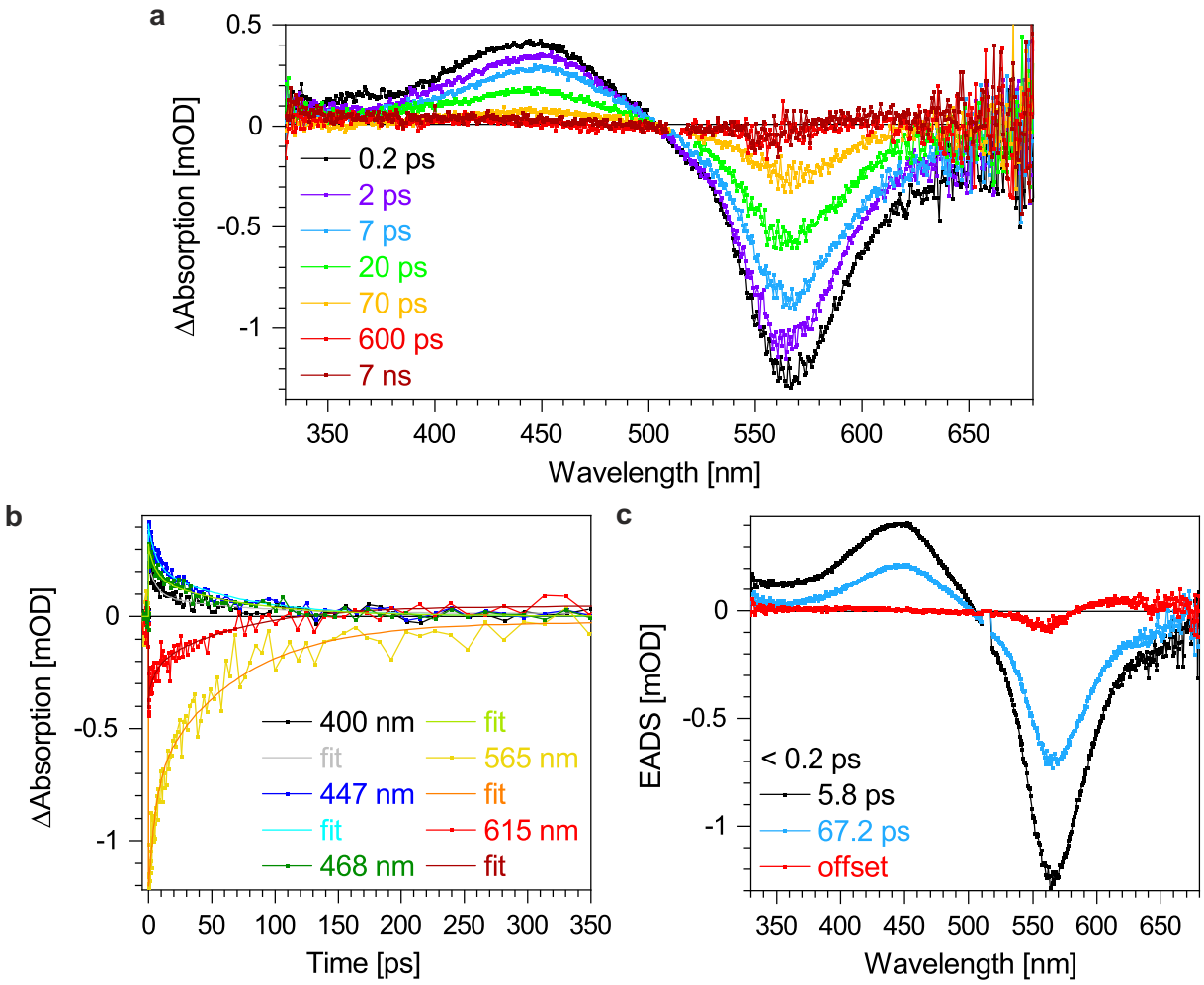

Figure 5.42. TA data of an Azo and DASA film as PMMA blend simultaneously excited with 515 nm. (a) Chosen time traces, (b) selected wavelength traces with corresponding fits and (c) EADS as well as their time constants obtained by GA. The EADS of the short time constant being below the resolution of the laser setup is not shown since this EADS is not separable from the pump-probe artefact.

noticeable. This ESA located at about 400 nm stays at a small positive value which is reached after around 500 ps.

GA of the TA data (figure 5.42**b**) reveals three time constants τ_i of (< 0.2 ± 0.2), (5.8 ± 0.2) and (67.2 ± 0.7) ps as well as an offset (figure 5.42**c**). To identify all involved excited state species and their behaviour, a comparison of the data with the findings of the respective experiments with the single components is necessary (figures 5.40 and 5.41). This way, the coincident processes can be elucidated.

The dominating signals at early times are the ESA, GSB and SE at about 447, 565 and 600 nm, respectively. All of them are attributed to the DASA switching process. Despite Azo exhibiting various signals at early times upon photoswitching as well, no Azo features can be found in the 1:1 molar mixture of both photoswitches. However, comparing the intense DASA spectra (figure 5.41) with the less pronounced Azo data (figure 5.40) and bearing in mind that the excitation power is one order of magnitude

lower for thin films with incorporated DASA, it seems unsurprising that the low intensity signals of Azo are superimposed by DASA features (figure 5.42). At later times, the formation of *E*-DASA is witnessed by its ESA at around 615 nm and the remaining GSB of *Z*-DASA. However, those signals are quite weak in intensity and the signal-to-noise ratio is poor such that the signals are barely observed. By contrast, they can be easily observed in the EADS of the offset. Thinking of Azo features being less pronounced than DASA signals, it is difficult to imagine to recognise them. Indeed, Azo signals are barely identified. However, a small ESA in the spectral region of the *cis*-Azo photoproduct is obtained. Taking a glance at the determined lifetimes, the second and third time constant of 5.8 and 67.2 ps are similar to the ones received for pure DASA thin films. Furthermore, the spectral signatures found in the EADS fit. Thus, those are attributed to the DASA switching process being slightly decreased by 0.6 and 4.3 ps, respectively, im comparison with pure DASA. The short lifetime of below 0.2 ps is assigned to the Azo switching process since is it identical to the shortest time constant identified in pure Azo thin films. The remaining time constants of Azo switching are not be found in the mixed sample. This is due to the low intensity of those features and the poor signal-to-noise ratio. The latter is not possible to improve due to the low pump energy which needs to be kept in order not to damage the DASA molecules. The former can also not be optimised if the interaction and influences of both photoswitches are the first priority such that a 1:1 molar ratio is most advantageous. In summary, even if the Azo signals are hard to distinguish from the other signals of the TA data, individual Azo and DASA switching processes are assumed as in accordance with prior measurements such that the same relaxation pathways apply (detailed descriptions in section 5.3.1).

5.3.4. Comparison of the TA results

Comparing all results of orthogonally photoswitching Azo from trans to cis in different environments obtained by TA measurements, several trends are observed (table 5.1). All measurements share the same excited states as indicated by similar EADS and time constants. Upon excitation to S_2, ultrafast internal conversion to S_1 takes place as well as the movement of the wavepacket out of the Franck-Condon region towards the conical intersection of $S_1 \rightarrow S_0$. One of this processes is described by a time constant of below 0.2 ps in all experiments. The $S_2 \rightarrow S_1$ decay is only indirectly observed in a few experiments by a short rise time of the ESAs representing S_1 and S_0. The S_1 state is represented by an ESA in the long-wavelength region of the spectrum at about 600 nm. Next, $S_1 \rightarrow S_0$ conical intersection takes place in about 0.7 - 1.5 ps populating vibrationally excited S_0 levels of *trans*- and *cis*-Azo with the former absorbing at around 530 - 543 nm. Lastly, vibrational relaxation occurs on a time scale of about 3.3 - 16.8 ps. The GSB decays to a constant negative value as *trans*-Azo is success-

Table 5.1. Comparison of the lifetimes upon photoswitching Azo (trans-to-cis) in different environments obtained by GA. In addition to the listed time constants, a lifetime τ_4 >> 8 ns (experimental period) is identified in all measurements.

Mixture	τ_1 [ps]	τ_2 [ps]	τ_3 [ps]
Azo in Tol	< 0.2 ± 0.2	1.2 ± 0.2	4.7 ± 0.2
Azo+DASA in Tol	< 0.2 ± 0.2	1.3 ± 0.2	4.2 ± 0.3
Azo+switched DASA in Tol	< 0.2 ± 0.2	1.2 ± 0.2	4.0 ± 0.2
Azo MeCN	< 0.2 ± 0.2	0.7 ± 0.2	3.9 ± 0.2
Azo+DASA in MeCN	< 0.2 ± 0.2	0.8 ± 0.2	3.3 ± 0.2
Azo+switched DASA in MeCN	< 0.2 ± 0.2	0.7 ± 0.2	3.4 ± 0.2
Azo in PMMA	< 0.2 ± 0.2	1.2 ± 0.2	15.4 ± 0.2
Azo+DASA in PMMA	< 0.2 ± 0.2	1.5 ± 0.2	16.7 ± 0.4
Azo+switched DASA in PMMA	< 0.2 ± 0.2	1.5 ± 0.2	16.8 ± 0.4

fully switched into *cis*-Azo which is stable much longer than the experimental period of about 8 ns. The absorption of the photoproduct *cis*-Azo is observed as positive ESA at around 365 - 370 nm. An additional positive feature is detected at shorter wavelengths which is hard to assign as it may compose of several signals. The suggested excited state dynamics are supported by similar results of other push-pull azobenzenes studied in literature.[229] [233] [257]

Considering the findings in the non-polar solvent Tol with a dipole moment of 0.3 D[271] to the aprotic polar solvent MeCN with a dipole moment of 3.9 D,[272] the dynamics of the $S_1 \rightarrow S_0$ decay and the vibrational relaxation are accelerated in the latter by about 0.5 and 0.8 ps, respectively. However, quantum chemical calculations show barely polarity influence on the excitation dynamics such that dynamic effects, e.g. viscosity and energy dissipation, cause the acceleration.[258] Energy dissipation which plays a key role for vibrational relaxation is faster in MeCN than in Tol since the energy dissipation is proportional to the molecular weight.[273] In the PMMA blend, the S_1 decays with the same time constant as in Tol. In contrast, the vibrational cooling in the PMMA blend is decelerated by around 10.7 and 11.5 ps compared to Tol and MeCN solution, respectively. This is in line with slower energy dissipation due to the higher molecular weight of PMMA compared to the solvent molecules. Additionally, the more rigid environment in the thin film PMMA blends leads to steric hindrance of the photoresponsive molecule which requires space upon photoswitching. This further decelerates the vibrational relaxation in solid state.

The influence of the presence of DASA on the photoswitching properties of Azo is rather small. The similar lifetimes and EADS indicate no significant change in excited state dynamics as the two shortest time constants are unaltered upon addition of DASA beside a minor shortening of the second time constant by about 0.3 ps. The vibrational

relaxation, however, is affected. For solutions, the vibrational cooling is accelerated by around 0.6 ps in both solvents while it is decelerated in films by 1.3 ps. Considering the isomers *Z*-DASA and the closed zwitterionic DASA isomer **C'**, the effect of both on the switching behaviour of Azo is equal. The shortened time constant of the vibrational relaxation upon addition of DASA may be understood as environmental influence on the Azo photoswitch. The dipole moment of the *Z*-DASA and the closed zwitterionic isomer **C'** of 10.6 and 15.0 D, respectively, increase the environmental polarity but only to a small degree. The dipole moments of the photoswitches were thereby calculated using DFT with the Becke, 3-parameter, Lee-Yang-Parr (B3LYP) functional and 6-31++G(d,p) as basis set (tables B.1 and B.2 appendix B). However, since the polarity of the surrounding shows no influence on the excited state dynamics in quantum chemical calculations, dynamic effects induce the acceleration.[258] This fits to the observation that the vibrational relaxation not covered by the quantum chemical calculations is most affected. For the vibrational cooling in solid state, longer time constants upon addition of DASA are obtained. Since the mobility of the molecules is restricted in the solid PMMA matrix, different influences are present compared to solution.

Contrasting all results of the photoswitching properties of the backswitching process of the photoresponsive Azo molecule (cis-to-trans) obtained in different environments, several trends are found (table 5.2). However, all experiments share in general the same excited state dynamics as indicated by resembling lifetimes and EADS. Upon photoswitching *cis*-Azo, the electrons are promoted into the S_2 state. Next, $S_2 \rightarrow S_1$ conical intersection and the movement of the wavepacket out of the Franck-Condon region within the S_1 state takes place within the first 0.2 ps. The S_1 state is thereby witnessed by the ESA at about 600 nm. The transfer to the electronic ground state

Table 5.2. Comparison of the lifetimes upon photochemically backswitching Azo (cis-to-trans) in different environments obtained by GA. In addition to the listed time constants, a lifetime τ_4 >> 8 ns (experimental period) is identified in all measurements.

Mixture	τ_1 [ps]	τ_2 [ps]	τ_3 [ps]
Azo in Tol	< 0.2 ± 0.2	1.3 ± 0.2	7.3 ± 0.2
Azo+DASA in Tol	< 0.2 ± 0.2	1.3 ± 0.2	9.8 ± 0.3
Azo+switched DASA in Tol	< 0.2 ± 0.2	1.4 ± 0.2	7.9 ± 0.2
Azo MeCN	< 0.2 ± 0.2	0.8 ± 0.2	5.1 ± 0.2
Azo+DASA in MeCN	< 0.2 ± 0.2	0.8 ± 0.2	4.6 ± 0.2
Azo+switched DASA in MeCN	-	-	-
Azo in PMMA	< 0.2 ± 0.2	4.2 ± 0.2	210.1 ± 1.9
Azo+DASA in PMMA	< 0.2 ± 0.2	5.2 ± 0.2	266.9 ± 8.4
Azo+switched DASA in PMMA	< 0.2 ± 0.2	5.7 ± 0.2	288.6 ± 10.4

through the conical intersection $S_1 \rightarrow S_0$ happens in the next step with a time constant of about 0.8 - 5.7 ps. As a result, the electrons occupy higher vibrational states of the electronic ground state exhibiting an absorption at around 530 - 540 nm. The origin of a further ESA located at 335 - 340 nm is harder to assign since there are several components present in this spectral window.[257] Lastly, vibrational relaxation takes places with a time constant of about 4.6 - 288.6 ps. The successful cis-to-trans switching is indicated by the remaining GSB of *cis*-Azo at around 362 - 370 nm and the absorption of the photogenerated *trans*-Azo at about 425 - 450 nm. The general mechanism is thereby in accordance to literature.[237] [259] [260]

However, while the data in solution resemble each other well, the results of the thin films differ. In solid state, the signal of the photoproduct *trans*-Azo is at shorter wavelengths and exhibits an asymmetric shape with long tail towards longer wavelengths. In addition, the vibrational relaxation is slowed down by two orders of magnitude. This suggests the formation of long-lived trapped states at slightly higher energies compared to the vibrational ground state within the Azo-PMMA-blends. Hence, the electrons may be trapped in this state before reaching the vibrational ground state of the electronic ground state.

Comparing the time constants found in the different environments, namely Tol and MeCN, respectively, as well as a PMMA blend films, differences are found. The electronic transfer through the conical intersection $S_1 \rightarrow S_0$ is accelerated in MeCN by 0.5 ps while the vibrational cooling is also accelerated by 2.2 ps compared to Tol solutions. Again, quantum chemical calculations give no hint that polarity affects the excited state dynamics.[258] Hence, this follows the already identified trend of acceleration by an environment with lower molecular weight to speed up energy dissipation.[273] In solid state, the lifetime of the second step is extended by 2.9 and 3.4 ps compared to Tol and MeCN, respectively, whereas the third time constant is extended by 203.6 and 159.9 ps, respectively. Hence, the longer lifetimes in solid states compared to solutions are due to the higher molecular weight of PMMA and a higher rigidity of the environment inducing steric hindrance of the photoswitch which requires space upon photoswitching.

The presence of the DASA photoswitch influences the lifetimes but not the overall excited state dynamics since the spectral features remain unaltered by adding DASA but the time constants change slightly. In Tol solution, the vibrational relaxation is decelerated by 2.5 and 0.6 ps in the presence of *Z*-DASA and the closed zwitterionic isomer **C'**, respectively. This is opposite to the findings of the trans-to-cis isomerisation suggesting that DASA stabilises *cis*-Azo. In MeCN solution the trend of accelerated photoswitching found for trans-to-cis Azo switching due to the presence of DASA is validated also for photoinduced cis-to-trans isomerisation. For the cis-to-trans isomerisation of Azo, the time constant of the vibrational relaxation is shortened by 0.5 ps

if DASA is added to the mixture. Quantum chemical simulations show barely polarity influence on the excited state dynamics of Azo upon addition of a polar molecule.[258] Hence, dynamic effects affecting the energy dissipation important for vibrational cooling cause the acceleration. In solid state, an opposite trend is found. For PMMA blend films, the time constants for the conical intersection $S_1 \rightarrow S_0$ and the vibrational relaxation are extended by 1.0 and 56.8 ps, respectively, in the presence of *Z*-DASA as well as by 1.5 and 78.5 ps, respectively, in the presence of the closed zwitterionic DASA isomer **C'**. Both lifetimes are extended to a higher degree by the presence of the closed isomer **C'**, however, the differences are not significant. Since the environment in solid state is very rigid compared to solution, different influences and trends compared to solutions occur.

In a contrasting juxtaposition of all experimental results of the orthogonal photoswitching behaviour of DASA (*Z*-to-*E*) in different environments, several trends are identified (table 5.3). The common ground of all experiments, however, are the same relaxation pathways upon photoswitching. In all experiments, the photoswitches are promoted into the S_1 state upon excitation as confirmed by quantum chemical calculations.[261] [262] Next, the population migrates to the ground state of *E*-DASA but in higher vibrational levels. Lastly, vibrational cooling takes place to form the *E*-DASA photoproduct in its electronic and vibrational ground state. The respective excited state dynamics happen on a 3.3 - 8.8 and 5.3 - 77.9 ps time scale. In the TA data, the induced excitation is witnessed by the GSB at about 548 - 570 nm and the SE at around 602 - 625 nm. At early times, the GSB in all experiments exhibits a smaller FWHM compared to the steady state absorption due to the spectral overlap with the positive ESA. With increasing time delay, the maximum intensity of the former experiences a

Table 5.3. Comparison of the lifetimes upon switching DASA (*Z*-to-*E*) in different environments obtained by GA. In addition to the listed time constants, a lifetime τ_3 >> 8 ns (experimental period) is identified in all measurements.

Mixture	τ_1 [ps]	τ_2 [ps]
DASA in Tol	4.3 ± 0.2	9.2 ± 0.2
DASA+Azo in Tol	3.5 ± 0.2	7.1 ± 0.2
DASA+switched Azo in Tol	3.3 ± 0.2	7.3 ± 0.2
DASA MeCN	3.5 ± 0.2	5.8 ± 0.2
DASA+Azo in MeCN	3.3 ± 0.2	5.3 ± 0.2
DASA+switched Azo in MeCN	3.3 ± 0.2	5.3 ± 0.2
DASA in PMMA	5.5 ± 0.2	64.6 ± 0.3
DASA+Azo in PMMA	8.8 ± 0.2	77.9 ± 0.7
DASA+switched Azo in PMMA	5.7 ± 0.2	50.7 ± 0.4

hypsochromic shift. The intermediate S_1 state is observed by its ESA located at about 445 - 450 nm. The absorption of the generated *E*-DASA photoproduct in its electronic ground state is observed at later times. First, it is situated at around 575 - 600 nm due to the occupation of higher vibrational levels. The signal is spotted in the EADS of the offsets more easily than in the experimental data as it spectrally overlaps with the SE. Finally, vibrational relaxation occurs to form the final signal at about 602 - 625 nm of the photoproduct. The findings are in agreement with other literature reported donor-acceptor-Stenhouse adducts.[247][263][262][256]

Comparing the findings in the different environments, namely in a non-polar solution using Tol, an aprotic polar solution using MeCN and a solid state using PMMA blends, a general trend crystallises. Similar to the switching of Azo, quantum chemical simulations show that also the dynamics of photoswitching DASA are barely affected by the surrounding polarity.[258] However, MeCN exhibits a lower molecular weight and thus better energy dissipation accelerating vibrational relaxation.[273] Both time constants decrease by 0.8 and 3.4 ps by substituting Tol with MeCN, respectively. In solid state, both time constants increase by 1.2 and 55.4 ps, respectively, compared to Tol as well as by 2.0 ps and 58.8 ps, respectively, compared to MeCN. The molecular movement of the photoswitch is sterically hindered in solid state. Thus, slower dynamics in thin films in comparison to solutions are plausible.

More interestingly, the influences and interactions between the photoswitches are studied. In solution, the presence of Azo accelerates the excited state dynamics upon photoswitching DASA. Upon addition of Azo, both lifetimes are shortened by 0.9 and 2.0 ps in Tol, respectively, as well as by 0.2 and 0.5 ps in MeCN, respectively. The configuration of Azo did thereby not change the excited state dynamics. Thus, the found time constants in the presence of *trans*-Azo and *cis*-Azo do not differ within their error limits. However, as the lifetimes do not change dramatically, the impact of Azo on the switching behaviour of DASA is not related to interactions but rather to influences by changing the environment. The polarity of the environment increases slightly upon addition of Azo since *trans*-Azo and *cis*-Azo exhibit dipole moments of 6.8 and 4.2 D, respectively, as determined by DFT calculations using the 6-31++G(d,p) basis set (tables B.3 and B.4 appendix B). However, quantum chemical simulations reveal barely polarity influence on the excited state dynamics such that dynamic effects cause the acceleration upon adding Azo.[258] In thin film samples, both time constants are increased by adding Azo. Due to restricted mobility of the photoswitchable molecules in the PMMA matrix, other influences are present compared to solution leading to different impacts.

By comparing all obtained results from the simultaneous switching of both photoswitches Azo (trans-to-cis) and DASA (*Z*-to-*E*) in the examined environments, several conclusions can be drawn (table 5.4). First, all simultaneous switching processes have in common that Azo and DASA switch individually. No additional features are obtained

Table 5.4. Comparison of the lifetimes upon simultaneous switching of Azo (trans-to-cis) and DASA (*Z*-to-*E*) in different environments obtained by GA. In addition to the listed time constants, a lifetime τ_5 >> 8 ns (experimental period) is identified in all measurements. For better comparison of the time constants, related constants within one environment are lined up vertically.

Mixture	τ_1 [ps]	τ_2 [ps]	τ_3 [ps]	τ_4 [ps]
Azo in Tol	< 0.2 ± 0.2	0.9 ± 0.2	3.9 ± 0.2	
DASA in Tol			3.8 ± 0.2	7.5 ± 0.2
Azo+DASA in Tol	< 0.2 ± 0.2	1.3 ± 0.2	3.9 ± 0.2	8.8 ± 0.2
Azo MeCN	< 0.2 ± 0.2	0.6 ± 0.2	2.9 ± 0.2	
DASA in MeCN			4.1 ± 0.2	6.7 ± 0.2
Azo+DASA in MeCN	< 0.2 ± 0.2	0.3 ± 0.2	4.1 ± 0.2	7.1 ± 0.2
Azo in PMMA	< 0.2 ± 0.2	1.3 ± 0.2	27.1 ± 0.5	
DASA in PMMA			6.4 ± 0.2	71.5 ± 0.6
Azo+DASA in PMMA	< 0.2 ± 0.2		5.8 ± 0.2	67.2 ± 0.7

which would hint at mutual interactions. Accordingly, the excited state dynamics observed are unaltered and act as described in the above paragraphs for trans-to-cis photoisomerisation of Azo and *Z*-to-*E* photoisomerisation of DASA, respectively.
Considering the different environments, namely the non-polar solution in Tol, the polar aprotic solution in MeCN and the solid environment in a PMMA blend thin film, a clear trend shows up. The time constants increase with lower molecular weight of the environment due to dynamic effects[273] since the processes happen faster in MeCN than in Tol than in PMMA. No relationship to the polarity of the environment is drawn since quantum chemical calculations show no polarity effects on the excited states.[258] This holds true for the excited state dynamics of Azo, since both determinable lifetimes are shortened in MeCN by 0.3 and 1.0 ps, respectively, and of DASA, as the shortest time constants is barely affected but the second is abridged by 0.8 ps in MeCN compared to Tol. Regarding the PMMA blend film, all dynamics are decelerated. Again, this applies for Azo switching which exhibits lifetimes extended by 0.4 and 23.2 ps, respectively, compared to Tol solution and 0.7 and 24.2 ps, respectively, compared to MeCN solution, and for DASA switching featuring time constants prolonged by 2.6 and 64.0 ps, respectively, in comparison with Tol solution as well as by 2.3 and 64.8 ps, respectively, in comparison with MeCN solution. Slower processes in solid state are very comprehensible because the rearrangement of the molecules is prohibited compared to the conditions in solution due to a steric hindrance of the rigid solid environment.
In addition, the obtained lifetimes and spectral features are compared to the individual Azo and DASA switching processes induced by absorption wavelengths with higher cross sections, namely around 415 - 431 nm and 582 - 585 nm, respectively. Since

the Azo switching is in the current case induced by light of lower energy, the signals obtained are also at slightly lower energies resulting in a bathochromic shift of the data. In turn, DASA switching is initiated by light of higher energy in the current case, with the spectra in solution barely affected while the thin film data shows a small hypsochromic shift. Considering the time constants of Azo switching, they are accelerated in solution when excited with 506 - 515 nm compared to excitation with shorter wavelengths. More precisely, the lifetimes using the simultaneous switching wavelength are shortened by 0.3 and 0.8 ps in Tol, respectively, and by 0.1 and 1.0 ps in MeCN, respectively. In contrast, for thin films the time constants are extended using the simultaneous switching wavelength by 0.1 and 11.7 ps, respectively. For DASA, no clear trend emerges since both time constants are accelerated by 0.5 and 1.7 ps in Tol whereas they are decelerated by 0.6 and 0.9 ps in MeCN and slowed down in PMMA blend films by 0.9 and 6.9 ps, respectively, if an excitation wavelength of 506 - 515 nm is set compared to longer excitation wavelengths.
Comparing the determined lifetimes of the single switching processes if excited with 506 - 515 nm with the results of the 1:1 molar mixture, the latter results are not that simple. In Tol, the second and fourth lifetime is extended by 0.4 and 1.3 ps while the third remains unaltered. For MeCN solutions, the determined time constant related to Azo switching is shortened by 0.3 ps while the second lifetime assigned to DASA switching is extended by 0.4 ps. In thin film samples, both DASA related lifetimes are shortened by 0.6 and 4.3 ps, respectively. The outcomes of the measurements in solutions are not in line with the former found trend of accelerating processes upon addition of the other photoswitch due to dynamic effects. Furthermore, the previously observed behaviour of decelerated processes in solid samples upon addition of the other photoswitch is not met. However, as this time the other photoswitch is not only present but also switching, the changes upon photoexcitation have to be taken into account such that a more complex analysis is needed to fully understand the found tendencies.

5.4. UV/VIS kinetic measurements

Since TA measurements are beneficial to reveal excited state dynamics on the ultrashort time scale but only capture the first of four steps of the DASA switching process (figure 5.4), exclusively TA experiments are insufficient to describe and analyse the photoswitching and the influences of the photoswitches on each other. Hence, UV/VIS kinetic measurements of the trans-to-cis photoisomerisation of Azo and linear-to-closed photoisomerisation (DASA isomer **A** to **C'**) of DASA excited orthogonally and simultaneously in Tol are studied upon excitation with LEDs. Again, the mixtures of both photoresponsive materials are hold at an equimolar ratio to maximise possible interactions and influences. The orthogonal Azo switching is thereby induced by an LED

with maximum intensity at a wavelength of 434 nm holding an output power of 2.78 mW while the orthogonal DASA switching is induced by an LED with maximum intensity at a wavelength of 594 nm and an output power of 4.85 mW. In contrast, the simultaneous switching was stimulated by an LED with its maximum wavelength at 507 nm keeping an output power of 20.04 mW (all LED spectra in figure B.1 appendix B). Hence, the effective cross sections upon photoexcitation of Azo and DASA inducing trans-to-cis and linear-to-closed isomerisation, respectively, are calculated. Furthermore, the thermal backswitching processes are investigated as well (*cis*-Azo to *trans*-Azo and closed zwitterionic DASA isomer **C'** to linear *Z*-DASA). Due to the temperature control within the setup, the activation energies for the thermal steps can be determined.
MeCN solutions and PMMA blend films are not examined since DASA-PMMA blends are not stable upon irradiation with light without movement. Unfortunately, the UV/VIS spectrometer offers no opportunity to move the sample during the measurement as it was the case in the TA setup. MeCN solutions were not studied as the photoswitching in MeCN is too slow to be measured accurately with the available excitation powers. Even by changing the excitation wavelength to 560 nm to gain a better spectral overlap of the LED emission (figure B.1 appendix B) and the DASA absorption in MeCN, no good results could be obtained.
All data shown in this section are normalised to the highest intensity in an equilibrium state before turning on the LED to induce photoswitching. Thus, also for the backswitching processes, a normalised absorbance of 1 refers to the maximum intensity before starting the prior photoswitching with light.

5.4.1. Switching processes of Azo

First, the photoswitching (trans-to-cis) and the thermal backswitching (cis-to-trans) of Azo are examined. Orthogonal photoswitching of pure Azo and in the presence of DASA is thereby studied as well as the switching behaviour of Azo if the simultaneous switching wavelength is used, again for both pure Azo in Tol and for the simultaneously addressed mixture of Azo+DASA. For the thermal backswitching, however, the wavelength inducing the photoswitching beforehand is irrelevant. Thus, the thermal backswitching is fully investigated by the thermal backswitching of pure Azo, in the presence of non-switched *Z*-DASA and in the presence of backswitching DASA (closed-to-linear isomerisation) after simultaneous photoexcitation.

Switching Azo orthogonally

To begin with, the Azo photoswitching upon orthogonal excitation is studied (trans-to-cis) as well as its respective thermally induced back reaction (cis-to-trans) (figure 5.43). Upon photoexcitation, the broad absorption band decreases in its intensity, slightly

broadens and undergoes a small redshift while a new hypsochromically shifted peak is observed (figure 5.43**a**). The thermal backswitching (cis-to-trans) constitutes the reverse process with the same spectral features involved (figure 5.43**b**). In both cases, an isosbestic point located at about 386 nm is observed indicating the stoichiometric formation from one chemical species into another.

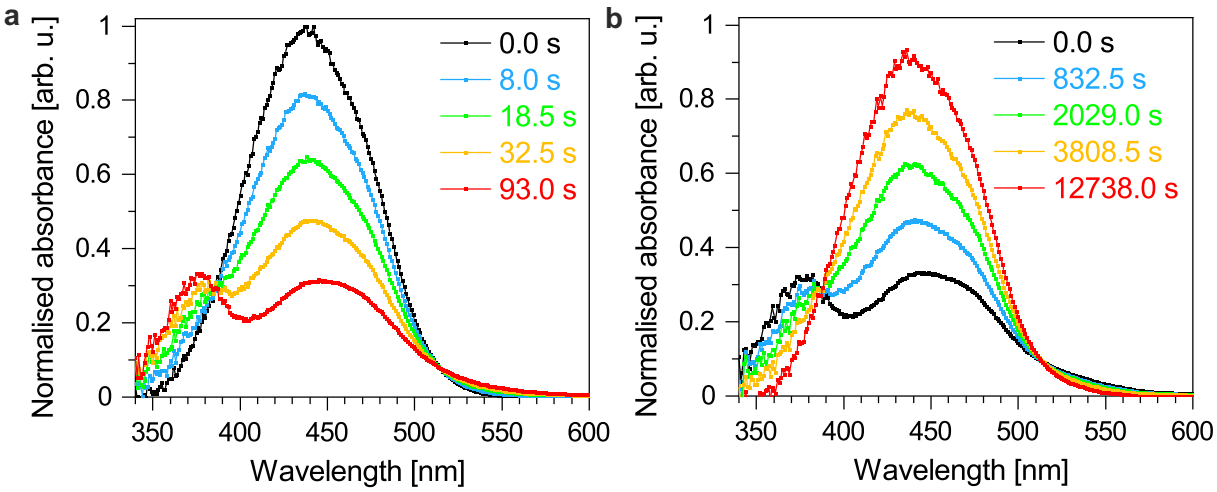

Figure 5.43. Absorption spectra of Azo in Tol at 30 °C upon (a) switching with an LED having its maximum wavelength at 434 nm (trans-to-cis) and (b) thermal backswitching (cis-to-trans).

The observed absorption bands are temperature dependent exhibiting slight blueshifts upon increasing temperature (figure 5.44). More precisely, the higher energy absorption attributed to *cis*-Azo shifts from 380 to 377 nm and the *trans*-Azo absorption maximum varies from 450 to 444 nm with increasing temperature (figure 5.44**a**). In contrast, the spectra of the solutions before switching, which contain a mixture of mainly *trans*-Azo but also to a small degree *cis*-Azo in the photostationary state in the dark, reveal maximum positions at 441 to 435 nm (figure 5.44**b**).

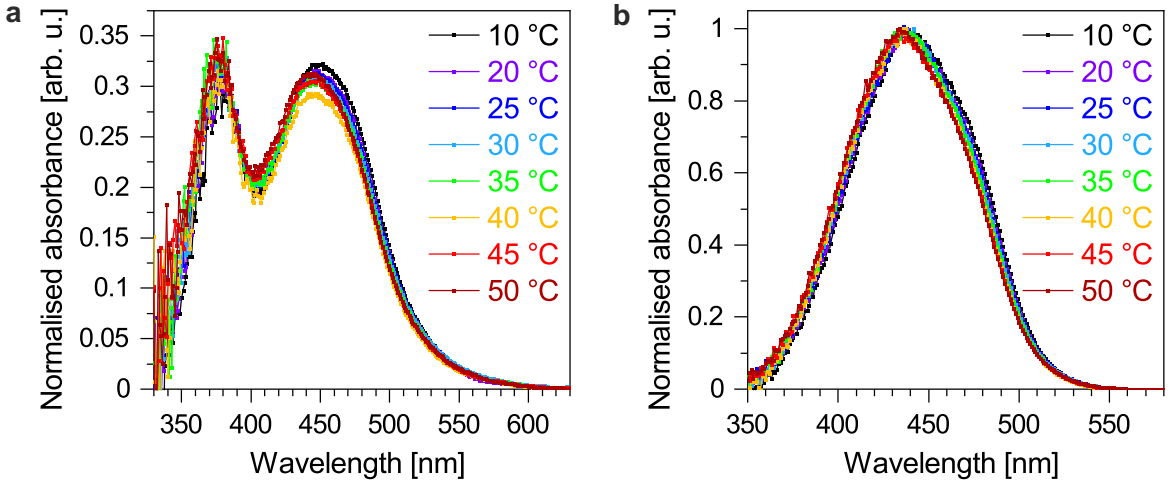

Figure 5.44. Absorption spectra of Azo in Tol at different temperatures (a) under LED illumination and (b) in the dark with both exhibiting small hypsochromic shifts.

To follow the kinetic upon excitation with light, the maximum position of *trans*-Azo is analysed versus time. In general, monitoring the absorption band of the trans species is advantageous as it is more intense than the *cis*-Azo absorption with the latter additionally being close to the short-wavelength end of the spectral window resulting in higher signal-to-noise ratios and thus less accuracy. As the trans-to-cis photoisomerisation of Azo contains no thermal step, no temperature dependence is observed and hence no activation energy can be determined. However, the effective cross section can be calculated according to equation 2.6 after determining the lifetime of *trans*-Azo by fitting the decay of the respective maximum absorption wavelength with a monoexponential fit and calculating the photon dose according to equation 2.7 resulting in $(5.21 \pm 0.26) \cdot 10^{-18}$ cm^{-2} (figure B.5**a** appendix B and table 5.5).
In contrast, the backswitching can be induced by thermal energy such that the thermal lifetimes and activation energies upon cis-to-trans isomerisation can be researched. Therefore, the maximum absorption of the trans species is monitored versus time at different temperatures (figure 5.45**a**). Beside the obvious shorter rise times with increasing temperature, higher temperatures lead to a higher percentage of backswitched molecules with all applied temperatures yielding more than 90 % backswitched molecules. To analyse the data, the rising curves are fitted with a monoexponential fit function to gain lifetimes of 2994.2, 1105.9, 382.6 and 138.8 s for 30, 40, 50 and 60 °C, respectively. In turn, the rate constants are obtained by inserting the determined lifetimes in equation 2.24. Following, an Arrhenius plot (section 2.2.4) is constructed to create a linear fit and extract an activation energy of (86.2 ± 2.1) kJ mol^{-1} based on the slope of the linear fit (figure 5.45**b**).

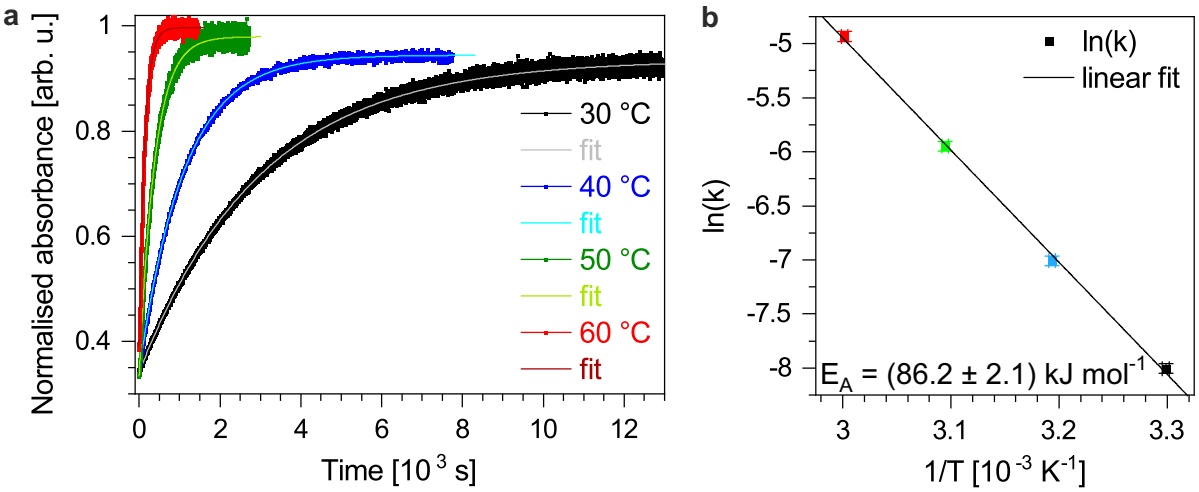

Figure 5.45. (a) Rises of the maximum absorption of Azo, which can be assigned to the trans-isomer, in Tol and their monoexponential fits upon thermal backswitching (cis-to-trans) at different temperatures. Using the rate constants of those fits, (b) an Arrhenius plot can be applied to determine the activation energy of the cis-to-trans isomerisation.

Switching Azo orthogonally in the presence of DASA

Next, a 1:1 molar ratio of Azo and DASA in Tol is studied upon orthogonal Azo excitation and thermal backswitching (figure 5.46). For the trans-to-cis photoisomerisation of Azo, the initial broad Azo absorption band slightly bathochromically shifts and broadens while a simultaneous rise of a higher energy band attributed to the photoproduct *cis*-Azo is observed upon photoexcitation (figure 5.46**a**). Again, an isosbestic point at 386 nm is present. The DASA absorption band stays essentially constant. For the thermal backswitching (cis-to-trans), the Azo features are reversed with the isosbestic point obtained as well (figure 5.46**b**). However, the absorption band of DASA gains about 10 % in its intensity in the measurement at 20 °C.

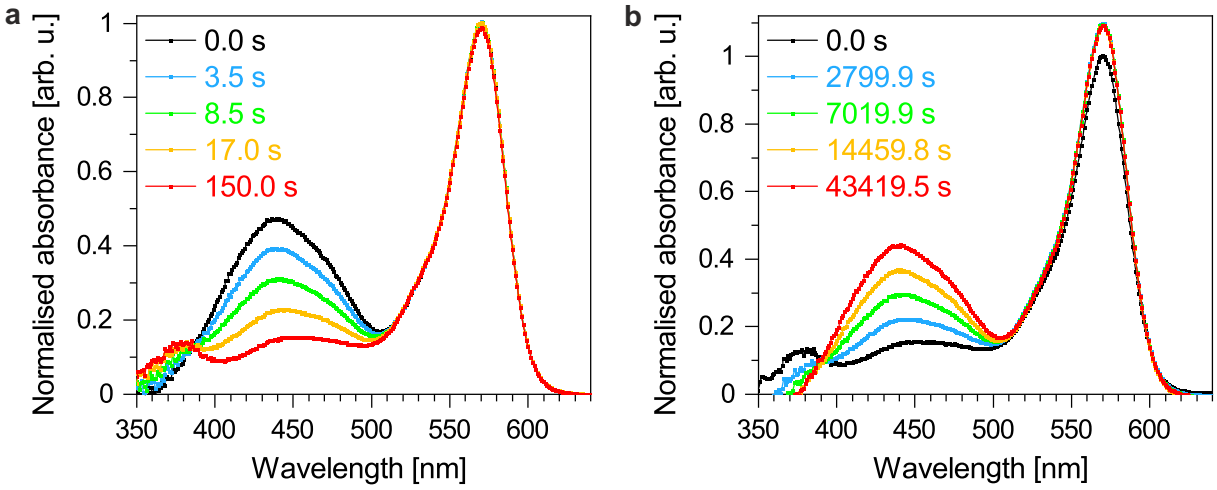

Figure 5.46. Absorption spectra of Azo in Tol at 20 °C while DASA is present upon (a) switching with an LED having its maximum wavelength at 434 nm and (b) thermal backswitching.

Taking a closer look at the absorption maxima of the involved species versus time upon orthogonal photoexcitation of Azo in the presence of DASA, a clear rise in intensity of the photoproduct *cis*-Azo with simultaneous decrease of *trans*-Azo is identified as expected (figure 5.47**a**). The absorption band of the linear DASA isomer **A** decreases slightly in its intensity by around 1.6 % (figure 5.47**b**) due to the broad spectral range of the illuminating LED which overlaps with the absorption of DASA in contrast to the TA laser in the prior section. However, this amount is negligible and no absorption of the *E*-isomer of DASA is detectable (figure 5.47**a**). Hence, the Azo switching can be denoted as orthogonal. The effective cross section is determined by fitting the decay curve of the maximum absorption wavelength of the trans-isomer of Azo with a monoexponential curve (figure B.5**b** appendix B). Following, the effective cross section is calculated using the determined lifetime and the respective photon dose according to equations 2.6 and 2.7 resulting in $(6.79 \pm 0.34) \cdot 10^{-18}$ cm^{-2} (table 5.5). Thus, the effective cross section of Azo is increased by $1.58 \cdot 10^{-18}$ cm^{-2} due to the presence of DASA.

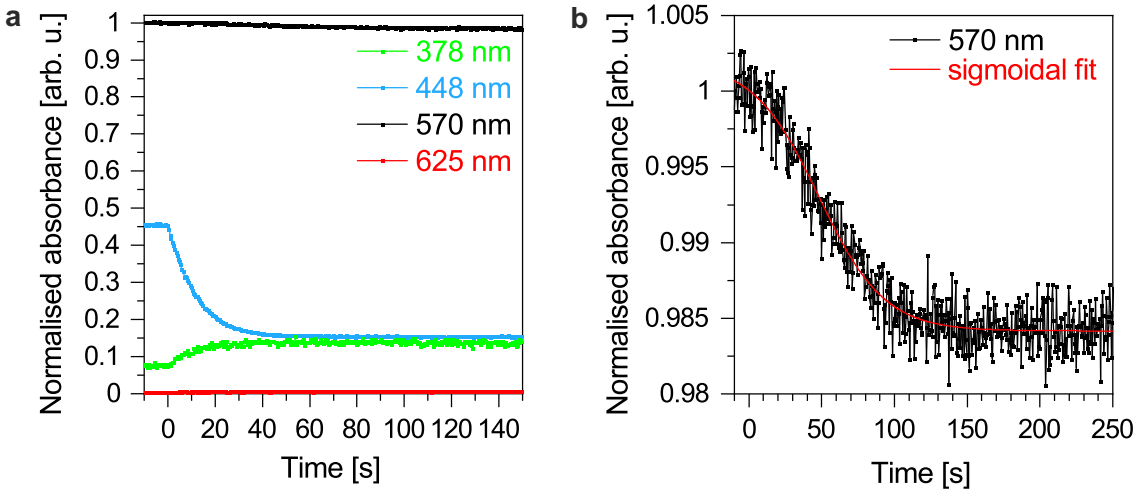

Figure 5.47. Change of absorbance of the signals at 378, 448, 570 and 625 nm upon switching Azo in Tol at 20 °C with light while DASA is present. (a) The signal of the *trans*-Azo at 448 nm decreases while the signal at 378 nm corresponding to *cis*-Azo increases. The signal at 570 nm attributed to the linear *Z*-isomer **A** of DASA decreases slightly while no transient signal of *E*-DASA at 625 nm could be detected. (b) The switched amount of DASA is negligible with about 1.6 %.

Examining the temporal behaviour of the absorption maxima of the involved species upon thermal backswitching of Azo in the presence of DASA, the intensity of the back-switched product *trans*-Azo rises while the intensity of *cis*-Azo decreases as expected (figure 5.48**a**). Referring to the DASA signals, no *E*-DASA is observed whereas the intensity of *Z*-DASA rises two orders of magnitude faster compared to the Azo features. Comparing the maximum DASA intensities at different temperatures, all experiments

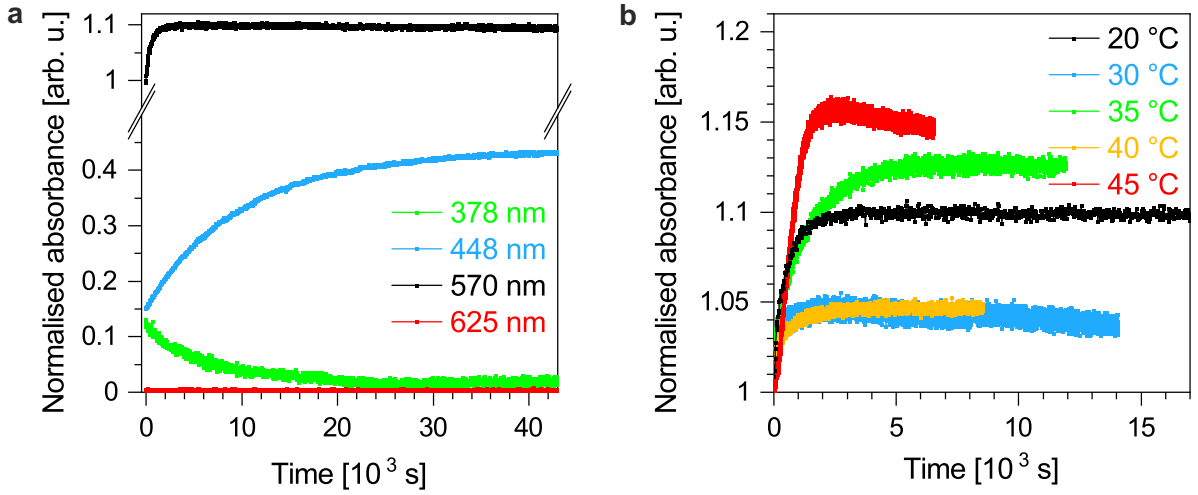

Figure 5.48. (a) Change of absorbance of the signals at 378, 448, 570 and 625 nm upon thermal backswitching of Azo in Tol at 20 °C while DASA is present. The signal at 448 nm representing the *trans*-Azo increases while the signal at 378 nm corresponding to *cis*-Azo decreases. No transient signal from *E*-DASA can be detected at 625 nm. The signal of the linear *Z*-DASA isomer **A** at 570 nm increases. (b) The latter holds true for all temperatures with no observed trend in temperature.

show a fast rise of about 4 - 16 % (figure 5.48**b**). Some traces contain a small decrease in intensity at later times. However, no clear trend with temperature is observed. Hence, the backswitching of Azo induces the formation of the linear DASA isomer **A** but in an undefined way such that DASA is probably not in an equilibrium state but its intensity may decrease after a longer time period.
Considering the rise of the maximum absorption assigned to *cis*-Azo in the presence of DASA upon thermal backswitching at different temperatures, the rise times decrease with increasing temperature but the percentage of backswitched Azo is high in all cases revealing only a small trend towards a higher amount of backswitching with higher temperatures (figure 5.49**a**). The lifetimes upon backswitching are determined by monoexponential fits. Thus, lifetimes of 10121.5, 3423.1, 1866.3, 1178.8 and 679.7 s are ascertained for 20, 30, 35, 40 and 45 °C, respectively. By calculating the rate constants according to equation 2.24, an Arrhenius plot (section 2.2.4) can be prepared (figure 5.49**b**). Next, a linear fit curve is applied to extract the activation energy based on the slope of the fit curve which amounts to (83.6 ± 1.4) kJ mol^{-1}. Thus, the activation energy for the thermally activated backswitching of Azo is decreased by 2.6 kJ mol^{-1} in the presence of DASA.

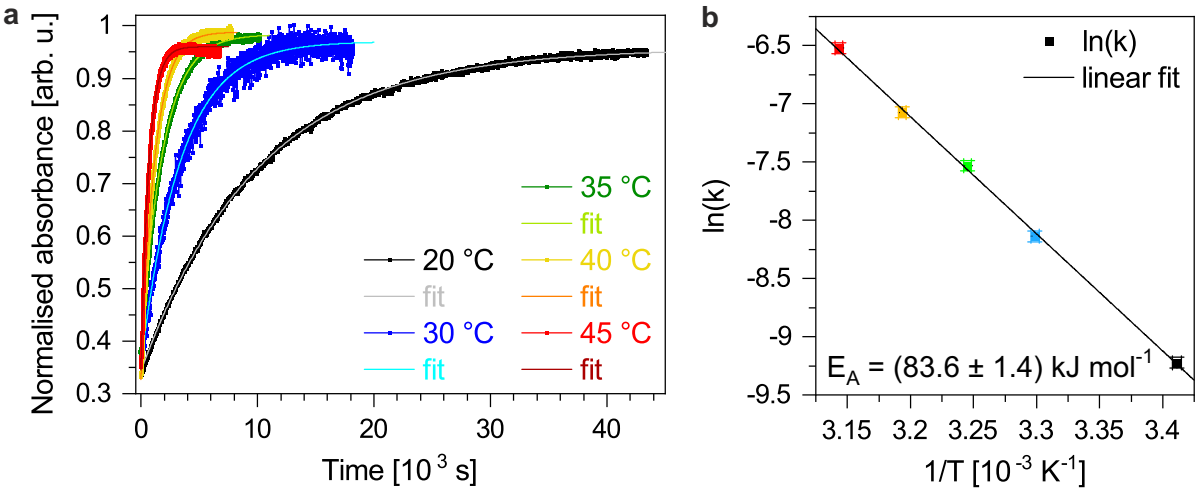

Figure 5.49. (a) Rises of the maximum absorption of Azo, which can be assigned to the trans-isomer, in Tol and their monoexponential fits upon thermal backswitching at different temperatures while DASA is present. Using the rate constants of those fits, (b) an Arrhenius plot can be applied to determine the activation energy of the cis-to-trans isomerisation.

Switching Azo simultaneously with DASA

Lastly, the Azo photoswitching (trans-to-cis) and thermal backswitching (cis-to-trans) behaviour upon simultaneous switching of both photoresponsive molecules is studied. Therefore, first the photoisomerisation of pure Azo excited by 507 nm is examined to gain the effective cross section at the varied photon wavelength. The decay curve of the maximum absorption wavelength of *trans*-Azo is analysed by a monoexponential

fit to obtain the respective lifetime (figure B.5**c** appendix B). Next, the effective cross section is calculated according to equation 2.6 by inserting the determined lifetime and the photon dose using equation 2.7 (table 5.5). Analogously, the effective cross section of Azo upon simultaneous photoswitching of Azo+DASA is assigned (figure B.5**d** and table 5.5). Hence, the effective cross sections number (0.97 ± 0.05) · 10^{-18} cm^{-2} and (1.74 ± 0.09) · 10^{-18} cm^{-2} for pure Azo and the Azo+DASA mixture, respectively, using a simultaneous switching wavelength of 507 nm. Hence, the effective cross section of Azo upon trans-to-cis photoswitching is about 4.24 · 10^{-18} cm^{-2} smaller for 507 nm excitation compared to 434 nm excitation and it is increased by the presence of DASA compared to pure Azo in Tol.

Taking a look at the change of absorbance upon photoexcitation, the absorptions of the thermodynamically more stable isomers of Azo and DASA both decay with the former decaying faster (figure 5.50**a**). Simultaneously, the absorption band of *cis*-Azo at shorter wavelengths increases in intensity and the transient absorption band of *E*-DASA occurs at longer wavelengths. The thermal backswitching, however, exhibits no transient DASA absorption (figure 5.50**b**). While the absorption of *cis*-Azo decreases in its intensity, the absorption bands of *trans*-Azo and *Z*-DASA increase. The backswitching of DASA is thereby faster than the backswitching of Azo. Similar to the thermal backswitching of Azo with DASA being present but not switching, the intensity of DASA increases above 1.

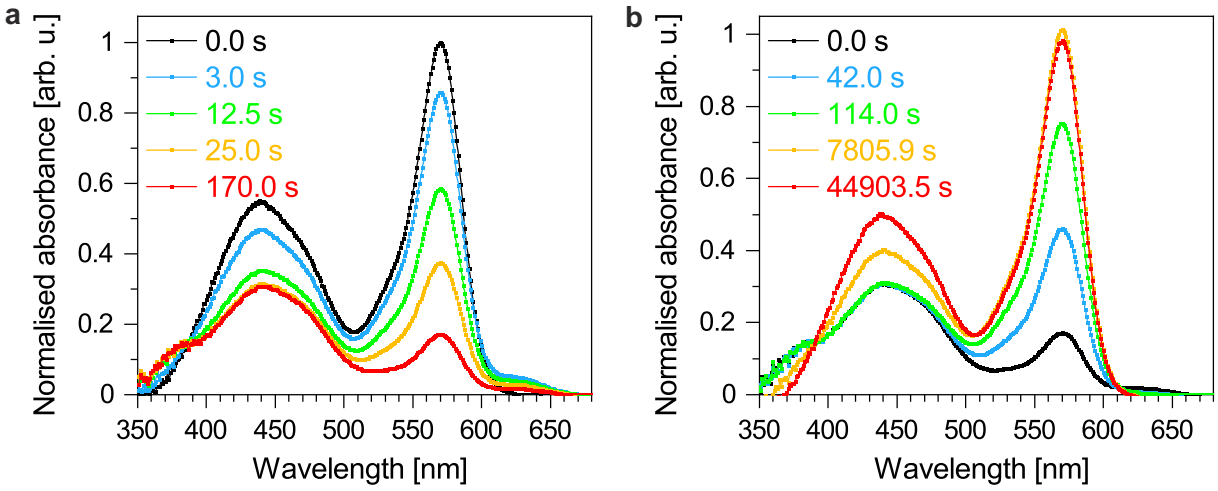

Figure 5.50. Absorption spectra of an equimolar mixture of Azo and DASA in Tol at 20 °C switched simultaneously. (a) Switching with an LED having its maximum wavelength at 507 nm (*trans*-Azo to *cis*-Azo and *Z*-DASA to the closed DASA isomer **C'**) and (b) thermal backswitching (*cis*-Azo to *trans*-Azo and closed DASA isomer **C'** to *Z*-DASA).

Subsequently, the thermally activated backswitching of Azo (cis-to-trans) while DASA undergoes simultaneously a thermal backswitching reaction is studied depending on the temperature (figure 5.51**a**). The rise times are thereby shorter for higher temperatures and the percentage of backswitched Azo molecules increase with increasing

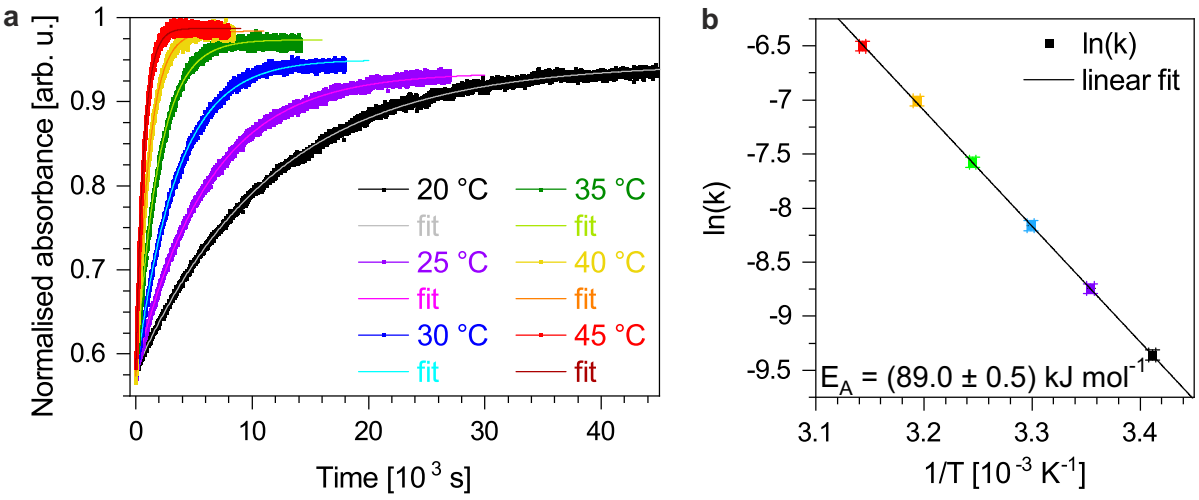

Figure 5.51. (a) Rises of the maximum absorption of Azo, which can be assigned to the trans-isomer, in Tol and their monoexponential fits upon thermal backswitching at different temperatures while DASA is thermally backswitched simultaneously. Using the rate constants of those fits, (b) an Arrhenius plot can be applied to determine the activation energy of the cis-to-trans isomerisation.

temperature. The rising curves of the respective maximum absorption of the trans-isomer result in shorter lifetimes and reveal a higher percentage of backswitched Azo molecules with increasing temperature. To analyse the kinetic data, all curves are fitted with monoexponential curves to extract the lifetimes of 11608.3, 6281.4, 3507.1, 1951.9, 1106.2 and 667.0 s for 20, 25, 30, 35, 40 and 45 °C, respectively. Next, the rate constants are calculated based on the lifetimes according to equation 2.24. Following, they are plotted in an Arrhenius plot (section 2.2.4) to construct a linear fit (figure 5.51**b**). Thus, the activation energy is determined using the slope of the linear fit curve which amounts to (89.0 ± 0.5) kJ mol^{-1}. Hence, the activation energy for the thermal backswitching of Azo is raised up to 5.4 kJ mol^{-1} for simultaneous backswitching of both photoresponsive molecules compared to pure Azo and Azo in the presence of non-switching DASA.

Comparison of the UV/VIS kinetics upon addressing Azo

Comparing the obtained results of the switching processes of Azo, first the percentages of switched (*cis*-Azo) and backswitched (*trans*-Azo) molecules compared to the initial number of molecules are examined. Therefore, their normalised absorption intensities are utilised to calculate the percentages. Applying a broad temperature range, the percentage of switched Azo molecules increase with increasing temperature (figure 5.52**a**). However, in the most interesting temperature region of room temperature and increased temperatures up to 50 °C, the number is quite constant around 67.5 % for pure Azo using the orthogonal switching wavelength. The presence of DASA does not affect the amount of switched molecules significantly such that the percentage

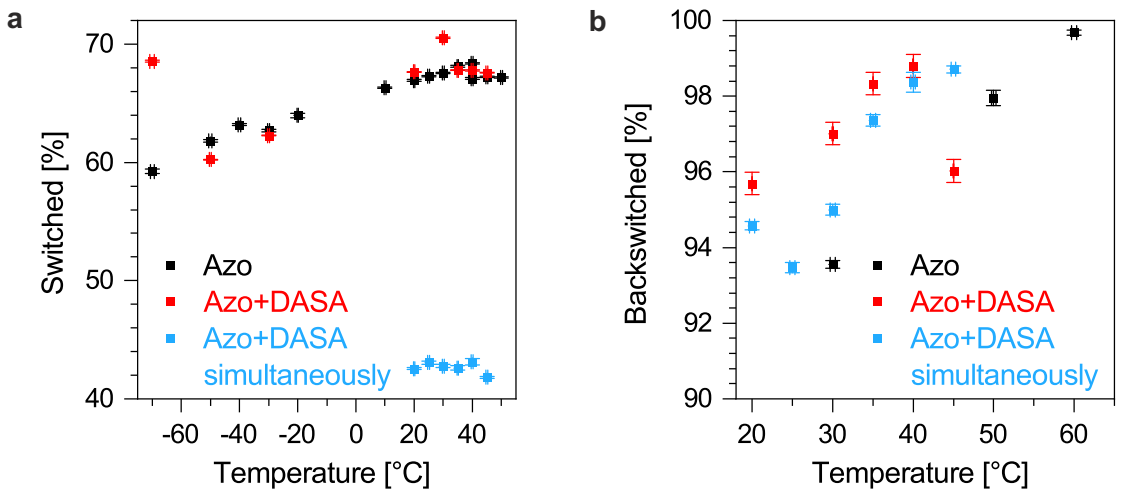

Figure 5.52. Percentage of (a) switched Azo after switching with light and of (b) backswitched Azo after thermal backswitching in Tol. If not labelled differently, the orthogonal switching wavelength was applied such that DASA was not switching or backswitching.

for room temperature or higher is about constant numbering around 67.7 %. In contrast, significantly less Azo molecules are switched by simultaneous excitation of both photoresponsive molecules with light using a wavelength of 507 nm. Again, the percentage of switched molecules stays essentially constant at room temperature and higher temperatures but amounts only to around 44.7 % which is about 22.9 % less compared to the orthogonal switching wavelength.

Considering the thermal backswitching, again higher amounts of backswitched molecules with higher temperatures are observed but the increase is more pronounced for the thermal backswitching (figure 5.52**b**) compared to the photoinduced switching (figure 5.52**b**). This holds true for pure Azo, in the presence of DASA and for backswitching Azo if DASA is backswitched simultaneously. By a rough estimation, the percentages of backswitched molecules is lowest for pure Azo, increases by about 2 % for backswitching Azo and DASA simultaneously and further increases by around 2 % for backswitching Azo in the presence of DASA.

In a contrasting juxtaposition of the effective cross sections upon photoisomerisation of Azo (trans-to-cis) in different environments, the presence of DASA increases the latter characteristic (table 5.5). This applies for the orthogonal photoswitching as well as for the simultaneous photoswitching process. Using the orthogonal switching wavelength, the effective cross section for pure Azo amounts to $(5.21 \pm 0.26) \cdot 10^{-18}$ cm^{-2} and increases significantly by $1.58 \cdot 10^{-18}$ cm^{-2} to $(6.79 \pm 0.34) \cdot 10^{-18}$ cm^{-2} in the presence of DASA. Contrasting the switching wavelengths of pure Azo, the simultaneous switching wavelength exhibits a much smaller effective cross section of $(0.97 \pm 0.05) \cdot 10^{-18}$ cm^{-2} reduced by $4.24 \cdot 10^{-18}$ cm^{-2} compared to the orthogonal switching wavelength. This is mostly due to the smaller spectral overlap of the Azo absorption in Tol and the excitation wavelength. Again, the addition of DASA increases the effective cross section

Table 5.5. Determined effective cross sections of orthogonal trans-to-cis photoswitching of Azo if used purely and in the presence of DASA and if the switching wavelength is changed to simultaneous switching using a pure Azo solution and both photoswitches.

	Azo orthogonally	Azo+DASA orthogonally	Azo simultaneously	Azo+DASA simultaneously
τ [s]	22.41 ± 0.10	17.20 ± 0.09	14.39 ± 0.05	7.95 ± 0.03
n_p [10^{15} s^{-1} cm^{-2}]	8.6 ± 0.4	8.6 ± 0.4	72 ± 4	72 ± 4
λ [nm]	434	434	507	507
σ [10^{-18} cm^{-2}]	5.21 ± 0.26	6.79 ± 0.34	0.97 ± 0.05	1.74 ± 0.09

by about $0.77 \cdot 10^{-18}$ cm^{-2} to $(1.74 \pm 0.09) \cdot 10^{-18}$ cm^{-2} which is $5.05 \cdot 10^{-18}$ cm^{-2} lower compared to the mixture using the orthogonal switching wavelength. Thus, the small effective cross section may cause the low percentage of switched Azo molecules using the simultaneous switching wavelength for excitation (figure 5.52**a**). To sum up, the presence of DASA increases the effective cross sections with the orthogonal excitation wavelength yielding much higher effective cross sections due to a better spectral overlap resulting in about one third more switched molecules.

Analysing the thermal backswitching of Azo (cis-to-trans) in different environments, the lifetimes at different temperatures are quite similar (table 5.6). All lifetimes decrease with higher temperatures as expected. The shortest lifetimes and thus the fastest backswitching is found for pure Azo in Tol solutions. The addition of DASA leads only to a small increase of the determined time constants. Thermal backswitching of Azo while DASA undergoes simultaneous thermal backswitching, however, reveals the longest

Table 5.6. Comparison of the lifetimes of the cis-to-trans isomerisation of Azo in Tol upon thermal backswitching when Azo is used purely or DASA is present or DASA is thermally backswitched simultaneously.

Temperature [°C]	Lifetime [s]		
	Azo	Azo+DASA	Azo+DASA simultaneously
20	-	10121.5 ± 12.1	11608.3 ± 12.7
25	-	-	6281.4 ± 5.7
30	2994.2 ± 1.9	3423.1 ± 17.9	3507.1 ± 4.2
35	-	1866.3 ± 2.0	1951.9 ± 2.2
40	1105.9 ± 1.9	1178.8 ± 0.4	1106.2 ± 0.9
45	-	679.7 ± 0.5	667.0 ± 0.8
50	382.6 ± 0.7	-	-
60	138.8 ± 0.3	-	-

time constants for temperatures below 40 °C. At higher temperatures, the lifetimes are shorter compared to the lifetimes of thermally backswitching Azo in the presence of DASA. In comparison to the results upon photoinduced backswitching of Azo investigated by TA measurements, the trend of slightly decreasing lifetimes upon addition of DASA in the latter experiments is reversed for the thermally induced reaction.
Considering the thermal backswitching, the activation energy and its dependence on the environment is of high interest (table 5.7). The activation energy for pure Azo solutions amounts to (86.2 ± 2.1) kJ mol^{-1} which is significantly less compared to 95 kJ mol^{-1} of the parent azobenzene molecule in solution.[228] Adding DASA to the solution decreases the activation energy slightly by 2.6 kJ mol^{-1} to (83.6 ± 1.4) kJ mol^{-1}. Changing the system to simultaneously thermally backswitching Azo and DASA, however, increases the activation energy significantly by 5.4 kJ mol^{-1} to (89.0 ± 0.5) kJ mol^{-1}.

Table 5.7. Comparison of the activation energies upon thermal cis-to-trans backswitching of Azo in Tol when Azo is used purely or DASA is present or DASA is thermally backswitched simultaneously.

Photoswitch	Activation energy of the cis-to-trans isomerisation [kJ mol^{-1}]
Azo	86.2 ± 2.1
Azo+DASA	83.6 ± 1.4
Azo+DASA simultaneously	89.0 ± 0.5

5.4.2. Switching processes of DASA

In this section, the photoswitching (linear-to-closed) and thermal backswitching (closed-to-linear) processes of DASA in Tol are studied for pure DASA solutions, in the presence of *trans*-Azo and while Azo is switched simultaneously (*trans*-Azo to *cis*-Azo during photoswitching and *cis*-Azo to *trans*-Azo during thermal backswitching). Since for DASA both the photoisomerisation and the thermally activated backswitching in the dark contain thermal steps which are rate determining as it will be shown in the next paragraph, the switching wavelength carry no weight but the environment in terms of Azo presence.

Switching DASA orthogonally

At first, the switching processes upon isomerisation of DASA in Tol both photoexcited (linear-to-closed) and the thermally activated back reaction (closed-to-linear) are researched. The UV/VIS spectra upon photoexcitation show the absorption peak of the linear *Z*-DASA isomer **A** at 571 nm decreasing in its intensity (figure 5.53**a**). Simultaneously, a transient absorption band located at around 625 nm is observed. The thermal

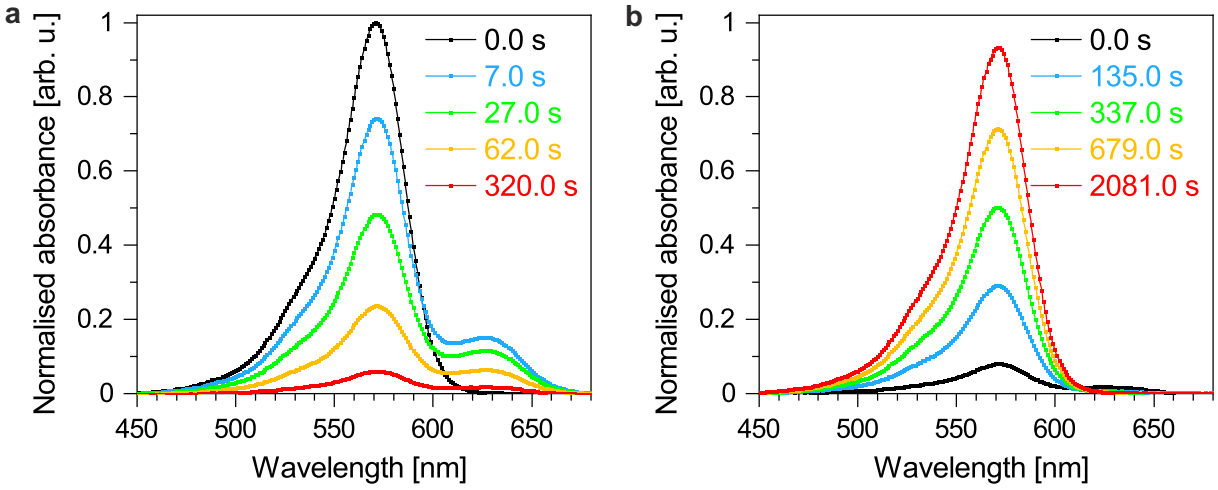

Figure 5.53. Absorption spectra of DASA in Tol at 0 °C upon (a) switching with an LED having its maximum wavelength at 594 nm (linear-to-closed) and (b) thermal backswitching (close-to-linear).

backswitching exhibits an intense rise of the absorption of the linear DASA isomer **A** (figure 5.53**b**). The transient absorption band, however, is not observed upon thermal backswitching.

Considering the involved steps and isomers upon DASA switching, three different absorption features are expected (figure 5.4). The linear *Z*-isomer **A** has its maximum absorption around 570 nm while the *E*-isomers **B**$^{(\prime)}$ cause the transient absorption at about 625 nm and the closed isomers **C**$^{(\prime)}$ exhibit no absorption in the VIS region as the conjugated π-system is broken.[247] Comparing the time evolution of the traces related to the initial DASA isomer and the transient species, a clear difference is observed (figure 5.54**a**). While the signal of *Z*-DASA decays within about 220 s, the transient

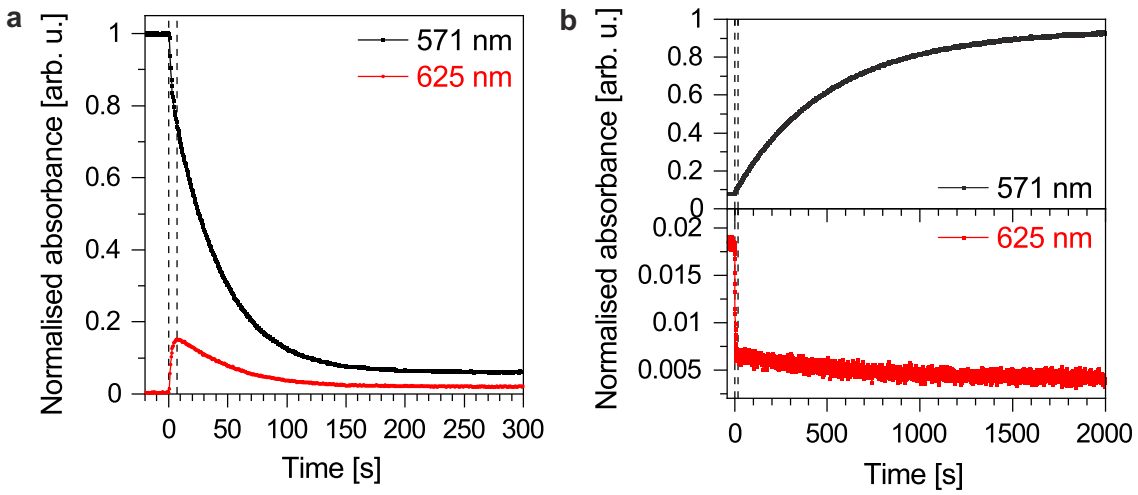

Figure 5.54. Change of absorbance of the signals at 571 and 625 nm (a) upon switching DASA with light using a wavelength of 594 nm and (b) upon thermal backswitching in Tol at 0 °C. The signal at 571 nm is attributed to the linear isomer **A** whereas the signal at 625 nm is assigned to the *E*-isomer **B**$^{(\prime)}$.

signal of *E*-DASA rises relatively very fast within the first 7 s. Subsequently, it decays roughly within the first 220 s. Thus, the *Z*-to-*E* isomerisation occurs on a very fast time scale compared to the ring closure as validated by the fast rise of the intensity found at 625 nm. The formation of the closed photoproduct, however, takes much longer. The same holds true for the thermal backswitching (figure 5.54**b**). In the course of backswitching, the remaining intensity of the transient species decays rapidly within about 15 s while the time of the rise of the product isomer **A** takes two orders of magnitude longer. Hence, as already pointed out in the introduction of DASA (section 5) and in the TA section (section 5.3), the *Z*-to-*E* isomerisation occurs on a much shorter time scale and reaches a photostationary state very fast compared to the ring closing reaction. Thus, the kinetics can be simplified to a monoexponential behaviour with the thermal ring closing step being the rate determining step.
In order to validate the above introduced theory to simplify the kinetics, the decay of the absorption band related to the linear DASA isomer **A** is fitted by a monoexponential decay curve upon photoswitching (figure 5.55**a**). The fit describes the data well resulting in a time constant of (39.43 ± 0.11) s. Next, the decay of the transient species due to the formation of the closed product in the same experiment is analysed by a monoexponential fit curve (figure 5.55**b**). The fit deviates slightly at early times at which the rise due to the formation of the transient species plays a decisive role. Beside this small variation, the data is described well by the fit curve yielding a lifetime of (40.07 ± 0.61) s. Hence, both time constants agree within their error limits such that it is sufficient to describe the absorption of the linear DASA isomer **A** with a monoexponential fit to gain the lifetime of the thermal step since the first step of photoisomerisation is negligible in terms of the lifetime. This holds true also for the respective thermally induced back reaction.

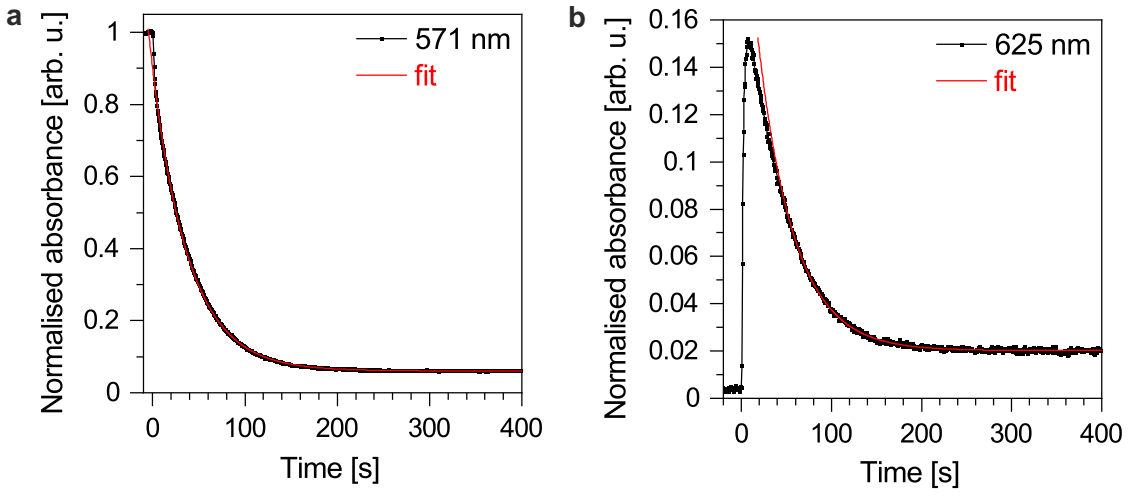

Figure 5.55. Monoexponential fits of the change of absorbance at (a) 571 nm corresponding to the linear *Z*-isomer **A** and (b) 625 nm corresponding to the *E*-isomer $\mathbf{B}^{(\prime)}$ in Tol at 0 °C upon switching with light.

Within the studied temperature window of 0 - 40 °C, the maximum absorption of DASA shifts similar to the Azo absorption slightly towards shorter wavelengths with increasing temperature (figure 5.56). Thus, values between 571 and 569 nm are observed. Hence, the absorption wavelength monitored is set at the respective maximum intensity at the specific temperature in the following.

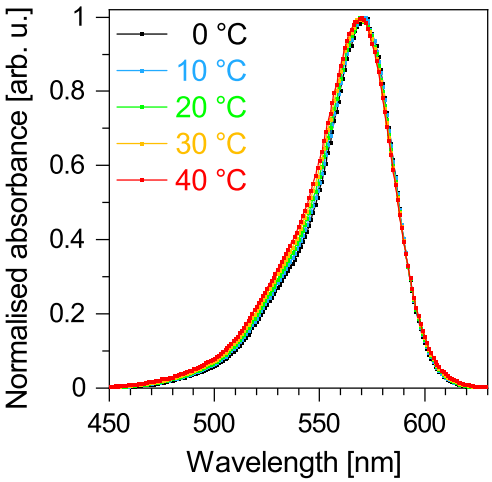

Figure 5.56. Absorption spectra of DASA in Tol at different temperatures. A slight blueshift occurs at higher temperatures.

In order to examine the switching of DASA upon photoexcitation at different temperatures, the maximum absorption wavelengths are studied versus time (figure 5.57**a**). The decay curves reveal shorter decay times for higher temperatures and indicate less switched molecules at higher temperatures which was the other way round for Azo. Following, the respective curves are fitted by monoexponential decay curves resulting

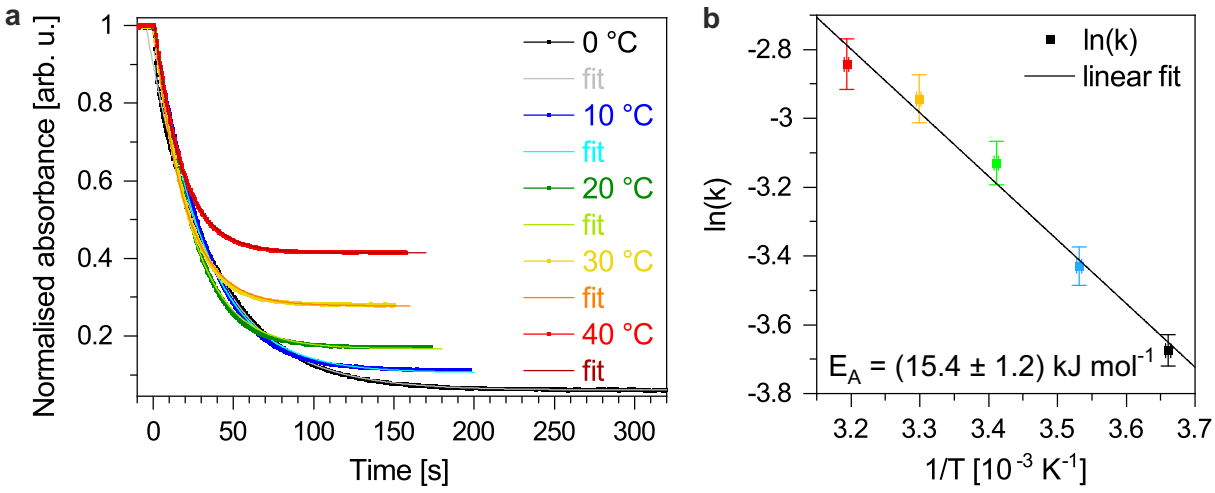

Figure 5.57. (a) Decays of the maximum absorption of DASA in Tol and their monoexponential fits upon irradiation with an LED having its maximum wavelength at 594 nm at different temperatures. Using the rate constants of those fits, (b) an Arrhenius plot can be applied to determine the activation energy of the thermal 4π-electrocyclisation generating the closed DASA isomer.

in lifetimes of 39.43, 30.87, 22.87, 18.97 and 17.17 s for 0, 10, 20, 30 and 40 °C, respectively. After calculating the applied photon dose according to equation 2.7, the effective cross sections are determined based on the lifetimes and the photon dose using equation 2.6 (table 5.8). Due to the thermal step included in the switching process, the effective cross sections are temperature dependent and vary between (1.24 - 2.85) · 10^{-18} cm^{-2} with higher cross sections obtained for higher temperatures.
Because of the thermal step and the simplification explained above, the activation energy for switching DASA can be investigated as well. Using the identified time constants, the respective rate constants are calculated according to equation 2.24. Subsequently, an Arrhenius plot (section 2.2.4) is created in order to extract the activation energy of the thermal 4π-electrocyclisation based on the slope of the linear fit function (figure 5.57**b**). It amounts to (15.4 ± 1.2) kJ mol^{-1}.
For the thermal backswitching of the closed DASA isomer **C'** to the linear isomer **A**, the respective maximum intensity of the latter is monitored versus time at different temperatures (figure 5.58**a**). The curves show thereby shorter rise times and slightly higher percentages of backswitched molecules for higher temperatures. The lifetimes are determined by fitting the traces with monoexponential rise curves yielding time constants of 518.63, 202.17, 99.71, 51.53 and 31.53 s for 0, 10, 20, 30 and 40 °C, respectively. In turn, the rate constants are obtained by inserting the lifetimes in equation 2.24. Following, an Arrhenius plot (section 2.2.4) is compiled to construct a linear fit curve (figure 5.58**b**). Based on the slope of the fit curve, the activation energy of the thermal backswitching of pure DASA in Tol is ascertained to (49.7 ± 2.2) kJ mol^{-1} which is 34.3 kJ mol^{-1} higher than the respective reverse photoisomerisation.

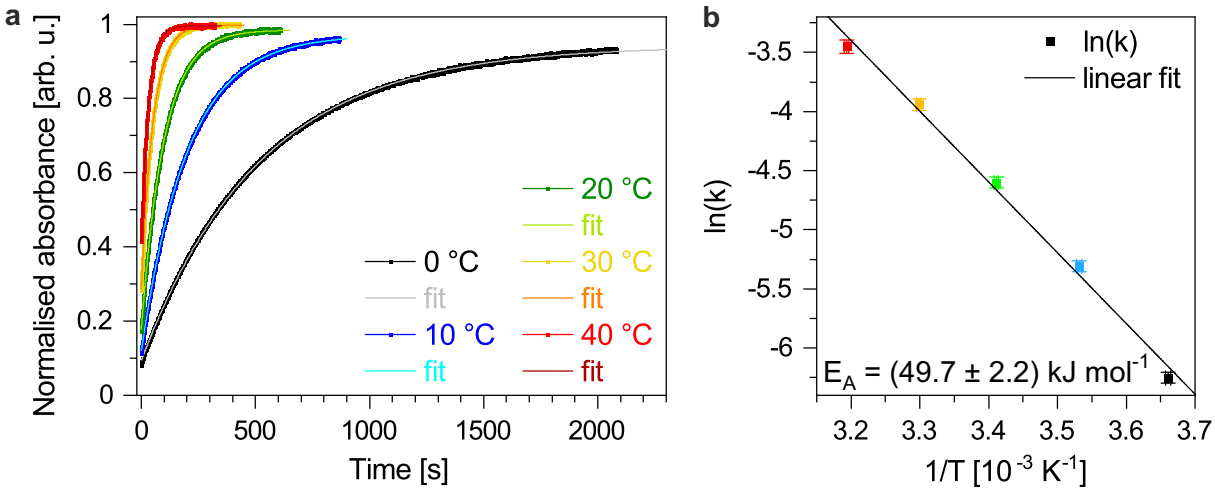

Figure 5.58. (a) Rises of the maximum absorption of DASA in Tol and their monoexponential fits upon thermal backswitching at different temperatures. Using the rate constants of those fits, (b) an Arrhenius plot can be applied to determine the activation energy of the ring opening.

Switching DASA orthogonally in the presence of Azo

Next, the switching behaviour of DASA in Tol is studied in the presence of Azo but without switching of the latter. Taking a look at the kinetic UV/VIS traces upon orthogonal photoisomerisation of DASA, the maximum absorption assigned to the initial *Z*-DASA isomer decreases in its intensity while a transient absorption band attributed to the transient *E*-DASA isomer **B**$^{(')}$ is obtained (figure 5.59**a**). The absorption of Azo stays essentially constant. In the reverse reaction upon thermal backswitching, the absorption feature of the linear DASA isomer **A** rises in its intensity while the Azo absorption stays again essentially constant (figure 5.59**b**). However, in contrast to the photoisomerisation, no transient absorption is observed during the backswitching process. Hence, on a first glance no big differences are observed in comparison to the switching processes without Azo being present (figure 5.53).

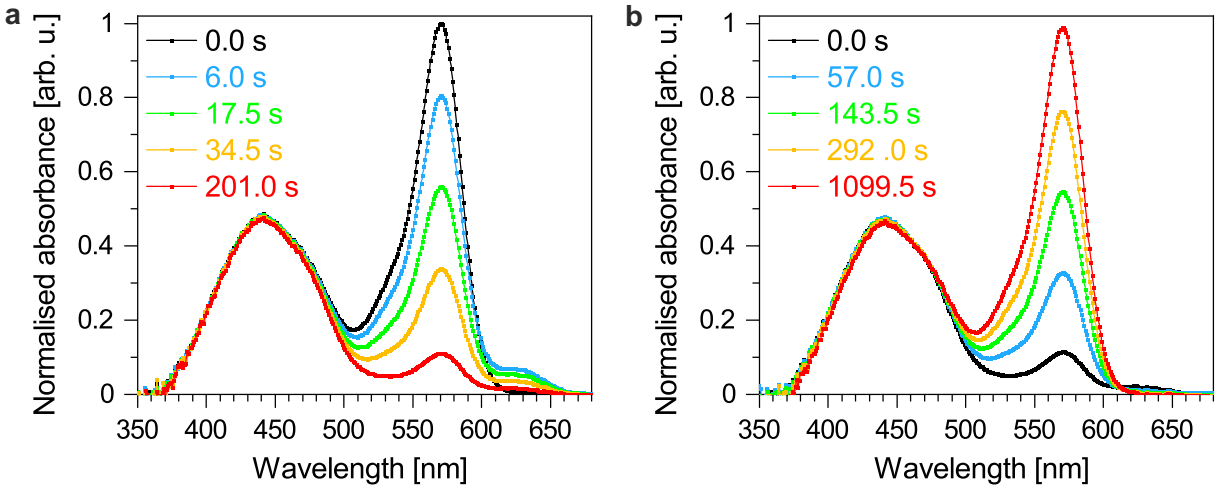

Figure 5.59. Absorption spectra of DASA in Tol at 10 °C while Azo is present upon (a) switching with an LED having its maximum wavelength at 594 nm and (b) thermal backswitching.

On closer inspection of the maximum absorption wavelengths of the species involved upon photoexcitation, the 570 nm trace, representing *Z*-DASA, drastically decreases while the 625 nm trace, depicting *E*-DASA intermediate, exhibits a fast rise and a subsequent slow decay (figure 5.60**a**). Simultaneously, the absorption at 441 nm, attributed to *trans*-Azo, slightly decreases in its intensity by around 1.7 % (figure 5.60**b**) due to the broad spectral range of the illuminating LED which overlaps with the absorption of Azo. However, the amount is negligible such that the DASA switching in the presence of Azo is denoted as orthogonal.

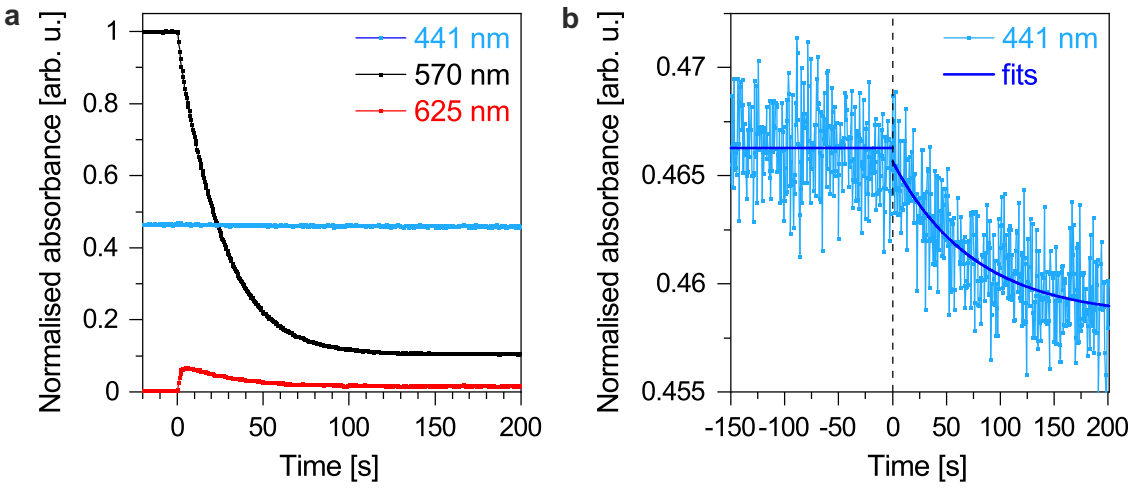

Figure 5.60. Change of absorbance of the signals at 441, 570 and 625 nm upon switching DASA in Tol at 10 °C with an LED with maximum intensity at a wavelength of 594 nm while Azo is present. (a) The signal of *Z*-DASA at 570 nm decreases and a transient signal at 625 nm corresponding to *Z*-DASA is detected. By analysing the signal at 441 nm corresponding to *trans*-Azo, (b) a negligible amount of about 1.7 % of switching is observed.

Following, the switching process is studied by observing the temporal behaviour of the respective maximum absorption of the initial *Z*-DASA isomer upon photoexcitation at different temperatures (figure 5.61**a**). Similar to pure DASA in Tol, the decay times and the amount of switched molecules decrease with increasing temperature. Next, the decay curves are analysed by a monoexponential fit resulting in lifetimes of 25.17, 17.68, 16.59 and 12.75 s for 10, 20, 30 and 40 °C, respectively. The temperature dependent effective cross sections are subsequently calculated according to equation 2.6 using the determined lifetimes and the photon dose computed by means of equation 2.7 (table 5.8). The results are in the range of (1.94 - 3.83) · 10^{-18} cm^{-2} with higher values

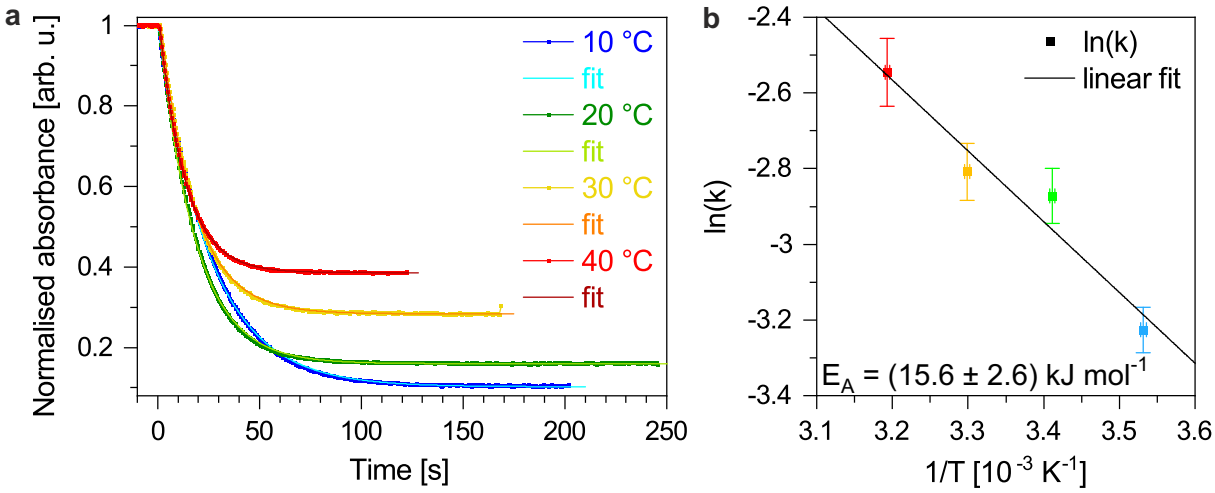

Figure 5.61. (a) Decays of the maximum absorption of DASA in Tol and their monoexponential fits upon irradiation with an LED with maximum intensity at a wavelength of 594 nm at different temperatures while Azo is present. Using the rate constants of those fits, (b) an Arrhenius plot is applied to determine the activation energy of the thermal 4π-electrocyclisation.

obtained for higher temperatures. Compared to the effective cross sections of pure DASA switching, the former are increased by 14 - 34 %. In addition, with the aid of an Arrhenius plot (section 2.2.4), the activation energy for the electrocyclisation is determined (figure 5.61**b**). Therefore, the rate constants are calculated using equation 2.24 based on the lifetimes. The slope of the linear fit yields an activation energy of (15.6 ± 2.6) kJ mol^{-1} which agrees with the activation energy of pure DASA switching.

Regarding the thermal backswitching of DASA in Tol in the presence of Azo, the maximum intensity of the linear *Z*-DASA isomer increases with time with the number of backswitched molecules staying about constant for all investigated temperatures (figure 5.62**a**). In order to quantify the backswitching process, the curves are fitted with monoexponential rise curves resulting in time constants of 218.98, 98.76, 47.15 and 27.97 s for 10, 20, 30 and 40 °C, respectively. Next, the respective rate constants are calculated according to equation 2.24 to construct an Arrhenius plot (section 2.2.4) to apply a linear fit curve (figure 5.62**b**). The slope of the latter contains the information of the activation energy which amounts to (51.1 ± 2.3) kJ mol^{-1}. Hence, the activation energy of thermally backswitching DASA does not change due to the presence of Azo.

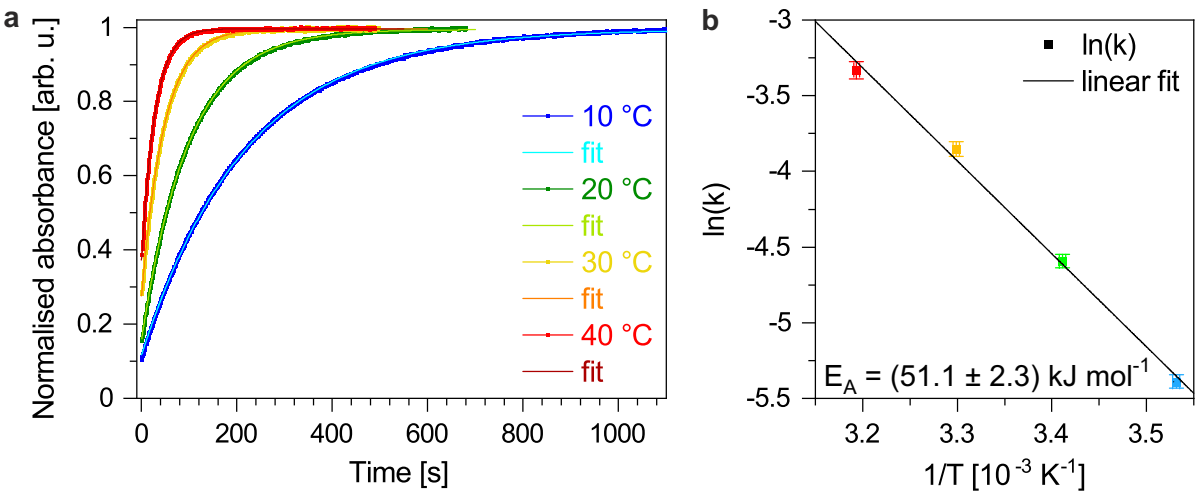

Figure 5.62. (a) Rises of the maximum absorption of DASA in Tol and their monoexponential fits upon thermal backswitching at different temperatures while Azo is present. Using the rate constants of those fits, (b) an Arrhenius plot can be applied to determine the activation energy of the ring opening.

Switching DASA simultaneously with Azo

Lastly, the switching processes of DASA are studied with Azo switching simultaneously (figure 5.50). Since the photoswitching and the thermal backswitching depend on a thermal rate determining step, there is no change expected for DASA upon changing the wavelength such that the mixture of DASA and Azo upon simultaneous switching can be researched directly. Using 507 nm for simultaneously addressing both pho-

toswitches, the maximum absorption of the linear *Z*-DASA isomer decreases whereby the decay times decrease with increasing temperature (figure 5.63**a**). Furthermore, in contrast to Azo, the percentage of switched molecules decline with increasing temperature. The decay curves upon photoswitching are fitted with monoexponential decays resulting in lifetimes of 17.91, 15.39, 13.00, 11.23, 10.15 and 8.87 s for 20, 25, 30, 35, 40 and 45 °C, respectively. To account for the efficiency, the effective cross sections of the photoresponsive switch is computed based on equation 2.6, the lifetimes and the photon dose (table 5.8). The values are temperature dependent and within a range of $(0.77 - 1.56) \cdot 10^{-18}$ cm^{-2}. Thus, higher effective cross sections are observed for higher temperatures but they are smaller compared to orthogonally switching DASA.

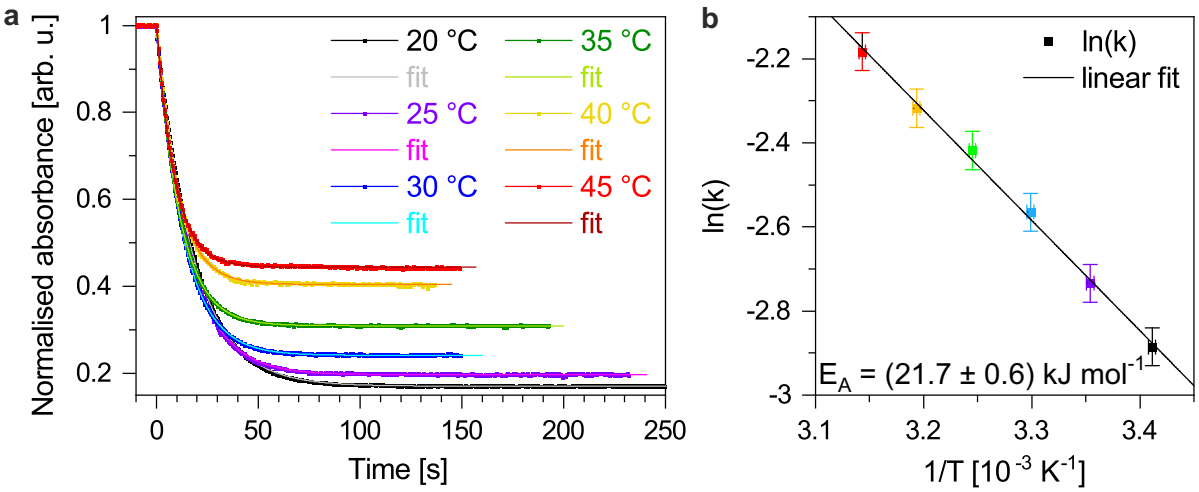

Figure 5.63. (a) Decays of the maximum absorption of DASA in Tol and their monoexponential fits upon irradiation with an LED having its maximum wavelength at 507 nm at different temperatures while Azo is photoswitched simultaneously. Using the rate constants of those fits, (b) an Arrhenius plot can be applied to determine the activation energy of the thermal 4π-electrocyclisation.

In order to determine the activation energy of the thermal 4π-electrocyclisation, an Arrhenius plot (section 2.2.4) is constructed with the help of the rate constants calculated by using the determined time constants and equation 2.24 (figure 5.63**b**). Hence, an activation energy of the electrocyclisation of (21.7 ± 0.6) kJ mol^{-1} results which is significantly higher than the activation energies observed in pure DASA solution and in the presence of Azo.

In turn, the thermal backswitching of DASA in Tol while Azo switches back simultaneously leads to an increase of the maximum absorption assigned to *Z*-DASA for all temperatures (figure 5.64**a**). However, after a fast rise within the first few hundred seconds, an undefined rise is observed (figure 5.64**b**). All traces rise above 1 with the maximum being 109 %. Furthermore, all curves include decays after reaching their maximum value but in an undefined way. Thus, no trend with increasing temperature is observed. This behaviour has already been observed upon backswitching Azo in the

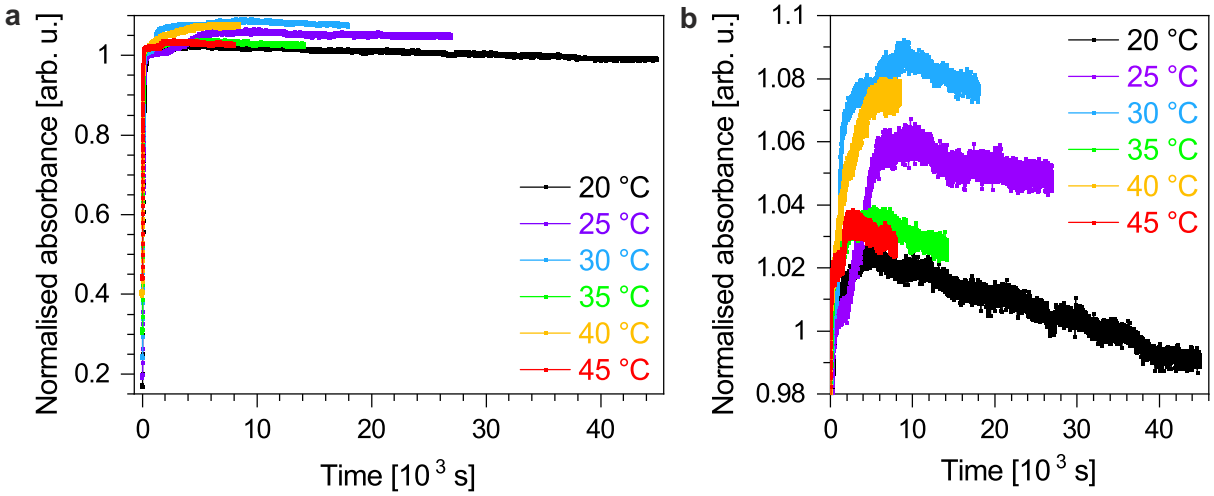

Figure 5.64. (a) Rises of the maximum absorption of DASA in Tol upon thermal backswitching at different temperatures when Azo is backswitched simultaneously. (b) The switching behaviour at longer times shows no clear trend in temperature.

presence of DASA (section 5.4.1). Hence, the thermal backswitching of Azo induces a *Z*-DASA signal above 100 % with respect to the solutions before switching. This observation is thereby independent of DASA being switched back simultaneously or just present.

To get reliable numbers of the thermal backswitching of DASA while Azo is backswitched simultaneously, only the first 1000 s are taken into account before the undefined rise above 100 % plays a decisive role (figure 5.65**a**). Higher temperatures lead thereby to shorter rise times and the amount of backswitched molecules is quite constantly near 100 % with a slightly higher percentage observed for higher temperatures. The rising curves are analysed with monoexponential curves resulting in time

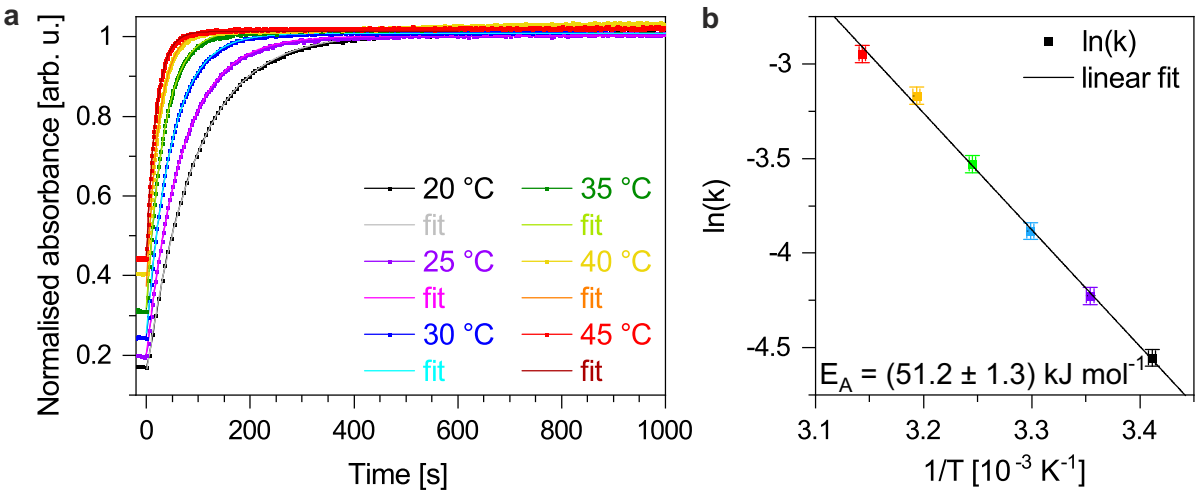

Figure 5.65. (a) Rises of the maximum absorption of DASA in Tol during the first 1000 s after turning off the LED and their monoexponential fits upon thermal backswitching at different temperatures while Azo is present. Using the rate constants of those fits, (b) an Arrhenius plot can be applied to determine the activation energy of the ring opening.

constants of 94.97, 68.51, 48.58, 34.09, 23.78 and 19.06 for 20, 25, 30, 35, 40 and 45 °C, respectively. Next, the respective rate constants are calculated according to equation 2.24 to create an Arrhenius plot (section 2.2.4) which is necessary to determine the activation energy (figure 5.65**b**) . Applying a linear fit curve and analysing its slope, an activation energy of (51.2 ± 1.3) kJ mol^{-1} is ascertained. Hence, the activation energy agrees with the ones investigated for backswitching DASA thermally independent on the presence of Azo.

Comparison of the UV/VIS kinetics upon addressing DASA

Finally, the obtained results of the switching processes upon addressing DASA in different surroundings related to Azo are compared. To begin with, the percentages upon switching DASA by light and upon thermal backswitching are contrasted. The percentage of switched DASA molecules in Tol is thereby independent of the presence of Azo no matter if Azo is simultaneously switched or not (figure 5.66**a**). Additionally, a temperature dependence is observed with less switched molecules obtained at higher temperatures. This is the other way round than the temperature dependence found for Azo both light induced switching and thermal backswitching. A further difference concerns the behaviour with temperature increase. While the trend for Azo observed in the analysed temperature range is rather linear, the temperature dependence for switching DASA is rather exponential. Regarding the thermal backswitching, for pure DASA a reversed trend is found with an increased number of backswitched molecules detected at higher temperatures (figure 5.66**b**). Interestingly, the percentage of switched molecules is affected by the presence of Azo such that the amount of backswitched DASA mo-

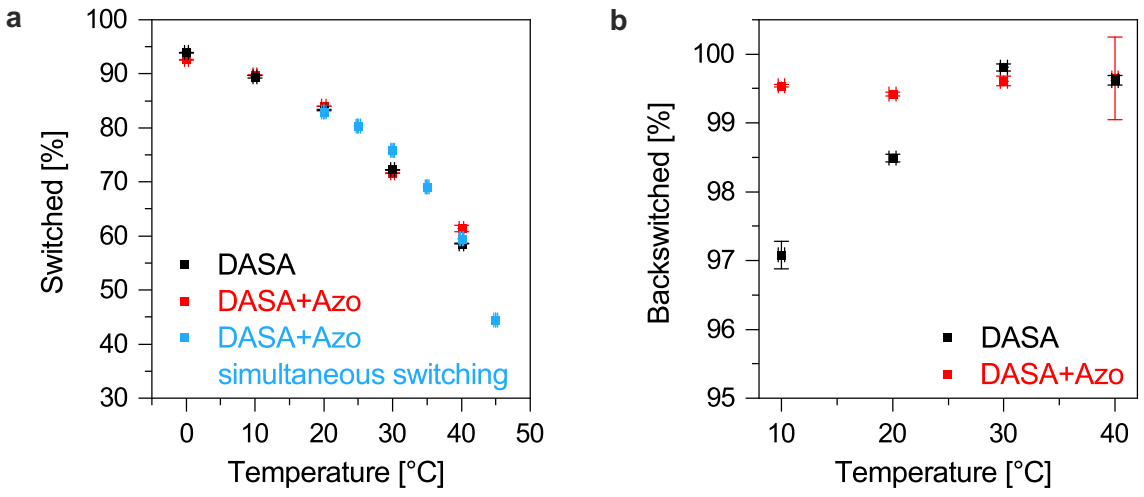

Figure 5.66. Percentage of (a) switched DASA after switching with light and of (b) backswitched DASA after thermal backswitching. The percentages of backswitched DASA when Azo was backswitched simultaneously were omitted as those did not stabilise within the experimental period.

lecules is constantly near 100 % independent of the temperature when Azo is present. The number of backswitched DASA molecules if Azo is backswitched simultaneously, however, were all above 100 %.
Comparing the determined effective cross sections of *Z*-DASA upon light induced switching, all values are temperature dependent due to the thermal step involved (table 5.8). Hence, an increasing temperature leads to higher effective cross sections. The effective cross sections are rather small compared to the ones obtained for Azo which range between (0.97 - 6.79) · 10^{-18} cm^{-2}. For DASA, however, the highest effective cross section obtained is 3.83 · 10^{-18} cm^{-2}. While the presence of Azo upon orthogonally addressing DASA increases the numbers by up to about 1 · 10^{-18} cm^{-2}, they significantly decrease by up to around 2 · 10^{-18} cm^{-2} if Azo is switched simultaneously.

Table 5.8. Comparison of the effective cross sections of DASA in Tol upon linear-to-closed photoisomerisation if DASA is used purely or Azo is present or Azo is photoswitched simultaneously.

Temperature [℃]	Effective cross section [10^{-18} cm^{-2}] based on λ = 594 nm and n_p = (20 ± 1) · 10^{15} s^{-1} cm^{-2}		
	DASA	DASA+Azo	DASA+Azo simultaneously
0	1.24 ± 0.06	-	-
10	1.58 ± 0.08	1.94 ± 0.10	-
20	2.14 ± 0.11	2.77 ± 0.14	0.77 ± 0.04
25	-	-	0.90 ± 0.05
30	2.58 ± 0.13	2.95 ± 0.15	1.07 ± 0.05
35	-	-	1.23 ± 0.06
40	2.85 ± 0.14	3.83 ± 0.19	1.36 ± 0.07
45	-	-	1.56 ± 0.08

Similarly, the determined lifetimes defining the above discussed effective cross sections change with temperature variation (table 5.9). Thus, the time constants decrease with increasing temperature for all environments with respect to Azo. However, the lifetimes are shortened by the presence of Azo in comparison to pure DASA in Tol. Switching Azo simultaneously further increases the switching resulting in even shorter time constants. The trend of decreasing lifetimes in the presence of Azo is also found in the TA experiments in which switching already stops after the formation of the Z-DASA isomer **B**.

Table 5.9. Comparison of the lifetimes of the thermal 4π-electrocyclisation of DASA in Tol upon switching with an LED having its maximum intensity at 594 nm if DASA is used purely or Azo is present or Azo is switched simultaneously.

Temperature [°C]	Lifetime [s]		
	DASA	DASA+Azo	DASA+Azo simultaneously
0	39.43 ± 0.11	-	-
10	30.87 ± 0.12	25.17 ± 0.05	-
20	22.87 ± 0.09	17.68 ± 0.03	17.91 ± 0.02
25	-	-	15.39 ± 0.02
30	18.97 ± 0.06	16.59 ± 0.04	13.00 ± 0.02
35	-	-	11.23 ± 0.01
40	17.17 ± 0.04	12.75 ± 0.02	10.15 ± 0.03
45	-	-	8.87 ± 0.03

Considering the time constants of the thermal backswitching reaction of DASA, a trend towards shorter lifetimes at higher temperatures is observed as well (table 5.10). Referring to the presence of *trans*-Azo and thermally backswitching Azo (cis-to-trans), however, differences are found. While the presence of Azo decreases the obtained time constants of thermally backswitching DASA similar to the reverse photoswitching at higher temperatures, longer lifetimes are observed in the presence of Azo for lower temperatures. If the Azo molecule is not only present but also backswitching, most lifetimes are shortened compared to the orthogonal switching of DASA in the mixture and

Table 5.10. Comparison of the lifetimes of the ring opening of DASA in Tol upon thermal backswitching when DASA is used purely or Azo is present or Azo is thermally backswitched simultaneously.

Temperature [°C]	Lifetime [s]		
	DASA	DASA+Azo	DASA+Azo simultaneously
0	518.63 ± 0.26	-	-
10	202.17 ± 0.10	218.98 ± 0.14	-
20	99.71 ± 0.06	98.76 ± 0.07	94.97 ± 0.21
25	-	-	68.51 ± 0.15
30	51.53 ± 0.05	47.15 ± 0.04	48.58 ± 0.09
35	-	-	34.09 ± 0.14
40	31.53 ± 0.04	27.97 ± 0.03	23.78 ± 0.11
45	-	-	19.06 ± 0.07

the pure DASA solution. Hence, the most cases of decreased lifetimes upon thermal backswitching due to the addition of Azo agree with the trend identified in the respective forward switching indicating a lower energy of the transition state.
In a final step, the activation energy of the 4π-electrocyclisation and the reverse ring opening are compared on the basis of the respective surroundings. The activation energy for the electrocyclisation thereby averages to about 15.5 kJ mol^{-1} for pure DASA and in the presence of Azo (table 5.11). However, if both photoresponsive molecules are addressed, the activation energy increases by 6.2 kJ mol^{-1} to 21.7 kJ mol^{-1}. In contrast, the activation barrier of the reverse ring opening is more than twice as big as for the light induced reverse switching. In all examined environments, independent of the presence and simultaneous switching of Azo, all activation energies of the ring opening agree to an averaged value of 50.7 kJ mol^{-1}.

Table 5.11. Comparison of the activation energies upon switching and backswitching of DASA in Tol if DASA is used purely or Azo is present or Azo is (back-)switched simultaneously.

Photoswitch	Activation energy [kJ mol^{-1}]	
	4π-Electrocyclisation	Ring opening
DASA	15.4 ± 1.2	49.7 ± 2.2
DASA+Azo	15.6 ± 2.6	51.1 ± 2.3
DASA+Azo simultaneously	21.7 ± 0.6	51.2 ± 1.3

5.5. IR kinetic studies of the switching processes of DASA

In order to gain deeper insight into the ring closing and opening upon switching DASA, kinetic IR measurements and theoretical calculations are carried out since no difference between the different closed isomers can be observed by UV/VIS spectroscopy. Comparing the different isomers included in the DASA switching process (figure 5.4), distinct IR spectroscopic differences are expected within the fingerprint region. Therefore, a spectral window of 1000 - 1800 cm^{-1} is analysed. Whereas *Z*-to-*E* isomerisation does not change the carbon environments significantly, upon destroying conjugated π-systems the respective IR bands are heavily affected. In addition, non-protonated and protonated amine groups as found in the isomers **A** - **C** and in the zwitterionic isomer **C'**, respectively, give clear differences in their IR absorptions.[133, pp. 35 ff.]
Hence, no spectral differences in the observed window are expected between the linear isomers **A** - **B'**. However, the closed isomer **C** and the zwitterionic isomer **C'** are expected to exhibit distinct differences. Thus, the last two steps upon photoswitching can be kinetically studied to ascertain the rate constants $k_{\mathbf{B'}\rightarrow\mathbf{C}}$ and $k_{\mathbf{C}\rightarrow\mathbf{C'}}$ of the interconversion of isomer **B** to isomer **C** and the formation of isomer **C'** from isomer **C**, respectively. Furthermore, the thermal backswitching processes are analysed at room

temperature and the respective rate constants $k_{(\mathbf{B'}\rightarrow\mathbf{C})\text{-}1}$ and $k_{(\mathbf{C}\rightarrow\mathbf{C'})\text{-}1}$ are researched. The differences due to the polarity of the environment are thereby studied by using the non-polar solvent Tol and the aprotic polar solvent MeCN but in their deuterated forms. To ensure no falsification of the IR spectra of DASA, the IR spectra are referenced to the pure solvent to subtract absorption bands of the latter. Solid samples could not be studied due to photodegradation as no movement of the sample is possible within the IR setup. Possible influences due to the presence of Azo were also not studied since the presence and changes of Azo distorts the IR spectra such that it is not possible to separate DASA and Azo IR bands. For all measurements, a maximum concentration was aimed for to get a good signal-to-noise ratio despite the small cuvette.

To assign the experimentally observed IR bands to the DASA isomers, DFT calculations were carried out. Since vibrational frequencies of quantum chemical calculations hold usually larger values than the experimentally observed modes due to the neglection of anharmonicity effects and incomplete incorporation of the electron correlation, scaling factors are applied. Therefore, the experimental frequencies are plotted versus the calculated frequencies. Next, a linear fit curve is applied with its slope providing the scaling factor.[274] [275]

Hence, the DFT result (optimised geometry in table B.5 appendix B) of the linear isomer **A** is first confronted with an IR spectrum of DASA in a KBr pellet exhibiting no environmental influences (figure 5.67**a**).[133, p. 33] By calculating a linear fit curve, a scaling factor of 0.9664 ± 0.0028 is obtained. This is in accordance with the literature known scale factor of 0.9682 for the B3LYP functional using a 6-311G(d,p) basis set.[274] Thus, the literature scaling factor is used in the following. In general, the experimental DASA

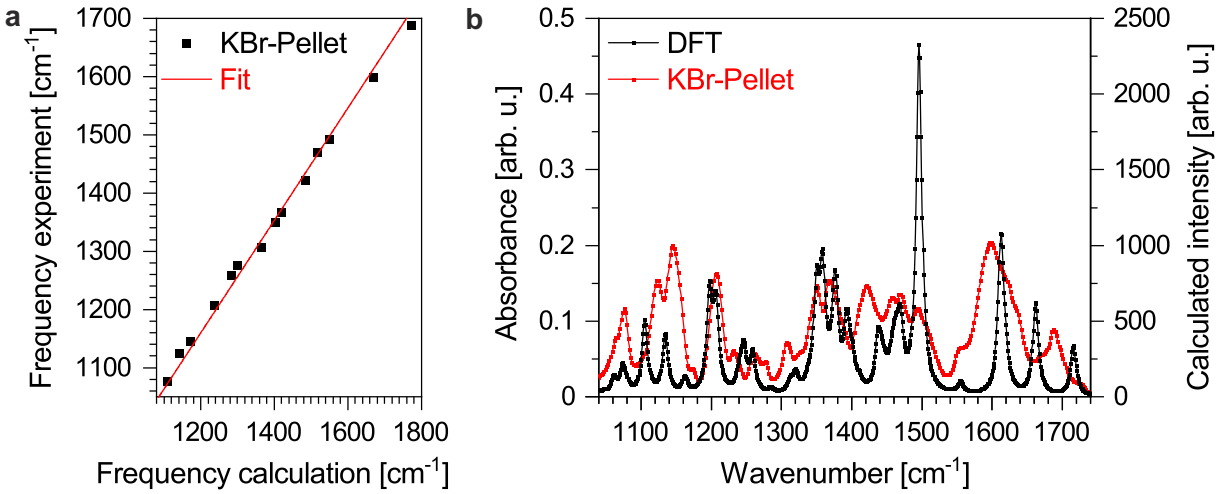

Figure 5.67. (a) Comparison of the calculated and experimental vibrational frequencies of the linear DASA isomer **A** in a KBr matrix in order to fit a frequency scaling factor and (b) comparison of the calculated spectrum considering a frequency scale factor of 0.9682 and the experimental spectrum of the DASA isomer **A** in a KBr matrix.

IR bands in a KBr matrix are in good agreement with the scaled DFT vibrational frequencies although the intensities differ (figure 5.67**b**).
Before starting with the switching experiments, DFT calculations are carried out for the closed intermediate isomer **C** and the closed zwitterionic isomer **C'** as well (optimised geometries in tables B.6 and B.7 appendix B). As expected from theory,[133, pp. 35 ff.] the isomers **A**, **C** and **C'** show distinct differences (figure 5.68). Whereas the linear isomer exhibits various bands in the spectral window analysed, the closed isomers **C** and **C'** show less IR absorption bands due to the chemical similarity of the carbon atoms. However, especially at higher wavenumbers, distinct differences between the closed isomers **C** and **C'** are found due to the protonation of the nitrogen atom in the latter.

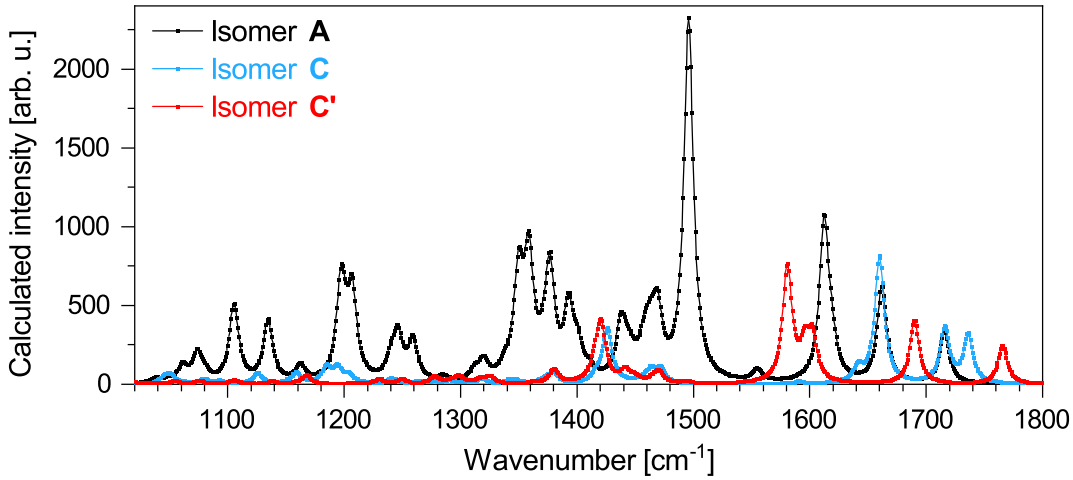

Figure 5.68. Calculated IR spectra of the DASA isomers **A**, **C** and **C'** using DFT with the B3LYP functional, the basis set 6-311G(d,p) and a scaling factor of 0.9682 assuming a FWHM of 5 cm^{-1}.

Following, the photoisomerisation induced by an LED with maximum intensity at a wavelength of 594 nm (figure B.1 appendix B) and thermal backswitching of DASA is studied at room temperature first in the non-polar solvent Tol and subsequently in the aprotic polar solvent MeCN.

Non-polar environment using toluene

Comparing the IR spectrum of DASA in Tol to the data of the KBr pellet containing DASA, the absorption bands observed at lower wavenumbers are in good agreement (figure 5.69). Especially at higher wavenumbers, however, there are marked differences. For example, the three distinct bands found in Tol above 1600 cm^{-1} are more than 10 cm^{-1} higher in energy compared to the KBr matrix. Most features are more separated in Tol with varied intensities compared to the solid sample. Comparing the DASA IR absorption of both environments to the calculated spectrum, all bands can be assigned such that the vibrational origin of the bands can be traced back (table B.8

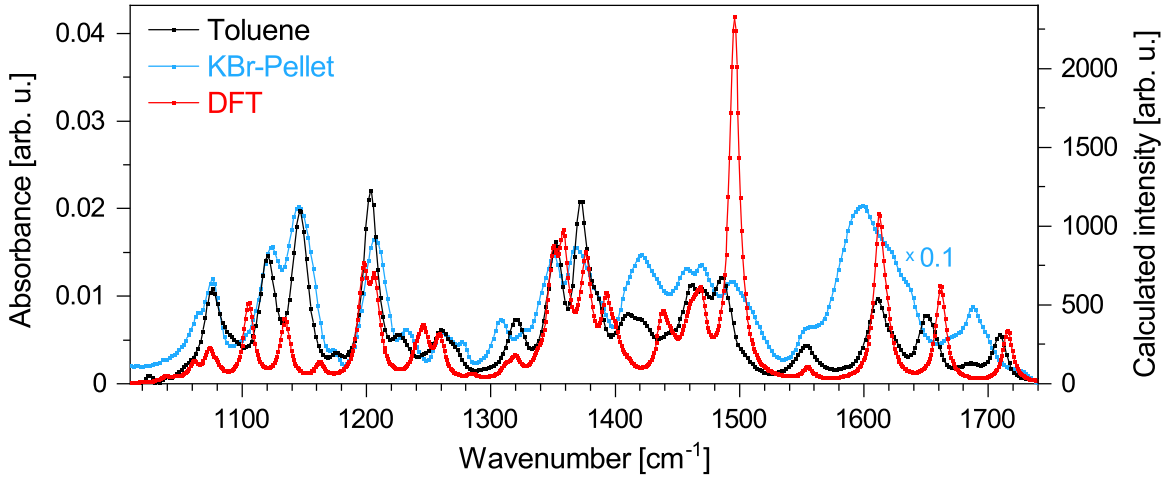

Figure 5.69. Comparison of the IR spectra of the linear DASA isomer **A** in Tol, in a KBr matrix and the DFT calculated spectrum. The latter was calculated using the B3LYP functional, the basis set 6-311G(d,p) and a FWHM of 5 cm^{-1} while taking a scaling factor of 0.9682 into account.

appendix B). However, the data in Tol fit slightly better to the theoretical vibrations most notably at higher wavenumbers.

In order to investigate the switching dynamics, the differences in IR absorption are analysed. Thus, the IR spectrum of DASA in Tol is referenced to itself resulting in a zero line before starting the illumination to induce switching (figure 5.70). Subsequently, the LED with its maximum wavelength at 594 nm is turned on for positive times to induce the ring closure. With increasing illumination time, negative bands are observed due to the decline of the absorption bands related to the linear DASA isomers as expected from the DFT calculations (figure 5.68). New features are observed especially in

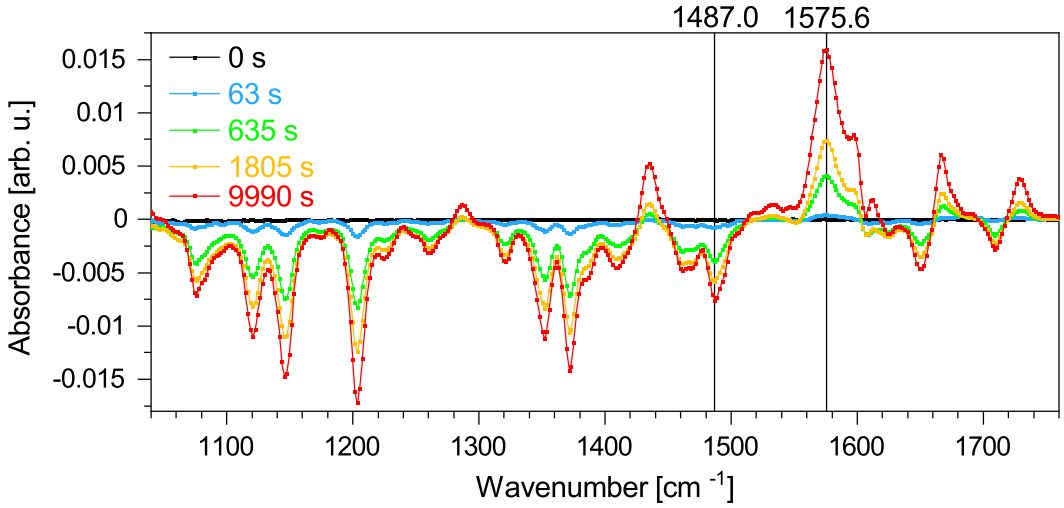

Figure 5.70. Change of absorbance of DASA in Tol at room temperature upon switching with light using an LED with its maximum intensity at a wavelength of 594 nm (linear-to-closed). The bands at 1487.0 cm^{-1} and 1575.6 cm^{-1} representing the decay of isomer **A** and the rise of isomer **C'**, respectively, are marked.

the high energy region of the IR spectrum with the most prominent band observed at around 1575.6 cm^{-1}.

To relate the observed IR bands to the involved species, the most pronounced band in the DFT spectrum of isomer **A** is chosen to represent the linear isomers. The vibration causing the most pronounced frequency at about 1495.8 cm^{-1} is related to a high vibrational activity of the C-C bonds between the six-membered ring and the hydroxyl group being present in all linear DASA isomers. Hence, the decrease of this band located at around 1487.0 cm^{-1} in the experimental data is attributed to the formation of the closed isomer **C**. In contrast, the dominating new IR absorption located at about 1575.6 cm^{-1} and 1580.7 cm^{-1} in the experimental and theoretical data, respectively, is caused by a new vibration mainly centred at the six-membered ring but with minor contribution of vibration of the proton newly attached to the nitrogen. Accordingly, the formation of the product closed zwitterionic isomer **C'** is characterised by the rise of the band at 1575.6 cm^{-1}.

Thus, by fitting monoexponential functions to the temporal evolution of the latter IR absorption bands, the time and rate constants can be determined (figure 5.71). Not only the intensity at the maximum position of the respective absorption band is fitted but an integral within ± 5 cm^{-1} of the maximum position. Applying a monoexponential decay fit to the change of IR absorption at 1487.0 cm^{-1}, which is attributed to the linear DASA isomers, a lifetime $\tau_{\mathbf{B'}\rightarrow\mathbf{C}}$ of (1216 ± 12) s is obtained (figure 5.71**a**). Using equation 2.24, the rate constant $k_{\mathbf{B'}\rightarrow\mathbf{C}}$ amounts to (822 ± 8) μs^{-1}. The formation of the photoproduct **C'** is analysed analogously. Hence, a monoexponential curve is fitted to the rise of the IR band located at 1575.7 cm^{-1}, which is assigned to the closed zwitterionic isomer **C'**, yielding a time constant $\tau_{\mathbf{C}\rightarrow\mathbf{C'}}$ of (3843 ± 35) s and the respective rate constant $k_{\mathbf{C}\rightarrow\mathbf{C'}}$ of (260 ± 2) μs^{-1} according to equation 2.24 (figure 5.71**b**). While the fit

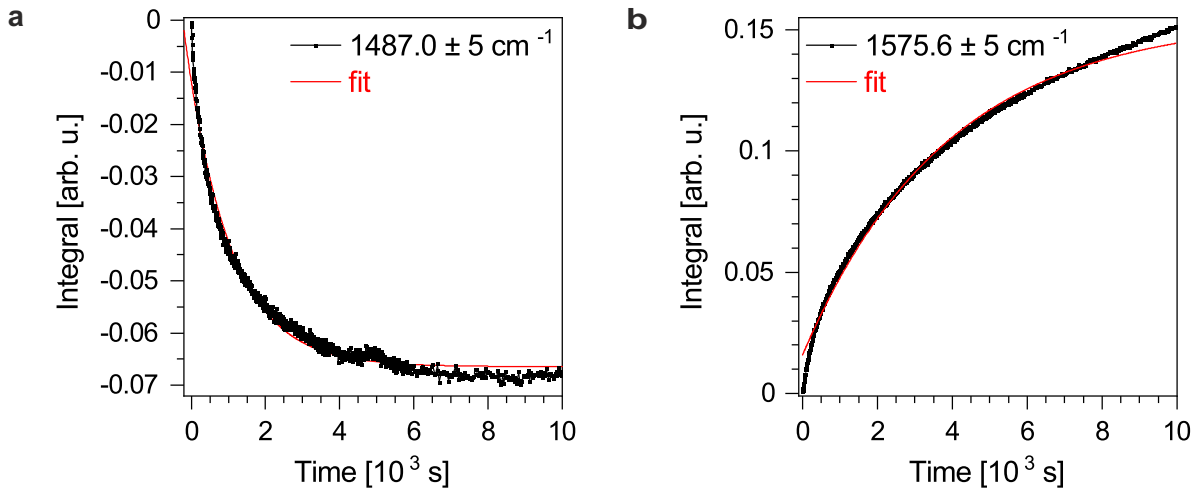

Figure 5.71. Kinetic traces of the integral of the bands at (a) 1487.0 cm^{-1} and (b) 1575.6 cm^{-1} with ± 5 cm^{-1} width upon switching DASA in Tol by irradiation with an LED having its maximum intensity at a wavelength of 594 nm in order to determine $k_{\mathbf{B'}\rightarrow\mathbf{C}}$ and $k_{\mathbf{C}\rightarrow\mathbf{C'}}$, respectively.

function applied to the decay of the IR band located at 1487.0 cm^{-1} describes the temporal behaviour well, the fit of the absorption at 1575.7 cm^{-1} deviates for early and late times from the experimental data. In the switching experiment, a photon dose of about $(10.5 \pm 0.5) \cdot 10^{15}$ s^{-1} cm^{-2} reaches the cuvette.
Subsequently, the thermal backswitching at room temperature is studied which induces the ring opening of the closed zwitterionic isomer **C'** to finally form the linear *Z*-isomer **A**. Therefore, the spectrum of DASA in the photostationary state during illumination is referenced to itself resulting in a zero line. Following, the LED is turned off for positive times such that only the change of absorbance due to thermal backswitching is observed (figure 5.72). Most striking, only positive absorption bands are observed. Studying the band at 1487.0 cm^{-1}, which represents the linear DASA isomers, an increase of about 44 mOD is observed with an increase being expected upon backswitching. In contrast, a decrease of the IR absorption at 1575.6 cm^{-1} is expected due to the disappearance of the closed zwitterionic isomer **C'**. However, the experimental data reveals a slight increase of 0.7 mOD.

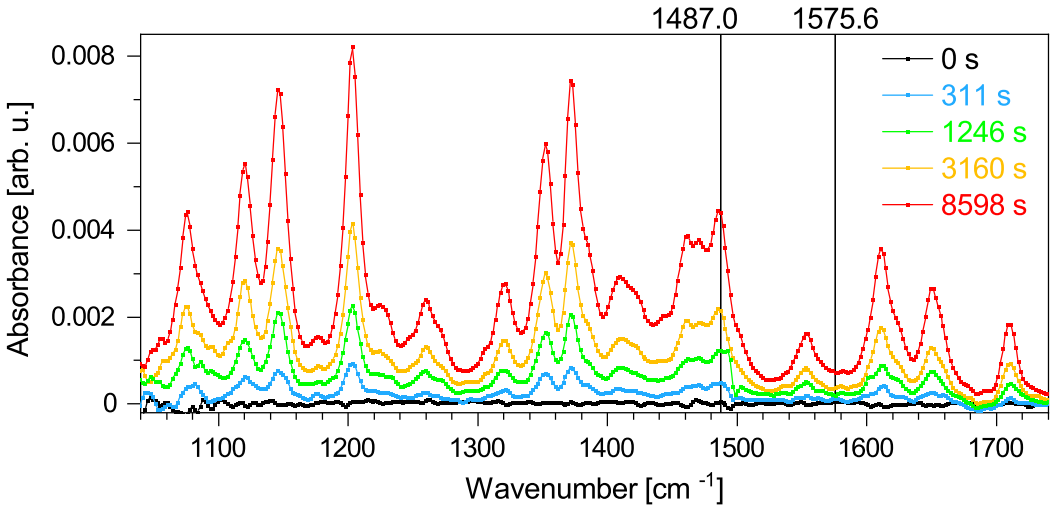

Figure 5.72. Change of absorbance of DASA in Tol at room temperature upon thermal backswitching (closed-to-linear). The IR bands at 1487.0 cm^{-1} and 1575.6 cm^{-1} representing the linear isomer **A** and the closed zwitterionic isomer **C'**, respectively, are labelled.

Furthermore, the temporal behaviour of both IR bands does not meet the expectations as both exhibit a linear rising behaviour instead of the expected exponential courses (figure B.6 appendix B). Hence, no time constants can be determined.
Since all IR bands show an increase in intensity, the question arises what happens during the thermal backswitching process. To research this observation, the spectra were referenced to the pure solvent to get the IR absorption bands of DASA with no absorption features of the solvent such that a comparison of the DASA solution in Tol before switching, the photoswitched sample and the thermally backswitched solution can be drawn (figure 5.73). Theoretically, the data before switching and after backswitching

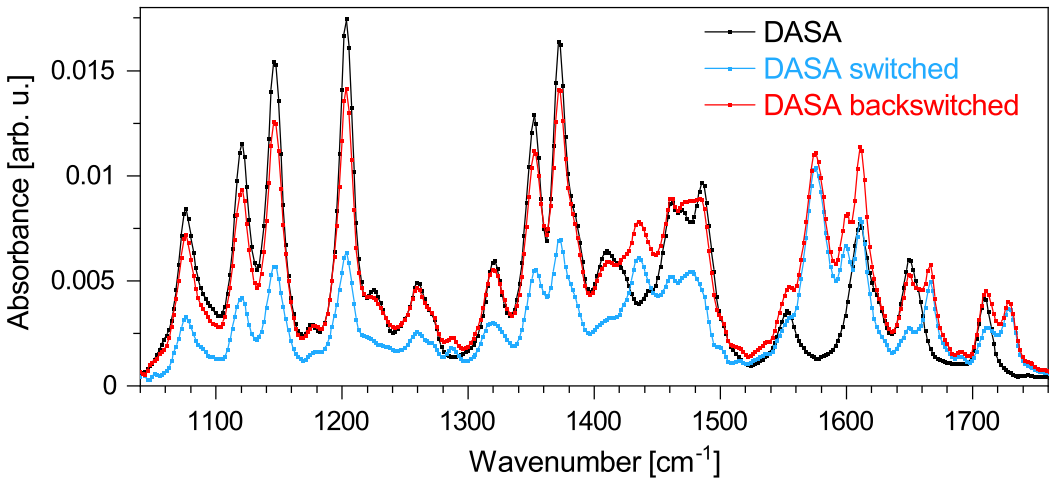

Figure 5.73. Comparison of the IR spectra of DASA in Tol at room temperature before photoswitching, after photoswitching and after thermal backswitching. The backswitched IR spectrum has contributions from all IR bands also found before switching and in the switched state.

should indicate the linear DASA *Z*-isomer **A** while the switched sample should feature signals related to the closed zwitterionic isomer **C'**. The initial DASA IR spectrum is in good agreement with the theoretical data of the linear isomer **A** as expected (figure 5.69). Comparing the switched DASA spectrum to the theoretical spectrum of isomer **C'**, a good accordance is observed. However, small absorption bands related to the linear DASA species are found due to incomplete photoswitching. The IR data of the thermally backswitched sample reveals several signals. In fact, the spectrum of the backswitched sample consists of all IR bands of the linear isomer **A** and closed zwitterionic isomer **C'**. No additional features are found. Thus, the data indicates that thermal backswitching takes place, which causes higher absorbance of the linear DASA IR bands due to the formation of the linear isomer **A**, while the signals related to the closed zwitterionic DASA isomer **C'** do not decrease but slightly increase. Considering the high concentration of DASA in Tol necessary to get enough signal in the small IR cuvette, aggregate formation should take place.[255] Hence, the aggregates can influence the absorption behaviour. For instance, the initially present aggregates could decrease the overall IR absorbance. During the thermal backswitching process, those aggregates could break resulting in single molecules with higher IR absorption such that the absorption bands of the closed zwitterionic isomer **C'** could increase due to the breakup of aggregates while the signals related to the linear isomer **A** increase due to the thermal backswitching process. This way, increasing IR absorption of all bands can be explained.

Polar environment using acetonitrile

To account for solvent and polarity influences, the photoswitching and thermal backswitching of DASA at room temperature is also studied using the aprotic polar solvent

MeCN. Comparing the IR spectrum of the linear *Z*-DASA isomer **A** in MeCN with the spectrum of *Z*-DASA embedded in a KBr matrix, the data is in good agreement (figure 5.74). Hence, the polar environment in solution does not significantly influence the vibrations of the molecules. In contrast, slightly more differences are observed in the non-polar Tol environment (figure 5.69). Comparing the IR bands found in the MeCN solution to the calculated spectrum, all IR bands in the experimental data can be related to the calculated signals such that the vibrational origin of each band can be retraced (table B.8 appendix B).

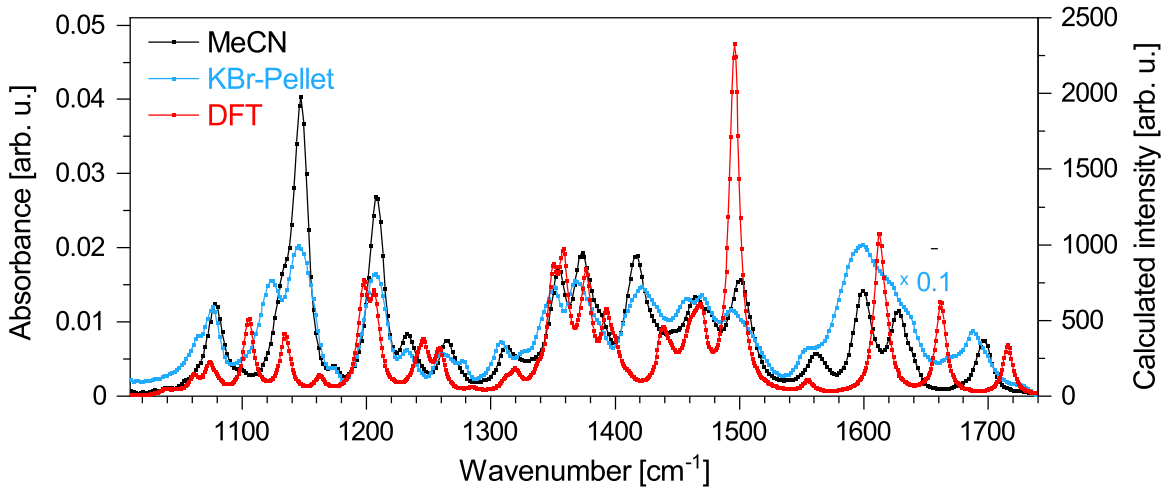

Figure 5.74. Comparison of the IR spectra of the linear DASA isomer **A** in MeCN, in a KBr matrix and DFT calculated spectrum. The latter was calculated using the B3LYP functional, the basis set 6-311G(d,p) and a FWHM of 5 cm^{-1} while taking a scaling factor of 0.9682 into account.

Next, the changes upon photoswitching are investigated which induces the linear-to-closed isomerisation. Therefore, the IR spectrum of the DASA in Tol solution is referenced to itself in the dark resulting in a zero line. This way, only the changes upon switching are monitored with the LED being turned on for positive times (figure 5.75). Most IR absorption bands decrease to negative values upon photoexcitation. Those bands are related to the linear DASA isomers. In addition, several new positive features emerge especially in the high wavenumber region which are related to closed DASA species.

In order to assign the observed signals to the DASA isomers involved and to explore the kinetics of the ring closure and the formation of the zwitterionic structure, one IR absorption band is attributed to the linear isomer **A** and one to the closed zwitterionic photoproduct **C'**. Again, the most prominent band in the DFT calculated spectrum of the linear isomer **A** at about 1495.8 cm^{-1} is chosen to represent the linear species as it includes high vibrational activity of the C-C bonds between the six-membered ring and the hydroxyl group being present in all linear DASA isomers. In the experimental data in MeCN, this vibrational mode is located at around 1500.6 cm^{-1}. Thus, the ring

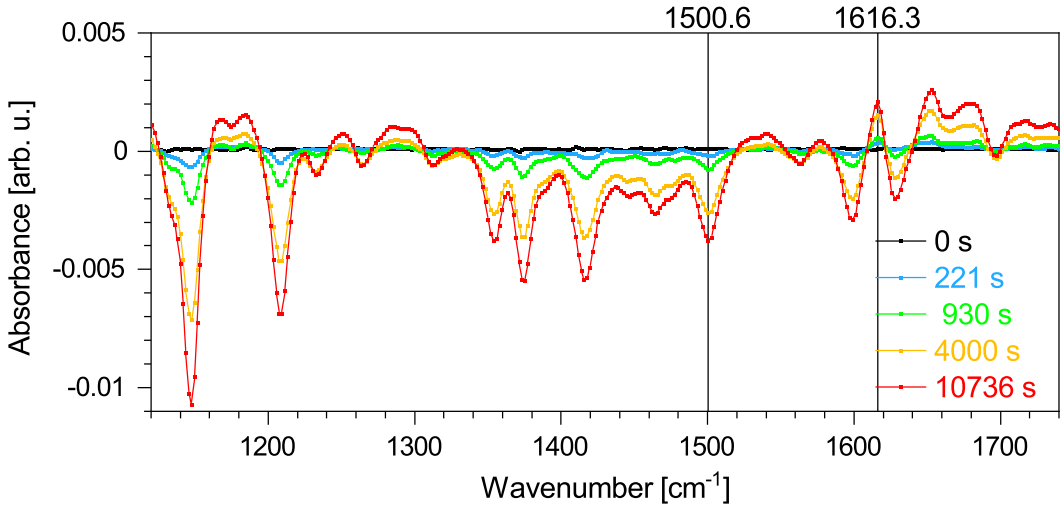

Figure 5.75. Change of absorbance of DASA in MeCN at room temperature upon switching with light using an LED with its maximum intensity at a wavelength of 594 nm (linear-to-closed). The bands at 1500.6 cm^{-1} and 1616.3 cm^{-1} representing the decay of isomer **A** and the rise of isomer **C'**, respectively, are marked.

closing reaction can be described by the decay of this absorption band related to the linear isomers. In contrast, the IR signal at about 1616.3 cm^{-1} represents the closed zwitterionic isomer **C'**. According to the theoretical DFT calculation, in which this band occurs at a frequency of 1598.2 cm^{-1}, this vibration includes an N-H vibration of the newly attached proton. Hence, the formation of the closed zwitterionic photoproduct **C'** can be kinetically described by the rise of this absorption band.
Following, the temporal evolutions of the IR bands at 1500.5 cm^{-1} and at 1616.3 cm^{-1} are examined (figure 5.76). Therefore, the decrease of the IR absorption band at 1500.5 cm^{-1} is fitted with a monoexponential decay function to determine the lifetime $\tau_{\mathbf{B'}\rightarrow\mathbf{C}}$ for the ring closing reaction generating the closed isomer **C** (figure 5.76**a**). It

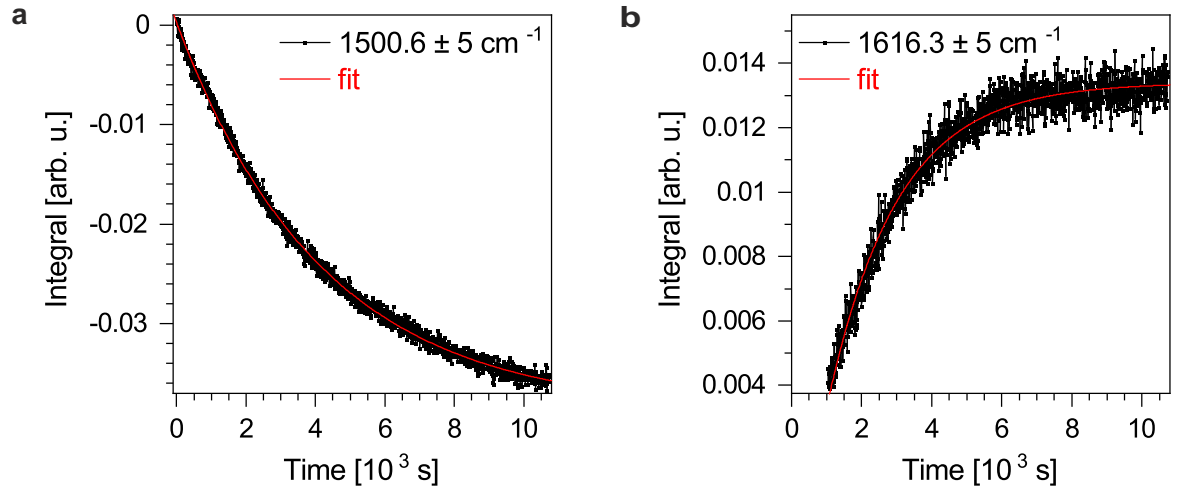

Figure 5.76. Kinetic traces of the integrals of the bands at (a) 1500.6 cm^{-1} and (b) 1616.3 cm^{-1} with ± 5 cm^{-1} width upon photoswitching DASA in MeCN in order to determine $k_{\mathbf{B'}\rightarrow\mathbf{C}}$ and $k_{\mathbf{C}\rightarrow\mathbf{C'}}$, respectively.

amounts to (4194 ± 21) s while the respective rate constant $k_{\mathbf{B'\rightarrow C}}$ numbers (238 ± 1) µs^{-1} according to equation 2.24. The formation of the closed zwitterionic photoproduct **C'** is identified by a monoexponential rise function fitted to the temporal evolution of the band at 1616.3 cm^{-1} (figure 5.76**b**). The fitted lifetime $\tau_{\mathbf{C\rightarrow C'}}$ is (1988 ± 25) s while the respective rate constant $k_{\mathbf{C\rightarrow C'}}$ calculated by equation 2.24 amounts to (503 ± 6) µs^{-1}. A photon dose of (2.4 ± 0.1) · 1017 s^{-1} cm^{-2} reaches thereby the cuvette.

Subsequently, the thermal backswitching of DASA in MeCN is studied. In that process, the closed zwitterionic isomer **C'** converts through several intermediates to the linear *Z*-DASA isomer **A**. To account for the changes of the IR absorbance upon thermal backswitching, the IR spectrum of DASA in the photostationary state under illumination is referenced to itself resulting in a zero line. Following, the LED is turned off for positive times such that only the changes due to thermal backswitching are monitored (figure 5.77). With increasing time delay, several absorption bands appear which can be related to the linear DASA isomers. Simultaneously, some IR bands, especially at higher wavenumbers, decrease in their intensity. Those bands are assigned to the closed isomers of DASA. As expected, the absorption band at 1500.6 cm^{-1}, attributed to the linear isomer **A**, increases while the band at 1616.3 cm^{-1}, representing the closed zwitterionic isomer **C'**, decreases.

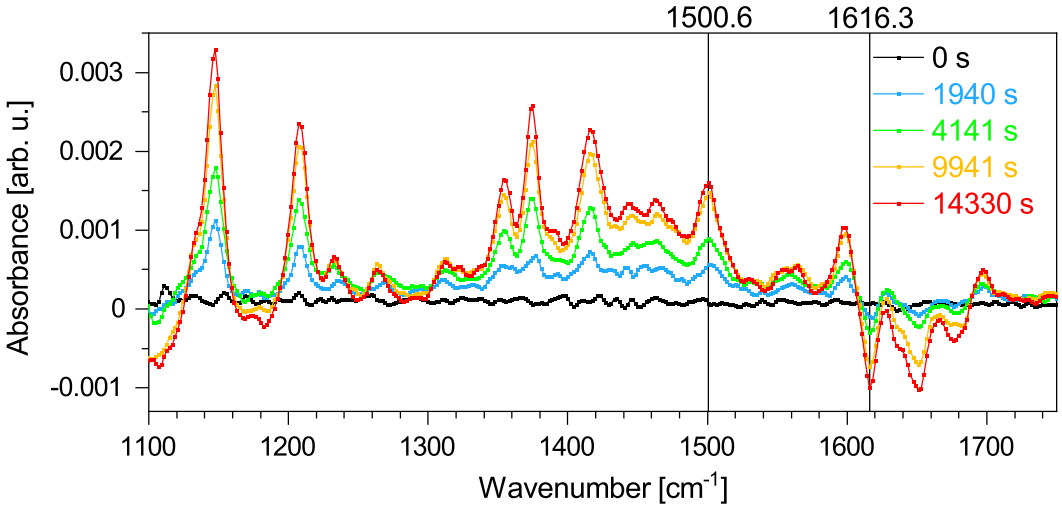

Figure 5.77. Change of absorbance of DASA in MeCN at room temperature upon thermal backswitching (closed-to-linear). The IR bands at 1500.6 cm^{-1} and 1616.3 cm^{-1} representing the linear isomer **A** and the closed zwitterionic isomer **C'**, respectively, are labelled.

Hence, the kinetics of the ring opening reaction and the conversion of the zwitterionic to the non-ionic closed isomer can be studied. Therefore, the latter IR bands are plotted versus time (figure 5.78). The monoexponential rise function fitted to the temporal behaviour of the absorption band at 1500.6 cm^{-1} provides the time constant $\tau_{(\mathbf{B'\rightarrow C})_{\text{-1}}}$ of (8332 ± 131) s of the ring opening (figure 5.78**a**). The respective rate constant $k_{(\mathbf{B'\rightarrow C})_{\text{-1}}}$

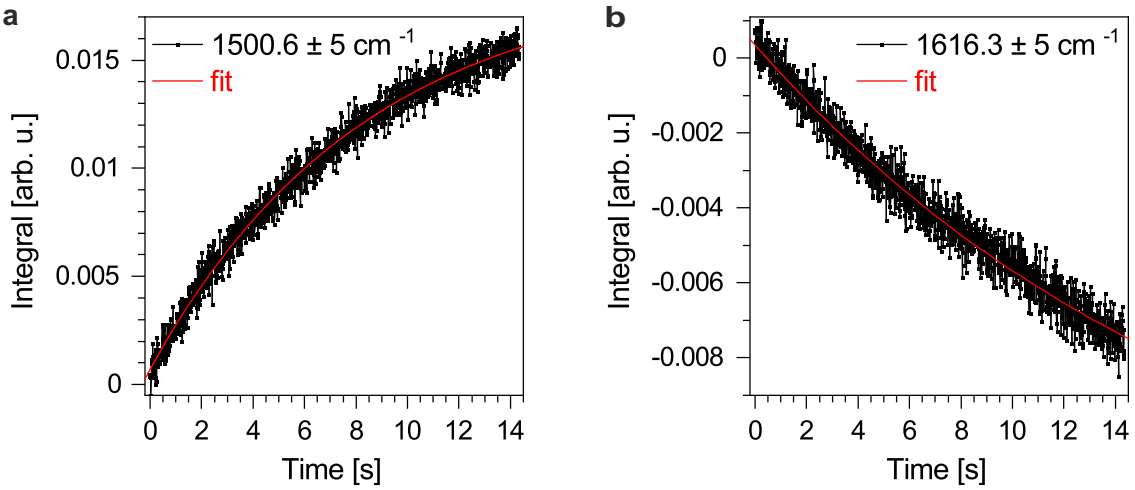

Figure 5.78. Kinetic traces of the integrals of the bands at (a) 1500.6 cm^{-1} and (b) 1616.3 cm^{-1} with ± 5 cm^{-1} width upon thermal backswitching of DASA in MeCN in order to determine $k_{(\mathbf{B'}\rightarrow\mathbf{C})_{-1}}$ and $k_{(\mathbf{C}\rightarrow\mathbf{C'})_{-1}}$, respectively.

numbers (120 ± 2) μs^{-1} according to equation 2.24. In contrast, the conversion of the closed zwitterionic isomer **C'** to the closed isomer **C** upon thermal backswitching takes much longer. According to the monoexponential decay function fitted to the temporal evolution of the IR absorption at 1616.3 cm^{-1}, the time constant $\tau_{(\mathbf{C}\rightarrow\mathbf{C'})_{-1}}$ amounts to (18384 ± 889) s (figure 5.78**b**). Using equation 2.24, the respective rate constant $k_{(\mathbf{C}\rightarrow\mathbf{C'})_{-1}}$ numbers (54 ± 3) μs^{-1}. To verify the long lifetime, the limit of the exponential fit is analysed. The IR absorption band at 1616.3 cm^{-1} refers to the closed zwitterionic isomer **C'** which was generated during the photoswitching process (figure 5.75) and its maximal integral upon photoswitching amounts to 0.014. Upon thermal backswitching, the closed zwitterionic isomer **C'** degrades but the kinetic trace of the integral of its absorption can only decay as much as it rose upon photoswitching. Accordingly, the integrals should have the same absolute value. Hence, the limit value of the integral upon thermal backswitching should amount to -0.014 which holds true (figure B.7 appendix B).

Comparison of the IR kinetics

To summarise, the IR kinetic measurements of DASA provided a detailed insight into the ring closing (generation of isomer **C**) and the formation of the zwitterionic photoproduct **C'** upon photoswitching as well as the reverse steps upon thermal backswitching. Comparing the determined rate constants and results in the different surroundings, distinct differences in the two solvent environments can be found (table 5.12).
In the non-polar solvent Tol, the ring closure to form the DASA isomer **C** happens about three times faster than the proton transfer to generate the zwitterionic photoproduct isomer **C'**. However, the fits do not accurately describe the time course of the

Table 5.12. Comparison of the determined rate constants of the ring closing and the formation of the zwitterionic structure of DASA using IR kinetic measurements upon photoswitching and the respective reverse reactions upon thermal backswitching in different solvents.

Rate constants	in Tol [µs^{-1}]	in MeCN [µs^{-1}]
$k_{\mathbf{B'\rightarrow C}}$	822 ± 8	238 ± 11
$k_{\mathbf{C\rightarrow C'}}$	260 ± 12	503 ± 23
$k_{(\mathbf{B'\rightarrow C})_{-1}}$	-	120 ± 2
$k_{(\mathbf{C\rightarrow C'})_{-1}}$	-	54 ± 3

respective IR absorption bands (figure 5.71). In contrast, the IR bands show linear behaviour in time during the thermal backswitching with all signals increasing such that no rate constants of the proton transfer to form isomer **C** and the ring opening could be investigated. Due to the high concentration required in the IR experiment, aggregate formation can distorts the kinetics. Most likely, the aggregates decrease the IR absorption. Upon thermal backswitching and may to a smaller degree upon photoswitching the aggregated molecules become disorganised such that their IR intensities increase which distorts the kinetic analysis.
Using the aprotic polar solvent MeCN, no distortion due to the high concentration can be detected. The kinetics upon photoswitching as well as upon thermal backswitching were studied successfully. The ring closure upon photoswitching forming the closed isomer **C** took about two times longer than the following proton transfer to generate the closed zwitterionic photoproduct isomer **C'**. In the reverse thermal backswitching reaction at room temperature, the proton transfer to create the non-ionic closed isomer **C** occurred one order of magnitude slower compared to all other rate constants in this experimental study. This suggests that the zwitterionic structure of the DASA isomer **C'** is highly stable in comparison to the non-ionic closed isomer **C**. The ring opening to form the linear DASA isomer **B'** upon thermal backswitching at room temperature happened around two times slower compared to the ring closing upon photoswitching.

5.6. Summary of the results of the orthogonal photoswitches

To summarise the chapter about orthogonal photoswitches, the switching properties of the two orthogonal photoresponsive molecules Azo (figure 5.1) and DASA (figure 5.4) have been investigated in great detail. Both molecules can be addressed individually as well as simultaneously in a 1:1 molar mixture to account for possible interactions and influences on each other. Furthermore, different environments were applied by using the non-polar solvent Tol, the aprotic polar solvent MeCN and PMMA blend thin films. If not stated otherwise, the following experiments were carried out at room temperature.

Azo undergoes trans-to-cis isomerisation upon excitation with light (figure 5.79). The cis-to-trans back reaction can be induced thermally or photochemically. The light induced isomerisations happen on the femtosecond to picosecond time scale with all time constants being below 10 ps in solutions (measured by TA in section 5.3). After excitation with light using $\lambda \leq 431$ nm to induce either trans-to-cis or cis-to-trans isomerisation of the solutions, the molecules are thereby promoted to the S_2 state. Following, conical intersection to S_1 and the movement of the wavepacket out of the Franck Condon regime towards the $S_1 \rightarrow S_0$ conical intersection takes place within below 200 fs. The $S_1 \rightarrow S_0$ conical intersection and the vibrational relaxation within the electronic ground state occur with time constants of 0.7 - 1.4 ps and 3.3 - 9.8 ps, respectively. Those results are in agreement with other push-pull azobenzene derivatives.[233] [234] [257] [260] The processes are slightly increased in MeCN compared to Tol not due to polarity influences but to dynamic effects as ascertained by quantum chemical calculations.[258] Especially the vibrational relaxation is thereby accelerated in MeCN due to the lower molecular weight of MeCN compared to Tol.[273] In thin PMMA blend film, which show higher molecular weight of the surrounding and with steric hindrance playing a role, the time constants are increased to below 0.2, 1.2 - 5.7 and 15.4 - 288.6 ps, respectively, with the latter much longer time constant may caused by a trapped state. Slightly increased lifetimes in thin films compared to solutions are thereby also found in literature.[230]

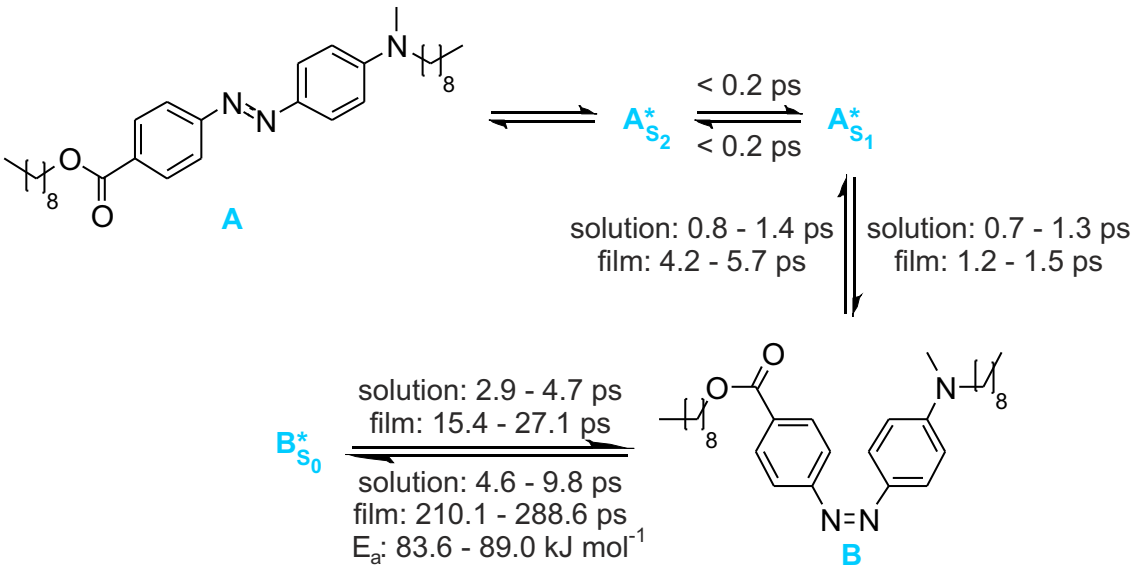

Figure 5.79. Scheme of the excited state dynamics of Azo after $S_0 \rightarrow S_2$ excitation by light and the reverse reaction induced by light or thermal energy. The stated time constants and activation energies represent a summary of all measurements of pure Azo, in the presence of *Z*/*E*-DASA and upon simultaneously addressing Azo and DASA.

In general, the light induced backswitching (cis-to-trans) takes longer than the respective photoswitching (trans-to-cis) with the reason being subject of current research. If

Azo is orthogonally addressed within a mixture of both photoswitches, the influence of DASA is rather small with the kinetics in general being slightly faster in solution but slightly slowed down in thin film compared to analogous samples without DASA. Applying the simultaneous switching wavelength of 506 - 515 nm accelerates the processes of Azo switching. Using a mixture of both photoresponsive materials, again only little impacts the time constants of Azo switching. Induction of the photoswitching (trans-to-cis) by an LED provides about 67 % and 43 % switched molecules at 20 °C by the orthogonal and the simultaneous switching wavelength, respectively, with effective cross sections ranging from 0.97 - 6.79 · 10^{-18} cm^{-2}. The latter are significantly increased by the presence of DASA with the reason being subject of current research. The switching efficiency is much higher compared to 15 - 35 % of literature known push-pull azobenzenes also featuring a carboxylic acid ester and a tertiary amine as electron acceptor and donor, respectively.[232] [235] Considering the thermal backswitching (cis-to-trans), the efficiency amounts to more than 92 % for room and higher temperature with an activation energy of 83.6 - 89.0 kJ mol^{-1} with little influence of DASA. Hence, the activation energy is lowered compared to the parent azobenzene exhibiting an activation energy for the thermal backswitching in solution of 95 kJ mol^{-1}.[228] The activation energy of the thermal backswitching process of Azo is slightly affected by DASA since it is decreased and increased for DASA being present and DASA being simultaneously thermally backswitched (closed-to-linear), respectively.

The photoswitching of DASA contains more steps with the *Z*-to-*E* isomerisation happening on the ultrafast time scale and the following thermal ring closure taking place on a longer time scale (figure 5.80). The respective backswitching is thermally induced. Upon photoisomerisation, the molecules are promoted to the S_1 state and decay to the electronic ground state first in higher vibrational levels with subsequent vibrational relaxation. The time constants vary in solution between 3.3 - 4.3 and 5.3 - 9.2 ps, respectively, with longer lifetimes in MeCN compared to Tol. Those results are comparable to literature.[256] Quantum chemical calculations reveal barely polarity influence on the excitation dynamics such that dynamic effects cause the different kinetics.[258] The energy dissipation happens thereby faster in MeCN compared to Tol due to the lower molecular weight of MeCN.[273] In PMMA blend thin films, the time constants increase to 5.5 - 8.8 and 50.7 - 77.9 ps, respectively, due to a higher molecular weight of the surroundings and to steric hindrance playing a role. The investigation of DASA films is the first in its kind since there is no comparable literature available. In all environments, Azo has little impact on the switching properties of DASA with slightly accelerated processes in solutions but slightly decelerated processes in thin film. Applying the simultaneous switching wavelength of 506 - 515 nm, the processes are slightly accelerated in Tol and decelerated in MeCN and PMMA blend films. The impact of Azo is again rather small leading to slightly increased lifetimes in all environments.

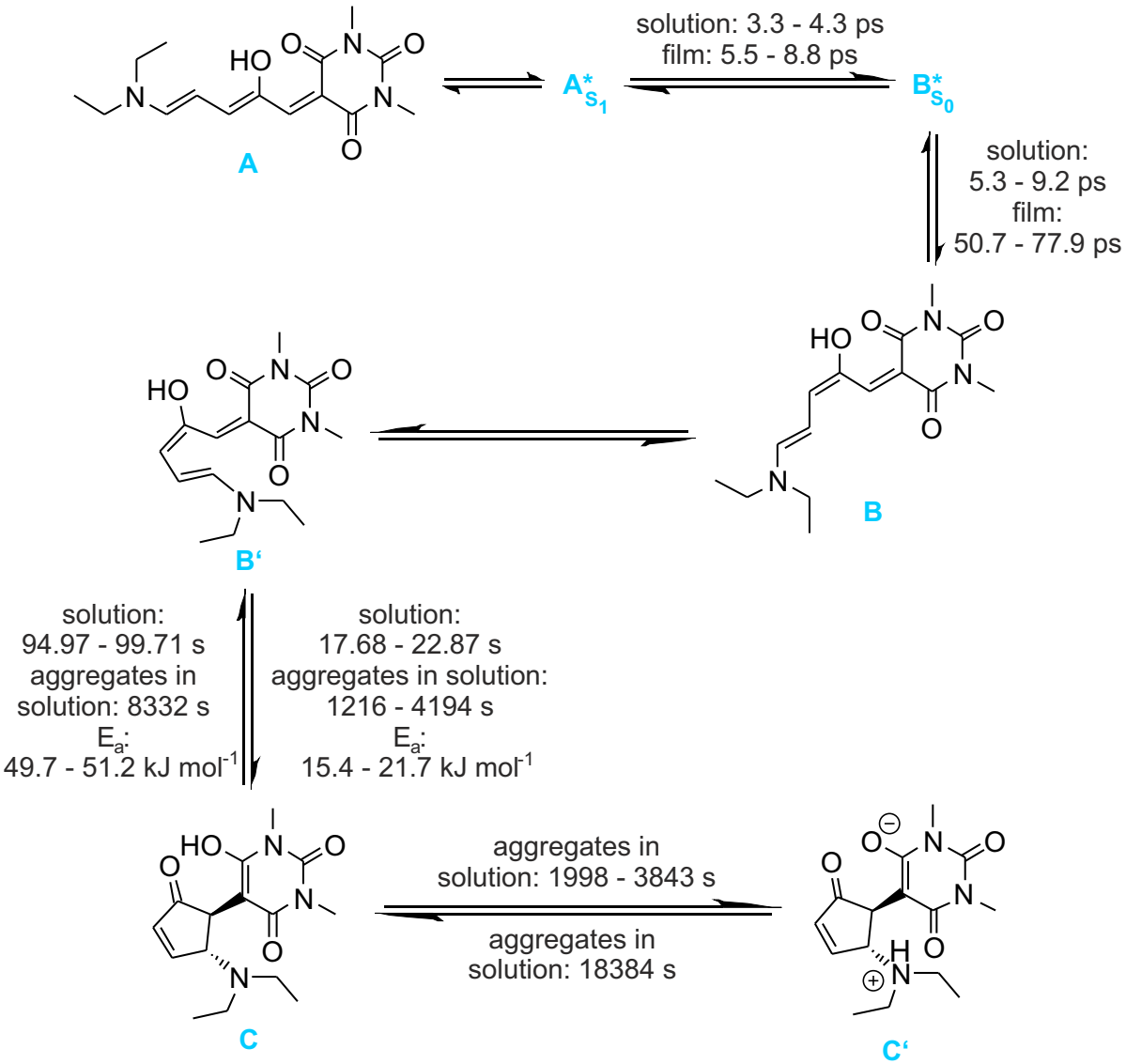

Figure 5.80. Scheme of the excited state dynamics of DASA after $S_0 \rightarrow S_1$ excitation by light and the reverse reaction induced by thermal energy. The stated time constants and activation energies represent a summary of all measurements of pure DASA, in the presence of *trans*/*cis*-Azo and upon simultaneously addressing DASA and Azo.

Considering the efficiency, up to 94 % of the DASA molecules undergo linear-to-closed isomerisation upon irradiation with light at 0 °C with lower yields at higher temperatures, e.g. about 84 % at 20 °C. In general, first generation donor-acceptor Stenhouse adducts show efficiencies ranging from 14 - 94 % at room temperature depending on the exact structure and solvent.[276]-[278] Studying the thermal ring closing reaction as well as the respective back reaction by temperature dependent UV/VIS measurements in Tol, the lifetime of the ring closing step at 20 °C is 17.68 - 22.87 s with the lifetime of the respective thermal backswitching in the dark being extended to 94.97 - 99.71 s. Those results are in line with literature as the literature suggests lifetimes of greater than 10 s for the ring closure of donor-acceptor Stenhouse adducts with diethylamino donors[279] and a similar time constant of 173 s for another diethylamino donor-acceptor

Stenhouse adduct upon thermal backswitching.[241] In both cases, the addition of Azo fastens the switching. The efficiency of thermal backswitching is around 100 % at temperatures above 30 °C and also at lower temperatures in the presence of Azo. Furthermore, the result of around 98.5 % of backswitched DASA molecules in a pure DASA solution at 20 °C agrees to literature data at room temperature.[240] The calculated activation energies for the ring closing and opening number 15.4 - 21.7 and 49.7 - 51.2 kJ mol^{-1}, respectively, which is significantly lower than the activation energies in the range of 76 - 93 kJ mol^{-1} stated in literature for comparable first generation donor-acceptor Stenhouse adducts.[247][277][279] While the activation energy of the electrocyclisation is increased if Azo is switched simultaneously (trans-to-cis), the reverse ring opening is unaffected by Azo.

Interestingly, the simultaneous thermal backswitching of Azo (cis-to-trans) entails an increase of the signal of *Z*-DASA. Investigating the ring closure and the proton transfer to generate the zwitterionic closed DASA photoproduct **C'** in Tol and MeCN by IR kinetic measurements using high concentrations, the kinetics are affected by aggregate formation in Tol leading to lifetimes of 1216 and 3843 s, respectively. The back reaction cannot be studied since the signal intensities are irregularly influenced by aggregates. In MeCN, however, the photoinduced ring closure and proton transfer to form the zwitterionic species as well as the back reactions can be studied. Thus, the lifetimes upon photoswitching amount to 4194 and 1988 s for the electrocyclisation and the proton transfer to form the zwitterionic isomer **C'**, respectively, and to 8332 and 18384 s upon thermal backswitching for the ring opening and the proton transfer to generate the non-zwitterionic closed isomer **C**, respectively. Analysing the literature, no study of the kinetics in the presence of aggregates is obtainable.

To sum up, the photoresponsive molecules switch independently according to the detailed studies. The mutual impacts of the orthogonal photoswitches on each other are rather small and resemble environmental changes rather than interactions since only dynamic effects on the excited state dynamics are observed. The profound study of the kinetic changes of an azobenzene derivative and an donor-acceptor Stenhouse adduct in an orthogonal mixture is the first of its kind with no comparable literature available.

6. Block copolymer

Beside small organic molecules, longer polymeric molecules can also be chosen as materials for 3D laser printing. The microstructure of the material is thereby crucial in order to control material properties. To design and control patterns in the tens-of-nanometer scale, block copolymers are an easy and useful tool.[31] [33] [34]
Due to their advantageous properties, block copolymers are widely used in high-resolution pattern applications, for example as large-area nanolithographic templates. Beside, they are implemented as e.g. upholstery foam, adhesive tape and asphalt additives to reduce pavement cracking and rutting. Furthermore, block copolymers are used as plastic additives for colloidal stabilisation, medical implantation and microelectronic fabrication.[31] [33]- [35]
Block copolymer molecules consist of two or more monomers which are organised in blocks composed of a single monomer type. The simplest architecture is a diblock copolymer AB made up of two covalently connected blocks with one block consisting of a long sequence of covalently bonded type A monomers and the other block representing a covalently connected homopolymer subunit of monomer B. For block copolymers, the number of monomer types and blocks can vary, generating for instance linear triblocks ABC or ABA. Since the blocks are chemically different due to the different monomers, their incompatibility drive microphase separation. As the entropy of mixing per unit volume of molecules with high molecular weight, such as polymers, is small, the mixing enthalpy plays an important role. Hence, even minor structural or chemical differences between the blocks can induce excess free energy contributions which are unfavourable for mixing. Thus, microphase segregation can take place forming microphases between 5 - 100 nm composed of one monomer type. Fluid-like disorder occurs thereby on the molecular scale but a high degree of order exists at longer length scales.
In this thesis, a diblock copolymer is investigated. An important diblock copolymer consisting of one block of polymethyl methacrylate (PMMA) and one block of polystyrene (PS) is PMMA-*b*-PS. In general, *b* within a chemical formula thereby indicates the formation of blocks. This block copolymer is the current industrial standard for block copolymer lithography due to its outstanding performance of microphase segregation. A perpendicular orientation of domains on a substrate is thereby achieved making PMMA-*b*-PS a promising candidate also for industrial manufactured devices based on this diblock copolymer.[34] [35]
In general, linear AB diblock copolymers occupy spherical, cylindrical, gyroid and lamellar morphologies depending on their composition *f* and the combination parameter χN. Here, the composition *f* represents the fraction of one monomer type compared to the total number of monomers in a macromolecule and the combination para-

meter χN is the product of the Flory-Huggins interaction parameter χ and the degree of polymerisation *N*. More precisely, χ is the segment-segment interaction energy of monomer A and B which is proportional to the heat of mixing monomer A and B while *N* constitutes the number of all monomers per macromolecule.[31][32][35][280]
For PMMA-*b*-PS, the surface energies of both homopolymer subunits are almost equal which benefits the formation of orthogonal oriented domains of the diblock copolymer due to the top free interface of a thin film. Since the Flory-Huggins interaction parameter χ of PMMA-*b*-PS is rather small, the smallest achievable domain size and the width of the domain interface is limited with the smallest domain size being 12 nm.[34][35]
The derivative of PMMA-*b*-PS used in this study is P(MMA-*co*-HEMA)-*b*-PS (figure 6.1). It differs from its parent polymer by replacing about 20 % of methyl methacrylate (MMA) monomers by hydroxyethylmethacrylate (HEMA) monomers forming the irregular copolymer subunit P(MMA-*co*-HEMA). The HEMA monomers are similar to the MMA monomers but with an additional CH_2-OH unit.

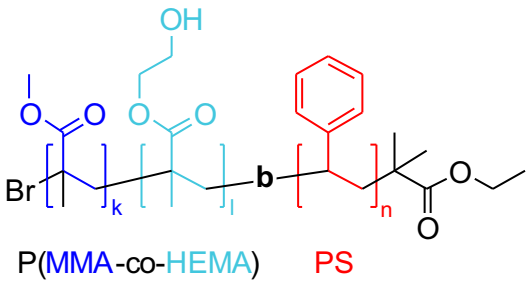

Figure 6.1. Structure of the P(MMA-*co*-HEMA)-*b*-PS block copolymer consisting of P(MMA-*co*-HEMA) and PS blocks.

The additional hydroxyl group is necessary for the following 3D printing. For the printing process, an acrylate group is introduced as photo-crosslinkable group which is done by esterification at the HEMA monomers. Upon the two-step 3D printing process, the polymers are crosslinked at the photo-crosslinkable acrylate groups to form a polymeric network. The fraction *f* of P(MMA-*co*-HEMA) and PS is nearly equal with 52 % and 48 %, respectively. Hence, lamellar structures are expected to be formed according to the parameters *f* and χN.
In the subsequent section 6.1, the IR absorption properties of the block copolymer P(MMA-*co*-HEMA)-*b*-PS and its subunits P(MMA-*co*-HEMA) and PS are studied in the far-field as well as in the near-field. Following, the microstructure of the diblock copolymer P(MMA-*co*-HEMA)-*b*-PS is analysed by s-SNOM techniques in section 6.2. Lastly, the structure of the polymeric network after 3D printing is studied in section 6.3.

6.1. IR characterisation of the blocks and the block copolymer

Before the structure of the diblock copolymer P(MMA-*co*-HEMA)-*b*-PS can be studied by s-SNOM techniques, the spectral features of the blocks and the block copolymer (all three synthesised by Britta Weidinger, Blasco research group, organic chemistry department of the Ruprecht-Karls-Universität Heidelberg) in the IR region are investigated in the far- and near-field. Since the near-field phase spectra are related to the absorptive properties of molecular samples (section 2.2.6), material identification is possible. However, a quantitative comparison of near- and far-field IR spectra reveal that the peak positions do not match in all cases but shifts are observed.[281] Hence, in a first step, the IR features in the far- and near-field have to be compared.

Starting with the P(MMA-*co*-HEMA) subunit of the diblock copolymer, the far-field IR spectrum of a P(MMA-*co*-HEMA) polymer shows the peak pattern of PMMA found in literature[282] [283] with no significant changes due to the incorporation of HEMA. The IR absorption maxima positions in the range of 1100 - 1800 cm^{-1} in the far- and near-field coincide within 6 cm^{-1} whereby the resolution of the far-field and the near-field data is 4 cm^{-1} and 8 cm^{-1}, respectively (figure 6.2). Thereby, most peak positions are slightly blue-shifted in the near-field compared to the far-field. The most prominent signals in the near-field spectrum are at about 1156, 1191, 1244, 1276, 1390, 1445, 1479 and 1733 cm^{-1} which could be addressed for mapping P(MMA-*co*-HEMA) using s-SNOM methods. The bands can thereby be assigned to several characteristic C=O, C-H and C-O-C vibrations.[284]

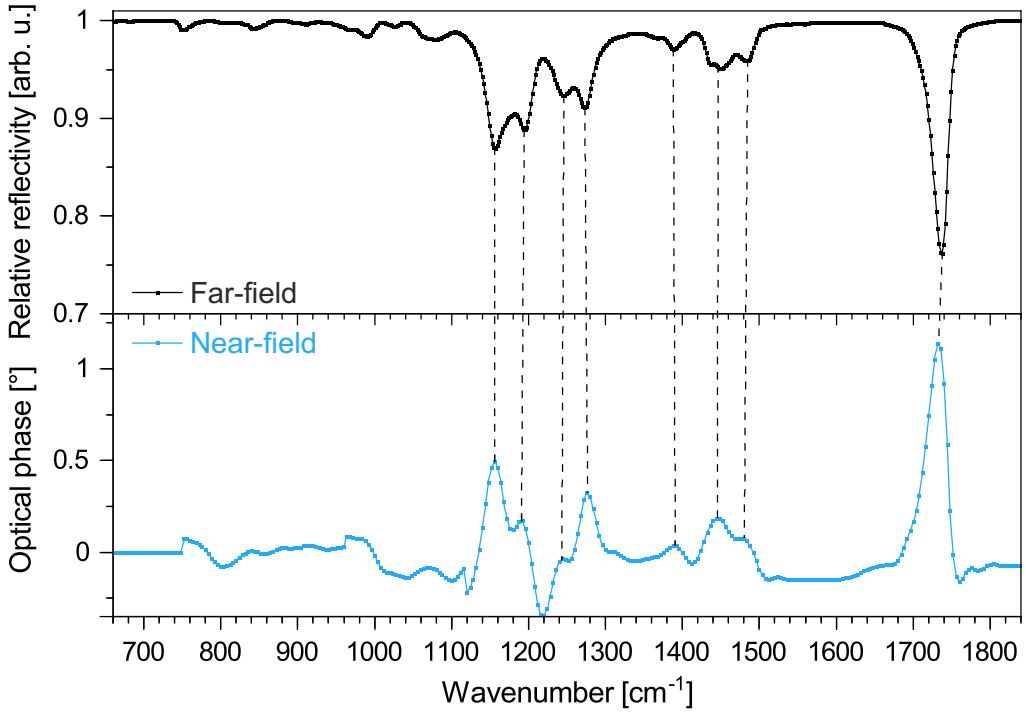

Figure 6.2. Comparison of the far-field and near-field IR spectra of P(MMA-*co*-HEMA) shown in black and blue, respectively.

Analysing the IR spectra of PS in the far- and near-field (figure 6.3), significantly less features are observed compared to P(MMA-*co*-HEMA). The observed peak pattern matches thereby the signals found in literature.[285] The IR absorption data in the far- and near-field agree within 3 cm^{-1} whereby the resolution of the far-field and the near-field data is 4 cm^{-1} and 8 cm^{-1}, respectively. The most intense signals are at about 701, 756, 1452, 1493 and 1602 cm^{-1} in the near-field IR spectrum which can be assigned to several characteristic C-H vibrations.[286] However, only a spectral window of about 1100 - 1800 cm^{-1} can be used for mapping with the QCL lasers of the s-SNOM setup (section 3.4). Hence, the most prominent band at 701 cm^{-1} as well as the band at 756 cm^{-1} cannot be addressed.

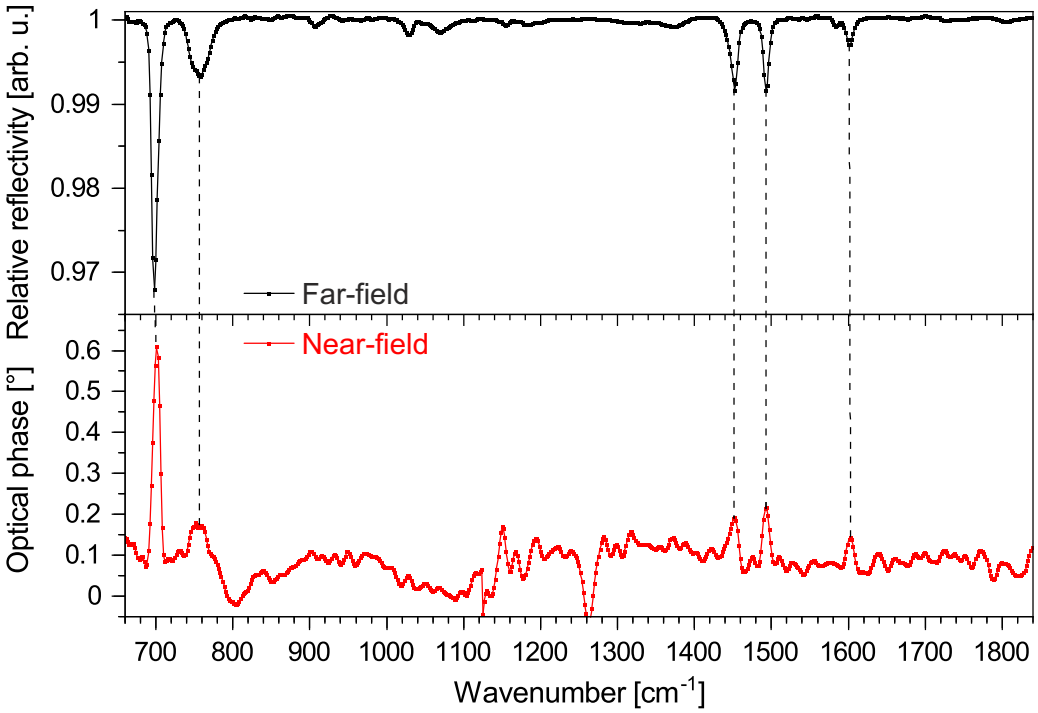

Figure 6.3. Comparison of the far-field and near-field IR spectra of PS shown in black and red, respectively.

Since the differences of the far- and near-field data of the polymers P(MMA-*co*-HEMA) and PS are minor, also the IR absorption bands of the respective diblock copolymer P(MMA-*co*-HEMA)-*b*-PS are expected to be at about the same spectral positions in the far- and near-field. Hence, the more convenient far-field spectra exhibiting a better signal-to-noise ratio are used to compare the block copolymer and its subunits in the following.

Comparing the far-field IR absorption data of the polymers P(MMA-*co*-HEMA) and PS to the diblock copolymer P(MMA-*co*-HEMA)-*b*-PS, the spectrum of the latter essentially consists of the sum of its single components (figure 6.4). All above mentioned absorption bands are also present in the block copolymer. However, some peaks are shifted up to 7 cm^{-1} with the resolution of all spectra being 4 cm^{-1}. According to the IR spectra,

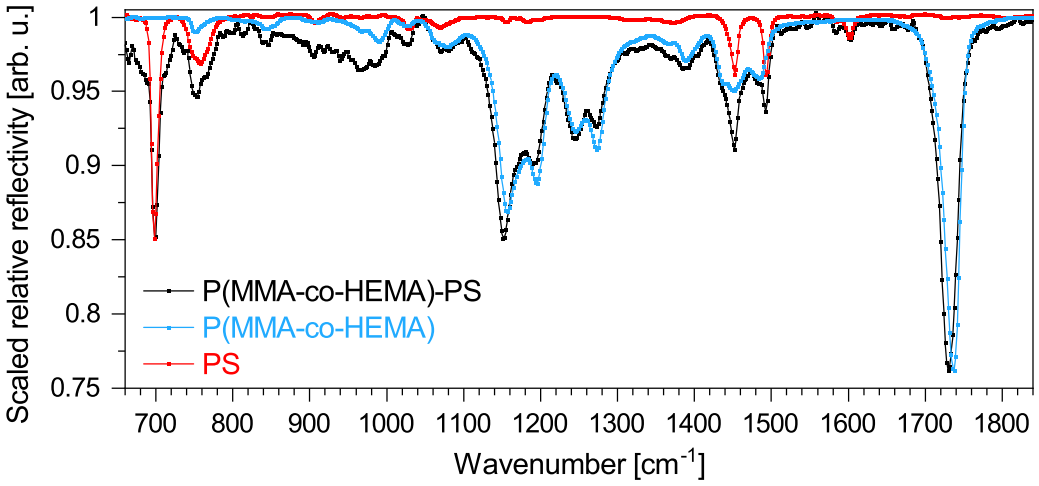

Figure 6.4. Far-field spectrum of the P(MMA-*co*-HEMA)-*b*-PS block copolymer in comparison to the spectra of P(MMA-*co*-HEMA) and PS. The far-field spectra of P(MMA-*co*-HEMA) and PS are scaled in order to match the maximum intensity of P(MMA-*co*-HEMA)-*b*-PS. The latter spectrum exhibits no additional features with respect to the single components.

most absorption bands of the block copolymer P(MMA-*co*-HEMA)-*b*-PS in the examined spectral window are related to P(MMA-*co*-HEMA). In order to map the positions of P(MMA-*co*-HEMA), the most intense absorption bands of P(MMA-*co*-HEMA) at about 1152 cm^{-1} and 1733 cm^{-1} are suitable with the latter being out of the accessible range for the PsHet mode (section 2.2.6). For PS, it is more difficult to define an absorption band for mapping. Since the most intense bands are outside of the accessible laser range, only three bands can be addressed. The two most intense bands of the latter, located at around 1452 and 1493 cm^{-1}, spectrally overlap with P(MMA-*co*-HEMA) IR absorption bands which make them unfavourable for mapping the locations of PS. Hence, only the low intense absorption at about 1602 cm^{-1} can be used to determine the location of PS in the mixed diblock copolymer P(MMA-*co*-HEMA)-*b*-PS.

6.2. Microscopic structure of the block copolymer

In order to analyse the microstructure and morphology of the diblock copolymer P(MMA-*co*-HEMA)-*b*-PS, it was fabricated by radical polymerisation and dried slowly within an desiccator in the course of one week to provide time for structural orientation of the block copolymer. Next, the solid block copolymer was cut into slices with thicknesses of around 90 - 500 nm by an ultramicrotome (synthesis and slicing done by Britta Weidinger, Blasco research group, organic chemistry department of the Ruprecht-Karls-Universität Heidelberg) and investigated by s-SNOM techniques.
First, the positions of the P(MMA-*co*-HEMA) block in the synthesised diblock copolymer P(MMA-*co*-HEMA)-*b*-PS samples were studied by addressing the second most intense IR absorption band of P(MMA-*co*-HEMA) in the PsHet mode. Thereby, different microstructures are found (figure 6.5**a**). In general, three different types of areas

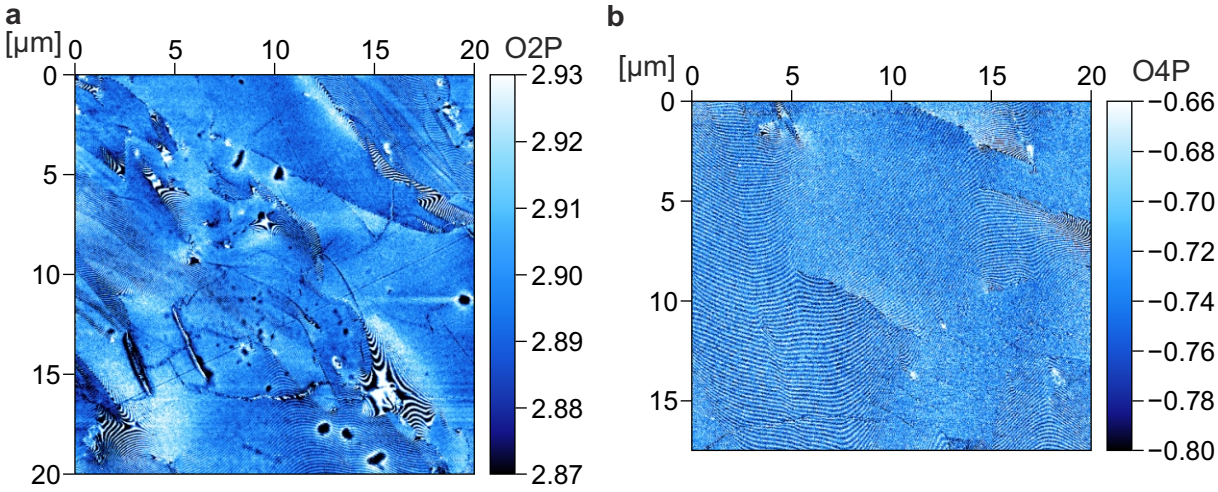

Figure 6.5. (a) Second and (b) forth order near-field phase optical imaging with a pixel size of 40 nm of the signal obtained by irradiation at 1152 cm^{-1} which is absorbed by the P(MMA-*co*-HEMA) part of the block copolymer P(MMA-*co*-HEMA)-*b*-PS. Beside regions with (a, b) regular lamellae, (a) defects can be found as well.

are observed. In some parts of the samples, no contrast in the SNOM data is seen (large middle-blue areas in figure 6.5**a**). In those areas, no microphase segregation took place such that the blocks P(MMA-*co*-HEMA) and PS are intermixed on a smaller level than the resolution. In contrast, there are also large areas with only one colour which are attributed to defects. The centre of those defects are mostly composed of P(MMA-*co*-HEMA) (large white spots in figure 6.5**a**). The broad and irregular shape indicates no good microphase separation as no regular structure is achieved. Furthermore, striped areas are also observed indicating good microphase segregation which lead to the formation of lamellae. In some spots of the P(MMA-*co*-HEMA)-*b*-PS block copolymer, large areas are found in which a higher order is received as recognised by extensive lamellar structures (figure 6.5**b**). However, even in those areas of more regular structures, the lamellae often change their spacing. This can be explained by the preparation method in which no substrate was used. Hence, there is less preference to form lamellae along one direction. Instead, the lamellae evolve in different directions. Thus, the surfaces of the sliced samples are not perpendicular to the lamellae such that different thicknesses are observed.

In order to determine the lamellae spacing, the smallest domain size present in several samples is examined. By analysing such an area of smallest regular structure, a domain size of about 70 nm is found (figure 6.6). This is significantly larger than the theoretical smallest domain size of 12 nm for PMMA-*b*-PS.[34][35] However, it is comparable and even smaller than the domain size of a similar literature known study of PMMA-*b*-PS having a domain size of 85 nm.[33] Since the goal of this study is not to optimise the lamellar structure towards smaller domains but to analyse and compare the structure of the block copolymer before and after printing, a domain size of 70 nm is sufficient.

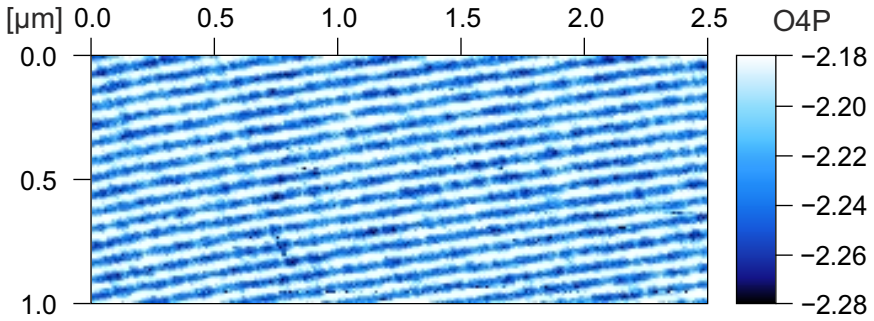

Figure 6.6. Fourth order near-field phase optical imaging with a pixel size of 10 nm using IR radiation at 1152 cm^{-1} being absorbed by the P(MMA-*co*-HEMA) part of the block copolymer P(MMA-*co*-HEMA)-*b*-PS. The regular lamellae are 70 nm wide.

To verify that the parts with low absorption of IR radiation of 1152 cm^{-1} represent the subunit composed of PS, complementary experiments were carried out. In order to map PS, excitation by IR radiation at 1602 cm^{-1} is used. Ideally, by mapping with IR radiation at 1152 cm^{-1} and 1602 cm^{-1}, complementary images are obtained. However, due to the small cross section of IR radiation at 1602 cm^{-1}, low contrast is observed and no complementary image could be obtained in the PsHet mode.
Next, the AFM-IR mode of the s-SNOM was utilised to check for better contrast using the same excitation energies. In this mode, the contrast upon excitation with IR radiation at 1602 cm^{-1} is higher. Hence, it was possible to record essentially complementary images by addressing P(MMA-*co*-HEMA) and PS (figure 6.7). In this images, lamellae with small domain size are observed as well as lamellae with greater domain size with different spatial orientation. Since the optical contrast is not optimal, the location and complementarity of the images using IR radiation at 1152 cm^{-1} absorbed by P(MMA-*co*-HEMA) (figure 6.7**a**) and of 1602 cm^{-1} absorbed by PS (figure 6.7**b**) is easier to recognise with the help of the topography. Hence, the topography is illustrated as 3D and coloured by the IR amplitude optical image if P(MMA-*co*-HEMA) (figure 6.7**c**) and if PS (figure 6.7**d**) is addressed. The topography reveals that the lamellae with small domain size are rather flat while the lamellae with greater domain size rise up to 60 nm height. In addition, the lamellae themselves are not flat but constitute a structure of hills and valleys. Particularly in the higher areas, the location of the two blocks P(MMA-*co*-HEMA) and PS can be observed. Thereby, P(MMA-*co*-HEMA) sits in the valleys of the lamellar structure while PS sits on the hills.

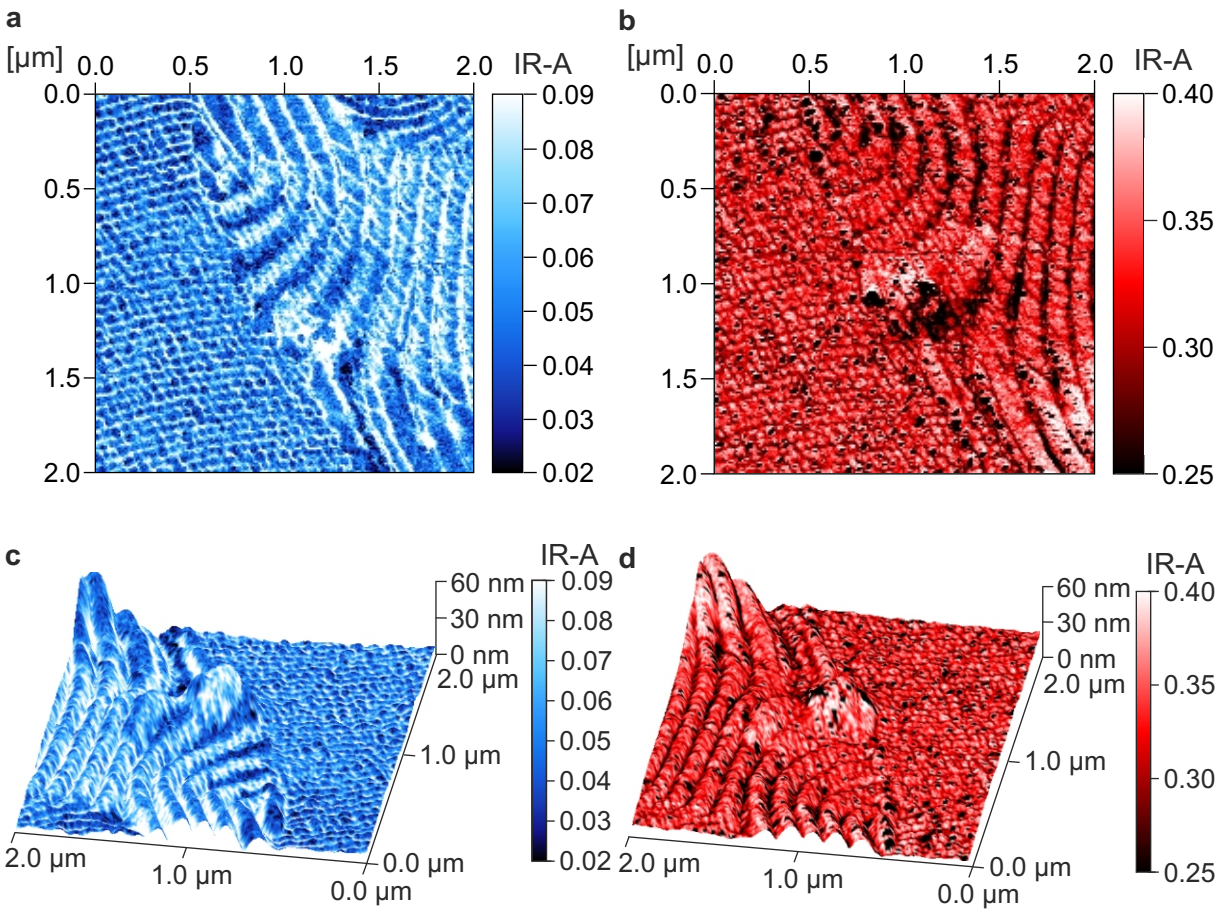

Figure 6.7. AFM-IR amplitude optical imaging using a pixel size of 10 nm and excitation by IR radiation at (a, c) 1152 cm^{-1} being absorbed by P(MMA-*co*-HEMA) and at (b, d) 1602 cm^{-1} being absorbed by PS, respectively, in the block copolymer P(MMA-*co*-HEMA)-*b*-PS. It can be seen that the near-field phase optical images are complementary and that (c) P(MMA-*co*-HEMA) sits in the valleys of the topographic structure whereas (d) PS sits on the hills of the topographic structure if the near-field phase signal is overlaid on the 3D topography.

6.3. 3D printed block copolymer

In the next step, the diblock copolymer P(MMA-*co*-HEMA)-*b*-PS is functionalised and the crosslinkable groups are introduced. Subsequently, the diblock copolymer is 3D printed using a direct laser writing system (Nanoscribe GmbH, printed by Britta Weidinger, Blasco research group, organic chemistry department of the Ruprecht-Karls-Universität Heidelberg). The dissolved block copolymer forms thereby a solid polymeric network.

Since no significant differences are found between the IR absorption bands of the P(MMA-*co*-HEMA) polymer and the literature known PMMA, no significant differences of the already identified IR absorption bands of the P(MMA-*co*-HEMA) block upon crosslinking are expected and hence no differences in IR absorption of the whole P(MMA-*co*-HEMA)-*b*-PS block copolymer before and after printing are presumed (section 6.1). Nevertheless, IR far-field spectra were recorded to ascertain differences and

additional bands (figure 6.8). In the printed blocks composed of the crosslinked block copolymer P(MMA-*co*-HEMA)-*b*-PS, the absorption bands located at 1601 cm^{-1} and 1730 cm^{-1} can be related to the PS and P(MMA-*co*-HEMA) subunit, respectively, since the spectral positions are about the same compared to the IR bands of the precursor block copolymer P(MMA-*co*-HEMA)-*b*-PS. However, two additional small absorption bands are present in the 3D printed crosslinked P(MMA-*co*-HEMA)-*b*-PS samples at around 1650 cm^{-1}. Those bands are related to the carbonyl groups of the crosslinkable and the crosslinked groups. No bands below 1550 cm^{-1} could be obtained due to the reststrahlen band caused by the glass substrate[287] which is necessary for the 3D printing process.

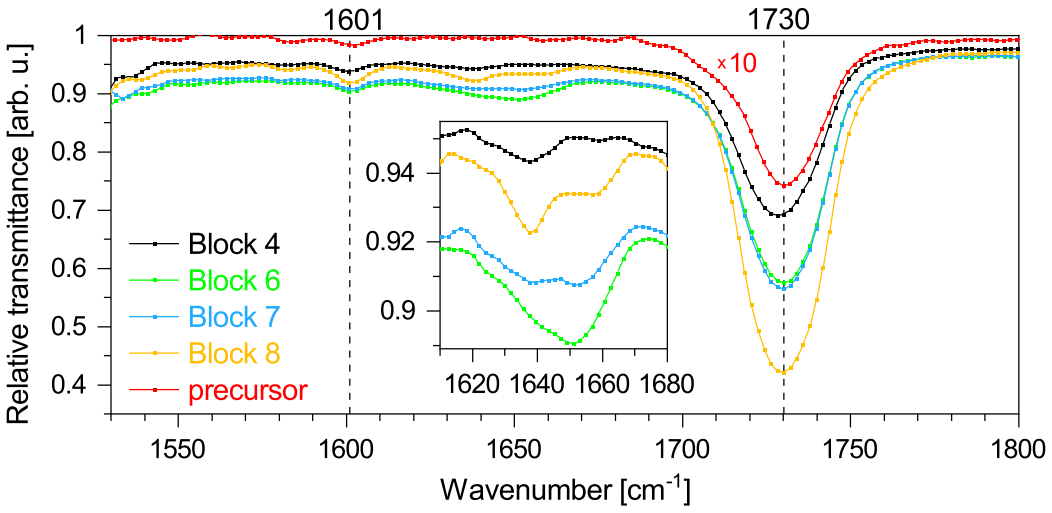

Figure 6.8. IR far-field spectra of printed crosslinked P(MMA-*co*-HEMA)-*b*-PS blocks and the P(MMA-*co*-HEMA)-*b*-PS starting material. The inset shows two additional bands related to the crosslinked groups.

Hence, in order to investigate the microstructure of the 3D printed block copolymer, the already identified absorption bands in the near-field at 1602 cm^{-1} and 1152/1733 cm^{-1} can be utilised to map the positions of PS and P(MMA-*co*-HEMA), respectively, using the PsHet and AFM-IR mode.

To analyse the structure and the microphase separation in the 3D printed sample, the PsHet and the AFM-IR mode can be used to map the positions of P(MMA-*co*-HEMA) and PS. However, as it is the case for the diblock copolymer P(MMA-*co*-HEMA)-*b*-PS precursor, the AFM-IR mode gives slightly higher signals for the stimulation of the PS absorption resulting in better signal-to-noise ratios by excitation with IR radiation at 1602 cm^{-1}. Printed blocks of different heights which range between 10 - 1100 nm show similar structures independent on the printed height. All areas show a granular structure (figure 6.9). Furthermore, the optical contrast is the same no matter if P(MMA-*co*-HEMA) (figure 6.9**a**) or PS (figure 6.9**b**) is excited. Hence, no microphase segregation took place which would form distinct areas with higher absorption

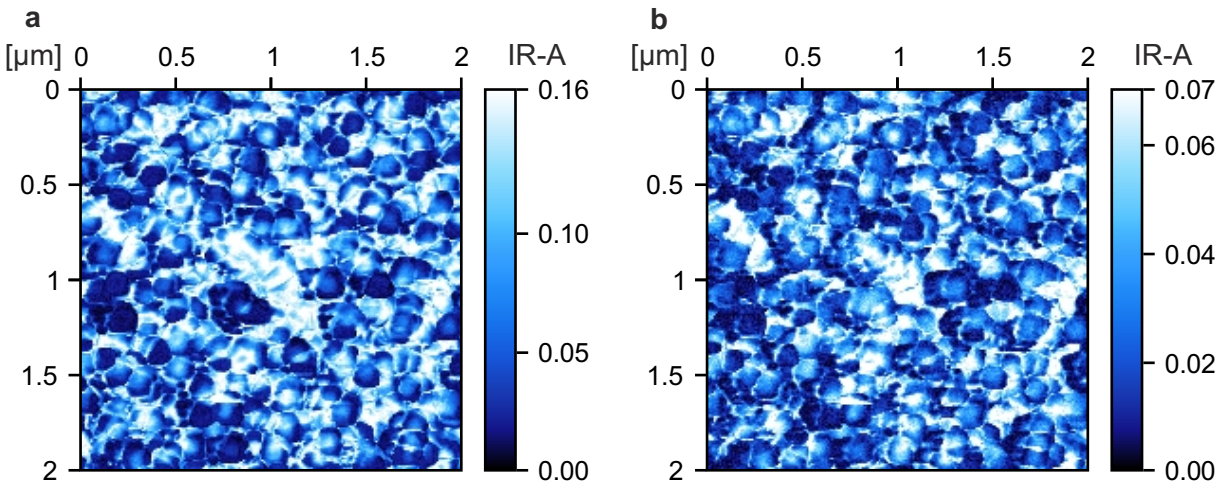

Figure 6.9. AFM-IR amplitude optical imaging with IR radiation at (a) 1733 cm^{-1} being absorbed by P(MMA-*co*-HEMA) and at (b) 1602 cm^{-1} being absorbed by PS, respectively, in the printed block copolymer P(MMA-*co*-HEMA)-*b*-PS. Both maps match each other such that upon crosslinking the block copolymer during the printing process, no lamellar microstructure is formed.

of P(MMA-*co*-HEMA) or PS. Instead, the two blocks are close together such that their positions cannot be separated with the s-SNOM setup.

Considering the printing process, the formation of the crosslinked network upon 3D printing happens on an ultrafast time scale compared to the preparation of the P(MMA-*co*-HEMA)-*b*-PS precursor material which took about one week. Hence, there is little time for the blocks to form microphases upon printing. Instead, the polymers form grains which harden during the 3D printing process.

In order to gain microphases not only in P(MMA-*co*-HEMA)-*b*-PS but also in the 3D printed crosslinked P(MMA-*co*-HEMA)-*b*-PS network, the microphase lamellae have to form already in the liquid phase prior to the 3D printing since the fast printing process allows no structural orientation upon printing. Thus, the conditions of the 3D printing process, for instance solvents and substrates, need to be optimised to gain also lamellar microphase structures in the 3D printed crosslinked P(MMA-*co*-HEMA)-*b*-PS network.

7. Conclusion

The presented studies utilise multiple laser spectroscopic techniques, such as 2PPE, TA and s-SNOM, to provide insights into different properties and behaviours of functional organic materials. First, a promising organic semiconductor for OFET or photovoltaic applications is investigated. Hence, the research focus is put on the electronic properties of the organic material in contact with a metal electrode simulating any device as the electronic structure on the metal/organic interface plays a crucial role in device performance. Following, a mixture of two individually (i.e. orthogonally) but also simultaneously addressable photoswitches is investigated which are used as smart materials delivering differentiated responses upon light exposure. The studied mixture is applied as 3D multi-responsive actuator for smart (micro)robotics since the materials can be 3D printed. In fact, the 3D printing of materials being responsive to light is termed 4D printing with the fourth dimension being the time. Further utilisation of those photoswitches in biomedical applications and information storage are in posse. All steps of photoisomerisation as well as influences of the environment and of the photoresponsive molecules on each other are thereby studied in detail. Lastly, another 3D printable mixture is investigated. It is a derivative of a standard diblock copolymer for high-resolution pattern applications e.g. for large-area nanolithography. Diblock copolymers consist of two different polymers covalently connected. The microstructure and self-assembly feature thereby prominently in the application such that the focus is put on the microstructural arrangement before and after 3D printing.
First, the adsorption and desorption properties as well as the electronic structure of a pentacene derivative is investigated when in contact with a gold substrate representing the metal electrode. The electronic structure of the nitrogen substituted pentacene derivative 6,13-diazapentacene (DAP) on Au(111) is analysed and its change at higher coverages since those factors are critical for device performance. Additionally, the adsorption and desorption properties are researched which are important also for the preparation of devices. Therefore, 2PPE and TPD techniques are utilised.
DAP stays intact upon evaporation in UHV as well as upon desorption. It adsorbs thereby in a planar manner on Au(111) with the molecular backbone oriented parallel to the substrate as HREELS data show. As affirmed by no significant peak broadening with increasing layer thickness, the molecules are highly ordered also at higher amounts of layers. Comparing the TPD results of DAP with the TPD results of its parent molecule, both form long-range interactions such that first a monolayer with double distance between the molecules is formed, represented by a tail in the TPD spectrum, and subsequently the same amount of molecules attach to the Au(111) surface in between the adsorbed DAP molecules, represented by a compressed phase in the TPD data. Several molecular electronic states are determined by 2PPE referred to as the LUMO,

exciton, HOMO, HOMO-1 and HOMO-2 using the molecular picture. The fundamental transport gap amounts to 2.43 eV while the optical gap numbers 1.92 eV which is reduced by the exciton binding energy of 0.51 eV. The accordance of the determined optical gap to the optical gap found by UV/VIS spectroscopy in solution suggests a weak adsorbate/substrate interaction. The optical gap is reduced by 0.1 eV by the introduction of two nitrogen atoms compared to pentacene which stabilise the valence molecular orbitals due to the increased electronegativity. Future work on DAP should implement it in organic devices such as OFETs since this work presents a detailed understanding of the molecular electronic states and suggests good long-range order favourable for charge transport. The fundamental research should be extended to other nitrogen substituted pentacene derivatives to have a palette of n-type semiconductors suitable for particular purposes.

Next, the switching properties of an orthogonal mixture of two photoresponsive molecules is researched in detail. Because this orthogonal mixture responds in differentiated ways to light, acting as sustainable external stimulus with high spatio-temporal resolution, it acts as smart material suitable for (micro)robotics, data storage and biomedical application. As one photoswitch, the push-pull azobenzene derivative Azo is chosen exhibiting a large change in volume and shape upon switching. The photoinduced switching of the thermodynamically stable *trans*-Azo to the metastable *cis*-Azo can thereby be reversed by light or thermal activation. Since Azo demands the VIS spectrum at its short wavelength side, the donor-acceptor Stenhouse adduct DASA absorbing in the long wavelength region of the VIS spectrum is used as complementary photoswitch. The photoswitching of the thermodynamically stable *Z*-DASA isomer **A** undergoes first ultrafast *Z*/*E*-isomerisation before the ring closure and proton transfer take place on a longer time scale to form the zwitterionic closed isomer **C'**. The switching is thereby characterised by a large solubility change. The reverse reaction is initiated by thermal energy.

First, the ultrafast excited state dynamics of both compounds are studied at room temperature using the pure photoswitch or a 1:1 molar mixture in Tol, MeCN and as PMMA blend thin film. The ultrafast photoinduced trans-to-cis and cis-to-trans isomerisation of Azo upon π-π^* excitation includes the conical intersection $S_2 \rightarrow S_1$ and the movement of the wavepacket out of the Franck-Condon region towards the conical intersection $S_1 \rightarrow S_0$ which happen in less than 200 fs, the deactivation into the electronic ground state but in higher vibrational levels within 0.7 - 1.4 ps and vibrational relaxation within 3.3 - 9.8 ps. This holds true for pure Azo, in the presence of *Z*/*E*-DASA and if the switches are addressed simultaneously in solution using both Tol and MeCN. The ultrafast switching of DASA upon photoexcitation involves *Z*-to-*E* isomerisation. After excitation to S_1, the electronic ground state is reached via internal conversion in higher vibrational levels and subsequently vibrational cooling occurs. The time constants in

Tol and MeCN solution for pure DASA, in the presence of *trans*/*cis*-Azo and if both switches are addressed simultaneously, amount to 3.3 - 4.3 and 5.3 - 9.2 ps, respectively. In thin PMMA blend films, the respective time constants upon addressing Azo and DASA increase due to steric hindrance. For the cis-to-trans isomerisation of Azo in thin film, likely a trapped state is found. In general, the processes fasten in the order of PMMA, Tol and MeCN and upon adding the other photoresponsive material due to dynamic effects causing a better energy dissipation whereas the electronic states are barely affected. Hence, no influences of the photoswitches on each other is observed beside environmental changes.
Studying the photoinduced trans-to-cis isomerisation of Azo and the *Z*-to-*E* isomerisation of DASA as well as the thermally activated reverse reactions on a longer time scale via temperature dependent UV/VIS spectroscopy in Tol allows the analysis of the ring closure and opening of DASA as well as the activation energies of all thermally induced processes. Considering the orthogonal switching performance of Azo, the number of switched and backswitched molecules is proportional to the temperature with about 67 % switched and 92 % backswitched Azo molecules, respectively, at 20 °C whereby the efficiency is significantly lower for the simultaneous switching wavelength having a smaller cross section. The percentage of photoswitched molecules is thereby much higher compared to similar literature known push-pull azobenzene derivatives. The thermally activated backswitching shows an activation energy of 83.6 - 89.0 kJ mol^{-1} for pure Azo, in the presence of *Z*-DASA and upon simultaneous backswitching. In general, the activation energy is lower compared to the parent azobenzene. Regarding the switching of DASA, the number of photoswitched molecules is inversely proportional to the temperature and not affected by the switching wavelength while the number of thermally backswitched molecules is direct proportional to temperature and near 100 % for all temperatures if *trans*-Azo is present. For a pure DASA solution, the photoswitched molecules and the thermally activated backswitched molecules at 20 °C amount to around 84 and 98 %, respectively. The activation energy of the electrocyclisation and ring opening for pure DASA, in the presence of *trans*-Azo and upon simultaneous photoswitching amount to 15.4 - 21.7 kJ mol^{-1} and 49.7 - 51.2 kJ mol^{-1}, respectively, which are significantly lower compared to similar donor-acceptor Stenhouse adducts. A striking observation is the increase of *Z*-DASA absorption upon thermally activated backswitching of Azo thereby exceeding 100 % if referred to the initial DASA absorption before photoswitching. In general, the key figures are little influenced within the mixture compared to the pure photoswitches.
Lastly, IR kinetic measurements open the opportunity to study the ring closing and opening as well as the proton transfer of the closed species upon switching DASA at room temperature. The IR absorption spectra of DASA in Tol and MeCN reveal little influence of the environment compared to a KBr pellet surrounding. The vibra-

tional bands of the linear isomers **A**, **B** and **B'**, the closed isomer **C** and the zwitterionic closed isomer **C'** can by assigned using DFT calculated spectra. In Tol, the rate constants $k_{\mathbf{B'}\rightarrow\mathbf{C}}$ and $k_{\mathbf{C}\rightarrow\mathbf{C'}}$ upon photoswitching number 822 and 260 µs^{-1} while the thermal backswitching shows an increase of all absorption bands of the isomers **A**, **C** and **C'** may due to the break-up of aggregates distorting the data. Aggregate formation may thereby take place in the high concentrations necessary to carry out the experiment. In MeCN, however, the photoswitching and thermal backswitching is not distorted due to aggregates resulting in rate constants $k_{\mathbf{B'}\rightarrow\mathbf{C}}$ and $k_{\mathbf{C}\rightarrow\mathbf{C'}}$ of 238 and 503 µs^{-1} upon photoswitching, respectively, and in $k_{(\mathbf{B'}\rightarrow\mathbf{C})_{-1}}$ and $k_{(\mathbf{C}\rightarrow\mathbf{C'})_{-1}}$ of 120 and 54 µs^{-1} upon thermal backswitching, respectively. The data show the high stability of the zwitterionic photoproduct since the proton transfer happens fast upon photoswitching but slow upon thermal backswitching.

To sum up, the in depth analysis of the switching properties of Azo, DASA and their orthogonal mixture revealed independent photoswitching with minor changes introduced by the other photoswitch compared to the pure compounds. Hence, the impact is rather an environmental change since dynamic effects occur but no electronic influences. The thermal backswitching performance of DASA is increased by the presence of Azo. Further studies should investigate the origin of the increase in absorption of *Z*-DASA upon thermal backswitching Azo. Additionally, the orthogonal mixture of photoresponsive molecules should be applied as smart device. This study revealed no negative influence of the photoswitches on each other on their photoswitching properties such that the performance of each photoswitch is not negatively influenced in the mixture. In fact, the performance of any 4D printed device fabricated on the basis of the investigated mixture increases due to the presence of the other photoswitch as the switching processes happen faster. Additionally, the amount of thermally backswitched DASA molecules is increased in the mixture compared to the single components boosting the performance. Co-workers already published the implementation of those switches in a 3D printed liquid crystalline matrix and the successful use as 3D microactuator. Further applications should be tested and optimised.

Lastly, the microstructure of the diblock copolymer P(MMA-*co*-HEMA)-*b*-PS constituted of one block of P(MMA-*co*-HEMA) at about 50 % and of one block of PS at about 50 % is investigated by s-SNOM techniques. In addition to its parent PMMA-*b*-PS block copolymer, which is the industry standard for nanolithographic templates, it features hydroxyl groups which can be functionalised to form a polymeric network upon 3D printing. P(MMA-*co*-HEMA)-*b*-PS shows microphase separation developing 70 nm wide lamellae with P(MMA-*co*-HEMA) and PS forming small topographic valleys and hills, respectively. However, in a first try to 3D print the diblock copolymer, no microphase segregation is observed since the printing process is fast compared to the preparation of the polymer. Hence, the microphase separation needs to be pre-formed in the vis-

cous solution prior to printing. In the ongoing experiments, co-workers changed the solvent such that lamellae are also found in the printed structure. In the future, the printing process should be optimised to form regular lamellae or other microstructures. Next, the post-functionalisation of only one block can open new ways of manufacturing 3D printed structures.

In summary, this work contributed to a better understanding of electronic and structural properties of functional materials. Investigations by advanced laser spectroscopies revealed the electronic structure of DAP on Au(111), the orthogonality of Azo and DASA, including a study of the impact of the environment and the photoswitches on each other, as well as the microphase separation of P(MMA-*co*-HEMA) and PS in their respective diblock copolymer before and after 3D printing. Future investigations, e.g. within the scope of the collaborative research centre SFB1249 and the 3D Matter Made to Order cluster of excellence, about N-heteropolycyclic materials and 3D printable materials should identify and study functional materials and implement improved materials in (smart) devices in order to counteract the increasing energy consumption and man-made global warming.

References

[1] Enerdata, Total energy consumption. 2023, date of access: 06.01.2023; *https://yearbook.enerdata.net/total-energy/world-consumption-statistics.html*.

[2] Flohn, H. Possible climatic consequences of a man-made global warming. *International Institute for Applied Systems Analysis* **1980**,

[3] Khairullina, E. R.; Bogdanova, V. I.; Slepneva, E. V.; Nizamutdinova, G. F.; Fatkhullina, L. R.; Kovalenko, Y. A.; Skutelnik, O. A. Global climate change: Cyclical nature of natural and permanent nature of man-made processes. *EurAsian Journal of BioSciences* **2019**, *13*, 2311–2316.

[4] Zhang, G.; Xie, C.; You, P.; Li, S. *Introduction to Organic Electronic Devices*, 1st ed.; Springer eBook Collection; Springer Nature Singapore: Singapore, 2022.

[5] Li, L. Organic Semiconductors: History and Applications. date of access: 25.11.2022; *https://www.iue.tuwien.ac.at/phd/li/node9.html*.

[6] Tang, C. W.; VanSlyke, S. A. Organic electroluminescent diodes. *Applied Physics Letters* **1987**, *51*, 913–915.

[7] Forrest, S. R.; Thompson, M. E. Introduction: Organic Electronics and Optoelectronics. *Chemical Reviews* **2007**, *107*, 923–925.

[8] Javadi, R. Application of Organic Field-Effect Transistors in Electronic Charge Transport. *Bulletin of Pure and Applied Sciences-Physics* **2013**, *32D*, 1–14.

[9] Sze, S. M.; Ng, K. K. *Physics of semiconductor devices*, 3rd ed.; Wiley-Interscience online books; Wiley-Interscience: Hoboken, NJ, 2007; Dateiformat Volltext: PDF.

[10] Zhao, W.; Yang, C.-F.; Meen, T.-H. *Intelligent Electronic Devices*; MDPI - Multidisciplinary Digital Publishing Institute: Basel, 2020.

[11] Ligon, S. C.; Liska, R.; Stampfl, J.; Gurr, M.; Mülhaupt, R. Polymers for 3D Printing and Customized Additive Manufacturing. *Chemical Reviews* **2017**, *117*, 10212–10290.

[12] Wu, J.-J.; Huang, L.-M.; Zhao, Q.; Xie, T. 4D Printing: History and Recent Progress. *Chinese Journal of Polymer Science* **2018**, *36*, 563–575.

[13] Knight, S. Local Motors unveils Strati, the world's first 3D-printed car. 2014, date of access: 28.12.2022; *https://www.techspot.com/news/58075-local-motors-unveils-strati-the-worlds-first-3d-printed-car.html*.

[14] Newatlas, "World's first" 3D printed car created and driven by Local Motors. 2014, date of access: 28.12.2022; *https://newatlas.com/local-motors-strati-imts/33846/*.

[15] Kuang, X.; Roach, D. J.; Wu, J.; Hamel, C. M.; Ding, Z.; Wang, T.; Dunn, M. L.; Qi, H. J. Advances in 4D Printing: Materials and Applications. *Advanced Functional Materials* **2019**, *29*, 1805290, https://doi.org/10.1002/adfm.201805290.

[16] Tibbits, S. The emergence of "4D printing". 2013, date of access: 28.12.2022; *https://www.ted.com/talks/skylar_tibbits_the_emergence_of_4d_printing*.

[17] Tibbits, S. 4D Printing: Multi-Material Shape Change. *Architectural Design* **2014**, *84*, 116–121, https://doi.org/10.1002/ad.1710.

[18] Momeni, F.; M.Mehdi Hassani.N, S.; Liu, X.; Ni, J. A review of 4D printing. *Materials and Design* **2017**, *122*, 42–79.

[19] Khoo, Z. X.; Teoh, J. E. M.; Liu, Y.; Chua, C. K.; Yang, S.; An, J.; Leong, K. F.; Yeong, W. Y. 3D printing of smart materials: A review on recent progresses in 4D printing. *Virtual and Physical Prototyping* **2015**, *10*, 103–122.

[20] Scott, J. C. Metal-organic interface and charge injection in organic electronic devices. *Journal of Vacuum Science and Technology A* **2003**, *21*, 521–531.

[21] Fahlman, M.; Fabiano, S.; Gueskine, V.; Simon, D.; Berggren, M.; Crispin, X. Interfaces in organic electronics. *Nature Reviews Materials* **2019**, *4*, 627–650.

[22] Lee, S.; Koo, B.; Shin, J.; Lee, E.; Park, H.; Kim, H. Effects of hydroxyl groups in polymeric dielectrics on organic transistor performance. *Applied Physics Letters* **2006**, *88*, 162109.

[23] Podzorov, V.; Menard, E.; Borissov, A.; Kiryukhin, V.; Rogers, J. A.; Gershenson, M. E. Intrinsic Charge Transport on the Surface of Organic Semiconductors. *Physical Review Letters* **2004**, *93*, 086602, PRL.

[24] Anthony, J. E. Functionalized Acenes and Heteroacenes for Organic Electronics. *Chemical Reviews* **2006**, *106*, 5028–5048.

[25] Kitamura, M.; Arakawa, Y. Pentacene-based organic field-effect transistors. *Journal of Physics: Condensed Matter* **2008**, *20*, 184011.

[26] Chen, X.-K.; Guo, J.-F.; Zou, L.-Y.; Ren, A.-M.; Fan, J.-X. A Promising Approach to Obtain Excellent n-Type Organic Field-Effect Transistors: Introducing Pyrazine Ring. *The Journal of Physical Chemistry C* **2011**, *115*, 21416–21428.

[27] Russew, M.-M.; Hecht, S. Photoswitches: From Molecules to Materials. *Advanced Materials* **2010**, *22*, 3348–3360, https://doi.org/10.1002/adma.200904102.

[28] Hsu, L.-Y.; Mainik, P.; Münchinger, A.; Lindenthal, S.; Spratte, T.; Welle, A.; Zaumseil, J.; Selhuber-Unkel, C.; Wegener, M.; Blasco, E. A Facile Approach for 4D Microprinting of Multi-Photoresponsive Actuators. *Advanced Materials Technologies* **2022**, 2200801, https://doi.org/10.1002/admt.202200801.

[29] Li, M.; Yang, S.; Liang, W.; Zhang, X.; Qu, D. A novel multiphotochromic system with orthogonal light excitations. *Dyes and Pigments* **2019**, *166*, 239–244.

[30] Garcia-Fernandez, L.; Herbivo, C.; Arranz, V. S. M.; Warther, D.; Donato, L.; Specht, A.; del Campo, A. Dual Photosensitive Polymers with Wavelength-Selective Photoresponse. *Advanced Materials* **2014**, *26*, 5012–5017, https://doi.org/10.1002/adma.201401290.

[31] Bates, F. S.; Fredrickson, G. H. Block Copolymers - Designer Soft Materials. *Physics Today* **1999**, *52*, 32–38.

[32] Matsen, M. W. Effect of Architecture on the Phase Behavior of AB-Type Block Copolymer Melts. *Macromolecules* **2012**, *45*, 2161–2165.

[33] Lee, W.; Kim, J.; Jo, S.; Chae, B.; Ahn, H.; Ryu, D. Y. Microdomain homogeneity evaluation of perpendicular lamellar structures in block copolymer films: X-ray scattering and IR nanospectroscopy analyses. *Polymer Testing* **2021**, *104*, 107409.

[34] Wan, L.; Ruiz, R.; Gao, H.; Patel, K. C.; Albrecht, T. R.; Yin, J.; Kim, J.; Cao, Y.; Lin, G. The Limits of Lamellae-Forming PS-b-PMMA Block Copolymers for Lithography. *ACS Nano* **2015**, *9*, 7506–7514.

[35] Bates, C. M.; Maher, M. J.; Janes, D. W.; Ellison, C. J.; Willson, C. G. Block Copolymer Lithography. *Macromolecules* **2014**, *47*, 2–12.

[36] Hunklinger, S. *Festkörperphysik*, 5th ed.; De Gruyter Studium; De Gruyter: Berlin ; Boston, 2018.

[37] Ibach, H.; Lüth, H. *Festkörperphysik : Einführung in die Grundlagen*, 7th ed.; Springer-Lehrbuch; Springer Berlin Heidelberg: Berlin, Heidelberg, 2009.

[38] Stein, A. Electronic Structure, Band Formation and Singlet Fission Dynamics at Metal/Organic Interfaces. PhD Thesis, Ruprecht-Karls-Universität Heidelberg, 2019.

[39] Tamm, I. Über eine mögliche Art der Elektronenbindung an Kristalloberflächen. *Zeitschrift für Physik* **1932**, *76*, 849–850.

[40] Shockley, W. On the Surface States Associated with a Periodic Potential. *Physical Review* **1939**, *56*, 317–323, PR.

[41] Lüth, H. *Solid Surfaces, Interfaces and Thin Films*, 6th ed.; Graduate Texts in Physics; Springer: Cham, 2015.

[42] Malkova, N.; Ning, C. Z. Shockley and Tamm surface states in photonic crystals. *Physical Review B* **2006**, *73*, 113113, PRB.

[43] Giesen, K.; Hage, F.; Himpsel, F. J.; Riess, H. J.; Steinmann, W. Two-photon photoemission via image-potential states. *Physical Review Letters* **1985**, *55*, 300–303, PRL.

[44] Fauster, T.; Steinmann, W. In *Photonic Probes of Surfaces*; Halevi, P., Ed.; Elsevier: Amsterdam, 1995; pp 347–411.

[45] Dylla, H. F.; Corneliussen, S. T. John Ambrose Fleming and the beginning of electronics. *Journal of Vacuum Science and Technology A* **2005**, *23*, 1244–1251.

[46] Chiang, C. K.; Fincher, C. R.; Park, Y. W.; Heeger, A. J.; Shirakawa, H.; Louis, E. J.; Gau, S. C.; MacDiarmid, A. G. Electrical Conductivity in Doped Polyacetylene. *Physical Review Letters* **1977**, *39*, 1098–1101, PRL.

[47] Gsänger, M.; Bialas, D.; Huang, L.; Stolte, M.; Würthner, F. Organic Semiconductors based on Dyes and Color Pigments. *Advanced Materials* **2016**, *28*, 3615–3645, https://doi.org/10.1002/adma.201505440.

[48] Root, S. E.; Savagatrup, S.; Printz, A. D.; Rodriquez, D.; Lipomi, D. J. Mechanical Properties of Organic Semiconductors for Stretchable, Highly Flexible, and Mechanically Robust Electronics. *Chemical Reviews* **2017**, *117*, 6467–6499.

[49] Holleman, A. F.; Wiberg, E. *Lehrbuch der anorganischen Chemie*, 102nd ed.; de Gruyter: Berlin [u.a.], 2007.

[50] Petty, M. C. *Organic and Molecular Electronics: From Principles to Practice*; Wiley, 2019.

[51] Fritzsche, Note sur les carbures d'hydrogene solides, tires du goudron de houille. *Comptes rendus hebdomadaires des seances de l'Academie des sciences* **1867**, *69*, 1035–1037.

[52] Bouas-Laurent, H.; Dürr, H. Organic photochromism (IUPAC Technical Report). *Pure and Applied Chemistry* **2001**, *73*, 639–665.

[53] Hirshberg, Y. Photochromie dans la serie de la serie de la bianthrone. *Comptes rendus hebdomadaires des seances de l'Academie des sciences* **1950**, *69*, 1035–1037.

[54] Pianowski, Z. L. Recent Implementations of Molecular Photoswitches into Smart Materials and Biological Systems. *Chemistry – A European Journal* **2019**, *25*, 5128–5144, https://doi.org/10.1002/chem.201805814.

[55] Tian, H.; Zhang, J. *Photochromic Materials*; Wiley-VCH Verlag GmbH and Co. KGaA: Weinheim, 2016.

[56] Haydell, M. W.; Centola, M.; Adam, V.; Valero, J.; Famulok, M. Temporal and Reversible Control of a DNAzyme by Orthogonal Photoswitching. *Journal of the American Chemical Society* **2018**, *140*, 16868–16872.

[57] Raymo, F. M. Digital Processing and Communication with Molecular Switches. *Advanced Materials* **2002**, *14*, 401–414, https://doi.org/10.1002/1521-4095(20020318)14:6<401::AID-ADMA401>3.0.CO;2-F.

[58] Natali, M.; Giordani, S. Molecular switches as photocontrollable "smart" receptors. *Chemical Society Reviews* **2012**, *41*, 4010–4029.

[59] Nemoto, K.; Enoki, M.; Katoh, R.; Suzuki, K.; Murase, T.; Imazeki, S. Negative photochromism of a blue cyanine dye. *Chemical Communications* **2020**, *56*, 15205–15207.

[60] Broichhagen, J.; Frank, J. A.; Trauner, D. A Roadmap to Success in Photopharmacology. *Accounts of Chemical Research* **2015**, *48*, 1947–1960.

[61] Sun, C.-L.; Wang, C.; Boulatov, R. Applications of Photoswitches in the Storage of Solar Energy. *ChemPhotoChem* **2019**, *3*, 268–283, https://doi.org/10.1002/cptc.201900030.

[62] Hänsel, M.; Barta, C.; Rietze, C.; Utecht, M.; Rück-Braun, K.; Saalfrank, P.; Tegeder, P. Two-Dimensional Nonlinear Optical Switching Materials: Molecular Engineering toward High Nonlinear Optical Contrasts. *The Journal of Physical Chemistry C* **2018**, *122*, 25555–25564.

[63] Meschede, D. *Gerthsen Physik*, 24th ed.; SpringerLink: Bücher; Springer Berlin Heidelberg: Berlin, Heidelberg, 2010.

[64] Demtröder, W. *Experimentalphysik 2: Elektrizität und Optik*, 7th ed.; Springer-Lehrbuch; Springer Spektrum: Berlin, Heidelberg, 2017.

[65] Scheid, H.; Schwarz, W. *Elemente der Geometrie*, 5th ed.; Springer eBook Collection; Springer Spektrum: Berlin, Heidelberg, 2017.

[66] Margaritondo, G. 100 Years of Photoemission. *Physics Today* **1988**, *41*, 66–72.

[67] Hertz, H. Ueber einen Einfluss des ultravioletten Lichtes auf die electrische Entladung. *Annalen der Physik* **1887**, *267*, 983–1000.

[68] Hallwachs, W. Ueber den Einfluss des Lichtes auf electrostatisch geladene Körper. *Annalen der Physik* **1888**, *269*, 301–312.

[69] Thomson, J. J. LVIII. On the masses of the ions in gases at low pressures. *The London, Edinburgh, and Dublin Philosophical Magazine and Journal of Science* **1899**, *48*, 547–567.

[70] Lenard, P. Erzeugung von Kathodenstrahlen durch ultraviolettes Licht. *Annalen der Physik* **1900**, *307*, 359–375.

[71] Planck, M. Ueber irreversible Strahlungsvorgänge. *Annalen der Physik* **1900**, *306*, 69–122.

[72] Planck, M. Ueber das Gesetz der Energieverteilung im Normalspectrum. *Annalen der Physik* **1901**, *309*, 553–563.

[73] Einstein, A. Über einen die Erzeugung und Verwandlung des Lichtes betreffenden heuristischen Gesichtspunkt. *Annalen der Physik* **1905**, *322*, 132–148.

[74] Reinert, F.; Hüfner, S. Photoemission spectroscopy - from early days to recent applications. *New Journal of Physics* **2005**, *7*, 97–97.

[75] Bonzel, H. P.; Kleint, C. On the history of photoemission. *Progress in Surface Science* **1995**, *49*, 107–153.

[76] Himpsel, F. J. In *Characterization of Materials*; Kaufmann, E., Ed.; 2012; pp 1–13.

[77] Spicer, W. E. Photoemissive, Photoconductive, and Optical Absorption Studies of Alkali-Antimony Compounds. *Physical Review* **1958**, *112*, 114–122, PR.

[78] Spicer, W. E.; Berglund, C. N. d Band of Copper. *Physical Review Letters* **1964**, *12*, 9–11.

[79] Gross, R.; Marx, A. *Festkörperphysik*, 3rd ed.; De Gruyter Studium; De Gruyter: Berlin, 2018.

[80] Seah, M. P.; Dench, W. A. Quantitative electron spectroscopy of surfaces: A standard data base for electron inelastic mean free paths in solids. *Surface and Interface Analysis* **1979**, *1*, 2–11.

[81] Nguyen-Truong, H. T. Low-energy electron inelastic mean free path in materials. *Applied Physics Letters* **2016**, *108*, 172901.

[82] Feuerbacher, B.; Fitton, B. In *Electron Spectroscopy for Surface Analysis*; Ibach, H., Ed.; Springer Berlin Heidelberg: Berlin, Heidelberg, 1977; pp 151–203.

[83] Oswald, S. *Encyclopedia of Analytical Chemistry*; John Wiley and Sons, Ltd., 2013.

[84] Nordling, C.; Sokolowski, E.; Siegbahn, K. Precision Method for Obtaining Absolute Values of Atomic Binding Energies. *Physical Review* **1957**, *105*, 1676–1677, PR.

[85] Siegbahn, K.; Nordling, C.; Sokolowski, E. Chemical shifts of photo- and Auger electron lines. Proceedings of Rehovoth Conference Nuclear Structure. pp 291–293.

[86] Fahlman, A.; Nordling, C.; Siegbahn, K. *ESCA : atomic, molecular and solid state structure studied by means of electron spectroscopy*; Uppsala : Almqvist and Wiksell, 1967; (viaf).

[87] Chiang, T. C.; Seitz, F. Photoemission spectroscopy in solids. *Annalen der Physik* **2001**, *10*, 61–74.

[88] Siegbahn, K. Electron Spectroscopy for Atoms, Molecules and Condensed Matter. *Nobel lectures* **1981**,

[89] Himpsel, F. J.; Fauster, T. Probing valence states with photoemission and inverse photoemission. *Journal of Vacuum Science and Technology A* **1984**, *2*, 815–821.

[90] Smith, N. V. Inverse photoemission. *Reports on Progress in Physics* **1988**, *51*, 1227–1294.

[91] Himpsel, F. J. Inverse photoemission from semiconductors. *Surface Science Reports* **1990**, *12*, 3–48.

[92] Sakaue, M.; Kasai, H.; Okiji, A. Ultrafast dynamics induced by femtosecond laser pulse irradiation of atom-adsorbed metal surfaces. *Surface Science* **2001**, *493*, 292–297.

[93] Stein, A.; Rolf, D.; Lotze, C.; Feldmann, S.; Gerbert, D.; Günther, B.; Jeindl, A.; Cartus, J. J.; Hofmann, O. T.; Gade, L. H.; Franke, K. J.; Tegeder, P. Electronic Properties of Tetraazaperopyrene Derivatives on Au(111): Energy-Level Alignment and Interfacial Band Formation. *The Journal of Physical Chemistry C* **2021**, *125*, 19969–19979.

[94] Fauster, T. Two-photon photoemission. *Progress in Surface Science* **1994**, *46*, 177–186.

[95] Gerbert, D.; Hofmann, O. T.; Tegeder, P. Formation of Occupied and Unoccupied Hybrid Bands at Interfaces between Metals and Organic Donors/Acceptors. *The Journal of Physical Chemistry C* **2018**, *122*, 27554–27560.

[96] Laude, L. D.; Wautelet, M. Double-beam photoemission and the electronic structure of tellurium. *Il Nuovo Cimento B* **1977**, *39*, 734–738.

[97] Anisimov, S. I.; Benderskii, V. A.; Farkas, G. Nonlinear photoelectric emission from metals induced by a laser radiation. *Soviet Physics Uspekhi* **1977**, *20*, 467–488.

[98] Rudolf, H. W.; Steinmann, W. Two photon photoelectric effect in the surface plasma resonance of aluminium. *Physics Letters A* **1977**, *61*, 471–472.

[99] Rudolf, H. W.; Rieger, D.; Steinmann, W. Two-photon photoemission from Ni (1 1 0) and (1 1 1) surfaces. *Solid State Communications* **1980**, *34*, 427–430.

[100] Schoenlein, R. W.; Fujimoto, J. G.; Eesley, G. L.; Capehart, T. W. Femtosecond Studies of Image-Potential Dynamics in Metals. *Physical Review Letters* **1988**, *61*, 2596–2599, PRL.

[101] Chan, W.-L.; Ligges, M.; Jailaubekov, A.; Kaake, L.; Miaja-Avila, L.; Zhu, X. Y. Observing the Multiexciton State in Singlet Fission and Ensuing Ultrafast Multielectron Transfer. *Science* **2011**, *334*, 1541–1445.

[102] Bronner, C. Electronic structure and ultrafast charge carrier dynamics at the interfaces between molecular switches and the Au(111) surface investigated with time-resolved photoemission. Diploma Thesis, Freie Universität Berlin, 2010.

[103] Velic, D.; Hotzel, A.; Wolf, M.; Ertl, G. Electronic states of the C6H6/Cu111 system: Energetics, femtosecond dynamics, and adsorption morphology. *The Journal of Chemical Physics* **1998**, *109*, 9155–9165.

[104] Ueba, H.; Mii, T. Transition to fixed final states in two-photon photoemission from adsorbate–metal systems. *Applied Surface Science* **2001**, *169-170*, 63–67.

[105] Fauster, T. In *Solid-State Photoemission and Related Methods*; Schattke, M., Wolfgang; Van Hove, Ed.; 2003; pp 247–268.

[106] Velic, D.; Knoesel, E.; Wolf, M. Observation of a direct transition in the sp-band of Cu(111) and (3×3)R30°-CO/Cu(111) in one- and two-photon photoemission. *Surface Science* **1999**, *424*, 1–6.

[107] Koopmans, T. Über die Zuordnung von Wellenfunktionen und Eigenwerten zu den Einzelnen Elektronen Eines Atoms. *Physica* **1934**, *1*, 104–113.

[108] Atkins, J., Peter W.; de Paula *Physikalische Chemie*, 4th ed.; Wiley-VCH: Weinheim, 2006.

[109] Ajdari, M.; Schmitt, T.; Hoffmann, M.; Maass, F.; Reiss, H.; Bunz, U. H. F.; Dreuw, A.; Tegeder, P. Electronic Properties of 6,13-Diazapentacene Adsorbed on Au(111): A Quantitative Determination of Transport, Singlet and Triplet States, and Electronic Spectra. *The Journal of Physical Chemistry C* **2020**, *124*, 13196–13205.

[110] Sickafus, E. N. Linearized secondary-electron cascades from the surfaces of metals. I. Clean surfaces of homogeneous specimens. *Physical Review B* **1977**, *16*, 1436–1447, PRB.

[111] Bronner, C. Photoinduced and Thermal Reactions of Functional Molecules at Surfaces. PhD Thesis, Freie Universität Berlin, 2014.

[112] Pellegrini, B. Properties of silicon-metal contacts versus metal work-function, silicon impurity concentration and bias voltage. *Journal of Physics D: Applied Physics* **1976**, *9*, 55–68.

[113] Lisowski, M. J. Elektronen- und Magnetisierungsdynamik in Metallen untersucht mit zeitaufgelöster Photoemission. PhD Thesis, Freie Universität Berlin, 2005.

[114] Ibach, H. *Physics of surfaces and interfaces*; Springer: Berlin, Heidelberg, 2006.

[115] Weinelt, M. Time-resolved two-photon photoemission from metal surfaces. *Journal of Physics: Condensed Matter* **2002**, *14*, R1099–R1141.

[116] King, D. A. Thermal desorption from metal surfaces: A review. *Surface Science* **1975**, *47*, 384–402.

[117] Apker, L. R. Surface Phenemona Useful in Vacuum Technique. *Industrial and Engineering Chemistry* **1948**, *40*, 846–847.

[118] Becker, J. A.; Hartman, C. D. Field Emission Microscope and Flash Filament Techniques for the Study of Structure and Adsorption on Metal Surfaces. *The Journal of Physical Chemistry* **1953**, *57*, 153–159.

[119] Smith, A. W.; Aranoff, S. Thermodesorption of Gases from Solids. *The Journal of Physical Chemistry* **1958**, *62*, 684–686.

[120] Redhead, P. A. Thermal desorption of gases. *Vacuum* **1962**, *12*, 203–211.

[121] King, D. A.; Madey, T. E.; Yates, J. T. Interaction of Oxygen with Polycrystalline Tungsten. I. Sticking Probabilities and Desorption Spectra. *The Journal of Chemical Physics* **1971**, *55*, 3236–3246.

[122] Maaß, F. The Metal/Organic Interface - Binding, Adsorption Geometry, and Electronic Structure. PhD Thesis, Ruprecht-Karls-Universität Heidelberg, 2018.

[123] Maaß, F.; Jiang, Y.; Liu, W.; Tkatchenko, A.; Tegeder, P. Binding energies of benzene on coinage metal surfaces: Equal stability on different metals. *The Journal of Chemical Physics* **2018**, *148*, 214703.

[124] Wedler, G. *Lehrbuch der physikalischen Chemie*, 5th ed.; WILEY-VCH: Weinheim, [Bergstr.], 2004; Hier auch später erschienene, unveränderte Nachdrucke.

[125] Polanyi, M.; Wigner, E. The interference of characteristic vibrations as the cause of energy fluctuations and chemical change. *Z. Phys. Chem* **1928**, *139A*, 439.

[126] Collings, M. P.; Frankland, V. L.; Lasne, J.; Marchione, D.; Rosu-Finsen, A.; McCoustra, M. R. S. Probing model interstellar grain surfaces with small molecules. *Monthly Notices of the Royal Astronomical Society* **2015**, *449*, 1826–1833.

[127] Smith, R. S.; Kay, B. D. Desorption Kinetics of Benzene and Cyclohexane from a Graphene Surface. *The Journal of Physical Chemistry B* **2018**, *122*, 587–594.

[128] Tylinski, M.; Smith, R. S.; Kay, B. D. Structure and Desorption Kinetics of Acetonitrile Thin Films on Pt(111) and on Graphene on Pt(111). *The Journal of Physical Chemistry C* **2020**, *124*, 2521–2530.

[129] Ehrlich, G. Kinetic and Experimental Basis of Flash Desorption. *Journal of Applied Physics* **1961**, *32*, 4–15.

[130] Niemantsverdriet, J. W.; Dolle, P.; Markert, K.; Wandelt, K. Thermal desorption of strained monoatomic Ag and Au layers from Ru(001). *Journal of Vacuum Science and Technology A* **1987**, *5*, 875–878.

[131] Dresser, M. J.; Madey, T. E.; Yates, J. T. The adsorption of xenon by W(111), and its interaction with preadsorbed oxygen. *Surface Science* **1974**, *42*, 533–551.

[132] Schulze, M.; Bronner, C.; Tegeder, P. Adsorption energetics of azobenzenes on noble metal surfaces. *Journal of Physics: Condensed Matter* **2014**, *26*, 355004/1–6.

[133] Hesse, M.; Meier, H.; Zeeh, B. *Spektroskopische Methoden in der organischen Chemie*, 4th ed.; Thieme: Stuttgart, New York, 1991.

[134] Berera, R.; van Grondelle, R.; Kennis, J. T. M. Ultrafast transient absorption spectroscopy: principles and application to photosynthetic systems. *Photosynthesis Research* **2009**, *101*, 105–118.

[135] Stern, H. L. Femtosecond Transient Absorption Spectroscopy - Technical Improvements and Applications to Ultrafast Molecular Phenomena. PhD Thesis, University of Cambridge, 2016.

[136] Spektrum.de, Nobelpreis für Chemie 1999. 1999, date of access: 12.08.2022; *https://www.spektrum.de/news/nobelpreis-fuer-chemie-1999/343218*.

[137] Zhu, Y.; Cheng, J.-X. Transient absorption microscopy: Technological innovations and applications in materials science and life science. *The Journal of Chemical Physics* **2020**, *152*, 020901.

[138] Ruckebusch, C.; Sliwa, M.; Pernot, P.; de Juan, A.; Tauler, R. Comprehensive data analysis of femtosecond transient absorption spectra: A review. *Journal of Photochemistry and Photobiology C: Photochemistry Reviews* **2012**, *13*, 1–27.

[139] Nenov, A.; Borrego-Varillas, R.; Oriana, A.; Ganzer, L.; Segatta, F.; Conti, I.; Segarra-Marti, J.; Omachi, J.; Dapor, M.; Taioli, S.; Manzoni, C.; Mukamel, S.; Cerullo, G.; Garavelli, M. UV-Light-Induced Vibrational Coherences: The Key to Understand Kasha Rule Violation in trans-Azobenzene. *The Journal of Physical Chemistry Letters* **2018**, *9*, 1534–1541.

[140] van Stokkum, I. H. M.; Larsen, D. S.; van Grondelle, R. Global and target analysis of time-resolved spectra. *Biochimica et Biophysica Acta (BBA) - Bioenergetics* **2004**, *1657*, 82–104.

[141] Gelinas, S. Spectroscopic Study of Charge-Separation Dynamics in π-Conjugated Systems. PhD Thesis, University of Cambridge, 2013.

[142] Hestenes, M. R. Inversion of Matrices by Biorthogonalization and Related Results. *Journal of the Society for Industrial and Applied Mathematics* **1958**, *6*, 51–90.

[143] Bonneau, R.; Wirz, J.; Zuberbühler, A. Methods for the analysis of transient absorbance data. *Pure Appl. Chem. FIELD Full Journal Title:Pure and Applied Chemistry* **1997**, *69*, 979–992.

[144] Kelm, K. C. Capellos and B. H. J. Bielski: Kinetic Systems: Mathematical Description of Chemical Kinetics in Solution. *Berichte der Bunsengesellschaft für physikalische Chemie* **1973**, *77*, 470–470, https://doi.org/10.1002/bbpc.19730770618.

[145] Kanal, F. Femtosecond Transient Absorption Spectroscopy - Technical Improvements and Applications to Ultrafast Molecular Phenomena. PhD Thesis, Julius-Maximilians-Universität Würzburg, 2015.

[146] Wollscheid, N. The Ultrafast Singlet Fission Dynamics in Solution and Thin Film. PhD Thesis, Ruprecht-Karls-Universität Heidelberg, 2020.

[147] Huth, F.; Govyadinov, A.; Amarie, S.; Nuansing, W.; Keilmann, F.; Hillenbrand, R. Nano-FTIR Absorption Spectroscopy of Molecular Fingerprints at 20 nm Spatial Resolution. *Nano Letters* **2012**, *12*, 3973–3978.

[148] Amenabar, I.; Poly, S.; Nuansing, W.; Hubrich, E. H.; Govyadinov, A. A.; Huth, F.; Krutokhvostov, R.; Zhang, L.; Knez, M.; Heberle, J.; Bittner, A. M.; Hillenbrand, R. Structural analysis and mapping of individual protein complexes by infrared nanospectroscopy. *Nature Communications* **2013**, *4*, 2890.

[149] Rang, M.; Jones, A. C.; Zhou, F.; Li, Z.-Y.; Wiley, B. J.; Xia, Y.; Raschke, M. B. Optical Near-Field Mapping of Plasmonic Nanoprisms. *Nano Letters* **2008**, *8*, 3357–3363.

[150] Huber, A. J.; Keilmann, F.; Wittborn, J.; Aizpurua, J.; Hillenbrand, R. Terahertz Near-Field Nanoscopy of Mobile Carriers in Single Semiconductor Nanodevices. *Nano Letters* **2008**, *8*, 3766–3770.

[151] Stiegler, J. M.; Huber, A. J.; Diedenhofen, S. L.; Gómez Rivas, J.; Algra, R. E.; Bakkers, E. P. A. M.; Hillenbrand, R. Nanoscale Free-Carrier Profiling of Individual Semiconductor Nanowires by Infrared Near-Field Nanoscopy. *Nano Letters* **2010**, *10*, 1387–1392.

[152] Ockenga, W. A Brief History of Light Microscopy - From the Medieval Reading Stone to Super-Resolution. 2015, date of access: 17.08.2022; *https://www.leica-microsystems.com/science-lab/a-brief-history-of-light-microscopy-from-the-medieval-reading-stone-to-super-resolution/*.

[153] Wollman, A. J. M.; Nudd, R.; Hedlund, E. G.; Leake, M. C. From Animaculum to single molecules: 300 years of the light microscope. *Open Biology* **2015**, *5*, 150019.

[154] Abbe, E. Beiträge zur Theorie des Mikroskops und der mikroskopischen Wahrnehmung. *Archiv für Mikroskopische Anatomie* **1873**, *9*, 413–468.

[155] Cremer, C. Lichtmikroskopie unterhalb des Abbe-Limits. Lokalisationsmikroskopie. *Physik in unserer Zeit* **2011**, *42*, 21–29, https://doi.org/10.1002/piuz.201101251.

[156] Mastel, S. Enhancing resolution, efficiency, and understanding in IR and THz near-field microscopy. PhD Thesis, CIC nanoGUNE San Sebastián, 2018.

[157] Binnig, G.; Rohrer, H.; Gerber, C.; Weibel, E. Surface Studies by Scanning Tunneling Microscopy. *Physical Review Letters* **1982**, *49*, 57–61, PRL.

[158] Meyer, E.; Bennewitz, R.; Hug, H. J. *Scanning Probe Microscopy : The Lab on a Tip*, second edition ed.; Springer eBook Collection; Springer: Cham, 2021.

[159] Synge, E. H. XXXVIII. A suggested method for extending microscopic resolution into the ultra-microscopic region. *The London, Edinburgh, and Dublin Philosophical Magazine and Journal of Science* **1928**, *6*, 356–362.

[160] Pohl, D. W.; Denk, W.; Lanz, M. Optical stethoscopy: Image recording with resolution λ/20. *Applied Physics Letters* **1984**, *44*, 651–653.

[161] Lewis, A.; Isaacson, M.; Harootunian, A.; Muray, A. Development of a 500 Å spatial resolution light microscope: I. light is efficiently transmitted through λ/16 diameter apertures. *Ultramicroscopy* **1984**, *13*, 227–231.

[162] Hillenbrand, R. Nahfeldoptische Amplituden- und Phasenkontrastmikroskopie zur nanoskopischen optischen Abbildung von Materialkontrast und optisch resonanten Partikeln. PhD Thesis, Technische Universität München, 2001.

[163] Attocube Systems AG, *User Manual neaSNOM*; 2021.

[164] Attocube Systems AG, *User Manual Tapping AFM-IR+ neaSNOM*; 2021.

[165] Smith, B. C. *Fundamentals of Fourier transform infrared spectroscopy*; CRC press, 2011.

[166] Winkelmann, L. Vorstudien zur optischen Rasternahfeldmikroskopie und Spektroskopie an organischen Materialien. Bachelor Thesis, Ruprecht-Karls-Universität Heidelberg, 2019.

[167] Dinger, M. Untersuchungen von plasmonischen Nanoantennen mit der optischen Streulichtnahfeldmikroskopie und Spektroskopie. PhD Thesis, Ruprecht-Karls-Universität Heidelberg, 2020.

[168] Schwartz, J. J.; Jakob, D. S.; Centrone, A. A guide to nanoscale IR spectroscopy: resonance enhanced transduction in contact and tapping mode AFM-IR. *Chemical Society Reviews* **2022**, *51*, 5248–5267.

[169] Stiegler, J. M.; Abate, Y.; Cvitkovic, A.; Romanyuk, Y. E.; Huber, A. J.; Leone, S. R.; Hillenbrand, R. Nanoscale Infrared Absorption Spectroscopy of Individual Nanoparticles Enabled by Scattering-Type Near-Field Microscopy. *ACS Nano* **2011**, *5*, 6494–6499.

[170] Ocelic, N.; Huber, A.; Hillenbrand, R. Pseudoheterodyne detection for background-free near-field spectroscopy. *Applied Physics Letters* **2006**, *89*, 101124.

[171] Rao, V. J. Vibrational spectroscopy of macroscopic and liquid-phase exfoliated organic crystals. PhD Thesis, Ruprecht-Karls-Universitat Heidelberg, 2021.

[172] Hagen, S. Isomerization behavior of photochromic molecules in direct contact with noble metal surfaces. PhD Thesis, Freie Universität Berlin, 2009.

[173] LakeShore, User's Manual Model 340 Temperature Controller. **2004**, Ohio, USA.

[174] Belektronig, Manuelle Bestimmung von PID-Parametern. **2018**, Freital, Germany.

[175] Aggarwal, K., Roshan L. ; Alavi *Introduction to Optical Components*, 1st ed.; CRC Press: Boca Raton, 2018.

[176] Coherent, *Operator's Manual Verdi V-18 Diode-Pumped Lasers*; 2005.

[177] Meschede, D. *Optik, Licht und Laser*, 3rd ed.; Vieweg+Teubner: Wiesbaden, 2008.

[178] Coherent, *Operator's Manual The Coherent Mira Seed Laser*; 1996.

[179] Coherent, *RegA 9050 System Operators Manual preliminary Version 2.1*; 1997.

[180] Coherent, *Coherent Service Report RegA 9050*; Report, 2013.

[181] Demtröder, W. *Laserspektroskopie 1: Grundlagen*, 6th ed.; SpringerLink: Bücher; Springer Berlin Heidelberg: Berlin, Heidelberg, 2011.

[182] Coherent, *Operator's Manual The Coherent Modell 9400/9450 Optical Parametric Amplifier (OPA)*; 2006.

[183] Fork, R. L.; Martinez, O. E.; Gordon, J. P. Negative dispersion using pairs of prisms. *Optics Letters* **1984**, *9*, 150–152.

[184] Demtröder, W. *Laserspektroskopie 2: Experimentelle Techniken*, 6th ed.; SpringerLink: Bücher; Springer: Berlin, Heidelberg, 2013.

[185] Reinert, F.; Nicolay, G.; Schmidt, S.; Ehm, D.; Hüfner, S. Direct measurements of the L-gap surface states on the (111) face of noble metals by photoelectron spectroscopy. *Physical Review B* **2001**, *63*, 115415, PRB.

[186] Parson, W. W. *Modern Optical Spectroscopy : With Examples from Biophysics and Biochemistry*; SpringerLink : Bücher; Springer Berlin Heidelberg: Berlin, Heidelberg, 2007; In: Springer-Online.

[187] Schulzendorf, M.; Hinaut, A.; Kisiel, M.; Jöhr, R.; Pawlak, R.; Restuccia, P.; Meyer, E.; Righi, M. C.; Glatzel, T. Altering the Properties of Graphene on Cu(111) by Intercalation of Potassium Bromide. *ACS Nano* **2019**, *13*, 5485–5492.

[188] Gahl, C. Elektronentransfer- und Solvatisierungsdynamik in Eis adsorbiert auf Metalloberflächen. PhD Thesis, Freie Universität Berlin, 2004.

[189] Steidel, J. The Electronic Structure of N-Heteropolycycles on Au(111). Master Thesis, Ruprecht-Karls-Universität Heidelberg, 2020.

[190] National Instruments, *LabVIEW Versionshinweise Version 7.1*; 2004.

[191] National Instruments, *Hinweise zum Upgrade auf LabVIEW 2018*; 2018.

[192] National Instruments, What is NI-DAQmx? 2019, date of access: 28.01.2021; *https://knowledge.ni.com/KnowledgeArticleDetails?id=kA00Z000000P8baSAC&l=de-DE*.

[193] National Instruments, Archived: Traditional NI-DAQ (Legacy) and LabVIEW Compatibility. 2020, date of access: 20.10.2021; *https://www.ni.com/de-de/support/documentation/compatibility/17/traditional-ni-daq--legacy--and-labview-compatibility.html*.

[194] National Instruments, LabVIEW Statechart Module. 2021, date of access: 29.01.2021; *https://www.ni.com/de-de/support/downloads/software-products/download.labview-statechart-module.html*.

[195] Schott, S.; Steinbacher, A.; Buback, J.; Nuernberger, P.; Brixner, T. Generalized magic angle for time-resolved spectroscopy with laser pulses of arbitrary ellipticity. *Journal of Physics B: Atomic, Molecular and Optical Physics* **2014**, *47*, 124014.

[196] Lessing, H. E.; Von Jena, A. Separation of rotational diffusion and level kinetics in transient absorption spectroscopy. *Chemical Physics Letters* **1976**, *42*, 213–217.

[197] Alagna, N. Exploring the role of chemical substitution and geometrical changes on singlet fission via time resolved spectroscopy. PhD Thesis, Ruprecht-Karls-Universität Heidelberg, 2021.

[198] Buckup, T. date of access: 08.08.2022; *https://www.cam.uni-heidelberg.de/facilities/fslaser*.

[199] Snellenburg, J. J.; Laptenok, S.; Seger, R.; Mullen, K. M.; van Stokkum, I. H. M. Glotaran: A Java-Based Graphical User Interface for the R Package TIMP. *Journal of Statistical Software* **2012**, *1*.

[200] Sivanesan, V. Ultrafast Excited State Dynamics in Organic Semiconducting Systems. PhD Thesis, Ruprecht-Karls-Universität Heidelberg, 2021.

[201] Miao, Q. N-Heteropentacenes and N-Heteropentacenequinones: From Molecules to Semiconductors. *Synlett* **2012**, *2012*, 326–336.

[202] Wolak, M. A.; Jang, B.-B.; Palilis, L. C.; Kafafi, Z. H. Functionalized Pentacene Derivatives for Use as Red Emitters in Organic Light-Emitting Diodes. *The Journal of Physical Chemistry B* **2004**, *108*, 5492–5499.

[203] Jang, B.-B.; Lee, S. H.; Kafafi, Z. H. Asymmetric Pentacene Derivatives for Organic Light-Emitting Diodes. *Chemistry of Materials* **2006**, *18*, 449–457.

[204] Bakulin, A. A.; Morgan, S. E.; Kehoe, T. B.; Wilson, M. W. B.; Chin, A. W.; Zigmantas, D.; Egorova, D.; Rao, A. Real-time observation of multiexcitonic states in ultrafast singlet fission using coherent 2D electronic spectroscopy. *Nature Chemistry* **2016**, *8*, 16–23.

[205] Congreve, D. N.; Lee, J.; Thompson, N. J.; Hontz, E.; Yost, S. R.; Reusswig, P. D.; Bahlke, M. E.; Reineke, S.; Van Voorhis, T.; Baldo, M. A. External Quantum Efficiency Above 100Organic Photovoltaic Cell. *Science* **2013**, *340*, 334–337.

[206] Charlton, R. J.; Fogarty, R. M.; Bogatko, S.; Zuehlsdorff, T. J.; Hine, N. D. M.; Heeney, M.; Horsfield, A. P.; Haynes, P. D. Implicit and explicit host effects on excitons in pentacene derivatives. *The Journal of Chemical Physics* **2018**, *148*, 104108.

[207] Klues, M.; Witte, G. Crystalline packing in pentacene-like organic semiconductors. *CrystEngComm* **2018**, *20*, 63–74.

[208] Bogatko, S.; Haynes, P. D.; Sathian, J.; Wade, J.; Kim, J.-S.; Tan, K.-J.; Breeze, J.; Salvadori, E.; Horsfield, A.; Oxborrow, M. Molecular Design of a Room-Temperature Maser. *The Journal of Physical Chemistry C* **2016**, *120*, 8251–8260.

[209] Miao, Q. Ten Years of N-Heteropentacenes as Semiconductors for Organic Thin-Film Transistors. *Advanced Materials* **2014**, *26*, 5541–5549, https://doi.org/10.1002/adma.201305497.

[210] Liu, D.; Li, Z.; He, Z.; Xu, J.; Miao, Q. Induced crystallization of rubrene with diazapentacene as the template. *Journal of Materials Chemistry* **2012**, *22*, 4396–4400.

[211] Sosorev, A.; Dominskiy, D.; Chernyshov, I.; Efremov, R. Tuning of Molecular Electrostatic Potential Enables Efficient Charge Transport in Crystalline Azaacenes: A Computational Study. *International Journal of Molecular Sciences* **2020**, *21*.

[212] Hoffmann, M.; Ajdari, M.; Landwehr, F.; Tverskoy, O.; Bunz, U. H. F.; Dreuw, A.; Tegeder, P. Influence of N-introduction in pentacene on the electronic structure and excited electronic states. *Physical Chemistry Chemical Physics* **2022**, *24*, 3924–3932.

[213] Hanke, F.; Björk, J. Structure and local reactivity of the Au(111) surface reconstruction. *Physical Review B* **2013**, *87*, 235422, PRB.

[214] Barth, J. V.; Brune, H.; Ertl, G.; Behm, R. J. Scanning tunneling microscopy observations on the reconstructed Au(111) surface: Atomic structure, long-range superstructure, rotational domains, and surface defects. *Physical Review B* **1990**, *42*, 9307–9318, PRB.

[215] Paniago, R.; Matzdorf, R.; Meister, G.; Goldmann, A. Temperature dependence of Shockley-type surface energy bands on Cu(111), Ag(111) and Au(111). *Surface Science* **1995**, *336*, 113–122.

[216] McGuirk, G. M.; Shin, H.; Caragiu, M.; Ash, S.; Bandyopadhyay, P. K.; Prince, R. H.; Diehl, R. D. Au(111) surface structures induced by adsorption: LEED I(E) analysis of (1×1) and (5×5) Au(111)–S phases. *Surface Science* **2013**, *610*, 42–47.

[217] Maass, F.; Ajdari, M.; Kabeer, F. C.; Vogtland, M.; Tkatchenko, A.; Tegeder, P. Nonadditivity of the Adsorption Energies of Linear Acenes on Au(111): Molecular

Anisotropy and Many-Body Effects. *The Journal of Physical Chemistry Letters* **2019**, *10*, 1000–1004.

[218] France, C. B.; Schroeder, P. G.; Forsythe, J. C.; Parkinson, B. A. Scanning Tunneling Microscopy Study of the Coverage-Dependent Structures of Pentacene on Au(111). *Langmuir* **2003**, *19*, 1274–1281.

[219] Galbraith, M. C. E.; Marks, M.; Tonner, R.; Höfer, U. Formation of an Organic/Metal Interface State from a Shockley Resonance. *The Journal of Physical Chemistry Letters* **2014**, *5*, 50–55.

[220] Caplins, B. W.; Suich, D. E.; Shearer, A. J.; Harris, C. B. Metal/Phthalocyanine Hybrid Interface States on Ag(111). *The Journal of Physical Chemistry Letters* **2014**, *5*, 1679–1684.

[221] Nayak, P. K. Exciton binding energy in small organic conjugated molecule. *Synthetic Metals* **2013**, *174*, 42–45.

[222] Bochet, C. G. Wavelength-selective cleavage of photolabile protecting groups. *Tetrahedron Letters* **2000**, *41*, 6341–6346.

[223] Manna, D.; Udayabhaskararao, T.; Zhao, H.; Klajn, R. Orthogonal Light-Induced Self-Assembly of Nanoparticles using Differently Substituted Azobenzenes. *Angewandte Chemie International Edition* **2015**, *54*, 12394–12397, https://doi.org/10.1002/anie.201502419.

[224] Wang, D.; Schellenberger, F.; Pham, J. T.; Butt, H.-J.; Wu, S. Orthogonal photo-switching of supramolecular patterned surfaces. *Chemical Communications* **2018**, *54*, 3403–3406.

[225] Priestman, M. A.; Sun, L.; Lawrence, D. S. Dual Wavelength Photoactivation of cAMP- and cGMP-Dependent Protein Kinase Signaling Pathways. *ACS Chemical Biology* **2011**, *6*, 377–384.

[226] Lerch, M. M.; Hansen, M. J.; Velema, W. A.; Szymanski, W.; Feringa, B. L. Orthogonal photoswitching in a multifunctional molecular system. *Nature Communications* **2016**, *7*, 12054.

[227] Griffiths, J. II. Photochemistry of azobenzene and its derivatives. *Chemical Society Reviews* **1972**, *1*, 481–493.

[228] Bandara, H. M. D.; Burdette, S. C. Photoisomerization in different classes of azobenzene. *Chemical Society Reviews* **2012**, *41*, 1809–1825.

[229] Hagiri, M.; Ichinose, N.; Zhao, C.; Horiuchi, H.; Hiratsuka, H.; Nakayama, T. Sub-picosecond time-resolved absorption spectroscopy of a push-pull type p,p'-substituted trans-azobenzene. *Chemical Physics Letters* **2004**, *391*, 297–301.

[230] Hao, Y.-W.; Wang, H.-Y.; Huang, Y.-J.; Gao, B.-R.; Chen, Q.-D.; Li, L.-B.; Sun, H.-B. Evidence of concerted inversion for the photon-induced molecular switching of azobenzene using rotation-free azobenzene derivatives. *Journal of Materials Chemistry C* **2013**, *1*, 5244–5249.

[231] Bléger, D.; Hecht, S. Visible-Light-Activated Molecular Switches. *Angewandte Chemie International Edition* **2015**, *54*, 11338–11349.

[232] Jacquart, A.; Williams, R. M.; Brouwer, A. M.; Ishow, E. Decoupling Fluorescence and Photochromism in Bifunctional Azo Derivatives for Bulk Emissive Structures. *Chemistry - A European Journal* **2012**, *18*, 3706–3720, https://doi.org/10.1002/chem.201103411.

[233] Poprawa-Smoluch, M.; Baggerman, J.; Zhang, H.; Maas, H. P. A.; De Cola, L.; Brouwer, A. M. Photoisomerization of Disperse Red 1 Studied with Transient Absorption Spectroscopy and Quantum Chemical Calculations. *The Journal of Physical Chemistry A* **2006**, *110*, 11926–11937.

[234] Schmidt, B.; Sobotta, C.; Malkmus, S.; Laimgruber, S.; Braun, M.; Zinth, W.; Gilch, P. Femtosecond Fluorescence and Absorption Dynamics of an Azobenzene with a Strong Push-Pull Substitution. *The Journal of Physical Chemistry A* **2004**, *108*, 4399–4404.

[235] Wachtveitl, J.; Nägele, T.; Puell, B.; Zinth, W.; Krüger, M.; Rudolph-Böhner, S.; Oesterhelt, D.; Moroder, L. Ultrafast photoisomerization of azobenzene compounds. *Journal of Photochemistry and Photobiology A: Chemistry* **1997**, *105*, 283–288.

[236] Satzger, H.; Root, C.; Braun, M. Excited-State Dynamics of trans- and cis-Azobenzene after UV Excitation in the $\pi\pi^*$ Band. *The Journal of Physical Chemistry A* **2004**, *108*, 6265–6271.

[237] Moreno, J.; Gerecke, M.; Dobryakov, A. L.; Ioffe, I. N.; Granovsky, A. A.; Bléger, D.; Hecht, S.; Kovalenko, S. A. Two-Photon-Induced versus One-Photon-Induced Isomerization Dynamics of a Bistable Azobenzene Derivative in Solution. *The Journal of Physical Chemistry B* **2015**, *119*, 12281–12288.

[238] Stenhouse, J. Ueber die Oele, die bei der Einwirkung der Schwefelsäure auf verschiedene Vegetabilien entstehen. *Justus Liebigs Annalen der Chemie* **1850**, *74*, 278–297, https://doi.org/10.1002/jlac.18500740304.

[239] Lewis, K. G.; Mulquiney, C. E. Aspects of the formation and use of stenhouse salts and related compounds. *Tetrahedron* **1977**, *33*, 463–475.

[240] Helmy, S.; Leibfarth, F. A.; Oh, S.; Poelma, J. E.; Hawker, C. J.; Read de Alaniz, J. Photoswitching Using Visible Light: A New Class of Organic Photochromic Molecules. *Journal of the American Chemical Society* **2014**, *136*, 8169–8172.

[241] Sroda, M. M.; Stricker, F.; Peterson, J. A.; Bernal, A.; Read de Alaniz, J. Donor–Acceptor Stenhouse Adducts: Exploring the Effects of Ionic Character. *Chemistry – A European Journal* **2021**, *27*, 4183–4190, https://doi.org/10.1002/chem.202005110.

[242] Hemmer, J. R.; Page, Z. A.; Clark, K. D.; Stricker, F.; Dolinski, N. D.; Hawker, C. J.; Read de Alaniz, J. Controlling Dark Equilibria and Enhancing Donor–Acceptor Stenhouse Adduct Photoswitching Properties through Carbon Acid Design. *Journal of the American Chemical Society* **2018**, *140*, 10425–10429.

[243] Lerch, M. M.; Medved, M.; Lapini, A.; Laurent, A. D.; Iagatti, A.; Bussotti, L.; Szymanski, W.; Buma, W. J.; Foggi, P.; Di Donato, M.; Feringa, B. L. Tailoring Photoisomerization Pathways in Donor-Acceptor Stenhouse Adducts: The Role of the Hydroxy Group. *The Journal of Physical Chemistry A* **2018**, *122*, 955–964.

[244] Lee, J.; Sroda, M. M.; Kwon, Y.; El-Arid, S.; Seshadri, S.; Gockowski, L. F.; Hawkes, E. W.; Valentine, M. T.; Read de Alaniz, J. Tunable Photothermal Actuation Enabled by Photoswitching of Donor-Acceptor Stenhouse Adducts. *ACS Applied Materials and Interfaces* **2020**, *12*, 54075–54082.

[245] Mostafavi, S. H.; Li, W.; Clark, K. D.; Stricker, F.; Alaniz, J. R. d.; Bardeen, C. J. Photoinduced Deadhesion of a Polymer Film Using a Photochromic Donor–Acceptor Stenhouse Adduct. *Macromolecules* **2019**, *52*, 6311–6317.

[246] Helmy, S.; Read de Alaniz, J. *Advances in Heterocyclic Chemistry*; Chapter Three - Photochromic and Thermochromic Heterocycles; Academic Press, Elsevier: New York, USA, 2015; Vol. 117.

[247] Lerch, M. M.; Wezenberg, S. J.; Szymanski, W.; Feringa, B. L. Unraveling the Photoswitching Mechanism in Donor–Acceptor Stenhouse Adducts. *Journal of the American Chemical Society* **2016**, *138*, 6344–6347.

[248] Zeng, H.; Wasylczyk, P.; Parmeggiani, C.; Martella, D.; Burresi, M.; Wiersma, D. S. Light-Fueled Microscopic Walkers. *Advanced Materials* **2015**, *27*, 3883–3887, https://doi.org/10.1002/adma.201501446.

[249] Airinei, A.; Homocianu, M.; Dorohoi, D. O. Changes induced by solvent polarity in electronic absorption spectra of some azo disperse dyes. *Journal of Molecular Liquids* **2010**, *157*, 13–17.

[250] Masoud, M. S.; Ali, A. E.; Shaker, M. A.; Ghani, M. A. Solvatochromic behavior of the electronic absorption spectra of some azo derivatives of amino pyridines. *Spectrochimica Acta Part A: Molecular and Biomolecular Spectroscopy* **2004**, *60*, 3155–3159.

[251] Modrow, A.; Zargarani, D.; Herges, R.; Stock, N. The first porous MOF with photoswitchable linker molecules. *Dalton Transactions* **2011**, *40*, 4217–4222.

[252] Parker, R. M.; Gates, J. C.; Rogers, H. L.; Smith, P. G. R.; Grossel, M. C. Using the photoinduced reversible refractive-index change of an azobenzene copolymer to reconfigure an optical Bragg grating. *Journal of Materials Chemistry* **2010**, *20*, 9118–9125.

[253] Qin, C.; Feng, Y.; An, H.; Han, J.; Cao, C.; Feng, W. Tetracarboxylated Azobenzene/Polymer Supramolecular Assemblies as High-Performance Multiresponsive Actuators. *ACS Applied Materials and Interfaces* **2017**, *9*, 4066–4073.

[254] Akiyama, H.; Fukata, T.; Yamashita, A.; Yoshida, M.; Kihara, H. Reworkable adhesives composed of photoresponsive azobenzene polymer for glass substrates. *The Journal of Adhesion* **2017**, *93*, 823–830.

[255] Lui, B. F.; Tierce, N. T.; Tong, F.; Sroda, M. M.; Lu, H.; Read de Alaniz, J.; Bardeen, C. J. Unusual concentration dependence of the photoisomerization reaction in donor–acceptor Stenhouse adducts. *Photochemical and Photobiological Sciences* **2019**, *18*, 1587–1595.

[256] Lerch, M. M.; Di Donato, M.; Laurent, A. D.; Medved, M.; Iagatti, A.; Bussotti, L.; Lapini, A.; Buma, W. J.; Foggi, P.; Szymanski, W.; Feringa, B. L. Solvent Effects on the Actinic Step of Donor-Acceptor Stenhouse Adduct Photoswitching. *Angewandte Chemie International Edition* **2018**, *57*, 8063–8068, https://doi.org/10.1002/anie.201803058.

[257] Bahrenburg, J.; Röttger, K.; Siewertsen, R.; Renth, F.; Temps, F. Sequential photoisomerisation dynamics of the push–pull azobenzene Disperse Red 1. *Photochemical and Photobiological Sciences* **2012**, *11*, 1210–1219.

[258] Schmitt, T.; Hsu, L.-Y.; Oberhof, N.; Rana, D.; Dreuw, A.; Blasco, E.; Tegeder, P. Ultrafast excited states dynamics of orthogonal photoswitches for 4D printing. *Advanced Functional Materials* **2023**, *in preparation*.

[259] Nägele, T.; Hoche, R.; Zinth, W.; Wachtveitl, J. Femtosecond photoisomerization of cis-azobenzene. *Chemical Physics Letters* **1997**, *272*, 489–495.

[260] Quick, M.; Dobryakov, A. L.; Gerecke, M.; Richter, C.; Berndt, F.; Ioffe, I. N.; Granovsky, A. A.; Mahrwald, R.; Ernsting, N. P.; Kovalenko, S. A. Photoisomerization Dynamics and Pathways of trans- and cis-Azobenzene in Solution from Broadband Femtosecond Spectroscopies and Calculations. *The Journal of Physical Chemistry B* **2014**, *118*, 8756–8771.

[261] Laurent, A. D.; Medved, M.; Jacquemin, D. Using Time-Dependent Density Functional Theory to Probe the Nature of Donor-Acceptor Stenhouse Adduct Photochromes. *ChemPhysChem* **2016**, *17*, 1846–1851, https://doi.org/10.1002/cphc.201600041.

[262] Garcia-Iriepa, C.; Marazzi, M. Level of Theory and Solvent Effects on DASA Absorption Properties Prediction: Comparing TD-DFT, CASPT2 and NEVPT2. 2017; *https://mdpi-res.com/d_attachment/materials/materials-10-01025/article_deploy/materials-10-01025.pdf?version=1504430014*.

[263] Di Donato, M.; Lerch, M. M.; Lapini, A.; Laurent, A. D.; Iagatti, A.; Bussotti, L.; Ihrig, S. P.; Medved', M.; Jacquemin, D.; Szymański, W.; Buma, W. J.; Foggi, P.; Feringa, B. L. Shedding Light on the Photoisomerization Pathway of Donor–Acceptor Stenhouse Adducts. *Journal of the American Chemical Society* **2017**, *139*, 15596–15599.

[264] Ma, C.; Du, Y.; Kwok, W.; Phillips, D. Femtosecond Transient Absorption and Nanosecond Time-Resolved Resonance Raman Study of the Solvent-Dependent Photo-Deprotection Reaction of Benzoin Diethyl Phosphate. *Chemistry - A European Journal* **2007**, *13*, 2290–2305, https://doi.org/10.1002/chem.200600893.

[265] Fujitsuka, M.; Yahata, Y.; Watanabe, A.; Ito, O. Transient absorption study on photoinduced electron transfer between C60 and poly(N-vinylcarbazole) in polar solvent. *Polymer* **2000**, *41*, 2807–2812.

[266] Eslamian, M. Inorganic and Organic Solution-Processed Thin Film Devices. *Nano-Micro Letters* **2016**, *9*, 3.

[267] Wolf, H. C.; Port, H. Excitons in aromatic crystals: Trap states, energy transfer and sensitized emission. *Journal of Luminescence* **1976**, *12-13*, 33–46.

[268] Sugano, T. Atomically controlled surface and interface, and semiconductor device performance. *Applied Surface Science* **1992**, *60-61*, 698–701.

[269] Mbumba, M. T.; Malouangou, D. M.; Tsiba, J. M.; Akram, M. W.; Bai, L.; Yang, Y.; Guli, M. Compositional engineering solutions for decreasing trap state density and improving thermal stability in perovskite solar cells. *Journal of Materials Chemistry C* **2021**, *9*, 14047–14064.

[270] Krzystek, J.; Von Schütz, J. U. Triplet Excitons in Weak Organic Charge-Transfer Crystals. *Advances in Chemical Physics* **1993**, 167–329.

[271] Rudolph, H. D.; Dreizler, H.; Jaeschke, A.; Wendung, P. Mikrowellenspektrum, Hinderungspotential der internen Rotation und Dipolmoment des Toluols. *Zeitschrift für Naturforschung A* **1967**, *22*, 940–944.

[272] Gadhi, J.; Lahrouni, A.; Legrand, J.; Demaison, J. Moment dipolaire de CH3CN. *J. Chim. Phys.* **1995**, *92*, 1984–1992.

[273] Cofer-Shabica, D. V.; Menger, M. F. S. J.; Ou, Q.; Shao, Y.; Subotnik, J. E.; Faraji, S. INAQS, a Generic Interface for Nonadiabatic QM/MM Dynamics: Design, Implementation, and Validation for GROMACS/Q-CHEM simulations. *Journal of Chemical Theory and Computation* **2022**, *18*, 4601–4614.

[274] Merrick, J. P.; Moran, D.; Radom, L. An Evaluation of Harmonic Vibrational Frequency Scale Factors. *The Journal of Physical Chemistry A* **2007**, *111*, 11683–11700.

[275] Palafox, M. A. DFT computations on vibrational spectra: Scaling procedures to improve the wavenumbers. *Physical Sciences Reviews* **2018**, *3*.

[276] Duan, Y.; Zhao, H.; Xiong, C.; Mao, L.; Wang, D.; Zheng, Y. Learning from Spiropyrans: How to Make Further Developments of Donor-Acceptor Stenhouse Adducts. *Chinese Journal of Chemistry* **2021**, *39*, 985–998, https://doi.org/10.1002/cjoc.202000532.

[277] Mallo, N.; Foley, E. D.; Iranmanesh, H.; Kennedy, A. D. W.; Luis, E. T.; Ho, J.; Harper, J. B.; Beves, J. E. Structure-function relationships of donor-acceptor Stenhouse adduct photochromic switches. *Chemical Science* **2018**, *9*, 8242–8252.

[278] Huang, Y.; Du, Y.; Yuan, L.; Chu, Z.; He, L. Donor-acceptor Stenhouse adducts as new emerging photoswitches: synthesis, light-responsive properties, and applications in polymers science. *Journal of Macromolecular Science, Part A* **2021**, *58*, 717–724.

[279] Zulfikri, H.; Koenis, M. A. J.; Lerch, M. M.; Di Donato, M.; Szymański, W.; Filippi, C.; Feringa, B. L.; Buma, W. J. Taming the Complexity of Donor–Acceptor

Stenhouse Adducts: Infrared Motion Pictures of the Complete Switching Pathway. *Journal of the American Chemical Society* **2019**, *141*, 7376–7384.

[280] Bates, F. S.; Fredrickson, G. H. Block Copolymer Thermodynamics: Theory and Experiment. *Annual Review of Physical Chemistry* **1990**, *41*, 525–557.

[281] Mastel, S.; Govyadinov, A. A.; de Oliveira, T. V. A. G.; Amenabar, I.; Hillenbrand, R. Nanoscale-resolved chemical identification of thin organic films using infrared near-field spectroscopy and standard Fourier transform infrared references. *Applied Physics Letters* **2015**, *106*, 023113.

[282] Baumann, V. U.; Schreiber, H.; Tessmar, K. IR-spektroskopische untersuchungen zur taktizität von polymethylmethacrylat. *Die Makromolekulare Chemie* **1960**, *36*, 81–85, https://doi.org/10.1002/macp.1960.020360108.

[283] Huang, Y.; Yong, P.; Chen, Y.; Gao, Y.; Xu, W.; Lv, Y.; Yang, L.; Reis, R. L.; Pirraco, R. P.; Chen, J. Micellization and gelatinization in aqueous media of pH- and thermo-responsive amphiphilic ABC (PMMA82-b-PDMAEMA150-b-PNIPAM65) triblock copolymer synthesized by consecutive RAFT polymerization. *RSC Advances* **2017**, *7*, 28711–28722.

[284] Szilasi, S. Z.; Huszank, R.; Szikra, D.; Vaczi, T.; Rajta, I.; Nagy, I. Chemical changes in PMMA as a function of depth due to proton beam irradiation. *Materials Chemistry and Physics* **2011**, *130*, 702–707.

[285] Zolotarev, V. M. Comparison of polystyrene IR spectra obtained by the T, R, ATR, and DR methods. *Optics and Spectroscopy* **2017**, *122*, 749–756.

[286] Bhutto, A. A.; Vesely, D.; Gabrys, B. J. Miscibility and interactions in polystyrene and sodium sulfonated polystyrene with poly(vinyl methyl ether) PVME blends. Part II. FTIR. *Polymer* **2003**, *44*, 6627–6631.

[287] Antonova, K. T.; Yakovlev, V. A.; Zhizhin, G. N. Artificial dielectric films on crystalline quartz. *Thin Solid Films* **1987**, *151*, 1–8.

[288] Demtröder, W. *Experimentalphysik 1: Mechanik und Wärme*, 8th ed.; SpringerLink: Bücher; Springer Spektrum: Berlin, Heidelberg, 2018.

List of Publications, Conference contributions and supervised Theses

Publications related to this thesis

Electronic Properties of 6,13-Diazapentacene Adsorbed on Au(111): A Quantitative Determination of Transport, Singlet and Triplet States, and Electronic Spectra
Mohsen Ajdari, Tanja Schmitt, Marvin Hoffmann, Friedrich Maass, Hilmar Reiss, Uwe H. F. Bunz, Andreas Dreuw, and Petra Tegeder*
The Journal of Physical Chemistry C **2020**, *124* (24), 13196-13205.

Ultrafast excited states dynamics of orthogonal photoswitches for 4D printing
Tanja Schmitt, Li-Yun Hsu, Nils Oberhof, Debkumar Rana, Andreas Dreuw, Eva Blasco, Petra Tegeder*
Advanced Functional Materials **2023**, *in preparation*

Charateristics and long-term kinetics of orthogonal photoswitches for 4D printing
Tanja Schmitt, Christian Huck, Li-Yun Hsu, Peter Comba, Eva Blasco, Petra Tegeder*
in preparation

Modern ultramicrotomy facilitates multimodal imaging and volume analysis of soft matter across scales
Irene Wacker*, Ronald Curticean, Daniel Ryklin, Britta Weidinger, Frederik Mayer, Li-Yu Huang, Julian Hofmann, Monsur Islam, Nadine von Coelln, Christian Huck, Tanja Schmitt, Petra Tegeder, Jochen Kammerer, Christopher Barner-Kowollik, Martin Wegener, Eva Blasco, Rasmus R. Schröder*
Advanced Functional Materials **2023**, *in preparation*

Publications not related to this thesis

Stimulus-induzierte Anion-Kation-Exciplexbildung in Kupfer(I)-Komplexen als Mechanismus für mechanochrome Phosphoreszenz
Benjamin Hupp, Jörn Nitsch, Tanja Schmitt, Rüdiger Bertermann, Katharina Edkins, Florian Hirsch, Ingo Fischer, Michael Auth, Andreas Sperlich, Andreas Steffen*
Angewandte Chemie **2018**, *130* (41), 13860-13864.

Stimulus-Triggered Formation of an Anion-Cation Exciplex in Copper(I) Complexes as a Mechanism for Mechanochromic Phosphorescence
Benjamin Hupp, Jörn Nitsch, Tanja Schmitt, Rüdiger Bertermann, Katharina Edkins, Florian Hirsch, Ingo Fischer, Michael Auth, Andreas Sperlich, Andreas Steffen*
Angewandte Chemie International Edition **2018**, *57* (41), 13671-13675.

Control of Crystal Symmetry Breaking with Halogen-Substituted Benzylammonium in Layered Hybrid Metal-Halide Perovskites
Tanja Schmitt*, Sean Bourelle, Nathaniel Tye, Giancarlo Soavi, Andrew D. Bond, Sascha Feldmann, Boubacar Traore, Claudine Katan, Jacky Even, Siân E. Dutton, and Felix Deschler*
Journal of the American Chemical Society **2020**, *142* (11), 5060-5067.

Conference contributions related to this thesis

Electronic structure of diazapentacene on Au(111)
Tanja Schmitt, Hilmar Reiss, Uwe Bunz, Petra Tegeder
Poster awarded with poster price
5th International Fall School on Organic Electronics, Moscow, Russia, 2019.

Ultrafast excited states dynamics of two orthogonal molecular photoswitches
Tanja Schmitt, Li-Yun Hsu, Debkumar Rana, Eva Blasco, Petra Tegeder
Talk
DPG Meeting of the Condensed Matter Section, Regensburg, Germany, 2022.

Conference contributions not related to this thesis

Control of crystal symmetry breaking in aromatic hybrid metal-halide perovskites $(4\text{-}XC_6H_4CH_2NH_3)_2PbI_4$ with halogen substitution
Tanja Schmitt, Sean Bourelle, Sascha Feldmann, Giancarlo Soavi, Andrew Bond, Boubacar Traore, Claudine Katan, Siân Dutton and Felix Deschler
Poster
14th International Symposium on Functional π-Electron Systems, Berlin, Germany, 2019.

Halogen Substitution Controls Crystal Symmetry Breaking In Layered Hybrid Metal-Halide Perovskites
Tanja Schmitt, Sean Bourelle, Sascha Feldmann, Giancarlo Soavi, Andrew Bond, Boubacar Traore, Claudine Katan, Siân Dutton and Felix Deschler
Poster
13th International Conference on Optical Probes of Organic and Hybrid Optoelectronic Materials and Applications, Vilnius, Lithuania, 2019.

Supervised theses

The Electronic Structure of N-Heteropolycycles on Au(111)
Jakob Steidel
Ruprecht-Karls-Universität Heidelberg, February 2020, *Master thesis*

Acknowledgements

An dieser Stelle möchte ich mich bei allen bedanken, die mich im Laufe meiner Promotion unterstützt haben.
Zuerst danke ich ***Petra Tegeder***, die mich in Ihren Arbeitskreis aufgenommen und meine Doktorarbeit betreut hat. Herzlichen Dank für die vielen Möglichkeiten und die Unterstützung, die ich während meiner Promotion erfahren durfte. Es hat mir viel Freude bereitet, unterschiedliche Messmethoden kennenzulernen und zu verwenden sowie mein Wissen durch viele internationale Konferenzen zu bereichern.
Eva Blasco danke ich für die freundliche Übernahme des Zweitgutachtens, für den gelungenen wissenschaftlichen Austausch bei verschiedenen Kooperationsprojekten und für die Mitbenutzung ihrer Syntheselabore.
Hier sei auch dem Exzellenzcluster ***3D Matter Made to Order*** gedankt, in dessem Rahmen ich meine Promotion durchgeführt habe. Der ständige wissenschaftliche Austausch mit den anderen Clustermitgliedern und die Weiterbildungsmöglichkeiten sowohl innerhalb als auch außerhalb der Wissenschaft haben mir sehr gefallen.
Zudem möchte ich mich bei meinem Stipendiengeber der ***Carl-Zeiss Stiftung*** bedanken.
Ein herzliches Dankeschön gilt auch meinen Kollegen und meiner Kollegin aus meinem Arbeitskreis ***Mohsen Ajdari***, ***Vipilan Sivanesan***, ***Jakob Steidel***, ***Christian Huck***, ***Martin Richter***, ***Gabriel Sauter***, ***Nadine von Coelln***, ***Arnulf Stein***, ***Friedrich Maaß*** und ***Michael Tzschoppe***. Danke für die angenehme Atmosphäre, die gemeinsamen Pausen, Feiern und Ausflüge sowie für die fachliche Hilfe, wann immer nötig. Vielen Dank an Arnulf Stein für das Einlernen am 2PPE Setup sowie meinen Masteranden Jakob Steidel für die Hilfe beim Programmieren. Vielen Dank auch an Christian Huck für das Einlernen am s-SNOM, die Hilfe bei Matlab-Codes sowie die Begleitung bei IR Fernfeldmessungen und im Reinraum.
Des Weiteren bedanke ich mich bei meinen Synthese-Kooperationsparter und -partnerinnen ***Hilmar Reiss***, ***Britta Weidinger*** und ***Li-Yun Hsu***, die mich auch in Ihren lichtgeschützen Abzügen hat arbeiten lassen. Thank you Li-Yun! Des Weiteren bedanke ich mich bei ***Debkumar Rana***, der mich sowohl bei den transienten Absorptionsmessungen als auch deren Analyse unterstützt hat. Thank you Debkumar!
Auch gilt mein Dank ***Peter Comba***, der mich an seinem UV/VIS Spektrometer für temperaturabhängige Kinetikmessungen hat arbeiten lassen sowie ***Katharina Bleher*** und ***Thomas Josephy*** für die Einarbeitung.
Vielen Dank auch an ***Günter Meinusch*** für die Hilfe bei technischen Problemen von diversen elektronischen Geräten der experimentellen Aufbauten.
Danke auch an die Mitarbeiter des ***Massenspektrometrielabors*** für ihre Messungen diverser Moleküle, die ich gebracht habe.

Tiago Buckup danke ich für seine Hilfe und Expertise bei Laser- und Programmierfragestellungen.
Für die Unterstützung bei administrativen Tätigkeiten danke ich ***Angelika Neuner***, ***Marina Sommer*** und ***Anja Ihli***.
Vielen Dank an meine Freundin ***Lissa Eyre***, die mir trotz der räumlichen Distanz stets bei TA Fragen und englischsprachlichen Aspekten zur Seite stand. Thank you Lissa!
Zudem danke ich meinen Studienfreundinnen ***Chantal Roger*** und ***Lisa Lummel*** herzlich, die mir auch während der Promotion durch ihr Korrekturlesen und ihren emotionalen Beistand viel geholfen haben.
Ein riesiges herzliches Dankeschön geht an ***meine Eltern Angela und Harry Schmitt*** sowie ***meinem Bruder Wolfgang Schmitt***, die mich immer, sowie auch in der Entscheidung in Heidelberg zu promovieren, unterstützt haben. Nicht nur bei der Wohnungssuche und beim Umzug haben sie tatkräftig mitgeholfen, sondern standen mir auch stets beiseite, wenn es um die Strapazen der Doktorarbeit ging.
Und der Beste kommt zum Schluss: vielen lieben Dank an meinen Lebenspartner ***Andreas Stöcklin***, der mir stets zur Seite stand, mir immer auf die Beine half, meine Arbeit korrekturlas und mir als promovierter Chemiker auch fachlich oft weitergeholfen hat.

Appendix

In the following, additional data and information completing the results of the thesis can be found.

A. Data evaluation of 2PPE data

All 2PPE spectra were analysed using the Igor 6.3.7.2 software. They were fitted with the Multipeak Fitting 2 package applying an exponential background and Gaussian shaped peaks. To estimate the error Δx_0 of the obtained energetic positions x_0 of the signals, it was calculated by taking the x_0 error of the Igor fit Δx_{Igor} as well as the FWHM into account (see equation A.1). The latter was added as it is harder to determine x_0 of a broad peak than of a narrow one. Both parameters were weighted to gain a realistic error.

$$\Delta x_0 \;=\; \sqrt{(3\;\Delta x_{Igor})^2 \;+\; (0.2\;FWHM)^2} \tag{A.1}$$

To identify the energetic levels within an energy level diagram, the photon energies were subtracted from the energetic peak positions within a 2PPE spectrum according to the assignment to occupied or unoccupied states as explained in section 2.2.2.
The obtained energy levels $x_{0,i}$ were averaged according to equation A.2 and their errors $\Delta x_{0,i}$ were averaged according to equation A.3 to get the energy level $x_{0,tot}$ and the corresponding error $\Delta x_{0,tot}$, respectively.[288, p. 27 f.]

$$x_{0,tot} \;=\; \frac{1}{n}\;\sum_{i\;=\;1}^{n} x_{0,i} \tag{A.2}$$

$$\Delta x_{0,tot} \;=\; \sqrt{\frac{\sum_{i\;=\;1}^{n}\Delta x_{0,i}^2}{n\;(n\;-\;1)}} \tag{A.3}$$

For the 1C-2PPE measurements on DAP also measurements with a photon energy of 4.50 eV were conducted (figure A.1). Due to a poor cross section at this wavelength, the peaks are of weak intensity and not all peaks identified in section 4.3 can be fitted. Nevertheless, the signal of the excitonic state as well as the LUMO state could be fitted to the data. This excitonic signal located at (5.14 ± 0.10) eV is used to plot $E_{Final} - E_F$ versus the photon energy in figure 4.7 in order to assign all states correctly.

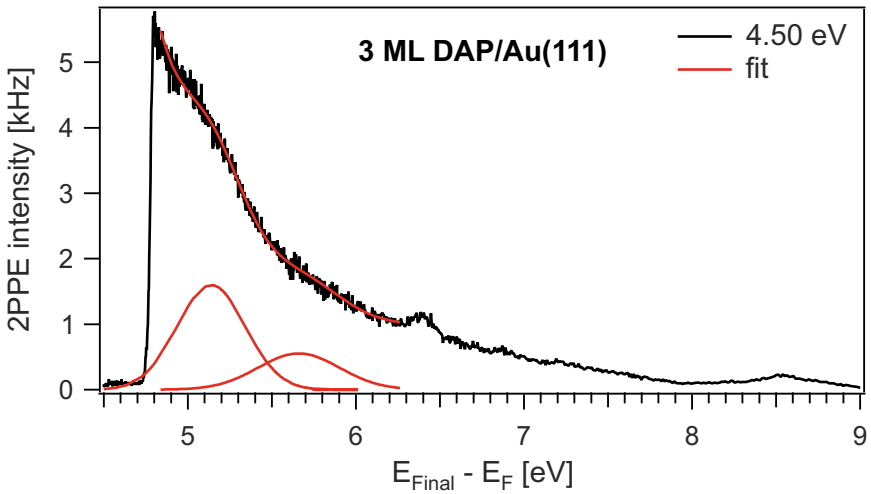

Figure A.1. 1C-2PPE spectrum of three ML thick layer of DAP on Au(111) with a photon energy of 4.50 eV. The peaks of the excitonic and the LUMO state are fitted to the data applying an exponential background.

In addition, 2C-2PPE experiments were carried out. The data reveals poor cross sections such that all signals posses weak intensity. At low coverages, two peaks can be identified in the spectra (figure A.2**a**) which both shift towards higher $E_{Final} - E_F$ energies for higher photon energies. Increasing the coverage leads to a broadening and intensity reduction of both peaks (figure A.2**b**). At higher coverages, no signals can be observed. This suggests adsorbate induced metal states.

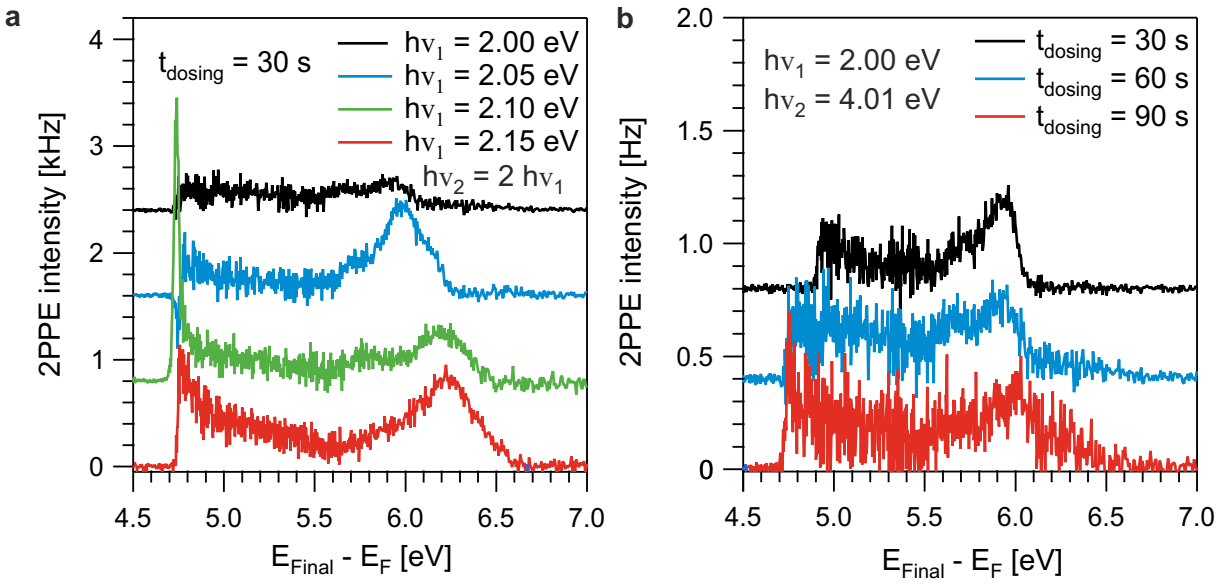

Figure A.2. 2C-2PPE spectra of DAP on Au(111) at different (a) photon energies and (b) coverages. All spectra consist of two peaks of weak intensity which are only present at low coverages but vanish for higher coverages.

Both states show dispersion (figure A.3**a**) with one state being occupied and one being unoccupied according to slope evaluation (figure A.3**b**). Due to their metal character,

their dispersion and their energetic location, the states can be assigned to the surface state and the image potential state, respectively.

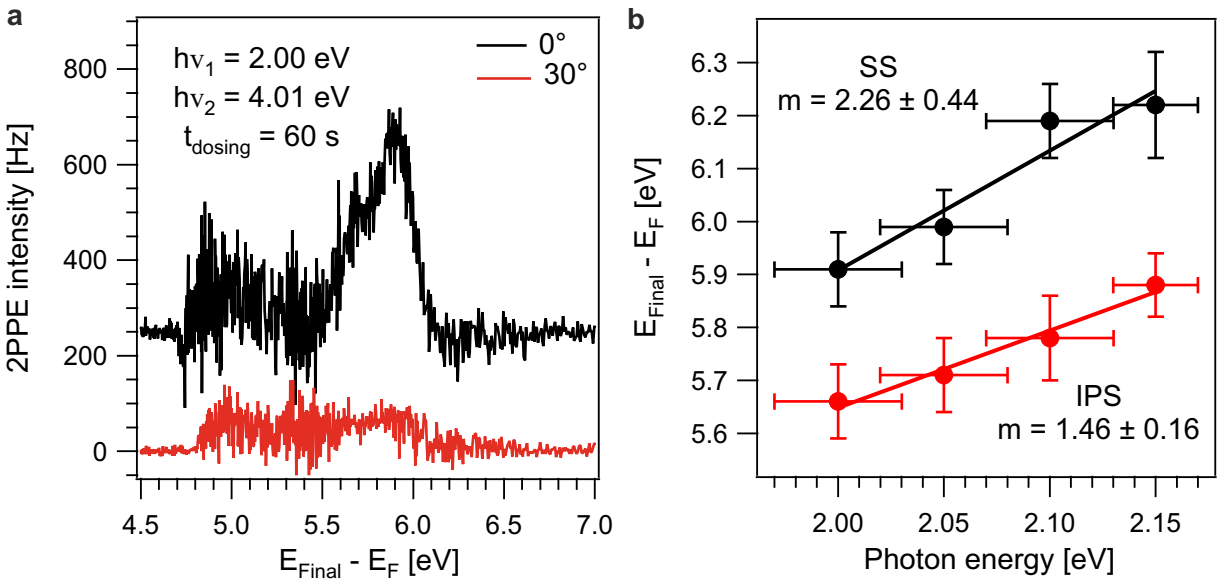

Figure A.3. Both peaks identified in the 2C-2PPE spectra of DAP on Au(111) (a) exhibit dispersion resulting in vanishing peak intensities at high angle and (b) can be related to the occupied SS and the unoccupied IPS.

B. Photoswitches

In order to estimate the spectral overlap of the absorption of the photoswitches Azo and DASA with the LEDs for inducing their switching, the knowledge of the UV/VIS spectra of the LEDs is required (figure B.1).

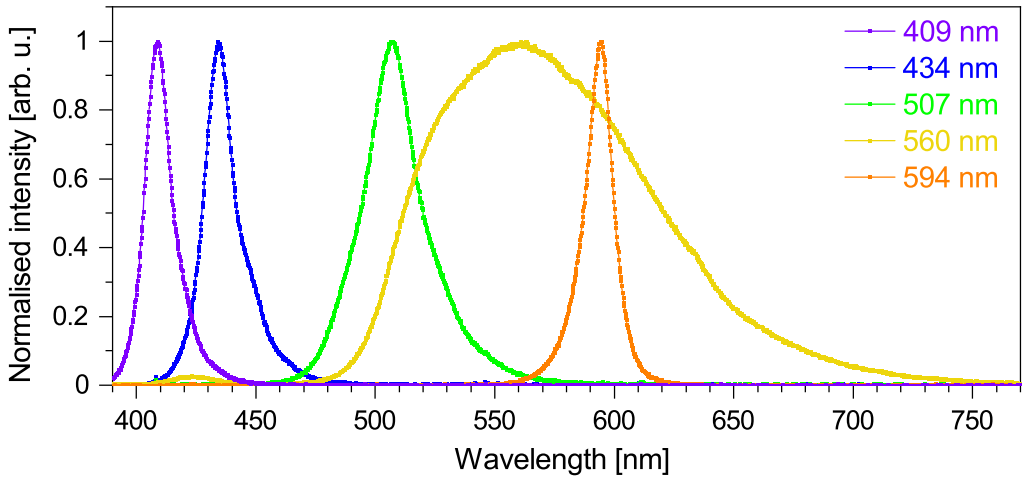

Figure B.1. Spectra of the LEDs used for switching DASA and Azo labelled with their maximum intensity wavelengths.

To ensure that no additional features are present in the 1:1 molar mixture which are not observed in the single photoswitches Azo and DASA, the absorption spectra in Tol are exemplarily shown in figure B.2. Thus, subtracting the absorption spectrum of Azo from the mixture agrees with the pure DASA spectrum and vice versa. This holds true for the MeCN and PMMA environment as well.

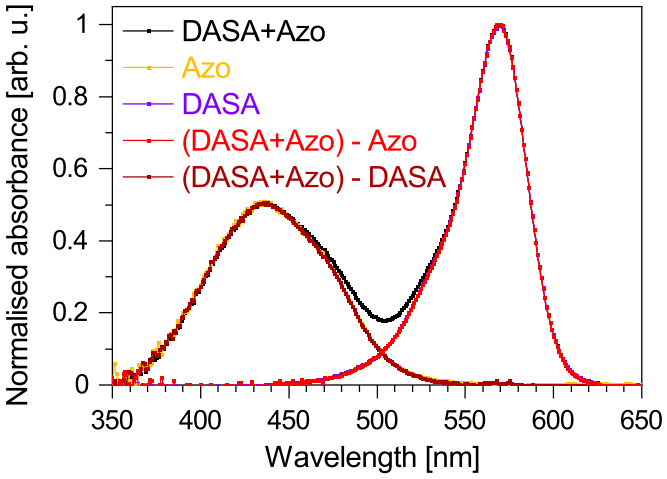

Figure B.2. Spectra of Azo, DASA and their equimolar mixture Azo+DASA. The spectra of the single compounds were subtracted from the mixture to account for additional features which are not observed.

To determine the amount of switched Azo and DASA molecules generated by LED illumination, which has its maximum intensity at a wavelength of 594 nm, in the TA experi-

ments, the geometric conditions of the TA setup were mimicked within a UV/VIS setup. The number of switched DASA molecules was thereby determined by comparing the absorptions at the maximum absorption wavelength 570 nm. Accordingly, about 80 % DASA molecules are switched in Tol (figure B.3**a**) while around 5 % DASA molecules are switched in MeCN (figure B.3**b**). As the DASA-PMMA blend film requires movement during illumination to prevent photobleaching, no analogous experiment could be carried out for the films since no movable sample holder is available in the UV/VIS setups.

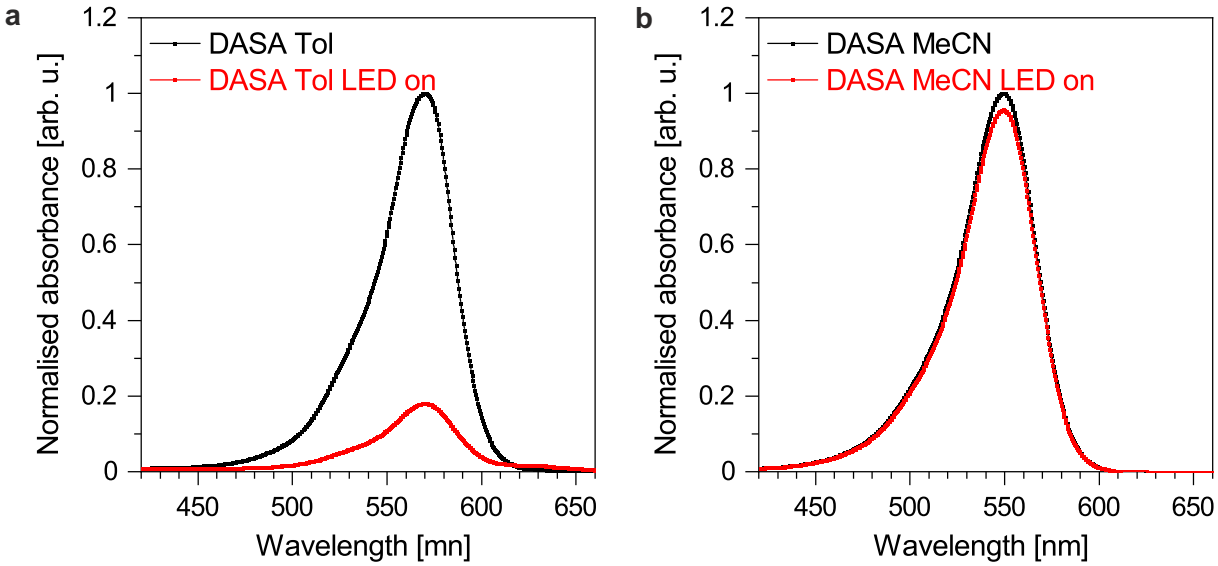

Figure B.3. Spectra of DASA before and during illumination by an LED with maximum intensity at 594 nm while mimicking the geometric conditions of the TA setup to determine the amount of switched molecules in (a) Tol and (b) MeCN.

For Azo, the maximum absorption shifts upon photoswitching. Thus, the integrals of the absorption band of *trans*-Azo before and during illumination by an LED with maximum intensity at a wavelength of 409 nm to induce photoswitching are compared to identify the amount of switched molecules. The absorption band before switching is integrated using the home-build integration function of the OriginPro software. However, the absorption band during illumination was fitted by two Gaussian peaks to obtain the integral of the *trans*-Azo absorption. Accordingly, the percentage of *cis*-Azo numbers about 60 % in Tol (figure B.4**a**), around 25 % in MeCN (figure B.4**b**) and about 50 % in the PMMA blend film (figure B.4**c**).

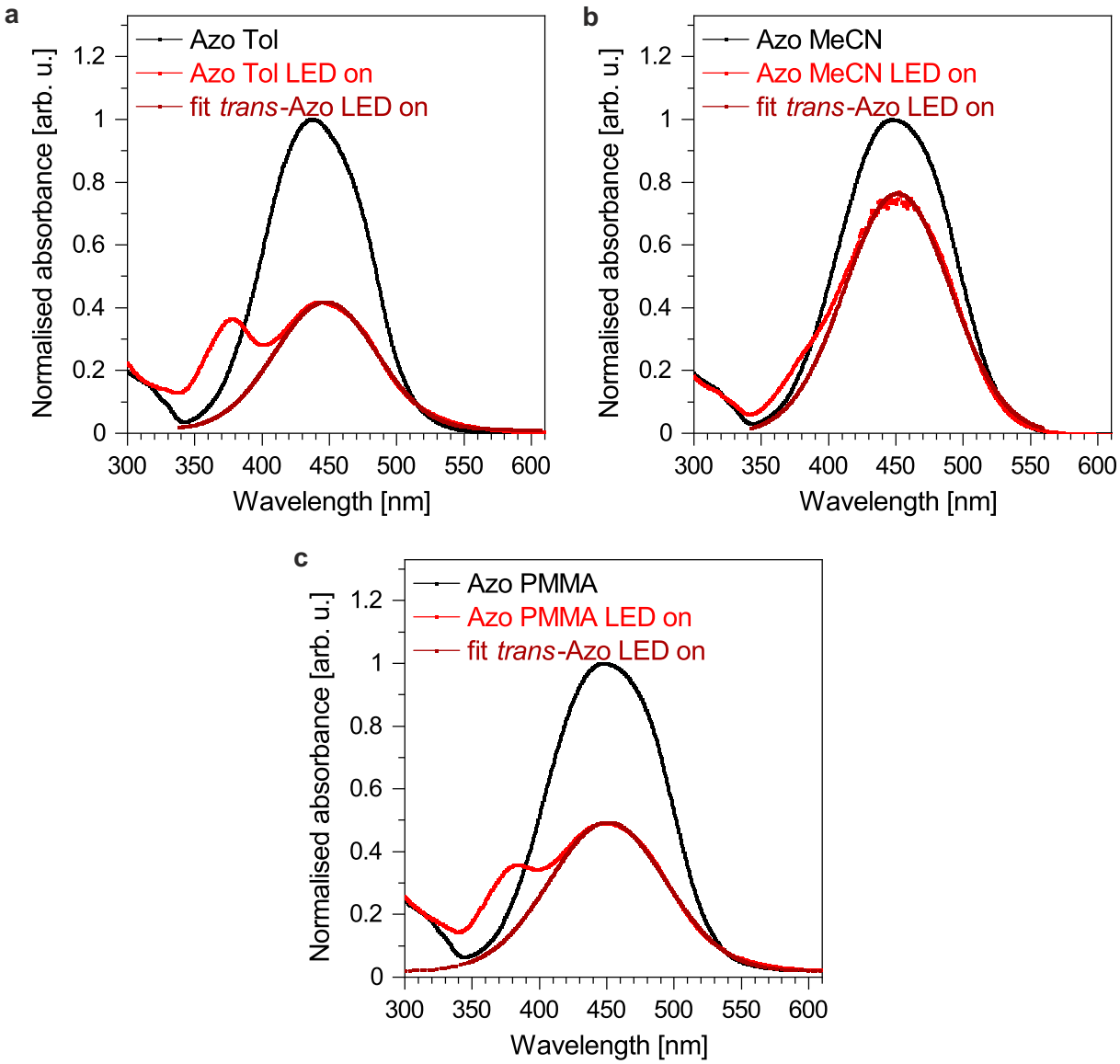

Figure B.4. Spectra of Azo before and during illumination by an LED with maximum intensity at 409 nm while mimicking the geometric conditions of the TA setup to determine the amount of switched molecules in (a) Tol, (b) MeCN and (c) as PMMA blend thin film.

To estimate the polarity influence of Azo and DASA on the photoswitching behaviour of the other photoswitch in comparison with the solvent polarity, their dipole moments were calculated by DFT using B3LYP as functional and 6-31++G(d,p) as basis set. The optimised geometries and dipole moments of DASA were calculated for the thermodynamically stable isomer **A** (table B.1) and the switched isomer **C'** (table B.2).

Table B.1. Optimised geometry and dipole moment of DASA isomer **A** by DFT calculations using the B3LYP functional and the basis set 6-31++G(d,p).

No.	Atom	x	y	z	No.	Atom	x	y	z
1	N	0.000000	0.000000	0.000000	23	H	-0.179811	-3.290559	-0.245175
2	C	0.000000	0.000000	1.732746	24	H	6.184757	-8.551381	-4.991846
3	N	1.425870	0.000000	2.046583	25	H	6.125769	-7.221185	-3.860407
4	C	2.055947	-1.174767	1.451163	26	H	5.288594	-7.051436	-5.003078
5	C	1.232271	-2.148387	0.661465	27	H	3.522693	-8.989723	-5.245769
6	C	0.325845	-1.397625	-0.268453	28	H	4.504838	-7.440034	-5.190271
7	O	-0.836343	0.000000	2.648241	29	H	-0.086819	-7.176814	-3.547231
8	C	2.431611	0.783801	2.757738	30	H	1.147320	-7.017842	-2.320572
9	O	3.271985	-1.367656	1.598281	31	H	1.088270	-5.887922	-3.652059
10	C	2.041986	-2.944474	-0.050016	32	H	1.250614	-8.491742	-4.722412
11	C	1.461063	-4.011517	-0.929761	33	H	1.428292	-8.260096	-3.285797
12	C	2.452068	-4.677060	-1.538500	34	H	4.214328	-5.907316	-2.660668
13	C	2.133462	-5.801593	-2.478666	35	H	1.710055	-6.196171	-1.578703
14	C	3.272386	-6.314179	-2.964164	36	H	3.470666	-4.406332	-1.353931
15	N	3.228038	-7.427827	-3.907254	37	H	3.102939	-2.818999	0.009411
16	C	4.110256	-8.295211	-4.682454	38	H	2.477600	1.762944	2.328713
17	C	5.538200	-7.915695	-4.423719	39	H	3.384766	0.305792	2.668827
18	O	-0.882746	-1.671564	-0.311643	40	H	-0.404869	1.736663	-1.066792
19	C	-0.166076	0.712375	-1.263543	41	H	-0.958373	0.262917	-1.824929
20	O	0.084177	-3.980561	-0.842427	42	H	0.822798	0.751042	-1.670403
21	C	1.838176	-7.797230	-4.159096	43	H	2.170816	0.850927	3.793296
22	C	0.931778	-6.906087	-3.362661					
Magnitude dipole moment 10.6 D									
Vector dipole moment (-10.6 D | 0.6 D | 0.1 D)									

Table B.2. Optimised geometry and dipole moment of DASA isomer **C'** by DFT calculations using the B3LYP functional and the basis set 6-31++G(d,p).

No.	Atom	x	y	z	No.	Atom	x	y	z
1	N	0.000000	0.000000	0.000000	23	H	-1.697056	-1.192085	-0.130000
2	C	0.000000	0.000000	1.460000	24	H	-0.688251	-1.192085	-1.556667
3	C	1.376501	0.000000	-0.486667	25	H	-0.183848	-2.065736	-0.130000
4	C	-0.688251	-1.192085	-0.486667	26	H	3.886970	2.154910	-0.265436
5	N	2.064752	1.192085	0.000000	27	H	3.954517	0.412178	-0.372158
6	C	0.707107	1.224745	1.960000	28	H	3.272010	1.342042	-1.684639
7	C	1.216360	2.106798	1.089228	29	H	1.385390	0.652263	3.877576
8	C	3.382567	1.281259	-0.622103	30	H	-1.657899	2.958220	5.145390
9	O	0.833553	3.382652	1.449856	31	H	0.769156	4.227282	4.651679
10	O	1.782064	-0.930000	-1.199561	32	H	2.244380	2.511815	2.858204
11	O	-0.536936	-0.930000	2.080000	33	H	2.459487	4.429914	2.898058
12	C	0.844154	1.462117	3.434745	34	H	3.562588	3.117046	1.873733
13	C	1.585038	2.745366	3.667908	35	H	4.228054	4.157884	3.109402
14	C	-0.518425	1.551552	4.055536	36	H	4.930906	3.064652	4.694655
15	C	-0.685927	2.894423	4.702559	37	H	5.270482	1.807896	3.529186
16	C	0.552244	3.233816	4.318703	38	H	6.088515	2.968350	3.389384
17	O	-1.441456	0.724510	4.095721	39	H	2.576510	4.567651	6.874852
18	N	2.654539	3.738730	3.636380	40	H	1.844774	5.406422	5.527970
19	C	3.801363	3.196350	2.913732	41	H	1.331778	3.785361	5.930538
20	C	3.213768	3.894437	4.976014	42	H	3.535659	2.941551	5.341109
21	C	5.058717	2.849232	3.654387	43	H	4.048655	4.562613	4.938541
22	C	2.166665	4.453536	5.893065					
Magnitude dipole moment 15.0 D									
Vector dipole moment (-12.8 D | -5.2 D | 5.7 D)									

The calculations of Azo were carried out for the thermodynamically stable isomer **A** (table B.3) and the switched isomer **B** (table B.4) but with shorter alkyl chains. Instead of the nonyl alkyl chains, the presented results of the *trans*-Azo isomer **A** feature a pentyl alkyl chain to minimise the calculation time. This simplification can be performed since the dipole moment stays unaltered in the range of ethyl to pentyl as side chains. For the *cis*-Azo isomer **B**, the results are shown for propyl side chains to minimise the calculation time since the dipole moment for ethyl and propyl side chains is equal.

Table B.3. Optimised geometry and dipole moment of Azo isomer **A** by DFT calculations using the B3LYP functional and the basis set 6-31++G(d,p).

No.	Atom	x	y	z	No.	Atom	x	y	z
1	C	-1.374658	1.788150	-0.288590	32	H	2.800377	0.917209	-1.524057
2	C	-0.959799	0.482961	-0.006459	33	H	-0.630886	2.564998	-0.448441
3	C	-1.931830	-0.501896	0.215957	34	H	-3.034417	3.125916	-0.591164
4	C	-3.294945	-0.193986	0.139110	35	H	-4.021466	-0.983618	0.313814
5	C	-3.704184	1.113646	-0.152973	36	H	-1.621519	-1.516803	0.452930
6	C	-2.735408	2.103359	-0.367122	37	H	8.272657	-1.403907	-0.812111
7	N	0.414068	0.206715	0.107616	38	H	7.114987	-0.346323	-1.551228
8	N	0.767722	-0.639693	-0.743325	39	H	7.801239	-3.037406	0.612564
9	C	2.139941	-0.911460	-0.608652	40	H	6.347786	-2.861355	1.593437
10	C	3.106622	-0.020392	-1.068423	41	H	6.349351	-3.899341	0.133997
11	C	4.472887	-0.319486	-0.946857	42	H	-7.515158	1.491791	0.703458
12	C	4.933061	-1.514155	-0.366220	43	H	-7.543655	1.082911	-0.995092
13	C	3.931989	-2.404138	0.066195	44	H	6.691000	0.669946	0.692787
14	C	2.563877	-2.114080	-0.052387	45	H	7.895284	-0.396899	1.374410
15	N	6.287995	-1.817774	-0.249295	46	H	9.568606	0.533389	-0.125951
16	C	6.709261	-2.958220	0.563562	47	H	8.364322	1.600234	-0.807575
17	C	-5.138625	1.503423	-0.237941	48	H	-7.851095	-1.261783	-0.425511
18	O	-5.940176	0.442624	0.030866	49	H	-7.822598	-0.852902	1.273040
19	C	-7.288351	0.733448	-0.016523	50	H	8.020751	2.609310	1.378805
20	C	-8.077902	-0.503439	0.294471	51	H	9.225033	1.542466	2.060428
21	C	-9.543309	-0.187326	0.242960	52	H	-9.770116	0.571017	0.962941
22	C	-10.332861	-1.424214	0.553955	53	H	-9.798613	0.162137	-0.735609
23	O	-5.514919	2.633098	-0.507463	54	C	-11.798269	-1.108102	0.502444
24	C	7.340275	-0.860974	-0.610911	55	H	-10.106054	-2.182558	-0.166027
25	C	7.589581	0.124943	0.491729	56	H	-10.077557	-1.773677	1.532524
26	C	8.670025	1.078391	0.075107	57	H	10.177615	3.721046	1.547674
27	C	8.919331	2.064308	1.177747	58	H	10.898358	2.472755	0.560066
28	C	9.999776	3.017758	0.761125	59	H	9.694074	3.539600	-0.121557
29	H	1.829625	-2.835082	0.295543	60	H	-12.361482	-1.990415	0.724287
30	H	4.189731	-3.362408	0.507057	61	H	-12.025076	-0.349758	1.222426
31	H	5.165826	0.426509	-1.321760	62	H	-12.053572	-0.758639	-0.476124
Magnitude dipole moment 6.8 D									
Vector dipole moment (5.8 D | -3.4 D | 0.9 D)									

Table B.4. Optimised geometry and dipole moment of Azo isomer **B** by DFT calculations using the B3LYP functional and the basis set 6-31++G(d,p).

No.	Atom	x	y	z	No.	Atom	x	y	z
1	C	0.000000	0.000000	0.000000	26	H	0.265631	4.533432	0.357037
2	C	0.000000	0.000000	1.400000	27	H	-0.193954	2.767720	2.050010
3	C	1.212436	0.000000	2.100000	28	H	1.212436	0.000000	3.189001
4	C	2.424870	0.000000	1.400001	29	H	3.367973	0.000000	1.944501
5	C	2.424870	0.000000	0.000000	30	H	1.212435	0.000000	-1.789000
6	C	1.212435	0.000000	-0.699999	31	H	-0.943102	0.000000	-0.544500
7	N	-1.264397	0.000000	2.130000	32	H	-0.471713	5.043276	-3.975079
8	N	-2.082051	0.851288	1.913781	33	H	0.204369	3.680754	-3.115131
9	C	-1.812467	1.887021	0.920715	34	H	-1.479181	3.670643	-3.582703
10	C	-2.577437	1.950283	-0.250105	35	H	-0.182116	6.204256	-0.588123
11	C	-2.318932	2.943451	-1.202359	36	H	0.952874	5.142838	-1.387034
12	C	-1.295456	3.873359	-0.983795	37	H	4.092155	0.889165	1.579511
13	C	-0.530486	3.810097	0.187025	38	H	4.092155	-0.889165	1.579511
14	C	-0.788992	2.816929	1.139280	39	C	5.688146	0.000000	3.541174
15	N	-1.025872	4.909092	-1.976861	40	H	6.523325	-0.873652	1.807936
16	C	-0.669286	4.284211	-3.247284	41	H	6.523324	0.873651	1.807937
17	C	3.723908	0.000000	-0.750000	42	C	1.491554	7.670547	-2.069245
18	O	4.919023	0.000000	-0.060000	43	H	0.617522	6.352446	-3.470522
19	C	4.663202	0.000000	1.316429	44	H	-0.517467	7.413863	-2.671611
20	C	5.962240	0.000000	2.066429	45	H	1.689126	8.429612	-2.797040
21	C	0.079218	5.746296	-1.519186	46	H	1.230220	8.128507	-1.138183
22	C	0.356188	6.810406	-2.539459	47	H	2.365210	7.067089	-1.937093
23	O	3.723908	0.000000	-1.970000	48	H	6.614793	0.000000	4.076174
24	H	-3.373555	1.226948	-0.420117	49	H	5.127063	0.873651	3.799666
25	H	-2.913969	2.992660	-2.113090	50	H	5.127063	-0.873651	3.799666
Magnitude dipole moment 4.2 D									
Vector dipole moment (-4.1 D | -0.8 D | -0.6 D)									

To determine the effective cross sections of *trans*-Azo according to equation 2.6 using equation 2.24, the decay curves in the different environments are fitted with monoexponential fits (figure B.5).

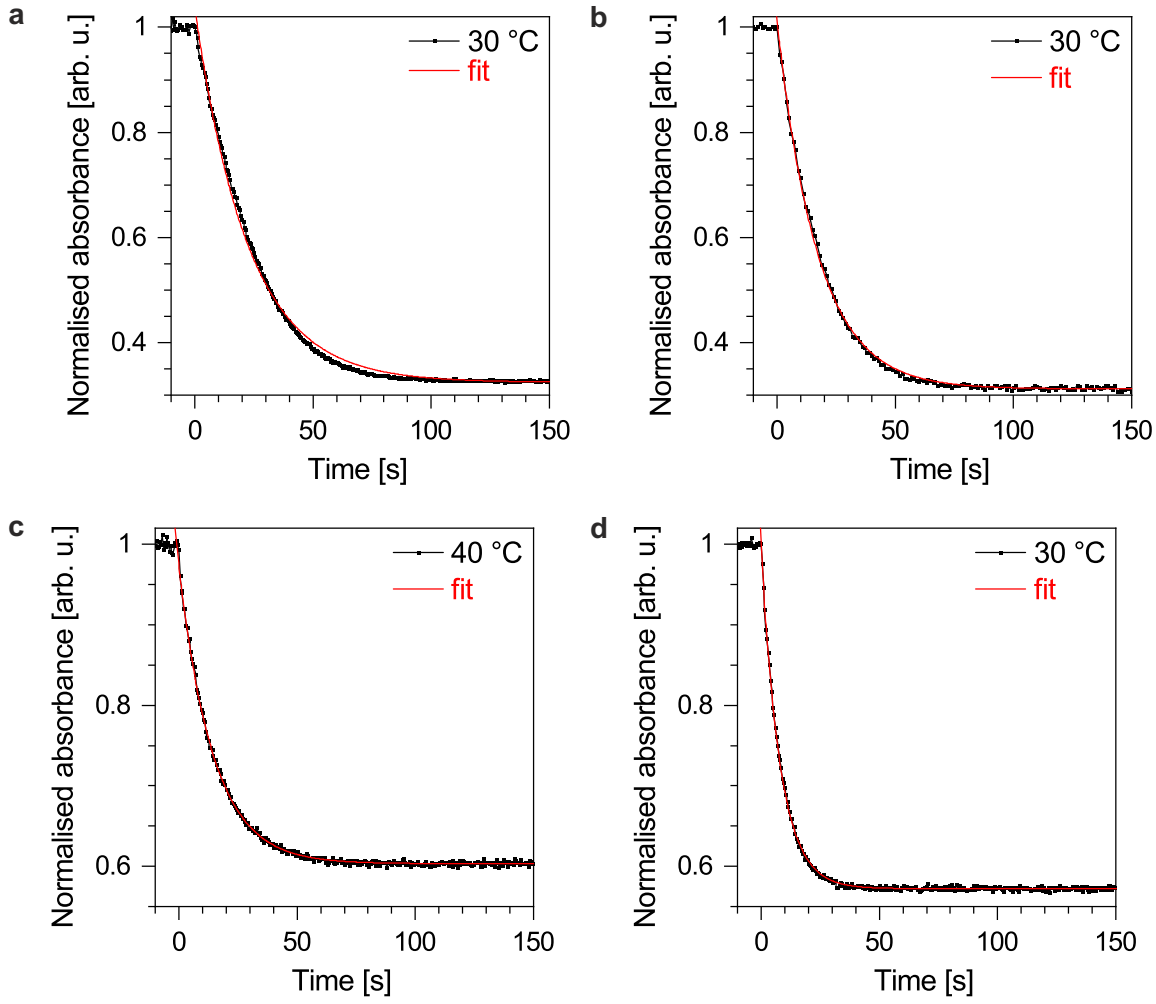

Figure B.5. Decay of the maximum intensity of *trans*-Azo in Tol upon orthogonal photoexcitation of (a) pure Azo and (b) Azo+DASA as well as upon photoexcitation with the simultaneous switching wavelength of (c) pure Azo and (d) simultaneously addressed Azo+DASA.

In order to assign the IR bands of the different DASA isomers, DFT calculations using the B3LYP functional were carried out with different basis sets relevant in literature.[256] In that course, the 6-311G(d,p) basis set was found to reproduce the experimental data best. Hence, the optimised geometries of the relevant DASA isomers **A** (table B.5), **C** (table B.6) and **C'** (table B.7) were calculated and their IR spectra are shown in section 5.5.

Table B.5. Optimised geometry of DASA isomer **A** by DFT calculations using the B3LYP functional and the basis set 6-311G(d,p).

No.	Atom	x	y	z	No.	Atom	x	y	z
1	C	0.000000	0.000000	0.000000	23	H	3.794957	-0.098282	-0.600773
2	N	0.000000	0.000000	1.460000	24	H	11.413155	2.286007	4.594696
3	C	1.376257	0.000000	1.947358	25	H	9.695471	2.024911	4.780285
4	C	2.516866	0.000000	0.973186	26	H	10.038177	2.912309	3.717059
5	C	2.247620	1.000000	-0.111944	27	H	11.618434	1.780892	1.940281
6	N	0.881547	1.444490	-0.372467	28	H	10.377361	2.722121	2.911388
7	C	3.649045	0.326983	1.611035	29	H	8.802610	0.647027	-1.219757
8	C	4.942395	0.397923	0.854585	30	H	8.181037	-0.066306	0.249212
9	O	4.717357	0.088605	-0.471341	31	H	7.887333	1.621458	-0.094671
10	O	1.602229	0.000000	3.166594	32	H	10.672673	1.187116	-0.166202
11	O	2.368090	0.671541	-1.301567	33	H	9.763948	0.142768	0.316132
12	C	-0.918238	0.000000	2.595094	34	H	7.749560	1.358478	3.171416
13	C	0.897716	2.838459	-0.806274	35	H	7.165243	-0.153469	0.958265
14	O	-0.559417	-0.916653	-0.620000	36	H	5.720239	0.914591	2.726032
15	C	5.931171	0.740525	1.691571	37	H	3.630510	0.537476	2.659962
16	C	7.333708	0.880018	1.178317	38	H	-1.530612	0.876162	2.547784
17	C	8.145786	1.226703	2.186256	39	H	-0.358248	0.000000	3.506857
18	N	9.571230	1.424628	1.940221	40	H	-0.103447	3.164215	-0.997205
19	C	9.859044	1.187118	0.528714	41	H	1.478273	2.926934	-1.700716
20	C	8.591678	0.821092	-0.185296	42	H	1.182434	3.379222	0.072027
21	C	10.804799	1.780892	2.635190	43	H	-1.531597	-0.876162	2.562994
22	C	10.509101	2.024909	4.085369					

Table B.6. Optimised geometry of DASA isomer **A** by DFT calculations using the B3LYP functional and the basis set 6-311G(d,p).

No.	Atom	x	y	z	No.	Atom	x	y	z
1	C	2.530030	-1.180650	-1.310640	23	H	4.271340	-0.882247	-1.998810
2	C	1.373230	-0.673751	-0.868843	24	H	0.583921	-4.757490	0.936458
3	C	0.247726	-1.565750	-0.419743	25	H	0.362284	-3.249600	1.926080
4	N	0.634426	-2.950250	-0.135943	26	H	-0.985541	-3.844230	0.860641
5	C	1.610830	-3.411850	-1.112640	27	H	4.783340	-2.247410	-1.818660
6	N	2.733830	-2.533650	-1.360940	28	H	4.406990	-3.709800	-0.807734
7	O	1.490050	-4.469330	-1.683980	29	H	4.010050	-3.704270	-2.581930
8	O	3.514870	-0.342174	-1.714440	30	H	2.137180	1.273030	-1.192320
9	O	-0.887768	-1.170660	-0.302170	31	H	-1.430560	2.968240	-1.210090
10	C	0.118669	-3.746680	0.960503	32	H	-0.500850	3.001740	1.185650
11	C	4.064320	-3.082160	-1.660630	33	H	0.552023	0.427910	1.267630
12	C	1.195010	0.811812	-0.820345	34	H	2.564620	-0.050042	2.033000
13	C	-0.002923	1.228900	-1.672880	35	H	3.268020	0.339859	0.402489
14	C	-0.650172	2.286030	-0.841858	36	H	1.866110	3.584530	0.143057
15	C	-0.166655	2.303420	0.404206	37	H	2.893680	2.287680	-0.610360
16	C	0.881502	1.260620	0.606710	38	H	4.293360	4.150830	0.285399
17	O	-0.342105	0.806996	-2.752790	39	H	4.601840	2.600460	1.181720
18	N	2.046360	1.814890	1.242110	40	H	3.574270	3.897320	1.935140
19	C	3.004040	0.754052	1.401250	41	H	4.999460	0.476789	2.195860
20	C	2.613700	2.785130	0.345112	42	H	4.697640	2.101960	1.440940
21	C	3.854250	3.399870	0.979666	43	H	3.994240	1.712060	3.071450
22	C	4.258220	1.297870	2.072690					

Table B.7. Optimised geometry of DASA isomer **A** by DFT calculations using the B3LYP functional and the basis set 6-311G(d,p).

No.	Atom	x	y	z	No.	Atom	x	y	z
1	N	0.000000	0.000000	0.000000	23	H	-1.697056	-1.192085	-0.130000
2	C	0.000000	0.000000	1.460000	24	H	-0.688251	-1.192085	-1.556667
3	C	1.376501	0.000000	-0.486667	25	H	-0.183848	-2.065736	-0.130000
4	C	-0.688251	-1.192085	-0.486667	26	H	3.886970	2.154910	-0.265436
5	N	2.064752	1.192085	0.000000	27	H	3.954517	0.412178	-0.372158
6	C	0.707107	1.224745	1.960000	28	H	3.272010	1.342042	-1.684639
7	C	1.216360	2.106798	1.089228	29	H	1.385390	0.652263	3.877576
8	C	3.382567	1.281259	-0.622103	30	H	-1.657899	2.958220	5.145390
9	O	0.833553	3.382652	1.449856	31	H	0.769156	4.227282	4.651679
10	O	1.782064	-0.930000	-1.199561	32	H	2.244380	2.511815	2.858204
11	O	-0.536936	-0.930000	2.080000	33	H	2.459487	4.429914	2.898058
12	C	0.844154	1.462117	3.434745	34	H	3.562588	3.117046	1.873733
13	C	1.585038	2.745366	3.667908	35	H	4.228054	4.157884	3.109402
14	C	-0.518425	1.551552	4.055536	36	H	4.930906	3.064652	4.694655
15	C	-0.685927	2.894423	4.702559	37	H	5.270482	1.807896	3.529186
16	C	0.552244	3.233816	4.318703	38	H	6.088515	2.968350	3.389384
17	O	-1.441456	0.724510	4.095721	39	H	2.576510	4.567651	6.874852
18	N	2.654539	3.738730	3.636380	40	H	1.844774	5.406422	5.527970
19	C	3.801363	3.196350	2.913732	41	H	1.331778	3.785361	5.930538
20	C	3.213768	3.894437	4.976014	42	H	3.535659	2.941551	5.341109
21	C	5.058717	2.849232	3.654387	43	H	4.048655	4.562613	4.938541
22	C	2.166665	4.453536	5.893065					

The kinetic traces of the bands at 1487.0 cm^{-1} and 1575.6 cm^{-1} upon thermal backswitching DASA in Tol show unexpected behaviour (figure B.6).

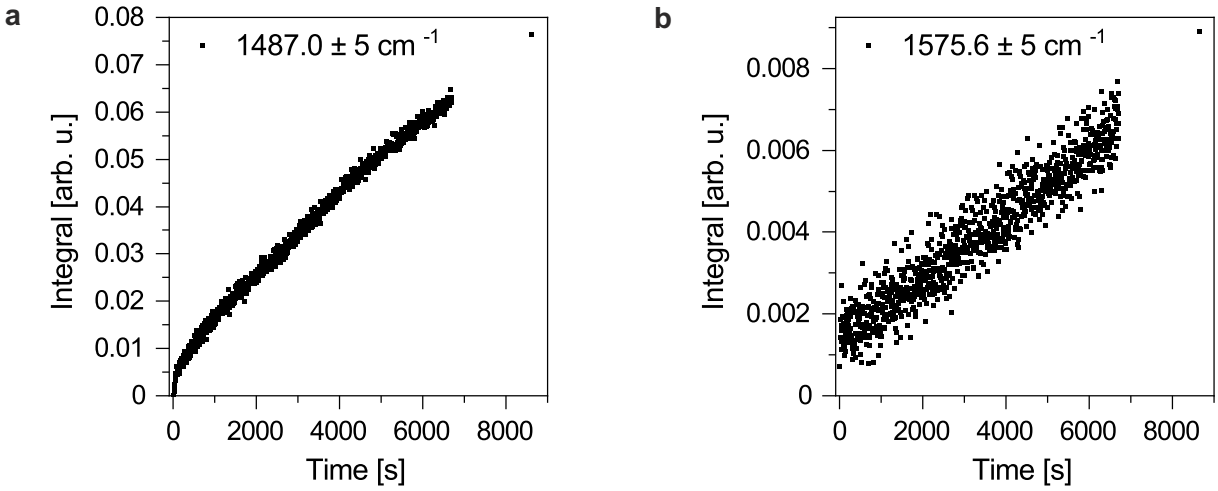

Figure B.6. Kinetic traces of the bands at (a) 1487.0 cm^{-1} and (b) 1575.6 cm^{-1} upon thermal backswitching DASA in Tol in order to determine $k_{(\mathbf{B'}\rightarrow\mathbf{C})_{-1}}$ and $k_{(\mathbf{C}\rightarrow\mathbf{C'})_{-1}}$, respectively. However, (a, b) both increase linearly instead of (a) exponentially increasing and (b) exponentially decreasing such that no time constants can be obtained.

With the aid of the DFT calculations, the IR absorption bands of *Z*-DASA in the different environments investigated can be assigned to the vibrational modes causing the absorption (table B.8).

Table B.8. Assignment of the frequencies found in DASA in a KBr, Tol and MeCN environment to the three dominating vibrational modes based on the theoretical calculated vibrations using DFT with the B3LYP functional, the 6-311G(d,p) basis set and a scaling factor of 0.9682.

Frequency DFT [cm^{-1}]	Frequency in KBr [cm^{-1}]	Frequency in Tol [cm^{-1}]	Frequency in MeCN [cm^{-1}]	Vibrational modes
1073.6	1076.3	1076.2	1078.2	$\upsilon(C\text{-}N)_{ring}$, $\delta(C\text{-}H)_{methyl}$, $\delta(C\text{-}H)_{chain}$
1079.6	1123.7	1120.5	1133.8	$\upsilon(C\text{-}N)_{chain}$, $\delta(C\text{-}H)_{ethyl}$, $\delta(C\text{-}H)_{chain}$
1105.2	1145.7	1146.5	1147.3	$\upsilon(C\text{-}N)_{chain}$, $\delta(C\text{-}H)_{ethyl}$, $\delta(C\text{-}C)_{chain}$
1162.2	1172.4	1175.8	1173.4	$\upsilon(C\text{-}N)_{chain}$, $\delta(C\text{-}H)_{ethyl}$, $\delta(C\text{-}H)_{chain}$
1197.4	1207.1	1208.2	1203.3	$\delta(C\text{-}H)_{chain}$, $\upsilon(C\text{-}C)_{chain}$, $\upsilon(C\text{-}N)_{ring}$
1245.7	1231.9	1225.2	1232.7	$\upsilon(C\text{-}N)$, $\delta(C\text{-}H)_{ethyl}$, $\delta(C\text{-}H)_{methyl}$
1258.8	1260.0	1260.5	1264.6	$\delta(C\text{-}H)_{chain}$, $\delta(C\text{-}C)_{chain}$, $\delta(C\text{-}H)_{ethyl}$
1319.7	1308.2	1320.5	1312.4	$\upsilon(C\text{-}N)_{chain}$, $\delta(C\text{-}C)_{chain}$, $\delta(C\text{-}H)_{chain}$
1349.7	1340.5	-	-	$\delta(C\text{-}H)_{ethyl}$, $\delta(C\text{-}H)_{chain}$, $\delta(O\text{-}H)$
1358.6	1350.8	1352.3	1354.6	$\upsilon(C\text{-}N)_{ring}$, $\delta(C\text{-}H)_{methyl}$, $\delta(O\text{-}H)$
1376.6	1367.8	1372.3	1373.3	$\delta(C\text{-}C)_{ring}$, $\upsilon(C\text{-}N)$, $\delta(C\text{-}C)_{chain}$
1392.8	-	1383.6	1387.7	$\upsilon(C\text{-}N)_{chain}$, $\delta(C\text{-}H)_{methyl}$, $\delta(O\text{-}H)$
1437.5	1421.1	1410.1	1416.8	$\upsilon(C\text{-}C)_{ring}$, $\upsilon(C\text{-}N)_{ring}$, $\upsilon(C\text{-}N)_{chain}$,
1440.6	-	1422.6	-	$\delta(C\text{-}H)_{ethyl}$, $\delta(O\text{-}H)$, $\delta(C\text{-}H)_{chain}$
1464.0	1457.3	1461.4	1464.2	$\delta(C\text{-}H)_{methyl}$, $\upsilon(C\text{-}N)_{ring}$, $\delta(C\text{-}H)_{ethyl}$
1469.2	1469.5	1468.9	1475.1	$\delta(C\text{-}H)_{ethyl}$, $\upsilon(C\text{-}C)_{chain}$, $\delta(O\text{-}H)$
1495.9	1493.5	1485.5	1500.3	$\upsilon(C\text{-}C)_{chain}$, $\upsilon(C\text{-}C)_{ring}$, $\delta(C\text{-}H)_{chain}$
1554.7	1555.4	1553.4	1561.9	$\upsilon(C\text{-}N)_{chain}$, $\upsilon(C\text{-}C)_{chain}$, $\upsilon(C{=}O)$
1612.3	1597.9	1610.8	1599.1	$\upsilon(C\text{-}C)_{chain}$, $\upsilon(C{=}O)$, $\delta(C\text{-}C)_{ring}$
1619.0	1622.0	1623.7	-	$\upsilon(C\text{-}C)_{chain}$, $\upsilon(C\text{-}N)_{chain}$, $\upsilon(C{=}O)$
1661.8	1635.5	1650.6	1627.4	$\upsilon(C{=}O)$, $\delta(C\text{-}C)_{ring}$, $\upsilon(C\text{-}C)_{chain}$
1715.6	1687.7	1709.1	1696.5	$\upsilon(C{=}O)$, $\delta(C\text{-}C)_{ring}$, $\delta(C\text{-}H)_{methyl}$

In order to validate the monoexponential fit applied to the decay of the IR absorption band at 1616.3 cm^{-1} referring to the closed zwitterionic isomer **C'**, the limit value is examined. Since the respective integral of the photoswitching amounts to 0.014, the absolute limit value of the backswitching process is expected to be the same but with different sign. This holds true (figure B.7).

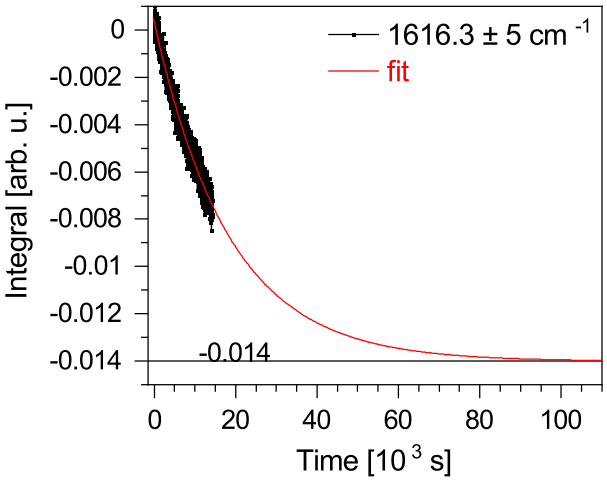

Figure B.7. Kinetic trace of the integral of the band at 1616.3 cm^{-1} with ± 5 cm^{-1} width upon thermal backswitching of DASA in MeCN in order to determine $k_{(\mathbf{C}\rightarrow\mathbf{C'})\text{-}1}$. The fit converges at the absolute value before starting the experiment as expected.

GESAMTFAKULTÄT FÜR MATHEMATIK, INGENIEUR- UND NATURWISSENSCHAFTEN

COMBINED FACULTY OF MATHEMATICS, ENGINEERING AND NATURAL SCIENCES

RUPRECHT-KARLS-
UNIVERSITÄT
HEIDELBERG

Eidesstattliche Versicherung gemäß § 8 der Promotionsordnung für die Gesamtfakultät für Mathematik, Ingenieur- und Naturwissenschaften der Universität Heidelberg / Sworn Affidavit according to § 8 of the doctoral degree regulations of the Combined Faculty of Mathematics, Engineering and Natural Sciences at Heidelberg University

1. Bei der eingereichten Dissertation zu dem Thema / The thesis I have submitted entitled

   Laser spectroscopy of functional materials

   handelt es sich um meine eigenständig erbrachte Leistung / is my own work.

2. Ich habe nur die angegebenen Quellen und Hilfsmittel benutzt und mich keiner unzulässigen Hilfe Dritter bedient. Insbesondere habe ich wörtlich oder sinngemäß aus anderen Werken übernommene Inhalte als solche kenntlich gemacht. / I have only used the sources indicated and have not made unauthorised use of services of a third party. Where the work of others has been quoted or reproduced, the source is always given.

3. Die Arbeit oder Teile davon habe ich ~~wie folgt~~/bislang nicht[1)] an einer Hochschule des In- oder Auslands als Bestandteil einer Prüfungs- oder Qualifikationsleistung vorgelegt. / I have not yet/have already[1)] presented this thesis or parts thereof to a university as part of an examination or degree.

   Titel der Arbeit / Title of the thesis: ——————————

   Hochschule und Jahr / University and year: ——————————

   Art der Prüfungs- oder Qualifikationsleistung / Type of examination or degree: ——————

4. Die Richtigkeit der vorstehenden Erklärungen bestätige ich. / I confirm that the declarations made above are correct.

5. Die Bedeutung der eidesstattlichen Versicherung und die strafrechtlichen Folgen einer unrichtigen oder unvollständigen eidesstattlichen Versicherung sind mir bekannt. / I am aware of the importance of a sworn affidavit and the criminal prosecution in case of a false or incomplete affidavit.

Ich versichere an Eides statt, dass ich nach bestem Wissen die reine Wahrheit erklärt und nichts verschwiegen habe. / I affirm that the above is the absolute truth to the best of my knowledge and that I have not concealed anything.

Heidelberg, den 09.01.2023 — Tanja Schmitt

Ort und Datum / Place and date — Unterschrift / Signature

[1)] Nicht Zutreffendes streichen. Bei Bejahung sind anzugeben: der Titel der andernorts vorgelegten Arbeit, die Hochschule, das Jahr der Vorlage und die Art der Prüfungs- oder Qualifikationsleistung. / Please cross out what is not applicable. If applicable, please provide: the title of the thesis that was presented elsewhere, the name of the university, the year of presentation and the type of examination or degree.

The German text is legally binding.